

**Universidade do Minho**  
Escola de Ciências

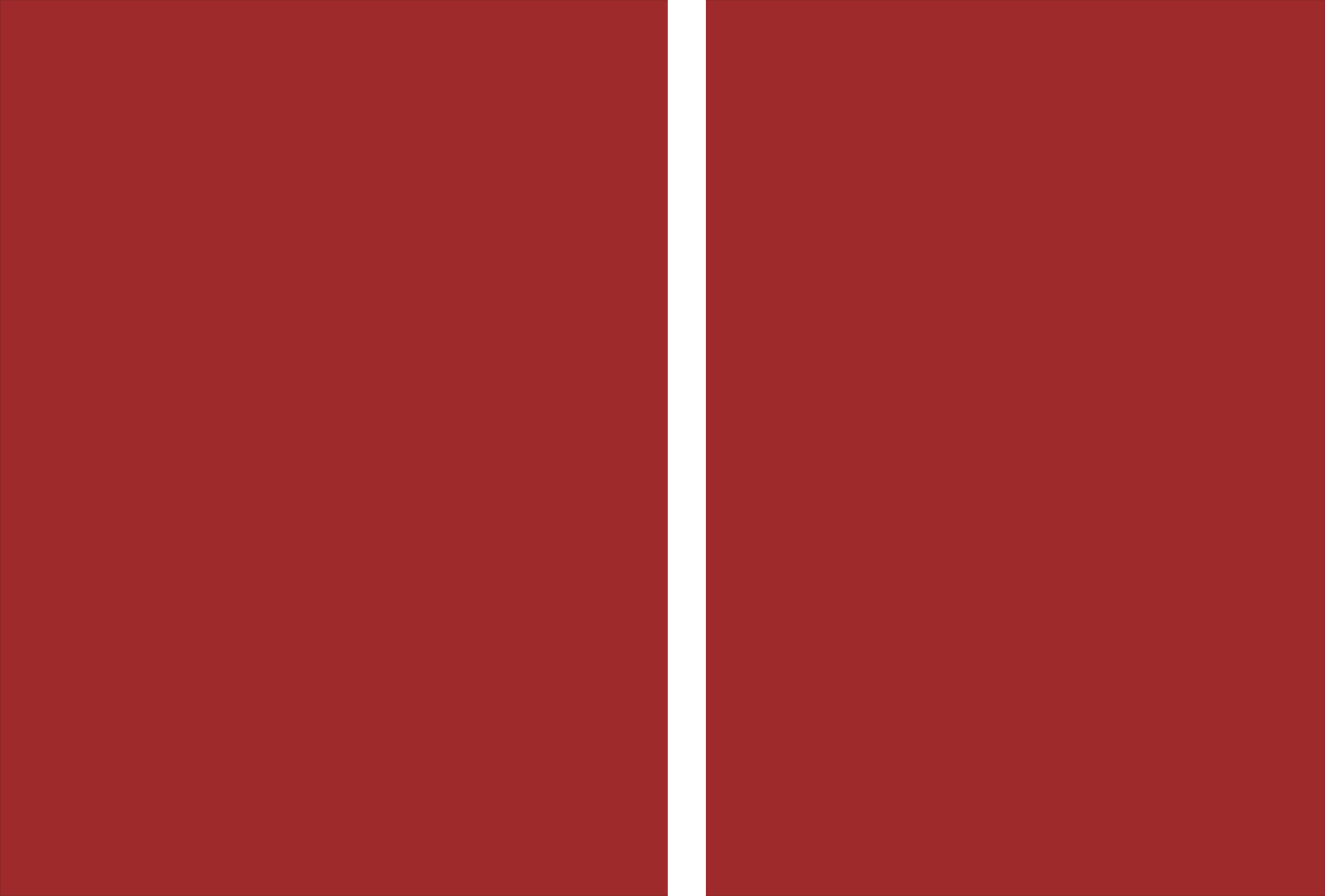
André Jorge Carvalho Chaves

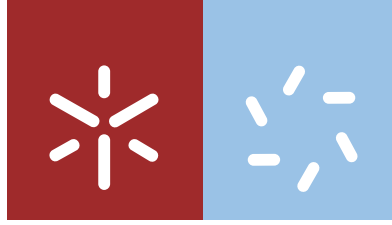
**Photonics of graphene and other  
two-dimensional materials heterostructures**

André Jorge Carvalho Chaves **Photonics of graphene and other two-dimensional materials heterostructures**

UMinho | 2018

março de 2018





**Universidade do Minho**  
Escola de Ciências

André Jorge Carvalho Chaves

**Photonics of graphene and other  
two-dimensional materials heterostructures**

Tese de Doutoramento em Ciências  
Especialidade em Física

Trabalho efetuado sob a orientação do  
**Professor Doutor Nuno Miguel Machado Reis Peres**

março de 2018

## DECLARAÇÃO

André Jorge Carvalho Chaves

Endereço electrónico: andrej6@gmail.com Telefone: 911 163 527

Número do Bilhete de Identidade: 14886500

Título da tese:

Photonics of graphene and other two-dimensional materials heterostructures

Orientador:


Nuno Miguel Machado Reis Peres Ano de conclusão: 2018

Designação do Ramo de Conhecimento do Doutoramento:

Ciências com Especialidade em Física

É AUTORIZADA A REPRODUÇÃO INTEGRAL DESTA TESE APENAS PARA EFEITOS DE INVESTIGAÇÃO, MEDIANTE DECLARAÇÃO ESCRITA DO INTERESADO, QUE A TAL SE COMPROMETE;

Universidade do Minho, 21 de Março de 2018

Assinatura: 

## STATEMENT OF INTEGRITY

I hereby declare having conducted my thesis with integrity. I confirm that I have not used plagiarism or any form of falsification of results in the process of the thesis elaboration. I further declare that I have fully acknowledged the Code of Ethical Conduct of the University of Minho.

University of Minho, 21 de Março de 2018

Full name:  
André Jorge Carvalho Chaves

Signature:  




# RESUMO

---

## Fotónica de heteroestruturas de grafeno e outros materiais bidimensionais

Essa tese aborda o tema da interação da luz com materiais bidimensionais. Ela inicia-se com uma revisão do estado da arte dos materiais bidimensionais, focando-se, em particular, naqueles que são mais promissores para o uso em nanofotónica: grafeno, monocamadas de dicalcogenetos de metais de transição e nitreto de boro hexagonal. De seguida discutimos as propriedades ópticas desses materiais e nas suas quasi-partículas/modos coletivos: plasmões, fonões, excitações e polaritões.

O objectivo primeiro desta tese é descrever microscopicamente a interação da luz com os portadores de carga nestes novos materiais bidimensionais. Para isso é desenvolvido em detalhe o formalismo das equações semicondutoras de Bloch. Também são derivadas as expressões para a susceptibilidade e a condutividade óptica do grafeno utilizando a fórmula de Mermin. Esses resultados são utilizados ao longo da tese.

As equações semicondutoras de Bloch são utilizadas para tratar o sistema de uma folha de grafeno com bombeamento óptico. Após um rápido período transiente, a distribuição eletrónica assumirá uma configuração diferente do equilíbrio termodinâmico e manter-se-á estável enquanto a luz de bombeamento persistir. Nessa situação derivamos a nova susceptibilidade eletrónica a que um segundo pulso de teste irá estar sujeito. A partir da susceptibilidade calculamos a relação de dispersão dos plasmões, a qual se revela fortemente anisotrópica. Finalmente encontramos fórmulas semianalíticas para a susceptibilidade, condutividade óptica e relação de dispersão do plasmão que dependem da intensidade, frequência e polarização do bombeamento.

Seguidamente tratamos o problema de excitações em monocamadas de dicalcogenetos de metais de transição. A partir das equações semicondutoras de Bloch deduzimos a equação de Bethe-Salpeter. As soluções da parte homogénea correspondem às funções de onda dos excitações e às suas energias. A partir da solução da parte não homogénea podemos calcular as propriedades ópticas. É utilizado o Hamiltoniano de Dirac em 2D com um termo de massa para tratar dos excitações no ponto K da zona de Brillouin. Para o ponto  $\Gamma$  utilizamos o modelo de *tight-binding* de três bandas

e um *cut-off* no espaço dos momentos que permite que a função de onda seja decomposta numa série de Fourier. A condutividade óptica de  $\text{MoS}_2$ ,  $\text{MoSe}_2$ ,  $\text{WS}_2$  e  $\text{WSe}_2$  é obtida e comparada com dados experimentais. Também deduzimos a fórmula de Elliot para o caso bidimensional: uma equação analítica útil para se obter a condutividade óptica devida às contribuições dos excitões.

Após estudar dois problemas microscópicos, voltamos a nossa atenção para um problema macroscópico: a passagem de luz por uma superrede desordenada de dielétricos alternados com folhas de grafeno. A presença de desordem tem como consequência o aparecimento da localização de Anderson. Em sistemas unidimensionais a localização de Anderson é caracterizada pelo comprimento de localização, que pode ser obtido a partir do expoente de Lyapunov. É utilizado o formalismo da matriz de transferência para se calcular numericamente o comprimento de localização. Também obtemos uma aproximação analítica para desordem fraca que coincide com o cálculo numérico. Também é estudado a propagação de luz na forma de modos evanescentes sustentados pela presença de grafeno.



# ABSTRACT

---

## Photonics of graphene and other two-dimensional materials heterostructures

This thesis describes the interaction of light with two-dimensional materials. It starts with a revision of the state of the art of the physics of two-dimensional materials. We focus on the most promising materials used in nanophotonics: graphene, monolayers of transition metal dichalcogenides, and hexagonal boron nitride. The optical properties of these materials and their quasiparticles/collective modes are discussed. They encompass plasmons, phonons, excitons, and polaritons.

The first objective of this thesis is to describe microscopically the interaction of light with the charge carriers in these new two-dimensional materials. To this end, the formalism of the semiconductor Bloch equations is derived in detail. Furthermore, the susceptibility and the optical conductivity of graphene are derived using Mermin's formula. These results are used throughout the thesis.

The Bloch semiconductor equations are first applied to a system consisting of a sheet of graphene under optical pumping. After a rapid transient period, the electronic distribution will assume a new configuration different from that in thermodynamical equilibrium. This new electronic distribution will remain stable while the pumping radiation persists. In this situation we derive the new electronic susceptibility that a probe pulse with a different frequency sees. From the susceptibility we calculate the plasmon dispersion relation, that will be strongly anisotropic. Finally we find semi-analytic formulas for the susceptibility, optical conductivity, and plasmon dispersion relation that depend on the pump intensity, frequency, and polarization of the optical pump.

Next, we deal with the problem of excitons in monolayers of transition metals dichalcogenides. From the semiconductor Bloch equations we derive the Bethe-Salpeter equation. The solution of the homogeneous part corresponds to the exciton wavefunctions and their energies. From the solution of the inhomogeneous part we calculate the optical conductivity. We used the 2D Dirac Hamiltonian with a mass term to deal with the excitons in the K point of the Brillouin zone. For the  $\Gamma$  point we use the tight-binding model with three bands and a cut-off in the momentum space that allows to decompose the wavefunction into a Fourier series. The optical

conductivity of  $\text{MoS}_2$ ,  $\text{MoSe}_2$ ,  $\text{WS}_2$ , and  $\text{WSe}_2$  is obtained and compared with the experimental data. We also derive the Elliot formula for the bidimensional case: an useful analytic equation for the optical conductivity contributions due to the excitons.

After studying two microscopic problems, we turn our attention to a macroscopic one: the passage of light through a disordered superlattice of dielectrics alternating with graphene sheets. The presence of disorder implies the onset of Anderson localization. In one-dimensional systems Anderson localization can be characterized by the localization length, that can be obtained from the Lyapunov exponent. We use the transfer matrix formalism to numerically calculate the localization length and so characterize the Anderson localization in those superlattices. Also, we obtain an analytical approximation for weak disorder that describes the numerical data with a very good accuracy. In addition it is studied the propagation of light through evanescent modes sustained by the presence of graphene.

# CONTENTS

---

<b>0. Published work</b>	<b>1</b>
<b>1. Introduction</b>	<b>3</b>
1.1. Outline	4
<b>2. 2D Materials in a nutshell</b>	<b>5</b>
2.1. Quasiparticles and collective excitations	5
2.2. Graphene	9
2.2.1. Graphene surface plasmon-polaritons	10
2.3. Hexagonal boron-nitride	10
2.4. Transition metal dichalcogenides	12
2.5. Final comment	13
<b>3. Semiconductor Bloch equations</b>	<b>15</b>
3.1. Formalism	16
3.1.1. Density matrix operator	17
3.1.2. Obtaining an explicit form for the equation of motion	17
3.1.3. Homogeneous electric field	19
3.2. Non-interacting Bloch equations	21
3.3. Including the electron-electron interaction: two-band system	23
3.A. Electron-electron interaction	26
<b>4. Graphene pump-probe systems</b>	<b>29</b>
4.1. Introduction	29
4.2. Non-equilibrium density-matrix and Bloch equation in the tight-binding approximation	32
4.2.1. Real time analysis	33
4.2.2. Steady-state solution	35
4.3. Intraband transitions of the non-equilibrium gas due to the probe field	35
4.4. Long wavelength limit: anisotropic plasmon dispersion relation	38
4.5. The anisotropic conductivity of graphene under pumping	40
4.6. Numerical results	42

4.7. Spectrum of the surface plasmon-polaritons in the out-of-equilibrium regime . . . . .	50
4.8. Final comments . . . . .	52
4.A. Steady-state equations for the distribution functions under continuous pumping . . . . .	53
4.B. Semi-analytical formula for the charge-charge correlation function . . .	54
<b>5. Excitons in 2D materials . . . . .</b>	<b>57</b>
5.1. <b>K</b> -point excitons . . . . .	59
5.1.1. Equation of motion and optical properties . . . . .	63
5.1.2. Calculation of the exchange energy . . . . .	64
5.1.3. Excitonic effects in the Rabi frequency . . . . .	66
5.1.4. Study of homogeneous Bethe-Salpeter Equation: Excitonic states	68
5.1.5. Integral equation for the vertex function . . . . .	69
5.1.6. Bright and Dark excitons: optical selection rules . . . . .	73
5.2. Excitons at the $\Gamma$ -point . . . . .	73
5.3. Results . . . . .	79
5.4. Discussion and conclusions . . . . .	84
5.A. Overlap of the four-body wavefunctions . . . . .	86
5.B. The Bethe-Salpeter kernel . . . . .	87
5.C. Exchange correction around the $\Gamma$ point . . . . .	89
<b>6. Disorder in photonic crystals . . . . .</b>	<b>91</b>
6.1. Introduction . . . . .	91
6.2. Analytical calculation of the localization length . . . . .	93
6.2.1. Unit cell made of two different dielectric materials and a graphene sheet at the interface . . . . .	95
6.2.2. Unit cell made of one dielectric material and a graphene sheet at the interface . . . . .	97
6.3. Numerical Simulations: Results and Discussions . . . . .	97
6.3.1. Simulation procedure . . . . .	97
6.3.2. Results . . . . .	98
6.3.3. Drude regime when: $\Re\sigma \approx 0, \Im\sigma > 0$ . . . . .	99
6.3.4. Complex interband regime when: $\Re\sigma \approx 0, \Im\sigma < 0$ . . . . .	104
6.4. Conclusions . . . . .	105
6.A. Matrix transformation . . . . .	105
6.B. Lyapunov Exponent . . . . .	106
<b>7. Concluding remarks . . . . .</b>	<b>107</b>
<b>Appendices . . . . .</b>	<b>109</b>

<b>A. Tight-binding model of graphene</b> . . . . .	<b>109</b>
<b>B. Graphene susceptibility and optical conductivity</b> . . . . .	<b>113</b>
B.1. Undoped susceptibility . . . . .	114
B.2. Contribution from the Fermi sea . . . . .	116
B.3. Summary . . . . .	122
B.4. Mermin's Formula and Optical Conductivity . . . . .	124
<b>C. Simplified form of SBE in time domain</b> . . . . .	<b>127</b>
<b>D. Keldysh potential: a RPA analysis</b> . . . . .	<b>129</b>
D.1. Gapless 2D Dirac system . . . . .	130
D.2. Gapped 2D Dirac system . . . . .	131
D.3. Final comments . . . . .	133
<b>E. Optical conductivity for a gapped Dirac system</b> . . . . .	<b>135</b>
E.1. Polarization operator and dipole-coupling Hamiltonian . . . . .	136
E.2. Longitudinal conductivity . . . . .	137
E.3. Transverse conductivity . . . . .	139
E.4. Absorption by a circular polarized light . . . . .	140
<b>F. The Elliot formula for excitons in 2D materials</b> . . . . .	<b>141</b>
F.1. Derivation of Elliot's formula . . . . .	141
<b>G. Transfer matrix elements for a photonic crystal</b> . . . . .	<b>143</b>
G.1. Unit cell made of two different dielectrics and a graphene sheet at the interfaces . . . . .	143
G.2. Unit cell made of one dielectric and a graphene sheet at the interface . . . . .	144









## PUBLISHED WORK

---

# O

Here is the list of published and submitted work during my PhD studies. The publications **E**, **F** and **H** are discussed throughout the thesis.

- A** **A. J. Chaves**, N. M. R. Peres, D. Costa, G. A. Farias  
*Localized surface plasmons in a continuous and flat graphene sheet*  
Submitted to Physical Review B (2018).
- B** **A. J. Chaves**, B. Amorim, Yu. V. Bludov, P. A. D. Gonçalves, N. M. R. Peres  
*Scattering of graphene plasmons at abrupt interfaces: An analytic and numeric study*  
Physical Review B, v. 97, p. 035434, (2018).
- C** **A. J. Chaves**, N. M. R. Peres, G. Smirnov, N. A. Mortensen  
*Hydrodynamic model approach to the formation of plasmonic wakes in graphene*  
Physical Review B, v.96, p. 195438 (2017).
- D** O. Oliveira, **A. J. Chaves**, W. de Paula, T. Frederico  
*Signature of curved QFT effects on the optical properties of deformed graphene*  
Europhysics Letters, v. 117, p. 27003 (2017).
- E** **A. J. Chaves**, R. M. Ribeiro, T. Frederico, N. M. R. Peres,  
*Excitonic effects in the optical properties of 2D materials: an equation of motion approach,*  
2D Materials v. 4, p. 025096 (2017).
- F** **A. J. Chaves**, N. M. R. Peres, T. Low  
*Pumping electrons in graphene to the M point in the Brillouin zone: Emergence of anisotropic plasmons*  
Physical Review B, v. 94, p. 195438 (2016).
- G** W. de Paula, **A. J. Chaves**, O. Oliveira, T. Frederico  
*Quantum field theory approach to the optical conductivity of strained and deformed graphene*  
Few-Body Systems, v. 56, p. 915, (2015).
- H** **A. J. Chaves**, N. M. R. Peres, F. A. Pinheiro  
*Anderson localization of light in disordered superlattices containing graphene layers*  
Physical Review B, v. 92, p. 195425 (2015).



# INTRODUCTION

---

# 1

In ancient times, mankind stared at the sun and the stars and associated those primordial light sources with deities. After controlling the fire, mankind could finally have its own light source. From rustic bonfires to sophisticated oil lamps, fire was the only source of light until the advent of the light bulb in the XIX century, that could finally transform electricity into light. A long development of experiments and theories culminated in Maxwell's equations and the famous Hertz experiment: it was discovered that light is electromagnetic radiation. From this, fast and exciting developments started. The electromagnetic spectrum was fully named and classified, and now all of it is available to be engineered. Naturally, the way to manipulate electromagnetic radiation is through materials: from Hertz experiments with brass to silica optical fibers, the generation, manipulation, and transmission evolved step by step with material science.

One of the last advancements in the material science was the thinning of layered crystals, such as graphite, to a single atom thick. It is surprising that such a thin material can strongly interact with light, but it does. Those new materials led by graphene are paving a new way to manipulate electromagnetic radiation.

The electromagnetic theory is described by Maxwell's equations plus constitutive relations, that describe how the electromagnetic fields interact with matter. In the early stages of electromagnetism, the constitutive relations were obtained from phenomenological approaches. The theory of the interaction of light with matter was put into a robust foundation with the development of quantum mechanics, solid state, and condensed matter physics. As a consequence, we can go from microscopic models to macroscopic relations between the charges and currents in matter.

This thesis starts with a short revision of two-dimensional materials. It is followed by a formal chapter about the semiconductor Bloch equations (SBE). The next two chapters are a direct application of the SBE, first in non-equilibrium optically pumped graphene. In the second we consider the effects of the electron-electron interaction in the optical properties of the monolayers of transition metal dichalcogenides. Those two applications are *microscopic* problems: we are interested in ob-

taining the optical conductivity, that is, the relation between the external electric field and the electronic current. After the study of these two microscopic problems, we study a *macroscopic* problem: the passage of light through a disordered photonic crystal containing graphene layers.

### 1.1. Outline

#### CHAPTER 2: 2D MATERIALS IN A NUTSHELL

Here, we briefly discussed the main 2D materials for the nanophotonics field: graphene, hBN and transition metal dichalcogenides. They present new and exciting properties. Also shown is the importance of polaritons in those 2D materials and it is discussed the coupling of light with some of the intrinsic excitations of those 2D materials: plasmons, excitons and phonons.

#### CHAPTER 3: SEMICONDUCTOR BLOCH EQUATIONS

In this chapter, the main tool used in the thesis is derived and discussed: the semiconductor-Bloch equations. With those equations we have a tool for the microscopic description of the interaction of light with the charge carriers of the 2D materials. The results derived in this chapter will be used throughout the rest of the thesis.

#### CHAPTER 4: GRAPHENE PUMP PROBE SYSTEM

In this chapter, the optical properties of graphene under a continuous intense laser are studied. The laser will drive the system to an out-of-equilibrium state, where the electronic distribution is no long described by the Fermi-Dirac statistics. We show that this kind of system possess plasmons that are described by an effective anisotropic Fermi energy.

#### CHAPTER 5: EXCITONS IN 2D MATERIALS

In this chapter we discuss excitons and their optical properties in monolayers of transition metal dichalcogenides. The Bethe-Salpeter equation is solved both for the homogeneous and inhomogeneous cases. In the former we obtain the excitons wave functions and eigenvalues; as for the latter we calculate the optical conductivity and absorbance.

#### CHAPTER 6: DISORDER IN PHOTONIC CRYSTALS

We have performed a theoretical investigation of light propagation and Anderson localization in one-dimensional disordered superlattices composed of dielectric stacks with graphene sheets in between. Disorder is introduced either on graphene material parameters (e.g., Fermi energy) or on the widths of the dielectric stacks. We find a good analytic approximation for the localization length of the electromagnetic field in comparison with the numerical calculations.

# 2D MATERIALS IN A NUTSHELL

---

# 2

The key concept that will guide all the topics discussed throughout this thesis is the interaction of light with two-dimensional materials: they have few atoms or even one atom of thickness. Some of the most promising 2D materials for the nanophotonics field are discussed in this chapter [3]: the semimetal graphene, the semiconductors monolayers of transition metal dichalcogenides (TMDCs), and the insulator hexagonal boron-nitride (hBN). However, before introducing these materials, we discuss some condensed matter concepts that are key elements to understand the most important optical properties of these 2D materials: plasmons, excitons, phonons and polaritons.

*See Ref. [1] for a review about 2D materials and van der Waals heterostructures and [2] for an extense list of all 2D materials discovered until 2014.*

## 2.1. Quasiparticles and collective excitations

The new class of two-dimensional materials has a rich variety of quasiparticles and collective modes with which light can strongly interact. These modes have specific properties, arising from their two dimensional nature, that lead to new and interesting effects and properties [1].

### PLASMONS

Plasmons are collective excitations of the electronic liquid in a material [4]. Starting from the equilibrium state, a deviation of the charge density will generate a restoration force towards equilibrium. Analogously to what happens in an harmonic oscillator, this restoration force can be characterized by a material dependent frequency  $\omega_{pl}$ . An external field with the same frequency  $\omega_{pl}$  will couple with the free charge density of the material: in this case we have the excitation of plasmons. This frequency can be obtained when the dielectric function of the electron-electron interaction is zero.

*The usual description of plasmons uses the random phase approximation (RPA) [4] to calculate the electronic susceptibility.*

## EXCITONS

For a dielectric thin sheet the Coloumb potential is replaced by the Keldish potential [6].

Excitons are bound states of an electron and a hole [5]. They cannot exist in gapless materials and are a consequence of the Coloumb interaction between electric charges. Excitons can have a strong coupling with light that is seen in optical experiments as absorption peaks below the material band gap.

The BSE for excitons is also called the Wannier equation.

They can be classified by their size: Frenkel excitons [7] have the size comparable to a single unit cell and as such are better described by an atomistic theory. Wannier excitons [8] comprises several unit cells and can be described by the solution of the Bethe-Salpeter equation (BSE)[9]. Excitons in 2D materials will be discussed in detail in chapter 5.

## PHONONS

Phonons are quanta of the lattice crystal vibrations [10]. Those vibrations in 2D crystals can be both in- and out-of-plane, generating longitudinal and transversal phonons, respectively. They play important roles in describing different physical phenomena in all crystals. An interesting property of 2D materials is, as crystalline membranes, that they can couple to the substrate lattice vibrations [11]. Further in this chapter is discussed the strong coupling of phonons with light in hBN.

## POLARITONS

Here we consider that the 2D material lies in the  $xy$ -plane.

First discovered in thin metal films, the polaritons are localized electromagnetic waves coupled with the surface sheet. They are evanescent along the direction perpendicular to the material sheet, i.e., the electromagnetic field has a dependence of the form  $\phi(\mathbf{q}, \omega, z) \propto e^{-\kappa_z |z|}$ , where  $\phi$  represents the non-vanishing components of the electromagnetic field,  $\mathbf{q}$  is the 2D in-plane wavevector, parallel to the material sheet and  $\kappa_z$  is the attenuation constant. Doped graphene and TMDCs can support surface plasmon-polaritons (SPP). Also TMDCs can support exciton-polaritons in the visible frequency. Finally, for hBN we have phonon-polaritons in the terahertz and infrared frequencies and exciton-polaritons in the UV range.

The 2D Fourier transform of the current is defined as:  $\mathbf{J}(\mathbf{q}, \omega, z) = \int d\mathbf{r} dt e^{i(\mathbf{q} \cdot \mathbf{r} - \omega t)} \mathbf{J}(\mathbf{r}, z, t)$ , where  $(\mathbf{r}, z)$  are usual cylindrical coordinates, with analogous definition for the electric field and the conductivity tensor.

The optical properties of 2D materials in the linear regime can be described by a two-dimensional conductivity tensor  $\sigma_{ij}(\mathbf{q}, \omega)$ , with  $i, j = x, y$  representing the directions along the material sheet and  $z$  is the direction perpendicular to it. Considering a planar 2D material parallel to the  $xy$  plane and localized at  $z = z_0$ , the electric current density  $J_i$  in this material is given by:

$$J_i(\mathbf{q}, \omega, z) = \sum_{j=1}^2 \sigma_{ij}(\mathbf{q}, \omega) \delta(z - z_0) E_j(\mathbf{q}, \omega, z), \quad (2.1)$$

with  $E_j(\mathbf{q}, \omega, z)$  the external electric field. Those quantities are represented as a 2D spatial Fourier transform. The optical properties of a system containing a 2D material

can be derived substituting Eq. (2.1) in Maxwell's equations. This will be the starting pointing when calculating plasmon-polaritons (see Chapter 4) and light transmission along a photonic crystal (Chapter 6).

To illustrate some properties of polaritons, we will describe the simplest case of an isotropic material without nonlocal effects,  $\sigma_{ij}(q, \omega) = \delta_{ij}\sigma(\omega)$ , cladded between two dielectrics whose constants are  $\varepsilon_1$  and  $\varepsilon_2$ . This is shown in Fig. 2.1, in this situation the transverse electric mode (TE) and the transverse magnetic mode (TM) can be treated separately. From the boundary conditions of Maxwell's equations [12], we have for the TM wave the following equation that gives the frequency of the SPP as function of the absolute value of the momentum along the propagation direction  $q$ :

$$\frac{\varepsilon_1}{\kappa_1} + \frac{\varepsilon_2}{\kappa_2} + i \frac{\sigma(\omega)}{\varepsilon_0 \omega} = 0, \quad (2.2)$$

while for TE waves, we have the following condition:

$$\kappa_1 + \kappa_2 - i\omega\mu_0\sigma(\omega) = 0. \quad (2.3)$$

From those equations, we can see that, for positive  $\varepsilon_i$ , we will only have solution for the TM mode 2.2 if  $\Im\sigma(\omega) < 0$  while the TE mode 2.3 has solution if  $\Re\sigma(\omega) > 0$ .

One way to characterize polaritons is through the loss function, that is an important tool because it can be determined through electron energy loss spectroscopy (EELS) [15]. It can be defined as minus the imaginary part of the inverse of the dielectric function:  $L(q, \omega) = -\Im \left\{ [\varepsilon(q, \omega)]^{-1} \right\}$  or as the imaginary part of the reflection coefficient [15]:

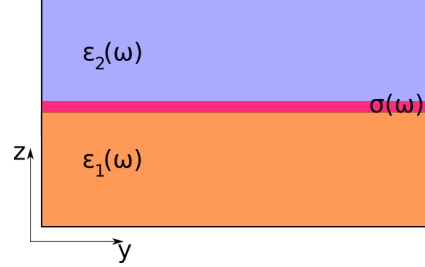
$$L_r(q, \omega) = \Im \{ r(q, \omega) \}, \quad (2.4)$$

where  $r(q, \omega)$  is the reflection coefficient for an electromagnetic wave with frequency  $\omega$  and in-plane wavenumber  $q$ . For a 2D material in vacuum the reflection coefficient reads [15]:

$$r(q, \omega) = \left[ 1 - 2i \left( \pi\alpha \frac{\sigma(q, \omega)}{\sigma_0} \sqrt{\frac{q^2 c^2}{\omega^2} - 1} \right)^{-1} \right]^{-1}, \quad (2.5)$$

where  $\sigma_0 = e^2/4\hbar$ ,  $\alpha \approx 137^{-1}$  is the fine structure constant, and  $c$  is the speed of light.

In Fig. 2.2 we compare the loss function for different 2D materials. The loss function allows to probe surface plasmon-polaritons in graphene, exciton-polaritons in MoS<sub>2</sub>, and phonon-polaritons in hBN. Those polaritons will be discussed throughout the chapter.



$\delta_{ij}$  is the Kronecker delta.

Figure 2.1.: A 2D material between two dielectrics.

See Refs. [13, 14] for reviews about polaritons in 2D materials.

## 2. 2D MATERIALS IN A NUTSHELL

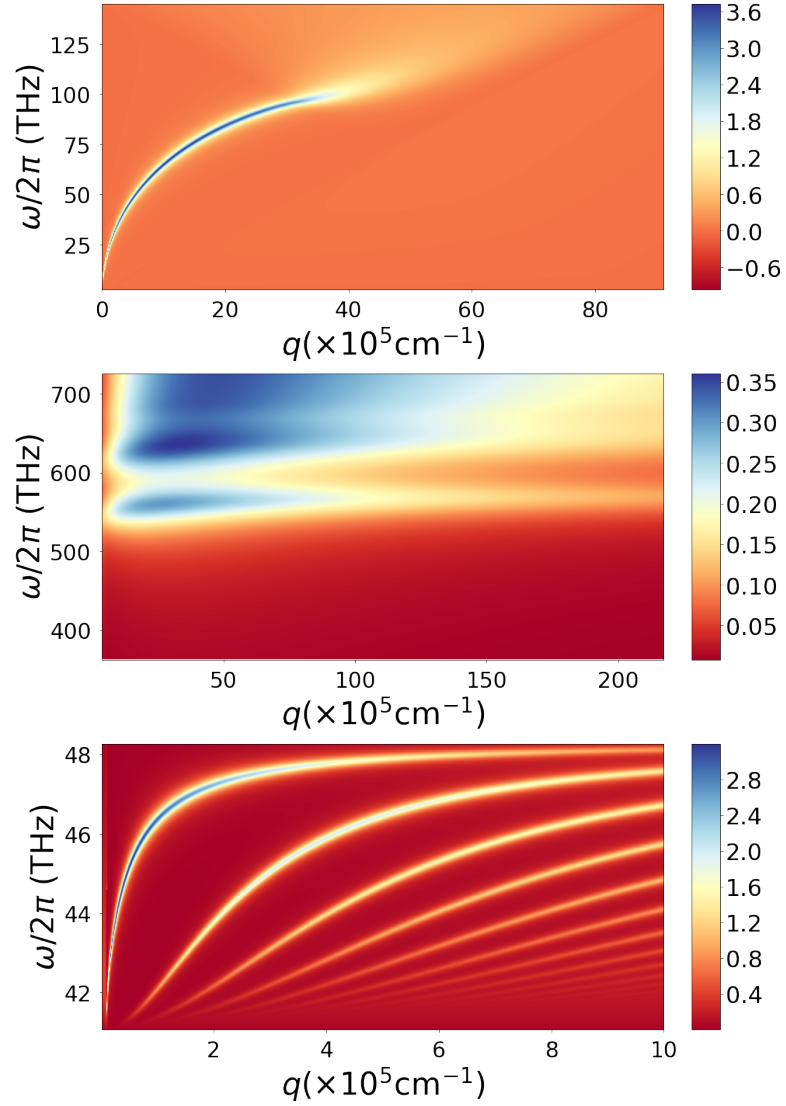


**Figure 2.2.:** Comparison of loss function (2.4) for different 2D materials and TM polarized electromagnetic field in logarithm scale:  $\ln(1 + \Im r(q, \omega))$ . Top panel: Loss function of graphene, the reflection coefficient is calculated with Eq. (2.5) and the conductivity is obtained through the Mermin equation (see appendix B for details), parameters:  $E_F = 0.3$  eV,  $\hbar\gamma = 4$  meV,  $v_F = c/300$ . Middle panel: Loss function for monolayer MoS<sub>2</sub>, the conductivity was calculated with the same procedure and parameters as presented in chapter 5 and with the reflection coefficient given by Eq. (2.5). Bottom panel: Loss function for a slab of hBN with width  $d = 100$  nm and dielectric function given by Eq. (2.10). The reflection coefficient in this case was calculated using Eq. (2.12).



## 2.2. Graphene

Graphene is a single layer of graphite, a honeycomb lattice of carbon atoms. It attracted a huge interest of the scientific community and several reviews about the synthesis and properties of graphene have been written [16, 17, 18, 19, 20]. The valence and conduction bands touches at the inequivalents K and K' points of the Brillouin zone. The electronic excitations near the K and K' points are described by a massless two dimensional Dirac equation and the resulting dispersion relation is linear and gapless [17].

*In graphene at charge neutrality point, the Fermi surface shrinks to the K and K' points, being called the Dirac points.*

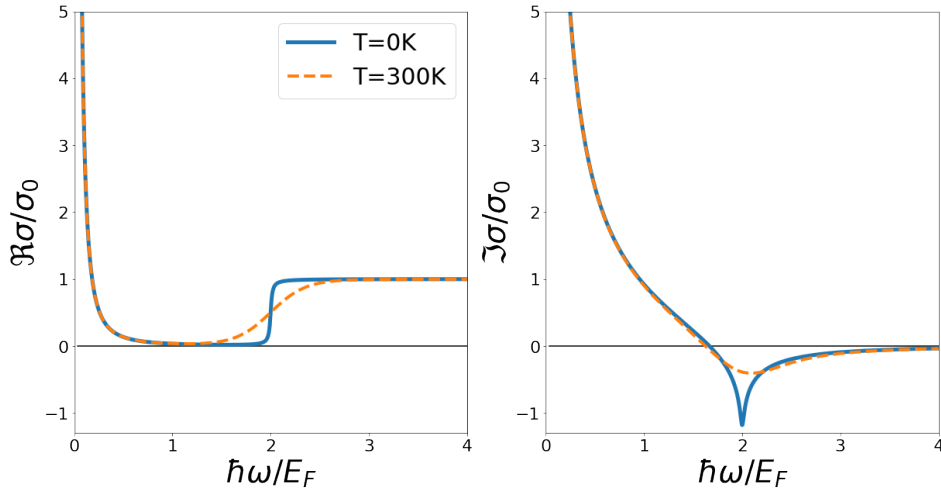


**Figure 2.3.:** Graphene optical conductivity. On the left(right) panel, we see the real(imaginary) part of graphene optical conductivity. The strong Drude peak, located at the lower frequencies, is originated from the intraband transitions. The step behavior at  $\hbar\omega = 2E_F$  corresponds to the interband transitions.

In figure 2.3 we show graphene optical conductivity. We have two different regimes, determined in frequency by the graphene Fermi energy  $E_F$ . For  $\hbar\omega < 2E_F$  the optical conductivity is dominated by the Drude term, with the broadening of the real part controlled by the relaxation rate  $\gamma$  and positive imaginary part. For  $\hbar\omega > 2E_F$  the step transition is controlled both by the temperature and the relaxation rate, and has a negative imaginary part. Remarkably, graphene conductivity for frequencies above  $2E_F/\hbar$  tends to a parameter-free plateau given by:

$$\sigma_0 = \frac{e^2}{4\hbar}, \quad (2.6)$$

and with frequencies above  $2E_F/\hbar$  graphene absorbs 2.3% of incident light [21], which is surprising high considering that it is an atom thick material.

*The Fermi energy in graphene can be controlled with chemical or electrostatic doping [17].*

Graphene, as a membrane, is subject to the environment properties. The optical conductivity can be controlled by an external potential [18], magnetic field [22], cutting into nanoribbons [23], and deformation [24, 25]. Due to its extraordinary electronic and optical properties, graphene has emerged as an alternative material platform for applications in photonics and optoelectronics [26, 27, 28]. A partial and far from exhaustive list of applications of graphene in photonics include high-speed photodetectors [29], optical modulators [30], plasmonic devices [31, 32, 33], and ultrafast lasers [34].

### 2.2.1. GRAPHENE SURFACE PLASMON-POLARITONS

In the intraband regime, graphene can support surface plasmon-polaritons (SPP), as can be seen in Fig. 2.3: the imaginary part of the conductivity for frequencies below  $2E_F/\hbar$  is positive and the real part can be neglected in a wide range of frequencies. The Drude conductivity of graphene reads:

$$\sigma(\omega) = \frac{4i}{\pi} \frac{|E_F|}{\hbar\omega + i\hbar\gamma} \sigma_0, \quad (2.7)$$

with  $\gamma$  the relaxation rate of electronic excitations. We have from Eq. 2.7 that the imaginary part of the conductivity will always be positive in this regime, as can be seen in Fig. 2.3. If we plug Eq. 2.7 in the TM polariton Eq. 2.2, in the electrostatic regime,  $q \ll \omega/c$ , it follows that  $\kappa_1 = q/\varepsilon_1$  and  $\kappa_2 = q/\varepsilon_2$ , and we have the dispersion relation:

$$\omega = \sqrt{\frac{4}{\varepsilon_1 + \varepsilon_2}} c \alpha \frac{E_F}{\hbar} q - i\frac{\gamma}{2}, \quad (2.8)$$

with  $\alpha \approx 137^{-1}$  the fine structure constant and  $c$  the speed of light in vacuum. The  $\sqrt{q}$  dependence is an universal property of any 2D system that can support plasmons in the long-wavelength regime<sup>1</sup>. This is the same dispersion relation when calculating the zero of the RPA dielectric function neglecting interband transitions:

$$\varepsilon_{\text{RPA}}(\omega, \mathbf{q}) = 1 - V(|\mathbf{q}|) \chi_{\text{RPA}}(\omega, \mathbf{q}) = 0, \quad (2.9)$$

with  $V(|\mathbf{q}|)$  the 2D Fourier transform of the Coulomb potential and  $\chi_{\text{RPA}}(\omega, \mathbf{q})$  the RPA susceptibility. The loss function is depicted in the top panel of Fig. 2.2, where the dispersion relation can be inferred. An alternative way to describe plasmons in graphene, that takes in account nonlocality is using an hydrodynamic model [35, 36].

## 2.3. Hexagonal boron-nitride

Hexagonal boron-nitride (hBN) has, as its name suggests, a honeycomb lattice similar to graphite. In monolayer hBN the sublattice symmetry is broken, with each

<sup>1</sup>A proof of this statement can be found in chapter 4.

See Appendix B for a derivation of the optical conductivity of graphene, including intraband and interband terms.

sublattice containing either only boron or nitrogen atoms. Breaking the sublattice symmetry implies that hBN will have a bandgap. For the monolayer case the bandgap is measured to be around  $\approx 7$  eV [37]. We can analyze the optical properties of few-layer hBN in two different frequency ranges. At the infrared, the dielectric function is dominated by phonons[38]. In this region the hBN is a hyperbolic material that presents birefringence, with a dielectric function given by [39]:

$$\varepsilon_m = \varepsilon_{\infty,m} + \varepsilon_{\infty,m} \frac{\omega_{\text{LO},m}^2 - \omega_{\text{TO},m}^2}{\omega_{\text{TO},m}^2 - \omega^2 - i\omega\gamma_m}, \quad (2.10)$$

with  $m = \perp, \parallel$ ,  $\omega_{\text{TO},\parallel}/2\pi = 23.38$  THz,  $\omega_{\text{LO},\parallel}/2\pi = 24.88$  THz,  $\omega_{\text{TO},\perp}/2\pi = 41.07$  THz,  $\omega_{\text{LO},\perp}/2\pi = 48.27$  THz,  $\varepsilon_{\infty,\parallel} = 2.95$ ,  $\varepsilon_{\infty,\perp} = 4.87$ ,  $\gamma_{\parallel}/2\pi = 0.12$  THz,  $\gamma_{\perp}/2\pi = 0.15$  THz.

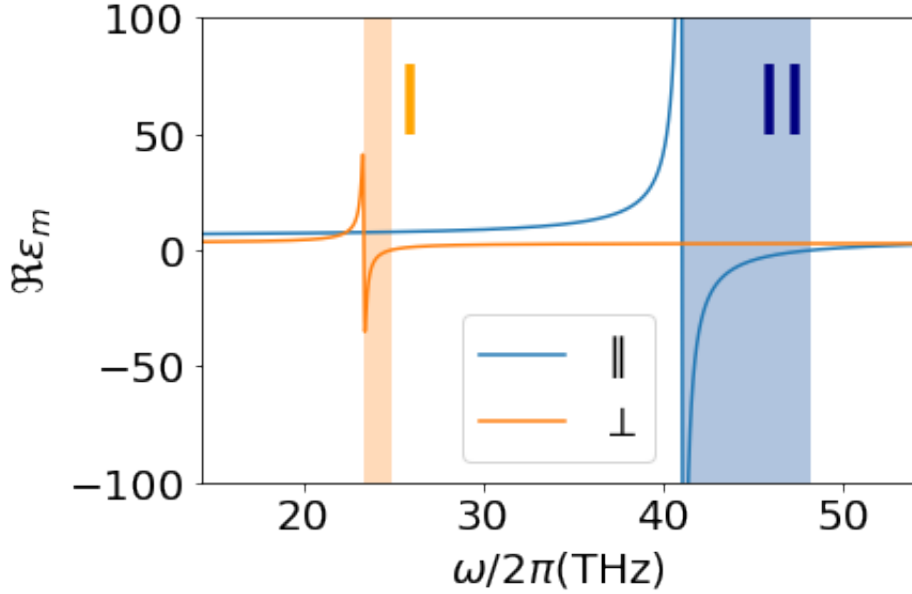


**Figure 2.4.:** Real part of the dielectric functions of hBN. The shaded area correspond to the type I and II Reststrahlen zones [40].

Whenever  $\varepsilon_{\perp}(\omega)\varepsilon_{\parallel}(\omega) < 0$ , the dielectric function is hyperbolic and guided polaritons modes can be achieved. The angle of propagation  $\theta_g$  with respect to the optical axis is given by [41]:

$$(\tan \theta_g)^2 = -\frac{\varepsilon_{\perp}(\omega)}{\varepsilon_{\parallel}(\omega)}. \quad (2.11)$$

At the angles  $\theta_g$  given by Eq. (2.11) we have directional propagation, that means that the propagation only occurs in the direction given by  $\theta_g$ . Super-resolution can

be achieved if  $\Im k_z d \approx 1$ , where  $k_z$  is the wavenumber inside the hBN slab at the direction perpendicular to the hBN sheets and  $d$  the slab thickness. Near-field optical imaging and focusing with hBN was reported in [42], the hybridization of graphene plasmon-polaritons with hBN phonon-polaritons was studied in [39].

The phonon-polaritons in hBN can be characterized also by the loss function defined in (2.4), the reflection coefficient for a dielectric slab with width  $d$  in vacuum or air is [43]:

$$r_{\text{hbn}}(q, \omega) = r_{\text{hbn}}^0(q, \omega), \quad (2.12)$$

where  $r_{\text{hbn}}^0$  is the interface air/hbn reflection coefficient [44]:

$$r_{\text{hbn}}^0 = -\frac{\kappa_e - \varepsilon_{\perp} \kappa_a}{\kappa_e + \varepsilon_{\perp} \kappa_a}, \quad (2.13)$$

where  $\kappa_e = \sqrt{\varepsilon_{\perp} \frac{\omega^2}{c^2} - \frac{\varepsilon_{\perp}}{\varepsilon_{\parallel}} q^2}$  and  $\kappa_a = \sqrt{\frac{\omega^2}{c^2} - q^2}$ . The loss function (2.4) for phonon-polaritons in hBN is show in the bottom panel of Fig. 2.2.

At the UV range, the optical properties are dominated by excitons with an optical gap of around 5.3-6.3 [45, 46, 47]. Other important application of hBN is as an encapsulating device to enhance the properties of another 2D materials, as it protects those materials from the environment. For graphene, the electronic mobility on hBN substrate is more than three times larger in comparison of a SiO<sub>2</sub> substrate [48]. For the excitons in TMDCs, the linewidth of photoluminescence at room temperature and on a SiO<sub>2</sub> substrate is around 50meV, while when encapsulated at hBN at  $T = 4\text{K}$  it is reduced down to 2meV [49, 50].

## 2.4. Transition metal dichalcogenides

The first synthesis of monolayers of transition metal dichalcogenide was in 2005 [51]. Soon all the combinations of the form MX<sub>2</sub> with M=Mo, W and X=S, Se, Te were synthesised. Bulk TMDCs are commonly found in two structural phases and can be classified according to the stacking order: the trigonal prismatic (2H) has an ABA stacking while the octahedral (1T) has an ABC stacking. We will draw our attention to the monolayers from the 2H phase, that has attracted recent attention for its excitonic properties [53]. As it happens in hBN and graphene, the low energy excitations of 2H monolayers TMDCs are described by a 2D Dirac equation with a mass term that comes from the breaking of sublattice symmetry as it happens in hBN. They have a direct band-gap in the two inequivalent K and K' points of the Brillouin zone and, as graphene, this can be used for valley dependent physics and devices [54].

More properties of TMDCs are discussed in chapter 5 with a strong focus on the exciton influence in the optical properties. From the results presented in chapter 5 the loss function (2.4) was calculated and presented in the middle panel of Fig. 2.2.

See Ref. [52] for a review about TMDCs.

## 2.5. Final comment

The 2D materials list, given in this chapter, with applications in nanophotonics is not exhaustive. Another promising materials for 2D nanophotonics, which are missing, includes phosphorene [55] and topological insulators [56, 57]. An interesting property of 2D materials is that they can be stacked to form van der Waals heterostructures [1]. In this case the material properties can change significantly, e.g., bilayer graphene has a band gap that depends on the perpendicular electric field [58] and so is very different from the gapless monolayer graphene. The crystal orientation between the stacked sheets can also change the material properties. The twisted bilayer graphene is very different from the Bernal-stacked bilayer graphene [59, 60]. Alloys of 2D materials can also be another way to engineer their optical properties [61, 62]. Finally, from a macroscopic view, polaritons modes of different 2D materials stacked together can also hybridize, e.g., forming plasmon-phonon-polariton in the graphene/hBN system [39].



# SEMICONDUCTOR BLOCH EQUATIONS 3

---

The study of the interaction of light with matter leads to a quantum many-body Hamiltonian that contains carrier-carrier interaction and carrier-electric field interaction terms, therefore implying a complex many-body problem without a viable exact solution. To quote Paul Dirac [63]:

“The underlying physical laws necessary for the mathematical theory of a large part of physics and the whole of chemistry are thus completely known, and the difficulty is only that the exact application of these laws leads to equations much too complicated to be soluble. It therefore becomes desirable that approximate practical methods of applying quantum mechanics should be developed, which can lead to an explanation of the main features of complex atomic systems without too much computation.”

To proceed further in the description of the many-body problem, several approaches and approximations were developed since the birth of quantum mechanics. Here we revisit the theory of the semiconductor Bloch equations (SBE), an approach to deal with the many-body problem for an electron gas in presence of an external electric field. The formalism developed in this chapter will be used in the next two chapters. It can be also used to derive graphene optical conductivity, that is a necessary ingredient in chapter 6 to study the transmission of light through a superlattice containing graphene layers.

The SBE started as an analogy to Bloch’s work in nuclear spins [64]. Those ideas were applied by Haken developments off laser theory [65] and further developed in Stahl’s paper on band-edge of semiconductors [66]. Haug *et al.* [67] used similar equations to study nonlinearities in semiconductors. Finally, the work of Lindberg and Koch [68] generalized the optical Bloch equations to include many-body effects that takes in account phase-space filling, excitonic effects and renormalization of the band gap. Those equations became an important tool to study semiconductor optical properties and is presented in several textbooks [69, 70, 71]. For example, it was used to study the optical properties of quantum wells [72], quantum dots [73],

and graphene [74, 75].

### 3.1. Formalism

In this section we formulate the SBE starting from a Hamiltonian that is composed of three parts: a one-body Hamiltonian that describes an independent particle  $\hat{H}_0$ , the carrier-light interaction  $\hat{H}_I$  and the electron-electron interaction  $\hat{H}_{ee}$ .

$$\hat{H} = \hat{H}_0 + \hat{H}_I + \hat{H}_{ee}. \quad (3.1)$$

Let  $\hat{a}_{\lambda\mathbf{k}}(t)$  be the annihilation operator written in the basis that diagonalizes  $\hat{H}_0$  in the Heisenberg picture. In this picture we can write:

$$\hat{H}_0 = \sum_{\mathbf{k}\lambda} E_{\lambda\mathbf{k}} \hat{a}_{\lambda\mathbf{k}}^\dagger(t) \hat{a}_{\lambda\mathbf{k}}(t), \quad (3.2)$$

where  $\lambda$  labels the band,  $\mathbf{k}$  is the wavenumber and  $E_{\lambda\mathbf{k}}$  the corresponding eigenvalue of  $\hat{H}_0$ . The creation and annihilation operators obey the anticommutation relation:

$$\{\hat{a}_{\lambda_1\mathbf{k}_1}^\dagger(t), \hat{a}_{\lambda_2\mathbf{k}_2}(t)\} = \delta_{\mathbf{k}_1,\mathbf{k}_2} \delta_{\lambda_1,\lambda_2}. \quad (3.3)$$

The dipole energy term, written classically as  $-\boldsymbol{\varepsilon} \cdot \mathbf{d}$  [76], with  $\mathbf{d}$  the dipole moment and  $\boldsymbol{\varepsilon}$  the electric field, act as an one-body operator and can be written as:

$$\hat{H}_I(t) = -\frac{1}{S} \sum_{\lambda_1,\lambda_2,\mathbf{k},\mathbf{q}} \boldsymbol{\varepsilon}(\mathbf{q},t) \cdot \mathbf{d}_{\lambda_1,\lambda_2}^{\mathbf{k}+\mathbf{q},\mathbf{k}} \hat{a}_{\lambda_1,\mathbf{k}+\mathbf{q}}^\dagger(t) \hat{a}_{\lambda_2\mathbf{k}}(t), \quad (3.4)$$

with  $\mathbf{q}$  the photon wavenumber,  $\lambda_1, \lambda_2$  the band indexes, and  $\mathbf{d}_{\lambda_1,\lambda_2}^{\mathbf{k}+\mathbf{q},\mathbf{k}}$  is the dipole matrix element. This is a general expression and can be obtained decomposing a generic one-body operator into a complete basis of the corresponding Fock space. The electron-electron interaction is a two-body operator:

$$\hat{H}_{ee} = -\frac{e}{2S} \sum_{\lambda_1,\lambda_2,\lambda_3,\lambda_4} \sum_{\mathbf{k},\mathbf{k}',\mathbf{q} \neq 0} V(|\mathbf{q}|) F_{\lambda_1,\lambda_2,\lambda_3,\lambda_4}(\mathbf{k},\mathbf{k}',\mathbf{q}) \times \hat{a}_{\lambda_1,\mathbf{k}'-\mathbf{q}}^\dagger(t) \hat{a}_{\lambda_3,\mathbf{k}+\mathbf{q}}^\dagger(t) \hat{a}_{\lambda_4,\mathbf{k}}(t) \hat{a}_{\lambda_2,\mathbf{k}'}(t), \quad (3.5)$$

with  $V(|\mathbf{q}|)$  the 2D Fourier transform of the electron-electron potential,  $\hbar\mathbf{q}$  is the exchanged momentum and  $S$  is the system area/volume. Finally,  $F_{\lambda_1,\lambda_4,\lambda_2,\lambda_3}(\mathbf{k},\mathbf{q})$  is the overlap of the eigenfunctions of  $\hat{H}_0$  (see 3.A):

$$F_{\lambda_1,\lambda_2,\lambda_3,\lambda_4}(\mathbf{k},\mathbf{k}',\mathbf{q}) \equiv \langle \lambda_1\mathbf{k}' - \mathbf{q} | \lambda_2\mathbf{k}' \rangle \langle \lambda_3\mathbf{k} + \mathbf{q} | \lambda_4\mathbf{k} \rangle. \quad (3.6)$$

*We will use a second quantization notation through all this chapter and also in chapters 4 and 5.*

*We suppose that the system posses discret or continuous translational symmetry, in the first case  $\mathbf{k}$  is the crystal wavenumber while in the latter it is the wavenumber.*

*The condition  $\mathbf{q} \neq 0$  comes from the exact compensantion between the term with  $\mathbf{q} = 0$  and the charged background of ions [69].*



### 3.1.1. DENSITY MATRIX OPERATOR

The density matrix operator of  $\hat{H}_0$  states can be defined as:

$$\hat{\rho}(t) \equiv \sum_{\lambda_1, \lambda_2, \mathbf{k}_1, \mathbf{k}_2} \hat{\rho}_{\lambda_1, \lambda_2}^{\mathbf{k}_1, \mathbf{k}_2}(t), \quad (3.7)$$

with the reduced density matrix operator given by:

$$\hat{\rho}_{\lambda_1, \lambda_2}^{\mathbf{k}_1, \mathbf{k}_2}(t) \equiv \hat{a}_{\lambda_1 \mathbf{k}_1}^\dagger(t) \hat{a}_{\lambda_2 \mathbf{k}_2}(t). \quad (3.8)$$

First we note that any one-body operator  $\hat{\mathcal{O}}$  can be written in terms of the density operator(3.7) [4]:

$$\langle \hat{\mathcal{O}}(t) \rangle = \sum_{\lambda_1, \lambda_2, \mathbf{k}_1, \mathbf{k}_2} \mathcal{O}_{\lambda_1, \lambda_2}^{\mathbf{k}_1, \mathbf{k}_2} \hat{a}_{\lambda_1 \mathbf{k}_1}^\dagger(t) \hat{a}_{\lambda_2 \mathbf{k}_2}(t) = \sum_{\lambda_1, \lambda_2, \mathbf{k}_1, \mathbf{k}_2} \mathcal{O}_{\lambda_1, \lambda_2}^{\mathbf{k}_1, \mathbf{k}_2} \hat{\rho}_{\lambda_1, \lambda_2}^{\mathbf{k}_1, \mathbf{k}_2}(t), \quad (3.9)$$

with

$$\mathcal{O}_{\lambda_1, \lambda_2}^{\mathbf{k}_1, \mathbf{k}_2} = \langle \lambda_1 \mathbf{k}_1 | \hat{\mathcal{O}}_S | \lambda_2 \mathbf{k}_2 \rangle, \quad (3.10)$$

calculated in terms of the eigenfunctions of  $\hat{H}_0$  and  $\hat{\mathcal{O}}_S$  written in the Schrödinger picture. The expectation value, if  $\hat{\mathcal{O}}$  is an observable, is simply given by:

$$\langle \hat{\mathcal{O}}(t) \rangle = \text{Tr}[\hat{\mathcal{O}}_S \hat{\rho}(t)]. \quad (3.11)$$

The goal now is to calculate the Heisenberg equation of motion for the reduced density operator (3.8):

$$-i\hbar \frac{d}{dt} \langle \hat{\rho}_{\lambda_1, \lambda_2}^{\mathbf{k}_1, \mathbf{k}_2}(t) \rangle = \langle [\hat{H}(t), \hat{\rho}_{\lambda_1, \lambda_2}^{\mathbf{k}_1, \mathbf{k}_2}(t)] \rangle, \quad (3.12)$$

as we will see, this equation gives rises to a hierarchy problem. If it was viable to obtain an exact solution of (3.12), it would be totally equivalent of solving the traditional Schrödinger equation. The task now is to compute each commutator that appears in the right hand side of Eq. (3.12), this is done in the next section.

### 3.1.2. OBTAINING AN EXPLICIT FORM FOR THE EQUATION OF MOTION

From now on, to obtain quick results, we use a very simple notation:

$$\hat{a}_{\lambda_1, \mathbf{k}_1}(t) \equiv 1, \quad \hat{a}_{\lambda_1, \mathbf{k}_1}^\dagger(t) \equiv 1^\dagger. \quad (3.13)$$

We use the results:

$$[3^\dagger 4, 1^\dagger 2] = \delta_{41} 3^\dagger 2 - \delta_{32} 1^\dagger 4, \quad (3.14a)$$

$$[3^\dagger 4^\dagger 56, 1^\dagger 2] = \delta_{16} 3^\dagger 4^\dagger 52 - \delta_{15} 3^\dagger 4^\dagger 62 + \delta_{24} 1^\dagger 3^\dagger 52 - \delta_{23} 1^\dagger 4^\dagger 56, \quad (3.14b)$$

*This equation cannot be confused with the von-Neumann equation. The difference is i) for the von-Neumann equation, the density operator is written in terms of the creation and annihilatin operators of the total Hamiltonian and ii) they are written in the Schrödinger picture while we consider here for the SBE the Heisenberg picture.*

*These results are obtained using the anticommutation relation of the creation and annihilation operators:  $\{1^\dagger, 2\} = \delta_{12}$ ,  $\{1, 2\} = 0$*

with this notation we can rewrite the Hamiltonians (3.2), (3.4), and (3.5) as:

$$H_0 = \sum_3 E_3 3^\dagger 3, \quad (3.15a)$$

$$H_I = \sum_{34} d_{34} 3^\dagger 4, \quad (3.15b)$$

$$H_{ee} = \frac{1}{2} \sum_{3456} V_{3456} 3^\dagger 4^\dagger 5 6, \quad (3.15c)$$

where we defined when necessary  $\mathbf{k}_i = \mathbf{k} \pm \mathbf{q}$  to simplify the notation and:

$$d_{34} \equiv -\frac{1}{S} \boldsymbol{\epsilon}(\mathbf{k}_3 - \mathbf{k}_4, t) \cdot \mathbf{d}_{\lambda_3, \lambda_4}^{\mathbf{k}_3, \mathbf{k}_4}, \quad (3.16)$$

$$V_{1234} \equiv -\frac{e}{S} V(|\mathbf{k}_2 - \mathbf{k}_3|) F_{\lambda_1, \lambda_4, \lambda_2, \lambda_3}(\mathbf{k}_3, \mathbf{k}_4, \mathbf{k}_2 - \mathbf{k}_3) \delta_{\mathbf{k}_2 - \mathbf{k}_3, \mathbf{k}_4 - \mathbf{k}_1}. \quad (3.17)$$

We have that the reduced density matrix (3.8) in this new notation is simply  $\rho_{12} = 1^\dagger 2$ . The commutators of the equation of motion (3.12), using (3.14), result:

$$[H_0, \hat{\rho}_{12}] = (E_1 - E_2) \hat{\rho}_{12}, \quad (3.18a)$$

$$[H_I, \hat{\rho}_{12}] = \sum_3 (d_{31} \rho_{32} - d_{23} \rho_{13}), \quad (3.18b)$$

$$[H_{ee}, \hat{\rho}_{12}] = \frac{1}{2} \sum_{345} (V_{3451} - V_{3415}) 3^\dagger 4^\dagger 5 2 + (V_{4253} - V_{2453}) 1^\dagger 4^\dagger 5 3. \quad (3.18c)$$

the commutators (3.18a) and (3.18b) only depend on the density matrix: after all, they are only one-body operators. However, the electron-electron interaction gives rise to a two-body operator. Thus, to proceed in an exact way, we need to write the equation of motion for the two-body density matrix operator  $1^\dagger 2^\dagger 3 4$ , and as we calculate the commutators for this operator, it will appear in the electron-electron commutator a three-body operator, and so on. It is an infinite hierarchy problem. Therefore, to find a closed set of equations, it is necessary to truncate at some point. Here we will stop at the simplest level that takes in account the electron-electron interaction in a non-trivial way: using the random phase approximation (RPA), we can write the expectation value of the two-body density matrix operator as the sum of the corresponding one-body ones:

$$\langle 1^\dagger 2^\dagger 3 4 \rangle \approx \langle 2^\dagger 3 \rangle \langle 1^\dagger 4 \rangle - \langle 2^\dagger 4 \rangle \langle 1^\dagger 3 \rangle. \quad (3.19)$$

Here we can draw a parallel with the Hartree-Fock approximation. The first term in the right hand side of Eq. (3.19) is equivalent to the Hartree term while the second term is analogous to the Fock term.

Therefore, with the RPA (3.19), Eq. (3.18c) can be written approximately as:

$$\langle [H_{ee}, \hat{\rho}_{12}] \rangle \approx \frac{1}{2} \sum_{345} (V_{3451} - V_{3415})(\rho_{45}\rho_{32} - \rho_{42}\rho_{35}) + (V_{4253} - V_{2453})(\rho_{45}\rho_{13} - \rho_{43}\rho_{15}), \quad (3.20)$$

this term can be further simplified using the property:  $V_{1234} = V_{2143}$ , and after some algebra we obtain:

$$\langle [H_{ee}, \hat{\rho}_{12}] \rangle \approx \sum_{345} (V_{3451} - V_{3415})\rho_{45}\rho_{32} + (V_{4253} - V_{2453})\rho_{45}\rho_{13}, \quad (3.21)$$

and the equation of motion (3.12), using Eqs. (3.18) and (3.21), becomes:

$$\begin{aligned} \left( -i\hbar \frac{d}{dt} - E_1 + E_2 \right) \rho_{12} &= \sum_3 (d_{31}\rho_{32} - d_{23}\rho_{13}) + \\ &+ \sum_{345} (V_{3451} - V_{3415})\rho_{45}\rho_{32} + (V_{4253} - V_{2453})\rho_{45}\rho_{13}, \end{aligned} \quad (3.22)$$

this is a set of integro-differential coupled equations for all matrix elements of the expectation value of the density matrix operator. The integral part is in respect to the wavevector and the differential is in time. This equation can be further simplified depending on the system properties and symmetries. We also note that in this procedure it is very easy to obtain the equation of motion when we add more terms in the Hamiltonian (for example, electron-phonon interaction). Also to deal with a system without translational symmetry, we can use Eq. (3.22) without the (implicit) wavenumber labels, only the band ones. In the next sections we will assume that the electric field is homogeneous over all the sample:

$$\mathcal{E}(\mathbf{q}, t) = \mathcal{E}(t)S\delta_{\mathbf{q},0}. \quad (3.23)$$

### 3.1.3. HOMOGENEOUS ELECTRIC FIELD

If the electric field impinging on the material is homogeneous (no spatial dependence), Eq. (3.22) can be simplified as a consequence of momentum conservation. Firstly, we only need the terms of the density matrix diagonal in momentum. We now go back to the old notation. The conservation of momentum implies that we only need to consider the matrix elements with  $\mathbf{k}_1 = \mathbf{k}_2$ , so we can write:

$$\rho_{12} = \rho_{\lambda_1\lambda_2}^{\mathbf{k}_1\mathbf{k}_2} = \langle a_{\lambda_1,\mathbf{k}_1}^\dagger a_{\lambda_2,\mathbf{k}_2} \rangle = \rho_{\lambda_1\lambda_2}^{\mathbf{k}_1\mathbf{k}_1} \delta_{\mathbf{k}_1,\mathbf{k}_2}, \quad (3.24)$$

now we make  $\mathbf{k}_1 = \mathbf{k}_2 = \mathbf{k}$ . The first summation on the right hand side of Eq. (3.22) can be written after simplifying the delta-function in (3.23) as:

$$\sum_3 (d_{31}\rho_{32} - d_{23}\rho_{13}) = -\mathcal{E}(t) \cdot \left[ \sum_{\lambda_3} \mathbf{d}_{\lambda_3\lambda_1}^{\mathbf{k},\mathbf{k}} \rho_{\lambda_3\lambda_2}^{\mathbf{k},\mathbf{k}} - \mathbf{d}_{\lambda_2,\lambda_3}^{\mathbf{k},\mathbf{k}} \rho_{\lambda_1,\lambda_3}^{\mathbf{k},\mathbf{k}} \right]. \quad (3.25)$$

### 3. SEMICONDUCTOR BLOCH EQUATIONS

The second summation in Eq. (3.23) leads to a more complicated calculation. The first term inside the summation is:

$$\begin{aligned} \sum_{345} (V_{3451} - V_{3415}) \rho_{45} \rho_{32} = & -\frac{e}{S} \sum_{\lambda_3 \lambda_4 \lambda_5} \sum_{\mathbf{k}_4} [V(\mathbf{k}_4 - \mathbf{k}_4) F_{\lambda_3 \lambda_1 \lambda_4, \lambda_5}(\mathbf{k}_4, \mathbf{k}, \mathbf{k}_4 - \mathbf{k}_4) - \\ & - V(\mathbf{k}_4 - \mathbf{k}_4) F_{\lambda_3 \lambda_5 \lambda_4, \lambda_1}(\mathbf{k}, \mathbf{k}_4, \mathbf{k}_4 - \mathbf{k})] \rho_{\lambda_4, \lambda_5}^{\mathbf{k}_4, \mathbf{k}_4} \rho_{\lambda_3, \lambda_2}^{\mathbf{k}, \mathbf{k}}, \end{aligned} \quad (3.26)$$

where we used Eq. (3.17). However, in the electron-electron Hamiltonian (3.5) the term with  $V(\mathbf{q} = \mathbf{0})$  is not included in the sum. Therefore as the potential in the first element inside the brackets of (3.26) depends on  $\mathbf{k}_4 - \mathbf{k}_4 = \mathbf{0}$ , its contribution is null. Making  $\mathbf{k}_4 = \mathbf{k} + \mathbf{q}$  we have:

$$\sum_{345} (V_{3451} - V_{3415}) \rho_{45} \rho_{32} = \frac{e}{S} \sum_{\mathbf{q} \neq 0} V(|\mathbf{q}|) \sum_{\lambda_3 \lambda_4 \lambda_5} F_{\lambda_3 \lambda_5 \lambda_4 \lambda_1}(\mathbf{k}, \mathbf{k} + \mathbf{q}, \mathbf{q}) \rho_{\lambda_4, \lambda_5}^{\mathbf{k} + \mathbf{q}, \mathbf{k} + \mathbf{q}} \rho_{\lambda_3, \lambda_2}^{\mathbf{k}, \mathbf{k}}. \quad (3.27)$$

For the second element of the second summation of (3.22), we obtain:

$$\sum_{345} (V_{4253} - V_{2453}) \rho_{45} \rho_{13} = -\frac{e}{S} \sum_{\mathbf{q}} V(|\mathbf{q}|) \sum_{\lambda_3 \lambda_4 \lambda_5} F_{\lambda_4 \lambda_3 \lambda_2 \lambda_5}(\mathbf{k} + \mathbf{q}, \mathbf{k}, -\mathbf{q}) \rho_{\lambda_4, \lambda_5}^{\mathbf{k} + \mathbf{q}, \mathbf{k} + \mathbf{q}} \rho_{\lambda_1, \lambda_3}^{\mathbf{k}, \mathbf{k}}, \quad (3.28)$$

where to simplify the notation we defined the overlapping function  $F$  (3.6) with two wavenumber arguments as:

$$F_{\lambda_1 \lambda_2 \lambda_3 \lambda_4}(\mathbf{k}_1, \mathbf{k}_2) \equiv F_{\lambda_1 \lambda_2 \lambda_3 \lambda_4}(\mathbf{k}_1, \mathbf{k}_2, \mathbf{k}_2 - \mathbf{k}_1) = \langle \lambda_1 \mathbf{k}_1 | \lambda_2 \mathbf{k}_2 \rangle \langle \lambda_3 \mathbf{k}_2 | \lambda_4 \mathbf{k}_1 \rangle. \quad (3.29)$$

Now putting together Eqs. (3.27) and (3.28) we have:

$$\begin{aligned} & \sum_{345} (V_{3451} - V_{3415}) (\rho_{45} \rho_{32} - \rho_{42} \rho_{35}) + (V_{4253} - V_{2453}) (\rho_{45} \rho_{13} - \rho_{43} \rho_{15}) = \\ & -\frac{e}{S} \sum_{\mathbf{q} \neq 0} V(|\mathbf{q}|) \sum_{\lambda_4 \lambda_5} \rho_{\lambda_4, \lambda_5}^{\mathbf{k} + \mathbf{q}, \mathbf{k} + \mathbf{q}} \sum_{\lambda_3} F_{\lambda_2 \lambda_5 \lambda_4 \lambda_3}(\mathbf{k}, \mathbf{k} + \mathbf{q}) \rho_{\lambda_1, \lambda_3}^{\mathbf{k}, \mathbf{k}} - F_{\lambda_3 \lambda_5 \lambda_4 \lambda_1}(\mathbf{k}, \mathbf{k} + \mathbf{q}) \rho_{\lambda_3, \lambda_2}^{\mathbf{k}, \mathbf{k}}. \end{aligned} \quad (3.30)$$

Using now Eqs.(3.25) and (3.30) into (3.22) we obtain the set of equations:

$$\begin{aligned} & \left( -i\hbar \frac{d}{dt} - E_{\lambda_1 \mathbf{k}} + E_{\lambda_2 \mathbf{k}} \right) \rho_{\lambda_1, \lambda_2}^{\mathbf{k}, \mathbf{k}} = \mathcal{E}(t) \cdot \sum_{\lambda_3} \left[ \mathbf{d}_{\lambda_2, \lambda_3}^{\mathbf{k}, \mathbf{k}} \rho_{\lambda_1, \lambda_3}^{\mathbf{k}, \mathbf{k}} - \mathbf{d}_{\lambda_3 \lambda_1}^{\mathbf{k}, \mathbf{k}} \rho_{\lambda_3 \lambda_2}^{\mathbf{k}, \mathbf{k}} \right] - \\ & -\frac{e}{S} \sum_{\mathbf{q} \neq 0} V(|\mathbf{q}|) \sum_{\lambda_4 \lambda_5} \rho_{\lambda_4, \lambda_5}^{\mathbf{k} + \mathbf{q}, \mathbf{k} + \mathbf{q}} \sum_{\lambda_3} F_{\lambda_2 \lambda_5 \lambda_4 \lambda_3}(\mathbf{k}, \mathbf{k} + \mathbf{q}) \rho_{\lambda_1, \lambda_3}^{\mathbf{k}, \mathbf{k}} - F_{\lambda_3 \lambda_5 \lambda_4 \lambda_1}(\mathbf{k}, \mathbf{k} + \mathbf{q}) \rho_{\lambda_3, \lambda_2}^{\mathbf{k}, \mathbf{k}}. \end{aligned} \quad (3.31)$$

this result is a generalization of the SBE obtained for a two-band system, such as the one presented in [68], and similarly for the multi-subband Bloch equations presented

in [69]. From now on we will consider the SBE for a non-interacting electron gas in graphene (Sec. 3.2 and Chapter 4) before studying interacting electrons in TMDCs (Sec. 3.3 and Chapter 5).

## 3.2. Non-interacting Bloch equations

We now calculate the optical response of graphene using the two-band tight-binding Hamiltonian that originates from the  $p_z$  orbitals of the carbon atoms. The results obtained in this section will be used in chapter 4 to study the optical properties of graphene with a non-equilibrium distribution function. We will neglect electron-electron interaction. Also, we consider an electric field  $\mathbf{E}$  that is homogeneous over the entire sample and the dipole operator being given by  $\hat{\mathbf{d}} = -e\hat{\mathbf{R}}$ , with  $e > 0$  the magnitude of the electron charge, so the total Hamiltonian reads

$$\hat{H} = \hat{H}_0 + e\mathcal{E} \cdot \hat{\mathbf{R}}, \quad (3.32)$$

where  $H_0$  is the nearest neighbor tight-binding Hamiltonian (A.1):

$$\hat{H}_0 = \sum_{i,n} t_{\text{TB}} \hat{a}_{\mathbf{R}_n}^\dagger \hat{b}_{\mathbf{R}_n + \delta_i} + \text{h.c.}, \quad (3.33)$$

and where  $\mathbf{R}_n$  is the lattice vector of the unit cell with label  $n$ , and  $\delta_i$ ,  $i = 1, 2, 3$ , are the three possible basis vectors, and  $t_{\text{TB}}$  is the hopping parameter. We have  $\hat{a}_{\mathbf{R}_n}^\dagger$  ( $\hat{b}_{\mathbf{R}_n + \delta_i}^\dagger$ ) as the creation operator at the sublattice A(B) and the orbital located at the position  $\mathbf{R}_n$  ( $\mathbf{R}_n + \delta_i$ ). To proceed further, we need the diagonalized version of  $\hat{H}_0$ , which is also obtained in Appendix A, and reads:

$$\hat{H}_0 = \sum_{\mathbf{k}} E_{\mathbf{k}} \left( \hat{c}_{\mathbf{k}}^\dagger \hat{c}_{\mathbf{k}} - \hat{d}_{\mathbf{k}}^\dagger \hat{d}_{\mathbf{k}} \right). \quad (3.34)$$

where  $\hat{c}_{\mathbf{k}}$  ( $\hat{d}_{\mathbf{k}}$ ) is the annihilation operator of the conduction (valence) band and  $E_{\mathbf{k}}$  the energy eigenvalue, see Eqs. (A.4).

Here we are considering a homogeneous electric field, whose 2D Fourier transform is  $\mathcal{E}\delta(\mathbf{q})$  and so we only need to consider the terms of the density matrix with  $\mathbf{k}_1 = \mathbf{k}_2$ . To simplify the notation, as we only have two bands, we define  $\lambda = c, v$ , where  $c$  ( $v$ ) stands for conduction (valence) band. We write the density matrix elements as:

$$\hat{n}_{c,\mathbf{k}}(t) \equiv \hat{c}_{\mathbf{k}}^\dagger(t) \hat{c}_{\mathbf{k}}(t) = \hat{\rho}_{c,c}^{\mathbf{k},\mathbf{k}}(t), \quad (3.35a)$$

$$\hat{n}_{v,\mathbf{k}}(t) \equiv \hat{d}_{\mathbf{k}}^\dagger(t) \hat{d}_{\mathbf{k}}(t) = \hat{\rho}_{v,v}^{\mathbf{k},\mathbf{k}}(t), \quad (3.35b)$$

$$\hat{p}_{cv,\mathbf{k}}(t) \equiv \hat{c}_{\mathbf{k}}^\dagger(t) \hat{d}_{\mathbf{k}}(t) = \hat{\rho}_{c,v}^{\mathbf{k},\mathbf{k}}(t), \quad (3.35c)$$

$$\hat{p}_{vc,\mathbf{k}}(t) \equiv \hat{d}_{\mathbf{k}}^\dagger(t) \hat{c}_{\mathbf{k}}(t) = \hat{\rho}_{v,c}^{\mathbf{k},\mathbf{k}}(t), \quad (3.35d)$$

*The two bands appears because of the presence of two carbons per unit cell.*

*The e-e interaction is taken partially in account by a phenomenological relaxation term.*

*See Appendix A for more details about the tight-binding method in graphene.*

and from now on the time dependence will not be shown explicitly.

The position operator is given by  $\hat{\mathbf{R}} = \hat{\mathbf{R}}_A + \hat{\mathbf{R}}_B$ , where:

$$\hat{\mathbf{R}}_A = \sum_n \mathbf{R}_n \hat{a}_{\mathbf{R}_n}^\dagger \hat{a}_{\mathbf{R}_n}, \quad (3.36a)$$

$$\hat{\mathbf{R}}_B = \sum_n (\mathbf{R}_n + \boldsymbol{\delta}_1) \hat{b}_{\mathbf{R}_n + \boldsymbol{\delta}_1}^\dagger \hat{b}_{\mathbf{R}_n + \boldsymbol{\delta}_1}. \quad (3.36b)$$

In Appendix A we rewrite the position operator  $\hat{\mathbf{R}}$  in the basis (A.4) that diagonalizes the Hamiltonian  $H_0$  (3.33), in which it results:

$$\hat{\mathbf{R}} = \sum_{\mathbf{k}} i\nabla_{\mathbf{k}} (\hat{n}_{c,\mathbf{k}} + \hat{n}_{v,\mathbf{k}}) + \frac{\nabla_{\mathbf{k}} \Theta_{\mathbf{k}}}{2} (\hat{p}_{cv,\mathbf{k}} + \hat{p}_{vc,\mathbf{k}}), \quad (3.37)$$

the  $i\nabla_{\mathbf{k}} (\hat{n}_{c,\mathbf{k}} + \hat{n}_{v,\mathbf{k}})$  term takes in account the intraband transitions and it is negligible at optical frequencies. The second term in the right hand side of Eq. (3.37) takes in account interband transitions.

For the purpose of the next chapter, we are interested in the effects of an UV incident electromagnetic field. In this regime, the intraband transitions will be negligible, so we approximate the position operator to its interband part:

$$\hat{\mathbf{R}} \approx \sum_{\mathbf{k}} \frac{\nabla_{\mathbf{k}} \Theta_{\mathbf{k}}}{2} (\hat{p}_{cv,\mathbf{k}} + \hat{p}_{vc,\mathbf{k}}), \quad (3.38)$$

and we identify the interband matrix elements as:

$$\mathbf{R}_{cv}^{\mathbf{k},\mathbf{k}} = \mathbf{R}_{vc}^{\mathbf{k},\mathbf{k}} = \frac{\nabla_{\mathbf{k}} \Theta_{\mathbf{k}}}{2}. \quad (3.39)$$

In the basis that diagonalizes  $\hat{H}_0$  we can use the result obtained in the previous section (3.22):

$$[-i\hbar\partial_t - E_{\lambda,\mathbf{k}} + E_{\lambda',\mathbf{k}}] \rho_{\lambda\lambda'}^{\mathbf{k},\mathbf{k}}(t) = e\mathcal{E}(t) \cdot \sum_{\lambda_1} \left( \mathbf{R}_{\lambda'\lambda_1}^{\mathbf{k},\mathbf{k}} \rho_{\lambda\lambda_1}^{\mathbf{k},\mathbf{k}}(t) - \mathbf{R}_{\lambda_1\lambda}^{\mathbf{k},\mathbf{k}} \rho_{\lambda_1\lambda'}^{\mathbf{k},\mathbf{k}}(t) \right). \quad (3.40)$$

Before advancing further, we introduce a phenomenological relaxation term in Eq. (3.40):

$$\begin{aligned} [-i\hbar\partial_t - E_{\lambda,\mathbf{k}} + E_{\lambda',\mathbf{k}}] \rho_{\lambda\lambda'}^{\mathbf{k},\mathbf{k}}(t) = e\mathcal{E}(t) \cdot \sum_{\lambda_1} \left( \mathbf{R}_{\lambda'\lambda_1}^{\mathbf{k},\mathbf{k}} \rho_{\lambda\lambda_1}^{\mathbf{k},\mathbf{k}}(t) - \mathbf{R}_{\lambda_1\lambda}^{\mathbf{k},\mathbf{k}} \rho_{\lambda_1\lambda'}^{\mathbf{k},\mathbf{k}}(t) \right) + \\ + i\hbar\gamma_{\lambda\lambda'} \left( \rho_{\lambda\lambda'}^{\mathbf{k},\mathbf{k}}(t) - \delta_{\lambda\lambda'} f_{\lambda,\mathbf{k}} \right), \end{aligned} \quad (3.41)$$

where  $f_{\lambda,\mathbf{k}}$  is the Fermi-Dirac distribution and  $\gamma_{\lambda\lambda'}$  is the relaxation rate for a transition between bands  $\lambda$  and  $\lambda'$ . This is another advantage of the SBE formalism: we do not need to use the finite temperature formalism (e.g. Matsubara's frequencies) to include thermodynamic properties. The added term forces the system to relax to the thermodynamic equilibrium, i.e., the diagonal elements of the density-matrix are the electronic distribution and thus in equilibrium are given by the Fermi-Dirac function. The non-diagonal elements are interband amplitudes and thus vanish in a system in equilibrium.

As we will see in the next chapter, the relaxation term  $\gamma_{\lambda\lambda'}$  plays a central role in the optical properties of the system under pumping. We will consider from now on that the relaxation term has different values for interband and intraband transitions:  $\gamma_{cc} = \gamma_{vv} = \gamma_0$  and  $\gamma_{cv} = \gamma_{vc} = \gamma_p$ . Using the explicit value of  $\hat{\mathbf{R}}$  (3.38) in Eq. (3.41) we obtain the set of equations for the interband components:

$$(-\partial_t + i\omega_{\mathbf{k}} - \gamma_p) p_{cv,\mathbf{k}}(t) = -i \frac{e\mathcal{E} \cdot \nabla_{\mathbf{k}} \Theta_{\mathbf{k}}}{2\hbar} (n_{c,\mathbf{k}}(t) - n_{v,\mathbf{k}}(t)), \quad (3.42a)$$

$$(-\partial_t - i\omega_{\mathbf{k}} - \gamma_p) p_{vc,\mathbf{k}}(t) = -i \frac{e\mathcal{E} \cdot \nabla_{\mathbf{k}} \Theta_{\mathbf{k}}}{2\hbar} (n_{v,\mathbf{k}}(t) - n_{c,\mathbf{k}}(t)), \quad (3.42b)$$

where  $\hbar\omega_{\mathbf{k}} = 2E_{\mathbf{k}}$ , and for the intraband ones:

$$-\partial_t n_{c,\mathbf{k}}(t) = \gamma_0 (n_{c,\mathbf{k}}(t) - f_{c,\mathbf{k}}) - i \frac{e\mathcal{E} \cdot \nabla_{\mathbf{k}} \Theta_{\mathbf{k}}}{2\hbar} (p_{cv,\mathbf{k}}(t) - p_{vc,\mathbf{k}}(t)), \quad (3.43a)$$

$$-\partial_t n_{v,\mathbf{k}}(t) = \gamma_0 (n_{v,\mathbf{k}}(t) - f_{v,\mathbf{k}}) - i \frac{e\mathcal{E} \cdot \nabla_{\mathbf{k}} \Theta_{\mathbf{k}}}{2\hbar} (p_{vc,\mathbf{k}}(t) - p_{cv,\mathbf{k}}(t)), \quad (3.43b)$$

those equations will be further studied in chapter 4.

### 3.3. Including the electron-electron interaction: two-band system

In the previous section, the effects of the electron-electron interactions are encoded partially in a phenomenological way through the introduction of relaxations rates in the graphene Bloch equations. This procedure has the effect of broadening the peaks and the sharp transitions of the optical conductivity. However, the simplicity has its price and numerous optical processes cannot be described without introducing electron-electron interactions, for example, excitonic effects.

Here we will particularize Eq. (3.31) for a two-band system. This procedure will be very useful for the purpose of Chapter 5. The extra considerations that we will do are the following: i) the system can be well described by a two-band model and ii) the intraband elements of the dipole Hamiltonian can be neglected. From i), for a matter of simplicity, we will label the two bands with  $\lambda = \pm$ , with  $+$  the conduction band and  $-$  the valence band. This labeling is useful as  $\lambda$  and  $-\lambda$  refers to the two different

$$f_{\lambda,\mathbf{k}} = \left[ \exp\left(\frac{E_{\lambda,\mathbf{k}} - E_F}{k_B T}\right) + 1 \right]^{-1}$$

possibilities, in this case the expectation values of the elements of the density matrix (3.24) can be written as:

$$n_\lambda(\mathbf{k}, t) \equiv \rho_{\lambda, \lambda}^{\mathbf{k}, \mathbf{k}}(t), \quad p_\lambda(\mathbf{k}, t) \equiv \rho_{\lambda, -\lambda}^{\mathbf{k}, \mathbf{k}}(t). \quad (3.44)$$

The dipole Hamiltonian (3.4) for a two-band system neglecting intraband terms and with a homogeneous electric field is given by:

$$\hat{H}_I = -\mathcal{E}(t) \cdot \sum_{\lambda, \mathbf{k}} \mathbf{d}_{\lambda, -\lambda}^{\mathbf{k}, \mathbf{k}} \hat{p}_\lambda(\mathbf{k}, t), \quad (3.45)$$

and we rewrite Eq. (3.31) as:

$$\left( -i\hbar \frac{d}{dt} - \hbar\omega_{12}^{\mathbf{k}} \right) \rho_{\lambda_1, \lambda_2}^{\mathbf{k}, \mathbf{k}} = \mathcal{E}(t) \cdot \mathcal{V}_{\lambda_1, \lambda_2}(\mathbf{k}) + \frac{e}{S} \sum_{\mathbf{q} \neq 0} V(|\mathbf{q}|) \Xi_{\lambda_1, \lambda_2}(\mathbf{q}, \mathbf{k}). \quad (3.46)$$

where we defined  $\hbar\omega_{12}^{\mathbf{k}} = E_1 - E_2$  and:

$$\mathcal{V}_{\lambda_1, \lambda_2}(\mathbf{k}) \equiv \sum_{\lambda_3} \left[ \mathbf{d}_{\lambda_2, \lambda_3}^{\mathbf{k}, \mathbf{k}} \rho_{\lambda_1, \lambda_3}^{\mathbf{k}, \mathbf{k}} - \mathbf{d}_{\lambda_3, \lambda_1}^{\mathbf{k}, \mathbf{k}} \rho_{\lambda_3, \lambda_2}^{\mathbf{k}, \mathbf{k}} \right], \quad (3.47)$$

and the term originating from the electron-electron interaction is defined as:

$$\Xi_{\lambda_1, \lambda_2}(\mathbf{q}, \mathbf{k}) \equiv \sum_{\lambda_3 \lambda_4 \lambda_5} \rho_{\lambda_4, \lambda_5}^{\mathbf{k}+\mathbf{q}, \mathbf{k}+\mathbf{q}} \left[ F_{\lambda_3 \lambda_5 \lambda_4 \lambda_1}(\mathbf{k}, \mathbf{k}+\mathbf{q}) \rho_{\lambda_3, \lambda_2}^{\mathbf{k}, \mathbf{k}} - F_{\lambda_2 \lambda_5 \lambda_4 \lambda_3}(\mathbf{k}, \mathbf{k}+\mathbf{q}) \rho_{\lambda_1, \lambda_3}^{\mathbf{k}, \mathbf{k}} \right]. \quad (3.48)$$

The term  $\mathcal{V}_{\lambda_1, \lambda_2}(\mathbf{k})$ , (3.47) that originates from the dipole Hamiltonian, can be written as

$$\mathcal{V}_{\lambda_1, \lambda_2}(\mathbf{k}) = \mathbf{d}_{\lambda_2, -\lambda_2}^{\mathbf{k}, \mathbf{k}} \rho_{\lambda_1, -\lambda_2}^{\mathbf{k}, \mathbf{k}} - \mathbf{d}_{-\lambda_1, \lambda_1}^{\mathbf{k}, \mathbf{k}} \rho_{-\lambda_1, \lambda_2}^{\mathbf{k}, \mathbf{k}}, \quad (3.49)$$

where we only take in account interband matrix elements of the dipole Hamiltonian. For the equation of motion of  $n_\lambda(\mathbf{k}, t)$ , we need  $\lambda_1 = \lambda_2 = \lambda$ :

$$\mathcal{V}_{\lambda, \lambda}(\mathbf{k}) = \mathbf{d}_{\lambda, -\lambda}^{\mathbf{k}, \mathbf{k}} p_\lambda(\mathbf{k}, t) - \mathbf{d}_{-\lambda, \lambda}^{\mathbf{k}, \mathbf{k}} p_{-\lambda}(\mathbf{k}, t), \quad (3.50)$$

and for  $p_\lambda(\mathbf{k}, t)$ :

$$\mathcal{V}_{\lambda, -\lambda}(\mathbf{k}) = \mathbf{d}_{-\lambda, \lambda}^{\mathbf{k}, \mathbf{k}} (n_\lambda(\mathbf{k}, t) - n_{-\lambda}(\mathbf{k}, t)). \quad (3.51)$$

Now we turn our attention for the electron-electron term (3.48) of the SBE (3.31). Here we consider the case when  $\lambda_1 = \lambda_2 = \lambda$ , that corresponds to the equation of motion for the diagonal part of the density matrix, and  $\lambda_1 = -\lambda_2 = \lambda$  corresponds to the term inside the equation of motion for the off diagonal elements. For the first case:

$$\begin{aligned} \Xi_{\lambda, \lambda}(\mathbf{q}, \mathbf{k}) = 2i\Im \{ & p_{-\lambda}(\mathbf{k}, t) [p_\lambda(\mathbf{k}+\mathbf{q}, t) F_{-\lambda-\lambda\lambda\lambda}(\mathbf{k}, \mathbf{k}+\mathbf{q}) + \\ & + F_{-\lambda\lambda-\lambda\lambda}(\mathbf{k}, \mathbf{k}+\mathbf{q}) p_{-\lambda}(\mathbf{k}+\mathbf{q}, t) + n_\lambda(\mathbf{k}+\mathbf{q}, t) F_{-\lambda\lambda\lambda\lambda}(\mathbf{k}, \mathbf{k}+\mathbf{q}) + \\ & + n_{-\lambda}(\mathbf{k}+\mathbf{q}, t) F_{-\lambda-\lambda-\lambda\lambda}(\mathbf{k}, \mathbf{k}+\mathbf{q})] \}, \end{aligned} \quad (3.52)$$



and for the off diagonal  $\lambda_1 = -\lambda_2 = \lambda$  we find:

$$\Xi_{\lambda, -\lambda}(\mathbf{q}, \mathbf{k}) = \sum_{i=1,2,3,4} \sum_{\lambda_1} X_{\lambda, \lambda_1}^i(\mathbf{q}, \mathbf{k}), \quad (3.53)$$

where:

$$X_{\lambda, \lambda_1}^1(\mathbf{q}, \mathbf{k}) = -p_{\lambda}(\mathbf{k}, t) n_{\lambda_1}(\mathbf{k} - \mathbf{q}, t) \left[ F_{-\lambda \lambda_1 \lambda_1 - \lambda}(\mathbf{k}, \mathbf{k} - \mathbf{q}) - F_{\lambda \lambda_1 \lambda_1 \lambda}(\mathbf{k}, \mathbf{k} - \mathbf{q}) \right], \quad (3.54a)$$

$$X_{\lambda, \lambda_1}^2(\mathbf{q}, \mathbf{k}) = -p_{\lambda_1}(\mathbf{k} - \mathbf{q}, t) F_{-\lambda - \lambda_1 \lambda_1 \lambda}(\mathbf{k}, \mathbf{k} - \mathbf{q}) \Delta n_{\lambda}(\mathbf{k}, t), \quad (3.54b)$$

$$X_{\lambda, \lambda_1}^3(\mathbf{q}, \mathbf{k}) = -p_{\lambda}(\mathbf{k}, t) p_{\lambda_1}(\mathbf{k} - \mathbf{q}, t) \left[ F_{-\lambda - \lambda_1 \lambda_1 - \lambda}(\mathbf{k}, \mathbf{k} - \mathbf{q}) - F_{\lambda - \lambda_1 \lambda_1 \lambda}(\mathbf{k}, \mathbf{k} - \mathbf{q}) \right], \quad (3.54c)$$

$$X_{\lambda, \lambda_1}^4(\mathbf{q}, \mathbf{k}) = n_{\lambda_1}(\mathbf{k} - \mathbf{q}, t) F_{-\lambda \lambda_1 \lambda_1 \lambda}(\mathbf{k}, \mathbf{k} - \mathbf{q}) \Delta n_{\lambda}(\mathbf{k}, t), \quad (3.54d)$$

where the difference in occupations reads  $\Delta n_{\lambda}(\mathbf{k}, t) = n_{\lambda}(\mathbf{k}, t) - n_{-\lambda}(\mathbf{k}, t)$ .

Finally, we need to substitute (3.50) and (3.52) into (3.46) to obtain the equation of motion for  $n_{\lambda}$ , and (3.51), and (3.53) to obtain the equation of motion for  $p_{\lambda}$ :

$$-i\partial_t p_{\lambda}(\mathbf{k}, t) = (\tilde{\omega}_{\lambda\mathbf{k}} + \mathcal{W}_{\mathbf{k}\lambda}(t)) p_{\lambda}(\mathbf{k}, t) + (\tilde{\Omega}_{\mathbf{k}\lambda}(t) + \mathcal{D}_{\mathbf{k}\lambda}(t)) \Delta n_{\lambda}(\mathbf{k}, t), \quad (3.55)$$

$$-\partial_t n_{\lambda}(\mathbf{k}, t) = 2\Im \left[ (\tilde{\Omega}_{\mathbf{k}\lambda}(t) + \mathcal{D}_{\mathbf{k}\lambda}(t)) p_{-\lambda}(\mathbf{k}, t) \right], \quad (3.56)$$

where the transition energy (also denoted bare optical band ahead) is  $\hbar\omega_{\lambda\mathbf{k}} = E_{\lambda, \mathbf{k}} - E_{-\lambda, \mathbf{k}}$  and the renormalized Rabi frequency  $\tilde{\Omega}_{\mathbf{k}\lambda}(t)$  reads:

$$\hbar\tilde{\Omega}_{\mathbf{k}\lambda}(\mathbf{k}, t) = \mathcal{E}(t) \cdot \mathbf{d}_{-\lambda, \lambda}^{\mathbf{k}, \mathbf{k}} + \mathcal{B}_{\mathbf{k}\lambda}(t), \quad (3.57)$$

and depends on the dipole moment, the electric field, and the excitonic correction  $\mathcal{B}_{\mathbf{k}\lambda}(t)$ . The different terms that appear in equations (3.55) and (3.57) are classified as:

- Excitonic Rabi frequency renormalization:

$$\mathcal{B}_{\mathbf{k}\lambda}(t) = -\frac{e}{S} \sum_{\mathbf{q}} V(|\mathbf{k} - \mathbf{q}|) \left[ p_{\lambda}(\mathbf{q}, t) F_{\lambda' \lambda' \lambda \lambda}(\mathbf{k}, \mathbf{q}) + p_{\lambda'}(\mathbf{q}, t) F_{\lambda' \lambda \lambda' \lambda}(\mathbf{k}, \mathbf{q}) \right], \quad (3.58)$$

and where in this expression we have the constraint  $\lambda' = -\lambda$ ,  $S$  is the area of the system, and  $F_{\lambda_1, \lambda_2, \lambda_3, \lambda_4}(\mathbf{k}_1, \mathbf{k}_2)$  is defined in equation (3.29)

- Renormalized transition energy (or interacting optical band):

$$\hbar\tilde{\omega}_{\lambda\mathbf{k}} = E_{\lambda, \mathbf{k}} - E_{-\lambda, \mathbf{k}} + \lambda \Sigma_{\mathbf{k}, \lambda}^{\text{xc}}, \quad (3.59)$$

where the exchange self-energy is:

$$\Sigma_{\mathbf{k},\lambda}^{\text{xc}}(t) = \frac{\lambda e}{S} \sum_{\mathbf{q},\lambda_1} V(q) n_{\lambda_1}(\mathbf{k} + \mathbf{q}, t) [F_{\lambda\lambda_1\lambda_1\lambda}(\mathbf{k}, \mathbf{k} + \mathbf{q}) - F_{\lambda'\lambda_1\lambda_1\lambda'}(\mathbf{k}, \mathbf{k} + \mathbf{q})], \quad (3.60)$$

and where in this expression we have the constraint  $\lambda' = -\lambda$ . This form of the exchange self-energy is the same we find in the jellium model, except for the non-trivial four-body structure factor  $F_{\lambda_1\lambda_2\lambda_3\lambda_4}(\mathbf{k}, \mathbf{k} - \mathbf{q})$ .

- Non-linear contribution:

$$\mathcal{W}_{\mathbf{k}\lambda}(t) = -\frac{e}{\hbar S} \sum_{\mathbf{q}\lambda_1} V(|\mathbf{k} - \mathbf{q}|) p_{\lambda_1}(\mathbf{q}, t) (F_{\lambda'\lambda_1\lambda_1\lambda'}(\mathbf{k}, \mathbf{q}) - F_{\lambda\lambda_1\lambda_1\lambda}(\mathbf{k}, \mathbf{q})), \quad (3.61)$$

where in this expression  $\lambda' = -\lambda$ ,  $\lambda_1' = -\lambda_1$ .

- Density term:

$$\mathcal{D}_{\mathbf{k}\lambda}(t) = -\frac{e}{\hbar S} \sum_{\mathbf{q}\lambda_1} V(q) n_{\lambda_1}(\mathbf{k} + \mathbf{q}, t) F_{\lambda'\lambda_1\lambda_1\lambda}(\mathbf{k}, \mathbf{k} + \mathbf{q}). \quad (3.62)$$

Now we neglect the density  $\mathcal{D}_{\mathbf{k}\lambda}(t)$  and the non-linear  $\mathcal{W}_{\mathbf{k}\lambda}(t)$  contributions, as we are essentially focused on the exchange self-energy and excitonic effects to the linear response. We also consider that the system is in thermodynamic equilibrium, where the electronic distribution  $n_{\lambda}(\mathbf{k}, t)$  is given by the Fermi-Dirac distribution function  $f_{\lambda,\mathbf{k}}$ :

$$n_{\lambda}(\mathbf{k}, t) = f_{\lambda,\mathbf{k}} = \left[ 1 + \exp\left(\frac{E_{\lambda,\mathbf{k}} - E_F}{k_B T}\right) \right]^{-1}. \quad (3.63)$$

The latter approximation is valid in the linear regime (weak external electric fields). In this case the SBE become:

$$-i\partial_t p_{\lambda}(\mathbf{k}, t) = \tilde{\omega}_{\lambda\mathbf{k}} p_{\lambda}(\mathbf{k}, t) + \tilde{\Omega}_{\mathbf{k}\lambda}(t) \Delta f_{\lambda}(\mathbf{k}), \quad (3.64)$$

this equation will be discussed in detail in chapter (5), where we show how to obtain and solve the corresponding Bethe-Salpeter equation, showing the influence of the excitonic effects on the optical properties of TMDCs.

### 3.A. Electron-electron interaction

Here we show how to obtain the electron-electron interaction in a second quantized form. In this chapter we are dealing with systems that have a discrete or continuous translational symmetry, with  $\mathbf{k}$  labeling the corresponding quantum number. Here

*We neglect the non-linear term  $\mathcal{W}_{\mathbf{k}\lambda}(t)$  (3.61) that only contributes to second-harmonic and higher frequency terms, and the density term  $\mathcal{D}_{\mathbf{k}\lambda}(t)$  that contributes indirectly to the linear response through equation (3.56).*

we will find the expression for the electron-electron interaction in second quantization for a system with discrete translational symmetry, however the demonstration for a system with continuous translational symmetry would be very similar.

Let  $V(|\mathbf{r}_1 - \mathbf{r}_2|)$  be the interparticle potential, the second quantized form of a operator can be written using the field operator [4]:

$$\hat{H}_{ee} = -\frac{e}{2} \int d\mathbf{r}_1 \int d\mathbf{r}_2 \hat{\psi}^\dagger(\mathbf{r}_1, t) \hat{\psi}^\dagger(\mathbf{r}_2, t) V(|\mathbf{r}_1 - \mathbf{r}_2|) \hat{\psi}(\mathbf{r}_2, t) \hat{\psi}(\mathbf{r}_1, t), \quad (3.65)$$

*The time-dependence appears from the Heisenberg picture.*

where the field operator is defined as:

$$\hat{\psi}(\mathbf{r}, t) = \frac{1}{\sqrt{N_c S_c}} \sum_{\mathbf{k}, \lambda} \phi_{\mathbf{k}, \lambda}(\mathbf{r}) \hat{a}_{\lambda \mathbf{k}}(t), \quad (3.66)$$

*Here and thereafter the summation in  $\mathbf{k}$  is over the first Brillouin zone.*

with  $S_c$  the unit cell area/volume,  $N_c$  the number of unit cells and  $\phi_{\mathbf{k}, \lambda}(\mathbf{r})$  are the eigenfunctions in the same basis that the operators  $\hat{a}_{\lambda \mathbf{k}}(t)$  are written. Those functions are normalized as:

$$\int d\mathbf{r} \phi_{\mathbf{k}_1, \lambda_1}^\dagger(\mathbf{r}) \phi_{\mathbf{k}_2, \lambda_2}(\mathbf{r}) = S_c \delta_{\mathbf{k}_1, \mathbf{k}_2} \delta_{\lambda_1, \lambda_2}, \quad (3.67)$$

where  $N_c$  is the number of unit cells.

For a system with discrete symmetry the eigenfunctions  $\phi_\lambda(\mathbf{k})$  can be written using the Bloch theorem:

$$\phi_{\mathbf{k}, \lambda}(\mathbf{r}) = e^{i\mathbf{k} \cdot \mathbf{r}} u_{\lambda \mathbf{k}}(\mathbf{r}), \quad (3.68)$$

with  $u_{\lambda \mathbf{k}}(\mathbf{r}) = u_{\lambda \mathbf{k}}(\mathbf{r} + \mathbf{R})$  obeying periodic conditions, where  $\mathbf{R}$  is a lattice vector. We also use the normalization condition:

$$\int_{\text{u.c.}} d\mathbf{r} u_{\lambda_1 \mathbf{k}}(\mathbf{r}) u_{\lambda_2 \mathbf{k}}(\mathbf{r}) = S_c \delta_{\lambda_1, \lambda_2}, \quad (3.69)$$

where the integration is over the unit cell.

The discret Fourier transform of the potential  $V(\mathbf{r})$  is given by:

$$V(|\mathbf{q}|) = \int \frac{d\mathbf{r}}{(2\pi)^d} e^{i\mathbf{q} \cdot \mathbf{r}} V(|\mathbf{r}|) \quad (3.70)$$

where  $d$  is the number of dimensions, with the inverse:

$$V(|\mathbf{r}|) = \frac{1}{S_c} \sum_{\mathbf{q} \in 1^{\text{st}} \text{B.Z.}} e^{-i\mathbf{q} \cdot \mathbf{r}} V(|\mathbf{q}|), \quad (3.71)$$

*Here the summation is over the first Brillouin zone (BZ)*

expanding the field operators in Eq. (3.65) using (3.66) and (3.68) we obtain:

$$\begin{aligned} \hat{H}_{ee} = & -\frac{e}{2N_c^2 S_c^3} \sum_{\mathbf{q}} V(|\mathbf{q}|) \sum_{\lambda_1 \lambda_2 \lambda_3 \lambda_4} \sum_{\mathbf{k}_1 \mathbf{k}_2 \mathbf{k}_3 \mathbf{k}_4} \int d\mathbf{r}_1 \int d\mathbf{r}_2 e^{i(\mathbf{q} + \mathbf{k}_2 - \mathbf{k}_1) \cdot \mathbf{r}_1} e^{i(-\mathbf{q} + \mathbf{k}_4 - \mathbf{k}_3) \cdot \mathbf{r}_2} \times \\ & \times \left[ u_{\lambda_1 \mathbf{k}_1}^\dagger(\mathbf{r}_1) u_{\lambda_2 \mathbf{k}_2}(\mathbf{r}_1) \right] \left[ u_{\lambda_3 \mathbf{k}_3}^\dagger(\mathbf{r}_2) u_{\lambda_4 \mathbf{k}_4}(\mathbf{r}_2) \right] \hat{a}_{\lambda_1 \mathbf{k}_1}^\dagger(t) \hat{a}_{\lambda_3 \mathbf{k}_3}^\dagger(t) \hat{a}_{\lambda_4 \mathbf{k}_4}(t) \hat{a}_{\lambda_2 \mathbf{k}_2}(t). \end{aligned} \quad (3.72)$$

### 3. SEMICONDUCTOR BLOCH EQUATIONS

We transform the integral over all the space for one over the first unit cell only.

We also use the result:

$$\begin{aligned}
 \int d\mathbf{r}_1 e^{i(\mathbf{q}+\mathbf{k}_2-\mathbf{k}_1)\cdot\mathbf{r}_1} \left[ u_{\lambda_1\mathbf{k}_1}^\dagger(\mathbf{r}_1) u_{\lambda_2\mathbf{k}_2}(\mathbf{r}_1) \right] &= \\
 &= \sum_{\mathbf{R}} \int_{\text{u.c.}} e^{i(\mathbf{q}+\mathbf{k}_2-\mathbf{k}_1)\cdot(\mathbf{r}_1+\mathbf{R})} u_{\lambda_1\mathbf{k}_1}^\dagger(\mathbf{r}_1+\mathbf{R}) u_{\lambda_2\mathbf{k}_2}(\mathbf{r}_1+\mathbf{R}) \\
 &= \sum_{\mathbf{R}} e^{i(\mathbf{q}+\mathbf{k}_2-\mathbf{k}_1)\cdot\mathbf{R}} \int_{\text{u.c.}} d\mathbf{r}_1 e^{i(\mathbf{q}+\mathbf{k}_2-\mathbf{k}_1)\cdot\mathbf{r}_1} u_{\lambda_1\mathbf{k}_1}^\dagger(\mathbf{r}_1) u_{\lambda_2\mathbf{k}_2}(\mathbf{r}_1)
 \end{aligned} \tag{3.73}$$

however:

$$\sum_{\mathbf{R}} e^{i(\mathbf{q}+\mathbf{k}_2-\mathbf{k}_1)\cdot\mathbf{R}} = N_c \delta_{\mathbf{k}_1, \mathbf{q}+\mathbf{k}_2}, \tag{3.74}$$

where  $N_c$  is the number of unit cells and  $S = N_c S_c$ , with an analogous result for the term that contains the indexes 3, 4, and we define:

$$F_{\lambda_1\lambda_2\lambda_3\lambda_4}(\mathbf{k}, \mathbf{k}', \mathbf{q}) = \frac{1}{S_c} \left[ \int_{\text{u.c.}} d\mathbf{r}_1 u_{\lambda_1\mathbf{k}+\mathbf{q}}^\dagger(\mathbf{r}_1) u_{\lambda_2\mathbf{k}}(\mathbf{r}_1) \right] \left[ \int_{\text{u.c.}} d\mathbf{r}_1 u_{\lambda_1\mathbf{k}+\mathbf{q}}^\dagger(\mathbf{r}_1) u_{\lambda_2\mathbf{k}}(\mathbf{r}_1) \right], \tag{3.75}$$

we will have:

$$\hat{H}_{ee} = -\frac{e}{2S_c} \sum_{\lambda_1\lambda_2\lambda_3\lambda_4} \sum_{\mathbf{k}\mathbf{k}'\mathbf{q}} V(|\mathbf{q}|) F_{\lambda_1\lambda_2\lambda_3\lambda_4}(\mathbf{k}, \mathbf{k}', \mathbf{q}) \hat{a}_{\lambda_1\mathbf{k}'-\mathbf{q}}^\dagger(t) \hat{a}_{\lambda_3\mathbf{k}+\mathbf{q}}^\dagger(t) \hat{a}_{\lambda_4\mathbf{k}}(t) \hat{a}_{\lambda_2\mathbf{k}'}(t), \tag{3.76}$$

for a system with a continuous symmetry the demonstration follows the same steps, and the  $S_c$  factor is replaced by the total volume/area of the system  $S$ . Another way to see this is to take the limit of an infinitely large unit cell.

## 4.1. Introduction

Light matter interaction at low energies occurs due to the interaction of electromagnetic radiation with weakly bound electrons in a material. The electron gas in a conductor is a well known form of weakly bound electrons which couple to electromagnetic radiation. Usually, we assume that the electron gas is in equilibrium and that the external perturbation is small, in which case the response of the gas can be computed in terms of its equilibrium properties —linear response theory. The situation is markedly different when a high-intensity electromagnetic radiation interacts with an electron gas driving it to an out-of-equilibrium regime. In this case the response of the system depends on intensity of incoming radiation and on the orientation of its polarization relatively to the real space lattice of the crystal. Moreover the distribution function of the electron gas occupancy is no longer a Fermi-Dirac distribution. It is this situation that will be studied in this chapter. Here we consider an intense pumping electromagnetic field interacting with the weakly bound electrons in graphene thus generating an out-of-equilibrium gas. The pumping is followed by a weak-probe electromagnetic-field, of frequency much smaller than that of the pumping field, which probes the out-of-equilibrium plasma created by the pumping. The physics of this process is depicted in Fig. 4.1.

Pumping graphene with electromagnetic radiation is a possible tool to study the dynamics of the charge carriers in graphene. In the work of George *et al.* [77] the recombination dynamics and carrier relaxation in graphene was studied with terahertz spectroscopy. When electrons in graphene are pumped by an intense light field pulse, the response is highly anisotropic as was shown in Ref. [78]. After about 1ps of the initial pumping pulse, the photogenerated electrons are described by an isotropic Fermi-Dirac distribution with a high temperature[79]. The graphene optical properties under such conditions were studied by Malic *et al.* [75] and Sun *et al.* [80]. The electron dynamics of photo-excited electrons, including the stimulated electron-hole recombination, was studied by Li *et al.*[81]. The plasmon dispersion

relation under a non-equilibrium hot Fermi-Dirac distribution was studied by Page *et al.* [82] and experimentally measured by Ni *et al.* [83]. We note that plasmons in graphene also offer a possible decay channel to cool down the hot electron gas [84]. The optical conductivity of doped and gapped graphene taking into account a non-equilibrium distribution and interband processes was studied theoretically by Singh *et al.* [85]. All these studies were made in a regime where the validity of the Dirac cone approximation holds, that is, the pumping field has a frequency in the IR/Vis region of the electromagnetic spectrum.

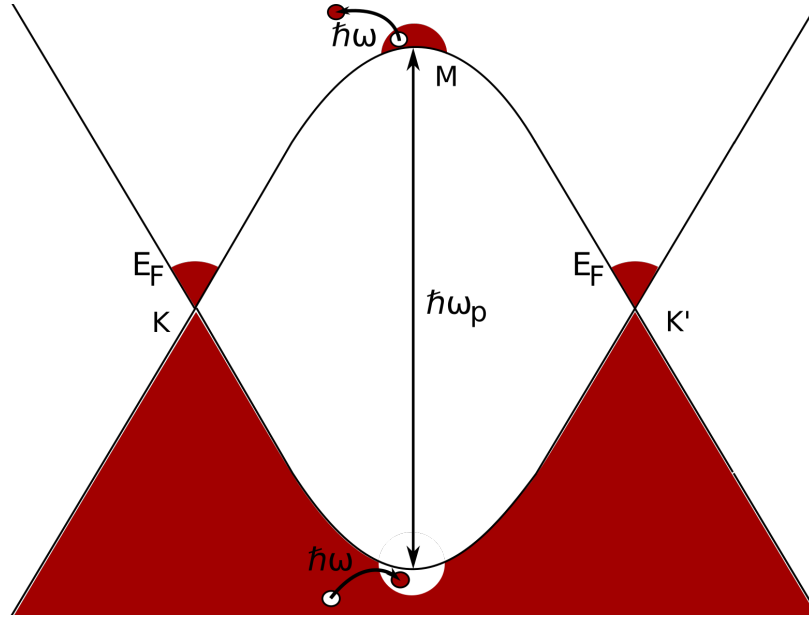


**Figure 4.1.:** This figure represents the physical situation we are considering in this chapter: a possibly doped graphene is driven out-of-equilibrium by an electric field of frequency  $\omega_p$  that creates an electron gas around the M-point in the Brillouin zone. The created plasma is then probed by a field of frequency  $\omega \ll \omega_p$ . We note that the mechanism we are discussing does not require an initially doped graphene, that is, we can have  $E_F = 0$ . Also note that the electronic spectrum at the M-point has a saddle-like nature (in the drawing only the steepest descent direction is shown). The probe field allows the excitation of an electron, belonging to the out-of-equilibrium gas, to higher energies.

For a pulsed laser beam with a pulse duration much larger than 1 ps—the case we will consider in this work—the carrier distribution will remain anisotropic for the duration of the pulse. In this case, electron-phonon and electron-electron interactions, as well as the effect of disorder can be encoded into a hot carrier relaxation rate. Under such conditions the surface plasmon-polariton (SPP) was studied in systems described by a gapped Dirac equation by Kumar *et al.* [86], who discussed the response of the electron gas to a circular polarized light. In this approach, the density matrix equations of motion are solved to determine the non-equilibrium electronic

distribution. In this chapter we study the electronic distribution and the plasmon spectrum of an optically pumped graphene. The material is subjected to a linearly polarized light beam, with a frequency that creates an electron gas beyond the regime where the Dirac approximation holds. This is relevant when graphene is subjected to UV radiation. In this case, the spectrum is no longer Dirac-like and the full band structure of the system has to be taken into account. Therefore, this work goes beyond that of Anshuman *et al.*[86] and includes also the regime studied by these authors.

The plasmons in graphene were first probed in real-space in the studies of Fei *et al.* [87] and Chen *et al.* [88]. In the work [83] the plasmons in graphene are generated by an infrared beam focused in the metalized tip of an atomic force microscope, after a first pumping pulse of electromagnetic radiation. The tip is also used to detect the plasmons that propagate along the graphene surface and after reflection in the sample edges standing waves are produced. This kind of experiment can be used to detect the plasmons discussed in the present chapter using a pulsed laser in the UV range (pulse duration much larger than 1 ps) for pumping the electrons in graphene. Due to excitonic effects[89] the position of the maximum of absorption associated to inter-band transitions at the M–point is reduced from 5.4 eV (independent-electron result) to about  $\sim 4.6$  eV ( $\lambda \sim 270$  nm), a wavelength for which there are available lasers.

Under intense and long times optical excitation, the carrier distribution maintains a non-equilibrium state and does not follow the Fermi Dirac distribution. The new electronic distribution has to be calculated using the semiconductor Bloch equation, with a phenomenological relaxation-term that tends to drive the system towards thermal equilibrium, characterized by a Fermi-Dirac distribution. Since we want to discuss plasmons in the non-equilibrium electron gas created around the M–point in the Brillouin zone, we need to describe the  $\pi$ –electrons in graphene using a tight-binding Hamiltonian. For graphene in the tight-binding approximation, we have a two-band (valence and conduction) system labeled by the crystal momentum  $\mathbf{k}$ , which runs over the full hexagonal Brillouin zone. In our calculations, carrier scattering is accounted for via a relaxation rate. As such, the resulting equations need to be solved for each point in the first Brillouin zone and different momentum values are not explicitly coupled.

The chapter is organized as follows: in Sec. 4.2 we write the Bloch equations, using the result obtained in Sec. 3.2, for the electrons in graphene within the tight-binding model, which is valid beyond the Dirac cone approximation. We study the transient response under a pulse laser and obtain analytical expressions for the out-of-equilibrium electronic distribution. In Sec. 4.3 we obtain the equations to calculate the out-of-equilibrium susceptibility from the new electronic distribution. In Sec. 4.4 we derive a semi-analytical formula, valid in the long-wavelength regime, for the susceptibility and in Sec. 4.5 the optical conductivity is obtained in the same conditions. In section 4.6 we compute numerically the susceptibility of the out-of-

equilibrium electron gas and obtain results for the plasmon dispersion and the loss function. In Sec. 4.7 we use the semi-analytical equations for the conductivity tensor to numerically calculate the dispersion relation of the surface plasmon-polariton and discuss its anisotropic properties. In Sec. 4.8 we provide the general conclusions of this chapter.

## 4.2. Non-equilibrium density-matrix and Bloch equation in the tight-binding approximation

From the previous chapter, we obtained the SBE for a non-interacting electron gas for graphene considering a tight-binding model with two bands. We assume a time-dependent and uniform electric field (that is, with null in-plane wave number). Thus the interaction term in the Hamiltonian does not couple electronic states from different points in the Brillouin zone. Those equations are a system with four unknown functions that are the matrix elements of the expectation value of the density matrix:  $n_{c,\mathbf{k}}$  ( $n_{v,\mathbf{k}}$ ) is the conduction (valence) electronic distribution and  $p_{cv,\mathbf{k}}$  ( $p_{vc,\mathbf{k}}$ ) is the valence to conduction (conduction to valence) transition amplitude.

The equations obtained for the electronic distribution are (3.43) and for the interband transition amplitudes (3.42):

$$-\partial_t n_{c,\mathbf{k}} = \gamma_0 (n_{c,\mathbf{k}} - f_{c,\mathbf{k}}) - i\Omega_{\mathbf{k}}(t)\Delta p_{\mathbf{k}}, \quad (4.1a)$$

$$-\partial_t n_{v,\mathbf{k}} = \gamma_0 (n_{v,\mathbf{k}} - f_{v,\mathbf{k}}) + i\Omega_{\mathbf{k}}(t)\Delta p_{\mathbf{k}}, \quad (4.1b)$$

$$(\partial_t - i\omega_{\mathbf{k}} + \gamma_p) p_{cv,\mathbf{k}} = i\Omega_{\mathbf{k}}(t)\Delta n_{\mathbf{k}}, \quad (4.1c)$$

$$(\partial_t + i\omega_{\mathbf{k}} + \gamma_p) p_{vc,\mathbf{k}} = -i\Omega_{\mathbf{k}}(t)\Delta n_{\mathbf{k}}, \quad (4.1d)$$

where the interband relaxation rate is represented by  $\gamma_p$  and intraband one by  $\gamma_0$ ; also we have  $\hbar\omega_{\mathbf{k}} = 2E_{\mathbf{k}}$ ,  $\Delta n_{\mathbf{k}} = n_{c,\mathbf{k}} - n_{v,\mathbf{k}}$ ,  $\Delta p_{\mathbf{k}} = p_{cv,\mathbf{k}} - p_{vc,\mathbf{k}}$ , and  $f_{c/v,\mathbf{k}}$  is the equilibrium Fermi-Distribution for the conduction/valence band. The time dependence of  $n_{c/v,\mathbf{k}}$  and  $p_{vc/cv,\mathbf{k}}$  has been omitted for simplicity of notation, and finally the Rabi frequency  $\Omega_{\mathbf{k}}$  is given by:

$$\Omega_{\mathbf{k}}(t) = \frac{ea_0\mathcal{E}(t) \cdot \nabla_{\mathbf{k}}\Theta_{\mathbf{k}}}{2\hbar}, \quad (4.2)$$

and couples the diagonal to the off-diagonal elements of the density matrix through the external pumping electric field  $\mathcal{E}(t)$ .

Equations (4.1) are the Bloch equations in graphene[90], with only interband contributions included (note that we want to excite electrons deep in the valence band to high up in the conduction band), and describe the evolution of the electronic distribution and the rate of interband transitions when an external intense and highly energetic electric field  $\mathcal{E}$  is applied. The vector field  $\nabla_{\mathbf{k}}\Theta_{\mathbf{k}}$  entering in the Rabi frequency does not depend on the external parameters and is shown in Fig. 4.2. The



two inequivalent Dirac points are located at the corners of the hexagon in this figure. Near these points the function  $\Theta_{\mathbf{k}}$  becomes the angle between the momentum  $\mathbf{k}$  and the  $x$ -axis.

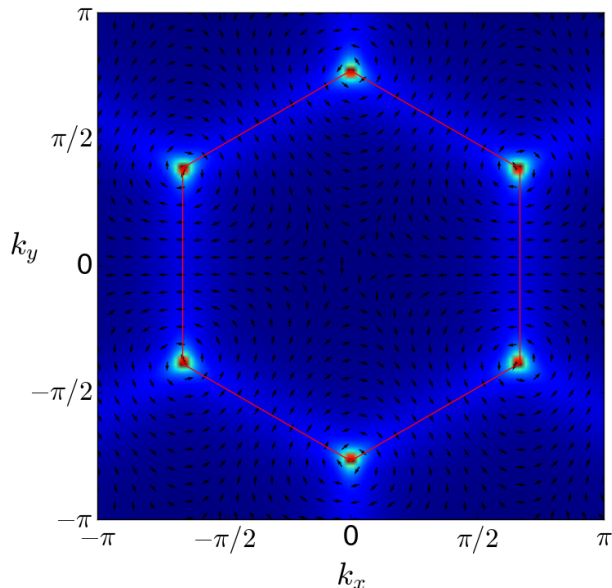


**Figure 4.2.:** Plot of the vector field  $\nabla_{\mathbf{k}}\Theta_{\mathbf{k}}/|\nabla_{\mathbf{k}}\Theta_{\mathbf{k}}|$ . This field controls the Rabi frequency and it can be probed by the polarization of the pumping field. Note that the rotation of the vector field in the two non-equivalent Dirac points has opposite senses. The red hexagon represents the first Brillouin zone and the intensity refers to the absolute value of the vector field  $\nabla_{\mathbf{k}}\Theta_{\mathbf{k}}$ ; it is more intense around the Dirac points (brighter spots) and along the directions connecting two Dirac points and passing through the  $\mathbf{M}$ -point.

#### 4.2.1. REAL TIME ANALYSIS

We can simplify the set of Eqs. (4.1), defined in terms of two real ( $n_{c,\mathbf{k}}, n_{v,\mathbf{k}}$ ) and two complex ( $p_{vc,\mathbf{k}}, p_{cv,\mathbf{k}}$ ) quantities, to three equations involving real quantities only. We will show that under an intense monochromatic wave, the electronic density can reach a steady-state.

Using Eqs. (C.5) and (C.6), we define the deviation from the equilibrium density as  $v_{\mathbf{k}}(t)$ :

$$n_{c,\mathbf{k}}(t) = f_{c,\mathbf{k}} + v_{\mathbf{k}}(t), \quad (4.3a)$$

$$n_{v,\mathbf{k}}(t) = f_{v,\mathbf{k}} - v_{\mathbf{k}}(t), \quad (4.3b)$$

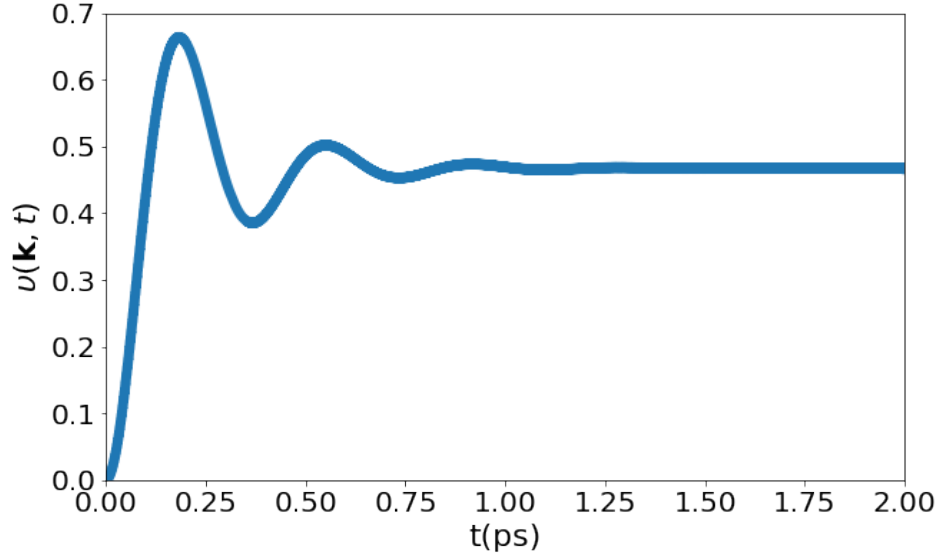


**Figure 4.3.:** Plot of the time evolution of the electronic distribution  $v_{\mathbf{k}}(t)$  for  $\mathbf{k} = 2\pi/a_0(3, 0)$ ,  $\hbar\omega_p = 2t_{\text{TB}}$ ,  $\tau_0 = 300$  fs (see Ref. [74]), which corresponds to  $\hbar\gamma_0 = 14$  meV (see also Ref. [91]),  $\hbar\gamma_p = 28$  meV,  $\varepsilon_0 = 0.5$  GV/m, and  $E_F = 0.2$  eV. The pumping field is linearly polarized along the  $x$ -axis.

and we split the transition rate into real and imaginary parts:

$$p_{vc,\mathbf{k}}(t) = x_{\mathbf{k}}(t) + iy_{\mathbf{k}}(t), \quad (4.4)$$

where  $x_{\mathbf{k}}(t)$  and  $y_{\mathbf{k}}(t)$  are real and  $p_{cv,\mathbf{k}}(t) = x_{\mathbf{k}}(t) - iy_{\mathbf{k}}(t)$ . From Eqs. (4.1) (see Appendix C), we can write:

$$\dot{x}_{\mathbf{k}} = -\gamma_p x_{\mathbf{k}} + \omega_{\mathbf{k}} y_{\mathbf{k}}, \quad (4.5a)$$

$$\dot{y}_{\mathbf{k}} = -\omega_{\mathbf{k}} x_{\mathbf{k}} - \gamma_p y_{\mathbf{k}} + \Omega_{\mathbf{k}}(t) (2v_{\mathbf{k}} + \Delta f_{\mathbf{k}}), \quad (4.5b)$$

$$\dot{v}_{\mathbf{k}} = -\gamma_0 v_{\mathbf{k}} - 2\Omega_{\mathbf{k}}(t) y_{\mathbf{k}}, \quad (4.5c)$$

where the time dependence in  $x$ ,  $y$  and  $v$  has been omitted and  $\Delta f_{\mathbf{k}} = f_{v,\mathbf{k}} - f_{c,\mathbf{k}}$ . Also note the different signs in front of  $v_{\mathbf{k}}(t)$  in Eqs. (4.3).

The set of coupled Eqs. (4.5) describes, using three real functions  $x$ ,  $y$ , and  $v$ , both the time evolution of the transition probability and the electronic density in the reciprocal space. Since we have included the effect of both electron-electron and electron-phonon interactions using only a constant relaxation rate, there is no coupling between excitations from different  $\mathbf{k}$ . Thus, for each point in the Brillouin zone we can solve Eqs. (4.5). In Fig. 4.3 we plot the time evolution of the function  $v_{\mathbf{k}}$ , for  $\mathbf{k} = 2\pi/a_0(3, 0)$  (that corresponds to the M-point in the Brillouin zone) for a monochromatic electric field of frequency  $\hbar\omega_p = 2t_{\text{TB}}$  (that corresponds to a vertical transition at the M-points) and intensity  $\varepsilon_0 = 0.5$  GV/m (this is a moderate field intensity), with linear polarization along the  $x$ -axis.

$a_0$  is the graphene lattice parameter.

### 4.2.2. STEADY-STATE SOLUTION

As shown in Fig. 4.3, the electronic distribution converges to a well defined value which we calculate in Appendix 4.A, when the electric field is given by a monochromatic wave with pumping frequency  $\omega_p$  and intensity  $\mathcal{E}_0$ :  $\mathcal{E} = \frac{1}{2}\mathcal{E}_0 e^{i\omega_p t} + \text{h.c.}$ . In this case the steady-state solution for the densities can be written as:

$$n_{c,\mathbf{k}} = \frac{(1 + \alpha_{\mathbf{k}})f_{c,\mathbf{k}} + \alpha_{\mathbf{k}}f_{v,\mathbf{k}}}{1 + 2\alpha_{\mathbf{k}}}, \quad (4.6a)$$

$$n_{v,\mathbf{k}} = \frac{(1 + \alpha_{\mathbf{k}})f_{v,\mathbf{k}} + \alpha_{\mathbf{k}}f_{c,\mathbf{k}}}{1 + 2\alpha_{\mathbf{k}}}, \quad (4.6b)$$

and from Eq. (4.3)

$$v_{\mathbf{k}} = \frac{\alpha_{\mathbf{k}}}{1 + 2\alpha_{\mathbf{k}}} (f_{v,\mathbf{k}} - f_{c,\mathbf{k}}), \quad (4.7)$$

where  $\alpha_{\mathbf{k}}$  is given by Eq. (4.40) and  $v_{\mathbf{k}}$  represents the deviation from the equilibrium Fermi-Dirac distribution. It should be noted that the steady state distribution functions are not given by a Fermi-Dirac distribution, but can be written in terms of combinations of  $f_{c,\mathbf{k}}$  and  $f_{v,\mathbf{k}}$ . The non-equilibrium distribution depends on the pumping frequency  $\omega_p$  and on the complex electric field  $\mathcal{E}_0$ . For the linear polarization the electric field can be written as a real quantity that depends on the intensity of the electric field  $\mathcal{E}_0$  and the angle of polarization  $\theta$ .

The distribution  $v_{\mathbf{k}}$  is plotted in Fig. 4.4 for different pumping frequencies  $\omega_p$  and polarization angles  $\theta$  of the pumping field. As the pumping frequency increases, the electronic distribution departs from the Dirac points (the corners of the blue hexagon). At  $\hbar\omega_p = 2t_{\text{TB}}$ , the M-point is populated. For  $\hbar\omega_p > 2t_{\text{TB}}$ , the electronic distribution becomes a circle around the  $\Gamma$ -point (center of the hexagon). We also see in this figure the polarization dependence coming from the term  $\nabla_{\mathbf{k}}\Theta_{\mathbf{k}} \cdot \mathcal{E}$ . For example, although we have three independent M-points, for  $\hbar\omega_p = 2t_{\text{TB}}$  and  $\theta = \pi/2$  only two are populated. We can use Fig. 4.2 to predict, for a given pumping polarization, what points in the Brillouin zone can be optically populated, noting that the electric field  $\mathcal{E}$  and the vector field  $\nabla_{\mathbf{k}}\Theta_{\mathbf{k}}$  need to be parallel to maximize the electronic occupation. This anisotropy in the population of the M-points is at the heart of other anisotropic effects that we will discuss ahead.

## 4.3. Intraband transitions of the non-equilibrium gas due to the probe field

The optical response of graphene is determined by intraband and interband transitions [18]. As shown in the previous section, in the steady state the pumping field changes the electronic distribution and therefore the optical conductivity of the material. This quantity is related to the charge-charge correlation function of graphene.

#### 4. GRAPHENE PUMP-PROBE SYSTEMS

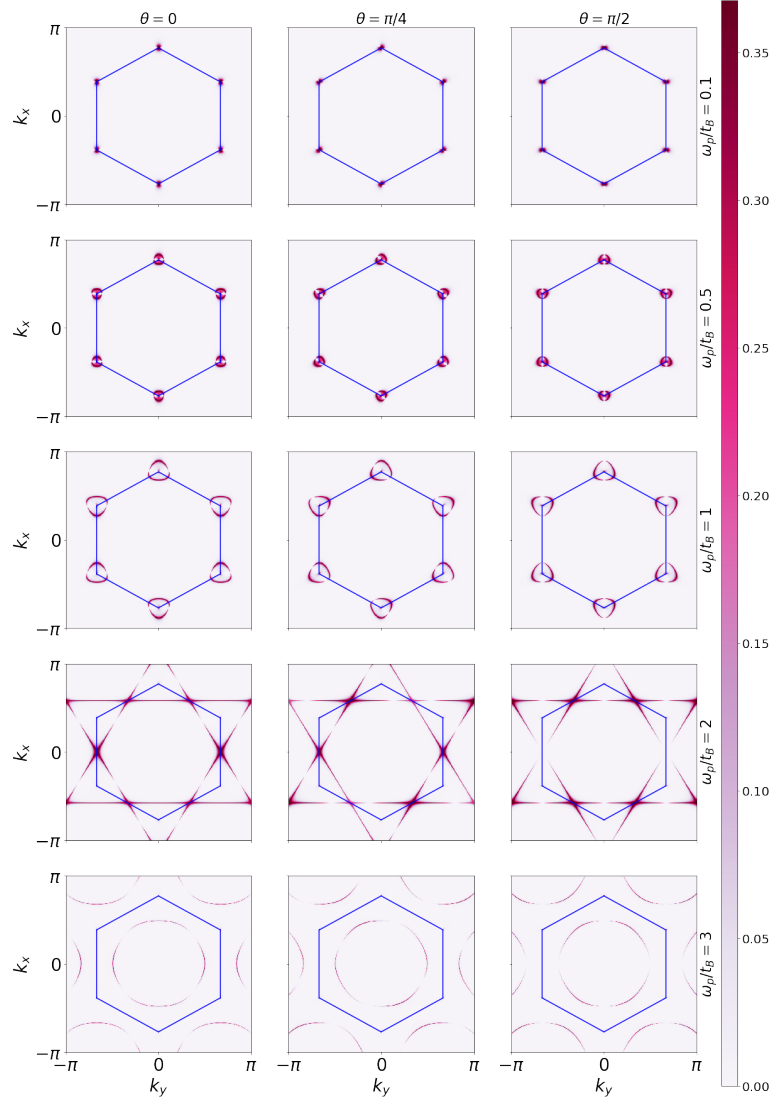


**Figure 4.4.:** Plot of the electronic density  $v_{\mathbf{k}}$  for different values of the pumping frequency  $\omega_p$  and pumping orientation  $\theta$  with intensity  $\mathcal{E}_0 = 0.5$  GV/m,  $E_F = 0$ ,  $\hbar\gamma_0 = 14$  meV, and  $\hbar\gamma_p = 28$  meV. The bright regions in the Brillouin zone depend on the value of  $\omega_p$  and have the orientation dependence of the term  $\nabla_{\mathbf{k}}\Theta_{\mathbf{k}} \cdot \boldsymbol{\mathcal{E}}$ , which in its turn depends on the polarization angle,  $\theta$ , of the incident field. Note that for low frequencies (left panels,  $\omega_p/t_{TB} = 0.1$ ) only momentum values near the Dirac points are excited. On the other hand, for  $\omega_p/t_{TB} = 2$  the brightest spots occur at the  $\mathbf{M}$ -point. Also note that the  $\mathbf{M}$ -points are not all excited at the same time, but depend on the polarization of the pumping field. This result contrasts with the case where the frequency of the pumping field pumps electrons to the Dirac cone (left panels). In this case, all the Dirac points are excited simultaneously.

The charge-charge correlation function can be calculated using the new electronic distribution obtained in Eqs. (4.6) and (4.7), instead of the equilibrium Fermi-Dirac distribution, as:

$$\chi(\mathbf{q}, \omega) = \frac{2e}{\hbar a_0^2} \sum_{\lambda, \lambda' = \pm} \int_{1^\circ \text{BZ}} \frac{d^2 \mathbf{k}}{(2\pi)^2} \frac{n_{\mathbf{k}+\mathbf{q}}^\lambda - n_{\mathbf{k}}^{\lambda'}}{\omega - \omega_{\mathbf{k}, \mathbf{q}}^{\lambda, \lambda'} + i\varepsilon} N_{\lambda' \lambda}^{\mathbf{k}, \mathbf{q}}, \quad (4.8)$$

where the factor 2 accounts for the spin degeneracy,  $n_{\mathbf{k}}^\lambda$  is the electronic distribution given by Eq. (4.6),  $\hbar\omega_{\mathbf{k}, \mathbf{q}}^{\lambda, \lambda'} = \lambda' E_{\mathbf{k}} - \lambda E_{\mathbf{k}+\mathbf{q}}$  is the energy transition, and the overlap of the eigenfunctions is given by:

$$N_{\lambda' \lambda}^{\mathbf{k}, \mathbf{q}} = \frac{1}{2} [1 + \lambda' \lambda \cos(\Theta_{\mathbf{k}} - \Theta_{\mathbf{k}+\mathbf{q}})], \quad (4.9)$$

Using Eq. (4.3) to split the density into the equilibrium  $f_{\mathbf{k}}^{c/v}$  and fluctuation  $v_{\mathbf{k}}$  parts, the susceptibility can be decomposed into an equilibrium  $\chi_0(\mathbf{q}, \omega)$  part, that is calculated using the equilibrium Fermi-Dirac distribution, and two pumped components, one intraband and the other interband, as:

$$\chi(\mathbf{q}, \omega) = \chi_0(\mathbf{q}, \omega) + \chi_{\text{pump}}^{\text{intra}}(\mathbf{q}, \omega) + \chi_{\text{pump}}^{\text{inter}}(\mathbf{q}, \omega), \quad (4.10)$$

where  $\omega$  is the frequency of the probe. The intraband pumped component of the susceptibility reads

$$\chi_{\text{pump}}^{\text{intra}}(\mathbf{q}, \omega) = \frac{2e}{\hbar a_0^2} \sum_{\lambda = \pm} \int_{1^\circ \text{BZ}} \frac{d^2 \mathbf{k}}{(2\pi)^2} \frac{\lambda(v_{\mathbf{k}+\mathbf{q}} - v_{\mathbf{k}})}{\omega - \lambda\omega_{\mathbf{k}, \mathbf{q}}^{\text{intra}} + i\eta} N_{-\lambda, \lambda}^{\mathbf{k}, \mathbf{q}}, \quad (4.11)$$

where  $\hbar\omega_{\mathbf{k}, \mathbf{q}}^{\text{intra}} = E_{\mathbf{k}} - E_{\mathbf{k}+\mathbf{q}}$ . Note that  $\chi_{\text{pump}}^{\text{intra}}$  is determined by the deviations to the Fermi-Dirac distribution:  $v_{\mathbf{k}+\mathbf{q}} - v_{\mathbf{k}}$ . The interband component reads as:

$$\chi_{\text{pump}}^{\text{inter}}(\mathbf{q}, \omega) = \frac{2e}{\hbar a_0^2} \sum_{\lambda = \pm} \lambda \int_{1^\circ \text{BZ}} \frac{d^2 \mathbf{k}}{(2\pi)^2} \frac{\lambda(v_{\mathbf{k}+\mathbf{q}} + v_{\mathbf{k}})}{\omega - \lambda\omega_{\mathbf{k}, \mathbf{q}}^{\text{inter}} + i\eta} N_{\lambda, \lambda}^{\mathbf{k}, \mathbf{q}}, \quad (4.12)$$

where  $\hbar\omega_{\mathbf{k}, \mathbf{q}}^{\text{inter}} = E_{\mathbf{k}} + E_{\mathbf{k}+\mathbf{q}}$ .

From now on we consider that  $\omega_p \gg \omega$ . This will be the case here because we will consider a probe in the THz range while the pump is in the UV range. From this consideration we can neglect the interband susceptibility  $\chi_{\text{pump}}^{\text{inter}}(\mathbf{q}, \omega)$ . This happens because the numerator of Eq. (4.12) is only non-zero for  $\mathbf{k}$  in the vicinity of the M-point (see Fig. 4.4) and so the denominator can be approximated as  $\omega - \lambda\omega_{\mathbf{k}, \mathbf{q}}^{\text{inter}} \approx \omega \pm \omega_p$ . This term will be negligible in comparison of  $\chi_{\text{pump}}^{\text{intra}}(\mathbf{q}, \omega)$  that has in the denominator a term that can be approximated as  $\omega - \lambda\omega_{\mathbf{k}, \mathbf{q}}^{\text{intra}} \approx \omega - \lambda \nabla_{\mathbf{k}} E_{\mathbf{k}} \cdot \mathbf{q}$ , and this quantity can be resonant with the probe frequency  $\omega$  depending on  $\mathbf{q}$ . In other

*See appendix 4.B for the approximation of the denominator of Eq. (4.11).*

words, the interband component of the pumped susceptibility is resonant with the pumping frequency and the intraband is resonant with the probe frequency.

We now want to introduce the effect of relaxation into the calculation of the charge susceptibility. This can be done using Mermin's approach developed for the 3D electron gas[92]. Following Mermin's work and making the necessary modifications for the graphene case, the total susceptibility, taking into account relaxation processes, is given by [15]:

$$\chi^M(\mathbf{q}, \omega) = \frac{(1 + i(\tau\omega)^{-1}) \chi(\mathbf{q}, \omega + i\gamma)}{1 + i(\tau\omega)^{-1} \chi(\mathbf{q}, \omega + i\gamma) / \chi(\mathbf{q}, \omega = 0)}, \quad (4.13)$$

where  $1/\tau = \gamma$  is the relaxation rate. For calculating Mermin's susceptibility we need the Lindhard susceptibility  $\chi(\mathbf{q}, \omega + i\gamma)$ , which needs to be computed for a complex frequency. In addition we also need the static susceptibility  $\chi(\mathbf{q}, \omega = 0)$ . The dielectric function can be obtained from the susceptibility as [15]:

$$\varepsilon(\mathbf{q}, \omega) = 1 - V(|\mathbf{q}|) \chi^M(\mathbf{q}, \omega), \quad (4.14)$$

where  $V(|\mathbf{q}|) = ea_0/(2\varepsilon_m q)$  is the 2D Fourier transform of the Coulomb potential and  $\varepsilon_m = \frac{\varepsilon_1 + \varepsilon_2}{2}$  is the effective dielectric constant of the environment for a graphene clad between two media of dielectric constants  $\varepsilon_1$  and  $\varepsilon_2$ . We recall that the term  $a_0$  appears in  $V(|\mathbf{q}|)$  because the wave number  $q$  is measured in units of the inverse lattice parameter  $a_0^{-1}$ .

Here we have an apparent disagreement with the rest of the chapter. Mermin's equation takes in account only one relaxation rate while we used interband and intraband transition rates in the SBE. However, as we neglect the interband contributions to the susceptibility, we can consider only the intraband transition rate and the intraband susceptibility:  $\chi(\mathbf{q}, \omega + i\gamma) \approx \chi^{\text{intra}}(\mathbf{q}, \omega + i\gamma)$  and  $\gamma \approx \gamma_0$ .

#### 4.4. Long wavelength limit: anisotropic plasmon dispersion relation

The calculation of the integral in Eq. (4.11) needs to be done for every different frequency  $\omega$  and wavenumber  $\mathbf{q}$ . However, as shown in Fig. 4.5, as  $\mathbf{q}$  decreases the conductivity reaches the long wavelength limit and we can show that in this regime the susceptibility in Eq. (4.11) behaves as  $q^2$ . In this limit, the static susceptibility appearing in the denominator of Eq. (4.13) tends to a constant value when  $q \rightarrow 0$ , and therefore Eq. (4.13) becomes:

$$\chi^M(\mathbf{q}, \omega) = (1 + i(\tau\omega)^{-1}) \chi(\mathbf{q}, \omega + i\gamma). \quad (4.15)$$

We now split the susceptibility in the right hand side of the Eq. (4.15) in the same way as we did in Eq. (4.10) —that is in an equilibrium and an out-of-equilibrium

parts. The equilibrium component  $\chi^0(\mathbf{q}, \omega)$  can be approximated by the Drude term for  $\hbar\omega < 2E_F$ , where  $E_F$  is the Fermi energy:

$$\chi^{\text{doped}}(\mathbf{q}, \omega) = \frac{4eE_F}{\pi\hbar^2 a_0^2} \frac{q^2}{(\omega + i\gamma)^2}. \quad (4.16)$$

For undoped graphene we have  $E_F = 0$  and the Drude contribution vanishes. For the out-of-equilibrium component, we obtain a similar expression in the long wavelength limit for the pumped susceptibility using Eq. (4.11) (details of the calculations are given in Appendix 4.B) in the form:

$$\chi_{\text{pump}}^{\text{intra}}(\mathbf{q}, \omega) = \sum_{i,j} C_{ij} \frac{q_i q_j}{(\omega + i\gamma)^2}. \quad (4.17)$$

The term in the right hand side of Eq. (4.17) corresponds to the intraband pumped contribution and can also be written as a quadratic dependence on the modulus of the wavevector  $\mathbf{q}$ . This is one of the central results of this chapter with far reaching implications.

Comparing Eq. (4.17) with the susceptibility of doped graphene in the long wavelength limit in Eq. (4.16), we can define an effective Fermi energy, that depends on the polarization angle  $\varphi$  of the probe field relative to the graphene lattice, as:

$$E_F^{\text{eff}}(\varphi) = E_F + f_0 + f_m \cos(2\varphi + \phi), \quad (4.18)$$

where  $f_0$ ,  $f_m$ , and  $\phi$  depend only on the properties of the pumping field —  $E_{\text{pump}}$ ,  $\theta$ , and  $\omega_p$  — which are defined in Appendix 4.B. Finally the susceptibility in Eq. (4.15) can be written as:

$$\chi^M(\varphi, \omega) = \frac{4e}{\pi\hbar^2 a_0^2} \frac{E_F^{\text{eff}}(\varphi) q^2}{\omega(\omega + i\gamma)}. \quad (4.19)$$

The plasmon dispersion is obtained from the condition  $\varepsilon(\mathbf{q}, \omega) = 0$  in Eq. (4.14), leading to:

$$\hbar\omega(\varphi, q) = \sqrt{2\alpha \frac{\hbar c}{a_0} E_F^{\text{eff}}(\varphi) q - i\frac{\gamma}{2}}, \quad (4.20)$$

where  $\alpha \approx 1/137$  is the fine structure constant of atomic physics. Equation (4.20) has the same  $\sqrt{q}$  dependence as that of plasmons in doped graphene without the pumping field [93, 15]. The difference lies in the presence of an effective Fermi energy  $E_F^{\text{eff}}(\varphi)$  that depends on the direction of the wavevector. Equation (4.20) is one of the central results of this chapter. Note that the dispersion will be anisotropic, as the effective Fermi energy depends on the orientation of the pumping electric field relatively to the graphene lattice. Furthermore, even in the case of neutral graphene, the system supports plasmons since  $E_F^{\text{eff}}(\varphi)$  is finite even for  $E_F = 0$ , due to the constant illumination of the pumping field.

## 4.5. The anisotropic conductivity of graphene under pumping

In this section we show that in an out-of-equilibrium situation we can define an anisotropic optical conductivity for graphene. The optical conductivity tensor  $\sigma_{ij}(\mathbf{q}, \omega)$  can be obtained via the continuity equation:

$$\mathbf{q} \cdot \mathbf{J} - \omega \rho = 0, \quad (4.21)$$

where  $\rho$  is the charge density and  $\mathbf{J}$  the surface density current. The current is described by

$$J_i = \sum_j \sigma_{ij}(\mathbf{q}, \omega) \mathcal{E}_j = -i \sum_j \sigma_{ij}(\mathbf{q}, \omega) q_j \Phi. \quad (4.22)$$

The previous result follows from the relation between the electric potential  $\Phi$ , with well defined momentum  $\mathbf{q}$ , and the electric field  $\mathcal{E}$  via the relation  $\mathcal{E} = -\nabla\Phi = -i\mathbf{q}\Phi$ . On the other hand, the charge density is obtained from the charge-charge susceptibility via  $\rho = -\chi^M(\mathbf{q}, \omega)\Phi$ . Thus, using Eq. (4.21), the relation between the conductivity tensor and the susceptibility is:

$$\sum_{i,j} \sigma_{ij}(\mathbf{q}, \omega) q_i q_j = i\omega \chi^M(\mathbf{q}, \omega). \quad (4.23)$$

The Equation (4.23) is not enough to determine the conductivity tensor from the susceptibility, but in the long wavelength limit,  $q \rightarrow 0$ , the dependence of each element of the conductivity tensor on the wavenumber disappear, and we can obtain three independent equations to the four quantities  $\sigma_{ij}$ . These three equations can be obtained changing the direction of the wavevector  $\mathbf{q}$  or, equivalently, we can compare the Taylor expansion of  $\chi^M(\mathbf{q}, \omega)$  to the left hand side of Eq. (4.23). This procedure would give four equations but one of them would not be independent of the other three. The missing equation can be obtained from the current-current response [94] where the intraband contributions to the conductivity tensor read<sup>1</sup>

$$\sigma_{ij}^{\text{intra}}(\mathbf{q}, \omega) = \frac{2ie^2}{\hbar\omega S} \sum_{\mathbf{k}, \lambda=\pm} \frac{n_{\mathbf{k}+\mathbf{q}/2}^\lambda - n_{\mathbf{k}-\mathbf{q}/2}^\lambda}{\omega - \lambda\omega_{\mathbf{k},\mathbf{q}}^{\text{intra}} + i\gamma} v_{i\mathbf{k},\mathbf{q}}^{\text{intra}} v_{j\mathbf{k},-\mathbf{q}}^{\text{intra}}, \quad (4.24)$$

with  $v_{i\mathbf{k},\mathbf{q}}^{\text{intra}}$  the components of:

$$\mathbf{v}_{\mathbf{k},\mathbf{q}}^{\text{intra}} = \frac{a_0 t_{\text{TB}}}{2\hbar} \left( e^{-i\Theta_{\mathbf{k}-\mathbf{q}/2}} \nabla_{\mathbf{k}} \phi_{\mathbf{k}-\mathbf{q}/2} + e^{i\Theta_{\mathbf{k}+\mathbf{q}/2}} \nabla_{\mathbf{k}} \phi_{\mathbf{k}+\mathbf{q}/2}^* \right). \quad (4.25)$$

<sup>1</sup>The use of the charge-charge current response is not totally consistent with the use of a phenomenological relaxation rate: the equilibrium density matrix now depends on the vector field [95]. However this does not change the results in this chapter: from this result we only need a simple symmetry property of the conductivity tensor.



and  $S = N_c a_0^2$ , where  $N_c$  is the number of unit cells and

$$\phi_{\mathbf{k}} = \sum_{i=1}^3 e^{i\mathbf{k} \cdot \delta_i}, \quad (4.26)$$

where  $\delta_i$  are the basis vectors (see appendix A for more details).

From Eq. (4.24) we can show that in the limit  $\mathbf{q} \rightarrow 0$ , we have:

$$\sigma_{ij}^{\text{intra}}(\mathbf{q} \rightarrow 0, \omega) = \sigma_{ji}^{\text{intra}}(\mathbf{q} \rightarrow 0, \omega), \quad (4.27)$$

thus it follows from Eq. (4.23) that:

$$\sigma_{ij}^{\text{pumped}} = \sigma_0 \frac{C_{ij}}{\omega + i\gamma}, \quad (4.28)$$

where  $\sigma_0 = e^2/(4\hbar)$  and  $C_{ij}$  are the coefficients of the expansion of  $\chi^{\text{pumped}}(\mathbf{q}, \omega)$  defined in Eq. (4.17), and the total intraband conductivity can be written as function of an effective Fermi energy tensor  $E_{ij}^{\text{eff}}$  as:

$$\frac{\sigma_{ij}}{\sigma_0} = i \frac{4}{\hbar\pi} \frac{E_{ij}^{\text{eff}}}{\omega + i\gamma}, \quad (4.29)$$

where we have defined the effective Fermi energy tensor as:

$$E_{ij}^{\text{eff}} = E_F \delta_{ij} + \frac{\pi}{4} C_{ij}. \quad (4.30)$$

Although the tensor  $E_{ij}^{\text{eff}}$  can be reduced to diagonal form by a rotation, doing so we loose the direct connection of the tensor components to the orientation of the graphene lattice.

We can also define the longitudinal conductivity along the direction defined by the unit vector  $\mathbf{u}_\varphi$  for a probing electric field of the form  $\mathcal{E} = \mathcal{E}_0 \mathbf{u}_\varphi$  as:

$$\sigma_\varphi = \frac{\mathbf{J} \cdot \mathbf{u}_\varphi}{\mathcal{E}_0} = \frac{4i}{\hbar\pi} \frac{E_F^{\text{eff}}(\varphi)}{\omega + i\gamma}, \quad (4.31)$$

where the angle  $\varphi$  (the polarization angle of the probing field) is the same as that of the momentum  $\mathbf{q}$ , since the electric field is proportional to  $\mathbf{q}$  via the gradient of the potential.

It is worth remembering that the effective parameters  $f_0, f_m$ , and  $\phi$  depend solely on the pumping field properties, that is, on the intensity  $\mathcal{E}_0$ , the polarization angle  $\theta$ , and the frequency  $\omega_p$ .

## 4.6. Numerical results

As shown before (see Fig. 4.4), graphene under intense and energetic light pumping presents a strong anisotropic electronic distribution. This changes the optical response due to intraband and interband transitions. In doped graphene, without electromagnetic pumping, the intraband transitions dominates for photon energy  $\hbar\omega < 2E_F$ , while interband transitions dominate for  $\hbar\omega > 2E_F$  [18]. For pumped graphene, we have a similar result, where intraband transitions dominate for  $\omega < \omega_p$ , where  $\omega_p$  is the frequency of the pumping radiation, and interband transitions dominates for  $\omega \approx \omega_p$ .

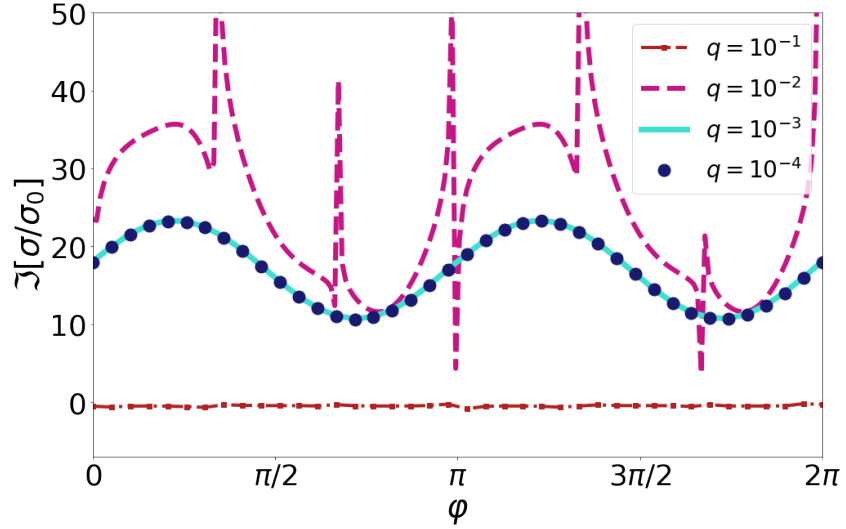


**Figure 4.5.:** Imaginary part of the longitudinal conductivity as function of the polarization angle of the pump field for different values of  $q$ . The parameters are:  $\epsilon_0 = 0.707$  GV/m,  $\hbar\omega_p = 2t_{TB}$ ,  $\theta = \pi/4$ ,  $E_F = 0.2$  eV and  $\hbar\gamma_0 = 14$  meV, and  $\hbar\gamma_p = 28$  meV. For  $q < 10^{-3}$  the susceptibility reaches the long wavelength limit. For  $q = 10^{-2}$  we can see the strong influence of the static susceptibility (see Fig. 4.14).

To show the effects of the pumping in graphene, we solve numerically the Eq. (4.11) and compute the pumped component of the intra-band susceptibility. The  $\chi_0(\mathbf{q}, \omega)$  component is calculated with the analytical expressions derived with the Dirac equation [15], since it is not necessary here to account for the full band structure of graphene. This is because for the equilibrium distribution, the probe frequency  $\omega$  in the range we are considering can only excite electron-hole pairs around the Dirac cone. This is not the case for the pumped electron gas around the M-point, that cannot be described by the Dirac equation. The out-of-equilibrium distribution is calculated using Eq. (4.7).

We plot in Fig. 4.5 the imaginary part of the longitudinal conductivity, Eq. (4.31), as function of the probe incidence angle  $\varphi$ , for different wave numbers  $q$ ; this quantity

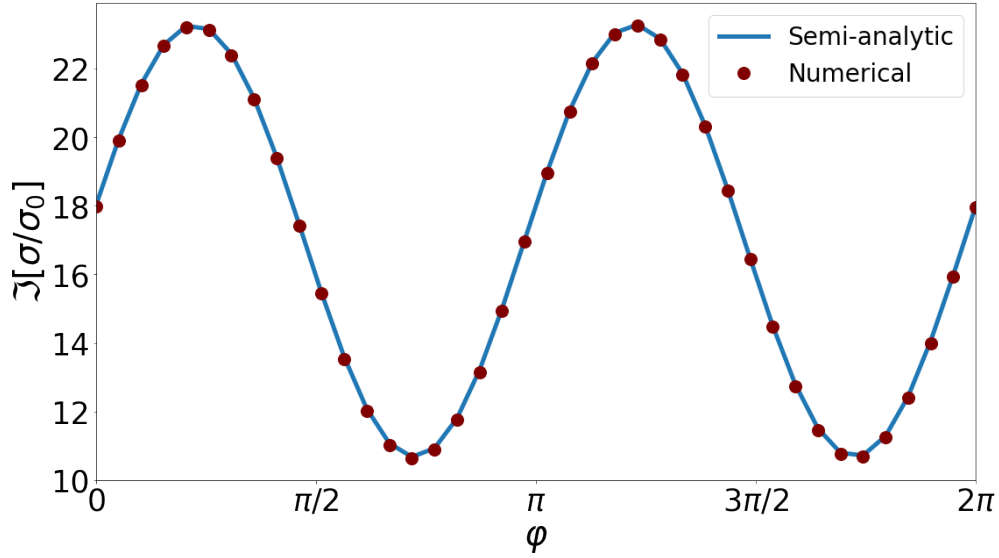


**Figure 4.6.:** Comparison between the semi-analytical approach and the numerical one for the imaginary part of the longitudinal conductivity, showing the validity of the semi-analytical approximation obtained in section 4.4. The dots correspond to the cyan solid curve in Fig. 4.5 and the solid line is the semi-analytical calculation. Note that  $\Im\sigma \in [10\sigma_0, 24\sigma_0]$ ; the difference between the maximum and the minimum of the conductivity depends on the magnitude of  $\varepsilon_0$ . The parameters are:  $q = 10^{-3}$ ,  $\varepsilon_0 = 0.707$  GV/m,  $\hbar\omega_p = 2t_{TB}$ ,  $\theta = \pi/4$ ,  $E_F = 0.2$  eV, and  $\hbar\gamma_0 = 14$  meV, and  $\gamma_p = 28$  meV.

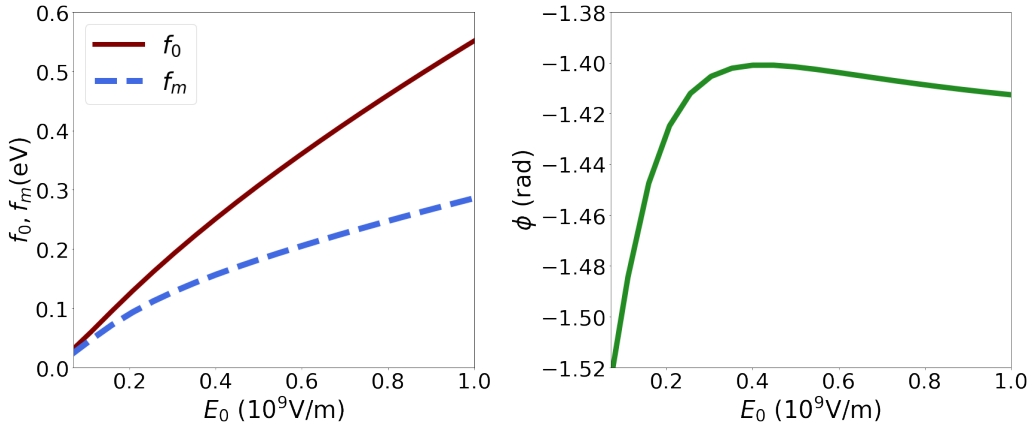


**Figure 4.7.:** Dependence of the parameters  $f_0$ ,  $f_m$ , and  $\phi$  on the intensity of the pumping radiation. The parameters are:  $\theta = \pi/4$ ,  $\hbar\omega_p = 2t_{TB}$ ,  $E_F = 0.2$  eV,  $\hbar\gamma_0 = 14$  meV, and  $\hbar\gamma_p = 28$  meV. The importance of the parameters  $f_0$  and  $f_m$  grows with the intensity of the pumping field. The minimum value of field intensity considered in this figure is 0.1 GV/m. We see that the anisotropy is observable for this field intensity. We note that the field intensities scanned in this figure are experimentally attainable.

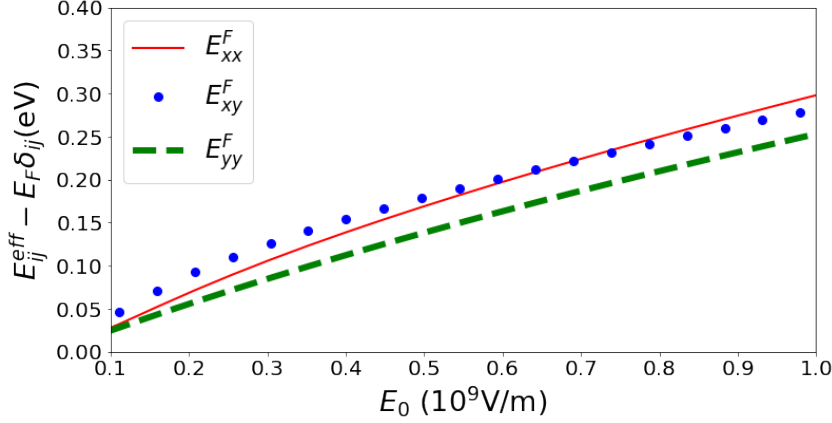
controls the dispersion of the surface plasmon-polariton in the out-of-equilibrium electron gas, as will be discussed in a forthcoming section. We show that the long wavelength limit is reached around  $q = 10^{-3}$ , where the conductivity has a sinusoidal shape as predicted by Eq. (4.18). Note that  $q$  is measured in units of  $1/a_0$ . In the same figure we also depict an example of the longitudinal conductivity away from the long wavelength limit ( $q = 10^{-2}$ ). It is clear that in this regime the distribution is, for some  $\varphi$  values, substantially different from the analytical approximation. Since we are interested here in the long wavelength limit, this result does not interest us and will not be discussed further.

Figure 4.6 shows the numerically computed imaginary part of the longitudinal conductivity, as a function of the probing polarization angle  $\varphi$ , for  $q = 10^{-3}$ , as defined by Eq. (4.31), compared with the semi-analytical result, which depends on the effective Fermi energy defined in Eq. (4.18). The two approaches show a very good agreement, showing that indeed for  $q = 10^{-3}$  the system is already in the long wavelength regime. The oscillatory variation of the imaginary part of the longitudinal conductivity will lead to an anisotropy in the spectrum of the surface plasmon-polariton, as it is this quantity that determines the behavior of the latter. Note that  $\Im\sigma \in [10\sigma_0, 24\sigma_0]$  (see Fig. 4.6).

From here on our analysis is focused on two ways of parameterizing the effective Fermi energy: by the function  $E_F^{\text{eff}}(\phi)$  that appears in the susceptibility (4.18) or the matrix  $E_{ij}^{\text{eff}}$  that appears in the optical conductivity (4.29). The function  $E_F^{\text{eff}}(\phi)$  also appears in the dispersion relation of the plasmon modes (4.20). The optical conductivity (4.29) is the input of Eq. (4.34). Therefore, it is useful to study in detail how those two quantities behave in function of the pumping frequency, intensity and polarization.

Figure 4.7 shows that the parameters  $f_0$  and  $f_m$  have a strong dependency on the intensity of the pumping field. The angle  $\phi$ , in contrast, changes very little by as much as  $\sim 0.1$  rad, and tends to saturate for large intensity fields. The parameters  $f_0$  and  $f_m$  can have a strong impact in the optical response of the system, depending on the initial doping level of graphene, characterized by  $E_F$ . For large doping, the effect of  $f_0$  and  $f_m$  is small, except for large pumping field intensities. However, for vanishing small Fermi energies, the effect of these two parameters has a large impact in the optical properties of the system, as the effective Fermi energy is essentially controlled by them.

The dependence of the effective Fermi energy  $E_{ij}^F$  on the intensity of the pumping radiation is depicted in Fig. 4.8. A clear anisotropy is seen in this quantity. Particularly interesting is the finite value of  $E_{xy}^F$ , which leads to a finite off-diagonal term for the non-equilibrium optical conductivity. The dependence of the parameters  $f_0$ ,  $f_m$ , and  $\phi$  on the energy of the pumping photons is depicted in Fig. 4.9. We see that there is a non-monotonous dependence on  $\omega_p$  with a local maximum (for  $f_0$ ,  $f_m$ , and  $\phi$ ) when the photon energy is equal to the electronic transition at the M-point ( $\hbar\omega_p/t_{\text{TB}} = 2$ ). This is, most likely, due to the enhanced density of states associated



**Figure 4.8.:** Dependence of the effective Fermi energy  $E_{ij}^{\text{eff}} - E_F \delta_{ij}$  on the intensity of the pumping radiation (in GV/m). The anisotropy grows with the increase of  $\varepsilon_0$ . The parameters are:  $\theta = \pi/4$ ,  $\hbar\omega_p = 2t_{\text{TB}}$ ,  $E_F = 0.2$  eV,  $\hbar\gamma_0 = 14$  meV, and  $\hbar\gamma_p = 28$  meV. The minimum value of field intensity considered in this figure is 0.1 GV/m.

with the van-Hove singularity.

In Fig. 4.10 the effective Fermi energy is depicted as function of the frequency of the pumping field. Clearly its behavior is controlled by the values of the parameters  $f_0$ ,  $f_m$ , and  $\phi$ , as can be seen from comparing Figs. 4.9 and 4.10. Again a local maximum is seen at the value of photon energy given by  $\hbar\omega = 2t_{\text{TB}}$ .

It is worthwhile to remark that the absolute maximum of the  $f_0$  and  $f_m$  parameters, in Fig. 4.9, takes place for  $\hbar\omega_p \approx 0.5t_{\text{TB}}$  ( $\sim 1.4$  eV), leading to an out-of-equilibrium gas with a larger effective Fermi energy than when the system is pumped with photons of frequency  $\hbar\omega_p \sim 2t_{\text{TB}}$ . This energy scale is controlled by the electric field intensity. Indeed, the system has an energy scale  $\Delta$ , for the parameters of Fig. 4.9, given by

$$\Delta/t_{\text{TB}} \sim \sqrt{\frac{\varepsilon_0 a_0}{t_{\text{TB}}}} \sim 0.2, \quad (4.32)$$

which is of the same order of magnitude of  $\hbar\omega_p \approx 0.5t_{\text{TB}}$ , the position of the absolute maximum of the parameters  $f_0$  and  $f_m$ . Note that apart from the gradient of the phase  $\Theta_{\mathbf{k}}$ ,  $\varepsilon_0 a_0$  is essentially the Rabi frequency. We have verified that by reducing the field intensity by five times, the position of the maximum red-shifts to an energy of about two times smaller the value of  $\hbar\omega = 0.5t_{\text{TB}}$ . This effect is represented in the inset of the bottom panel of Fig. 4.10. The scaling of the position of the maximum of  $f_0$  with  $\sqrt{\varepsilon_0}$  is evident. Note, however, that, for these energy scales, the anisotropy for the plasmon spectrum will be very small, as  $E_{xx}^F \approx E_{yy}^F$ . Let us also note here that the intensity of the density of the states at the van-Hove singularity is presumably controlled by the value of  $\gamma_0$ : the larger this parameter is the smaller is the density of states at the M-point, which otherwise would be a divergence in the absence of

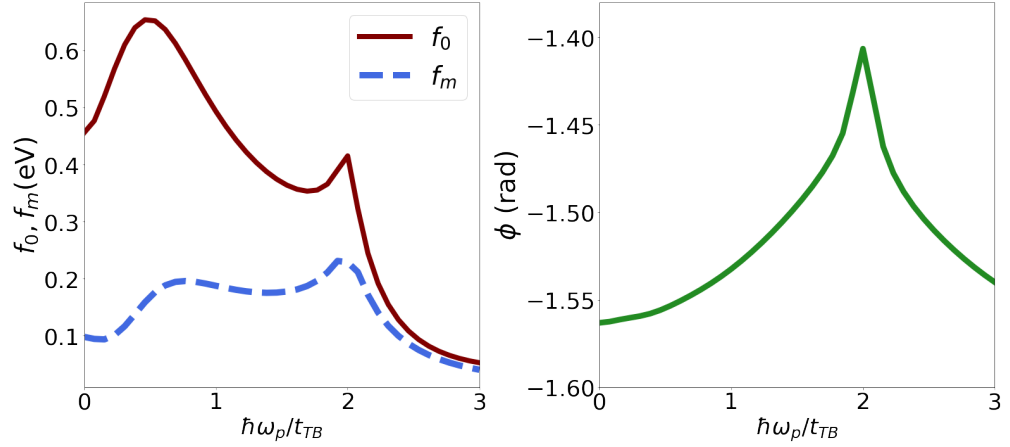


**Figure 4.9.:** Dependence of the parameters  $f_0$ ,  $f_m$ , and  $\phi$  on the energy of the photon of the pumping field. The parameters are:  $\varepsilon_0 = 0.707$  GV/m,  $\theta = \pi/4$ ,  $\hbar\omega_p = 2t_{TB}$ ,  $E_F = 0.2$  eV,  $\hbar\gamma_0 = 14$  meV, and  $\hbar\gamma_p = 28$  meV. A non-monotonous dependence on  $\omega_p$  is seen for the three parameters. We must however stress that for  $\hbar\omega_p \approx 0$  the behavior of  $f_0$ ,  $f_m$ , and  $\phi$  is not accurate, as we have not included the effect of interband transitions, due to probe of frequency  $\omega$ , which become relevant for  $\omega_p \sim \omega$ , specially in the case of neutral graphene. See Fig. 4.10 for a discussion of the position of the maximum of  $f_0$  and  $f_m$  located at low energies.

relaxation.

In Figs. 4.11 and 4.12 we show the strong anisotropy in the optical response. The parameter  $f_m$ , that measures the amplitude of the effective Fermi energy modulation, has maxima where the  $f_0$  presents minima for some specific angles. This is the origin of the strong anisotropy in the optical response of the system, which imparts in the anisotropy of the dispersion relation of the plasmons. In the Fig. 4.11 the parameter  $\phi$  is also depicted showing a large variation with the angle of polarization of the pumping field. The significant variation of  $f_0$ ,  $f_m$ , and  $\phi$  on  $\theta$  controls the dispersion of the plasmon in this system.

We emphasize that the results presented in Figs. 4.7-4.12 correspond to the contribution from intraband transitions that take place near the three independent M-points (in this case the concept of valley is meaningless). Note that Fig. 4.4 shows the effect of the anisotropic distribution near each M-point and the different occupations of each M-point. For this electronic distribution, the parity symmetry is broken (see Fig. 4.4), and, as a consequence, we can have a finite off-diagonal conductivity. The same symmetry is broken in the Hamiltonian studied by Kumar *et al.*[86]. However, in this case the parity symmetry is broken by a circular polarized pumping field that populates each valley differently (in graphene each valley is connected by the parity symmetry).

One experimental way of accessing the dispersion of the plasmons in a given ma-

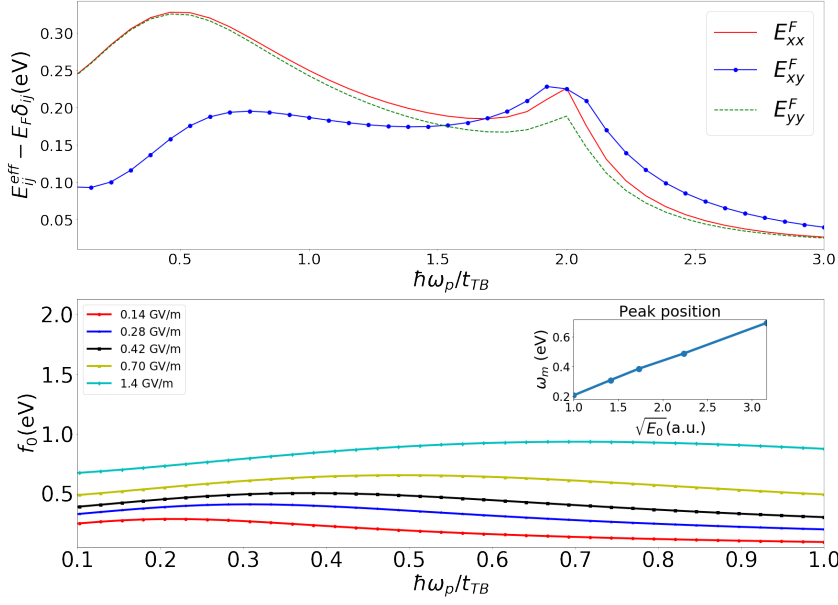


**Figure 4.10.:** Left panel: Dependence of the components of the effective Fermi energy tensor  $E_{ij}^{\text{eff}} - E_F \delta_{ij}$  on the pumping field frequency. The parameters are:  $\epsilon_0 = 0.707$  GV/m,  $\theta = \pi/4$ ,  $E_F = 0.2$  eV,  $\hbar\gamma_0 = 14$  meV, and  $\hbar\gamma_p = 28$  meV. Note the local maximum of the Fermi-energy tensor-elements around the photon energy  $\hbar\omega = 2t_{TB}$ . Also note that the largest difference between  $E_{xx}^F$  and  $E_{yy}^F$  occurs at the M–point which implies the largest anisotropy in the properties of the system, including the plasmon spectrum. We must stress that for  $\hbar\omega_p \approx 0$  the behavior the effective Fermi energy components are not accurate, as we have not included the effect of interband transitions, due to the probe of frequency  $\omega$ , which become relevant for  $\omega_p \sim \omega$ , specially in the case of neutral graphene. Right panel: Zoom in of the dependence of the parameter  $f_0$  with  $\epsilon_0$  near the absolute maximum. Inset panel: Scaling of the frequency of the maximum,  $\omega_m$ , with the  $\sqrt{\epsilon_0}$  (right panel); the linear scaling is evident. The values of  $\omega_m$  are extracted from the central panel, and correspond to the position of the maximum of the curves for  $f_0$ . Note that the larger  $\epsilon_0$  is the broader is the maximum and more intense is  $f_0$ .

terial is to perform a EELS experiment. This spectroscopic technique is based on the excitation of plasmons by moving charges. When exciting a plasmon wave, the incoming electrons lose part of their kinetic energy. Theoretically, the loss function, which encodes the excitation of the plasmons by the moving electrons, is defined in terms of the dielectric function (4.14) as:

$$\mathcal{L}(\mathbf{q}, \omega) = -\Im \left\{ \frac{1}{\epsilon(\mathbf{q}, \omega)} \right\}. \quad (4.33)$$

This quantity is depicted in Fig. 4.13, for different values of the probing polarization angle  $\varphi$ . The dielectric function was calculated using Eq. (4.14) and the pumping susceptibility is given by Eq. (4.11). In Fig. 4.13 we can see the characteristic plasmon signature in the loss function. It is clear that the plasmon spectrum depends

#### 4. GRAPHENE PUMP-PROBE SYSTEMS

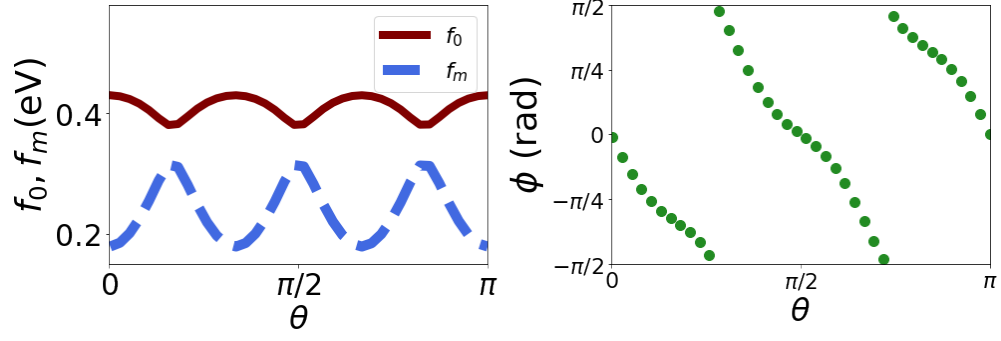


**Figure 4.11.:** Dependence of the parameters determining the effective Fermi energy on the pumping polarization angle. Note that for some values of  $\theta$  the magnitudes of  $f_0$  and  $f_m$  are almost identical. Also the angle  $\phi$  varies substantially with  $\theta$ . The largest anisotropy in the properties of the system occurs for the largest difference between  $f_0$  and  $f_m$ . The parameters are:  $\varepsilon_0 = 0.707$  GV/m,  $\hbar\omega_p = 2t_{TB}$ ,  $E_F = 0.2$  eV,  $\hbar\gamma_0 = 14$  meV, and  $\hbar\gamma_p = 28$  meV.

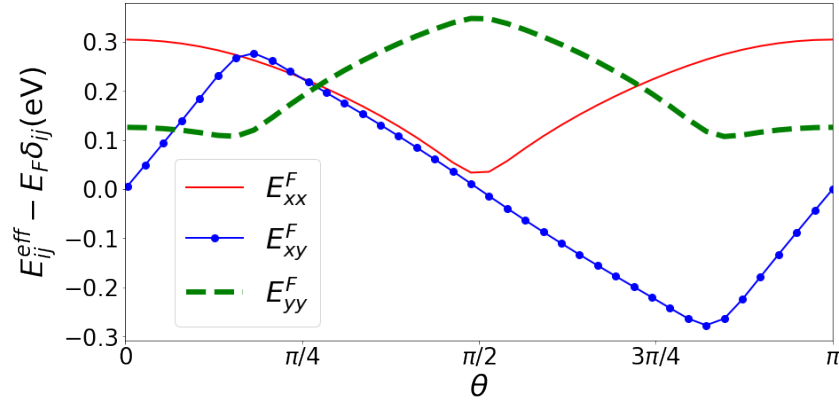


**Figure 4.12.:** Dependence of the effective Fermi-energy  $E_{ij}^{\text{eff}} - E_F \delta_{ij}$  on the polarization angle of the pumping field. We emphasize that our calculations take the three M-points into account simultaneously since we are making a tight-binding calculation. Therefore there is no cancellation of  $E_{xy}$ . The parameters are:  $\varepsilon_0 = 0.707$  GV/m,  $\hbar\omega_p = 2t_{TB}$ ,  $E_F = 0.2$  eV,  $\hbar\gamma_0 = 14$  meV, and  $\hbar\gamma_p = 28$  meV. Note the periodic behavior of the different parameters.

significantly on the polarization of the probing field, or, in other terms, on the direction of the momentum in the Brillouin zone. The width of the plasmon spectrum is proportional to the relaxation rate  $\gamma_0$ . For making apparent the anisotropy we also depict (solid line) the dispersion of the plasmon after an average of the effective Fermi energy on the polarization angle  $\varphi$ ; the anisotropy is obvious.

Let us now discuss the reason why the plasmon characterizing pumped graphene out-of-equilibrium is similar to that of doped graphene in equilibrium, in what con-



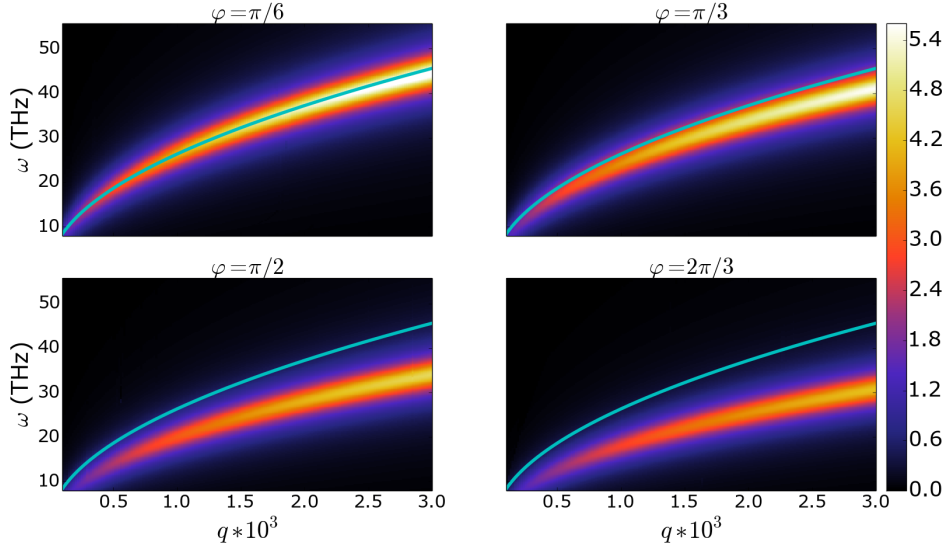


**Figure 4.13.:** Loss function for different polarizations of the probe field as function of the dimensionless wavenumber (multiplied by  $10^3$ ). The parameters are  $\epsilon_0 = 0.707$  GV/m,  $\theta = \pi/4$ ,  $\hbar\omega_p = 2t_{TB}$ ,  $E_F = 0.2$  eV,  $\hbar\gamma_0 = 14$  meV, and  $\hbar\gamma_p = 28$  meV. The solid (cyan) curve is the plasmon dispersion for the semi-analytical result in Eq. (4.20) after an average of the effective Fermi energy on the polarization angle  $\varphi$

cerns their small energy values. In the latter case, for  $\hbar\omega + \hbar v_F q < E_F$  and  $\omega > v_F q$ , where  $q$  is the wavenumber and  $\omega$  the frequency, interband processes are suppressed by Pauli-blocking and the susceptibility is dominated by intraband processes, where losses are proportional to the relaxation rate  $\gamma_0$  (for  $\gamma_0 = 0$  the usual plasmons are infinitely long-lived in this momentum-frequency window). In this regime, graphene supports plasmons with small attenuation with a dispersion relation proportional to  $\sqrt{q}$ . On the other hand, when we consider the case of the pumped distribution, the situation is similar, because interband process, that attenuates the plasmon, only occur for frequencies  $\omega$  near the pumped frequency  $\omega_p$ . Since we are considering the regime  $\omega \ll \omega_p$ , the attenuation of the plasmons of the non-equilibrium electron gas is essentially controlled by the value of  $\gamma_0$  (the plasmons cannot decay via particle-hole processes in this regime, as it happens in the case of an equilibrium plasma). Therefore, the correspondent pumped susceptibility is similar in the sense that the imaginary part is proportional to the scattering time [see Eq. (4.16)]. Thus, we can expect for plasmons in the out-of-equilibrium electron gas the same level of attenuation of the conventional plasmons in graphene. As consequence the former anisotropic plasmons are expected to be long lived as are their siblings in the equilibrium electron gas.

In Fig. 4.14 we show that the graphene static susceptibility have zeros that renders

the term  $(\tau\omega)^{-1}\chi(q,\omega)/\chi^0(q)$  ( $\tau = 1/\gamma$ ) in Mermin's susceptibility large, even at small  $q$ . In this case the use of the Mermin's equation is no longer valid, since the assumption that the fluctuations of the local Fermi Energy, which are proportional to  $1/\chi^0(q)$ , are small is no longer true and the approximation leading to Mermin's equation breaks down.

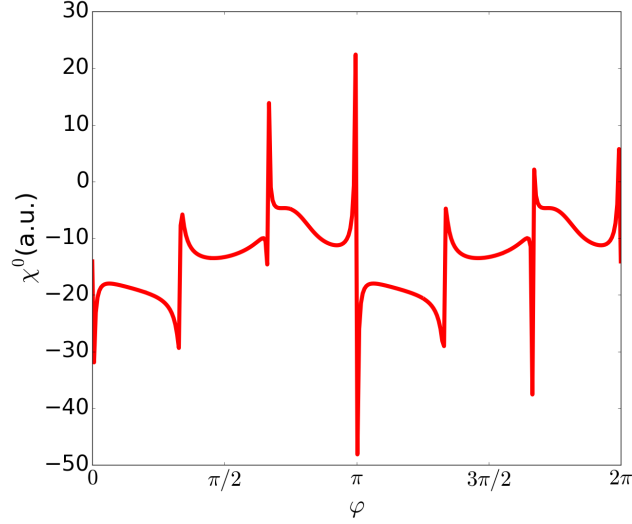


**Figure 4.14.:** Static susceptibility for  $q = 2.10^{-3}$ ,  $\varepsilon_0 = 0.707$  GV/m, and  $\theta = \pi/4$  as function of the polarization angle of the probe field. Note the existence of points where the susceptibility is zero. Near and at these points Mermin's approach breaksdown.

## 4.7. Spectrum of the surface plasmon-polaritons in the out-of-equilibrium regime

As a conductive two dimensional system, graphene supports surface plasmon-polaritons. We now want to address the propagation of these quasi-particles on the surface of graphene due to the electron gas created by the pumping field. We will see that the surface plasmon-polariton spectrum in pumped graphene shows a dispersion strongly dependent on the  $\varphi$  angle, the polarization angle of the probing field. A surface plasmon-polariton (SPP) is an hybrid particle that couples electromagnetic radiation to the free oscillations of an electron gas in a conductor. In graphene, the spectrum of an SPP depends critically on the nature of the optical conductivity of the system (for a discussion about surface plasmon-polariton in graphene see Refs. [12, 96]). Indeed, it can be shown that the condition for the existence of an SPP is

given by[12]

$$\left[ \frac{\varepsilon_1}{k_1} + \frac{\varepsilon_2}{k_2} + \frac{i\sigma_{xx}}{\omega\varepsilon_0} \right] \left[ \frac{k_1 + k_2}{\omega\mu_0} - i\sigma_{yy} \right] - \frac{\sigma_{xy}\sigma_{yx}}{\omega\varepsilon_0} = 0, \quad (4.34)$$

for a wave propagating along the  $x$  direction and decaying exponentially along the

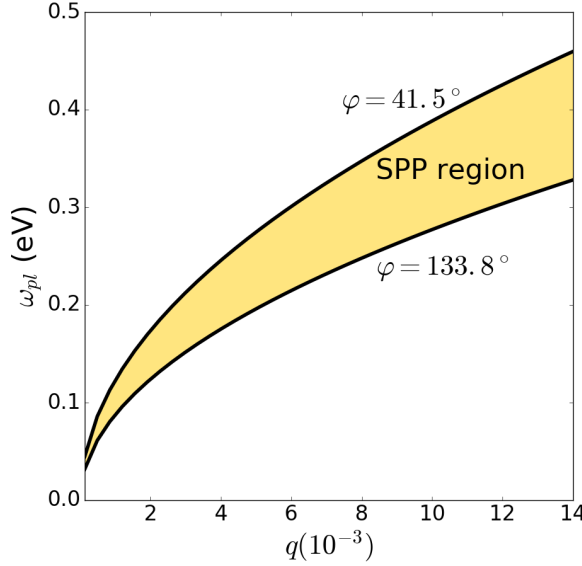


**Figure 4.15.:** Surface plasmon-polaritons dispersion relation, of the out-of-equilibrium electron gas, for different values of the angle  $\varphi$  of the polarization of the probing radiation as function of the dimensionless wave vector. Note that all the angles in the interval  $\varphi \in [0, 2\pi]$  are contained in the shaded region. The parameters are:  $\varepsilon_0 = 0.5$  GV/m,  $\hbar\omega_p = 2t_{TB}$ ,  $\theta = \pi/4$ ,  $E_F = 0.4$  eV,  $\hbar\gamma_0 = 14$  meV, and  $\hbar\gamma_p = 28$  meV.

direction perpendicular to the graphene plane. When  $\sigma_{xy} = \sigma_{yx} = 0$ , the transverse electric and the transverse magnetic modes decouple. In the case we are considering here this is not the case, since the non-equilibrium nature of the electron gas created by the pumping induces a finite value for  $\sigma_{xy}$ . However, since time reversal symmetry is not explicitly broken in this case, we have the condition that  $\sigma_{xy} = \sigma_{yx}$ . Using the calculated conductivity tensor in Eq. (4.29) and the coefficients  $C_{ij}$  calculated through Eq. (4.44), the spectrum of the SPP can be obtained.

The dispersion relation of the surface plasmon-polariton due to the non-equilibrium electron gas depends on the orientation of the direction of propagation of the wave with respect to the crystalline lattice. To describe the propagation along another direction, we can rewrite Eq. (4.34) in the new reference frame or, alternatively, rotate the conductivity tensor. The latter can be achieved with the usual 2D

rotation matrix  $M_\varphi$ ,  $\sigma' = M_\varphi \sigma M_\varphi^{-1}$ :

$$M_\varphi = \begin{pmatrix} \cos \varphi & -\sin \varphi \\ \sin \varphi & \cos \varphi \end{pmatrix}. \quad (4.35)$$

In Fig. 4.15 we show, for fixed  $\varepsilon_0$ ,  $\omega_p$ ,  $E_F$ , and  $\theta$ , the surface-plasmon polariton in graphene from the solution of Eq. (4.34). The shaded region corresponds to different values of the variable  $\varphi$ , between those represented by the black solid lines at the borders of the shaded region. We see again the strong dependence of the optical properties upon the probe angle  $\varphi$ , which is measured by the anisotropy in the SPP spectrum. Note that the variation of the spectrum with  $\varphi$  is quite substantial and therefore amenable to experimental verification.

## 4.8. Final comments

In this chapter we have considered a pump-probe problem, where the pumping field is a relatively intense and pulsed wave field, with a pulse duration much larger than 1 ps. In this situation we can reach a stationary state where an out-of-equilibrium electron gas is maintained in the conduction band in graphene. We have considered the case where the frequency of the pumping field lies in the UV-range of the electromagnetic spectrum. In this case the electrons are pumped to the M–point in the Brillouin zone. In addition to the pumping, a probe field of much smaller frequency probes the out-of-equilibrium electron gas. This allows us to access the collective plasma wave —plasmons— in the out-of-equilibrium electron gas. We have shown that for pumping field of this frequency the excitation of the three M–points in the Brillouin zone is uneven, at odds with the excitation of an electron gas near the Dirac points. This is a consequence of the strong deviation of the band structure of graphene from the Dirac cone approximation. Indeed, near the M–point the band structure has a saddle point nature being, therefore, very different from the Dirac cone. Interestingly enough, we have found that the plasmon in the out-of-equilibrium electron gas still scales with the  $\sqrt{q}$  as in the case of the Dirac plasmons. This is a consequence of the form of the charge-charge susceptibility, which scale as  $q_i q_j$  ( $i = x, y$ ) in the long wavelength limit (note that in the Dirac cone approximation the charge-charge susceptibility scales as  $q^2$ ). This scaling can still be written in terms of  $q^2$  if we introduce an effective Fermi energy, depending on the properties of the pumping field. The anisotropy of the plasmon dispersion in the Brillouin zone originates from the scaling  $q_i q_j$  and is encoded in the effective Fermi energy. At the more fundamental level, the fact that the out-of-equilibrium susceptibility scales with  $q_i q_j$  in the long wavelength limit is a consequence of the continuity equation (4.23) that links the susceptibility with the conductivity. If in the long wavelength limit the susceptibility scales with a power lower than  $q^2$  the conductivity would diverge and if the power is greater than  $q^2$ , the conductivity would be null.

Due to the relation between the charge-charge susceptibility and the optical conductivity, it is possible to define an out-of-equilibrium optical conductivity. Interestingly, the non-linear dependence of the out-of-equilibrium distribution function on the pumping field allows for a finite value of  $\sigma_{xy}^{\text{intra}} = \sigma_{yx}^{\text{intra}} \neq 0$ . This has an impact on the spectrum of the surface plasmon-polaritons (SPPs) that can be supported by the out-of-equilibrium electron gas, as in this case, the TE and TM polarization are coupled to each other. We have found that the measured values for SPP spectrum depend on the orientation of the polarization of the probing field. This is a consequence of the anisotropy of the optical conductivity of graphene in the regime considered.

What is missing from the analysis developed in this chapter is a detailed study of the effect of electron-phonon and electron-electron interactions, which has been included only at the level of a phenomenological scattering rate. Therefore phenomena such as carrier multiplication is not included in our description. It would be an interesting to discuss this problem in the regime we have considered, a problem that was not analysed in the literature before, but this is outside the scope of this chapter.

*For the interband conductivity the situation is identical  $\sigma_{xy}^{\text{inter}} = \sigma_{yx}^{\text{inter}} \neq 0$ . Onsagar relation requires  $\sigma_{xy}(H) = -\sigma_{yx}(H)$  in the presence of magnetic field  $H$ , or similarly broken time reversal symmetry. A Hamiltonian with circular polarized external light field is not time invariant, in which case we would have a different result from above.*

## 4.A. Steady-state equations for the distribution functions under continuous pumping

With the assumption that  $\partial_t n_{\mathbf{k}}^c = \partial_t n_{\mathbf{k}}^v = 0$  and considering a monochromatic incident field with frequency  $\omega_p$ , we can write Eqs. (4.1) as:

$$\gamma_0 (n_{c,\mathbf{k}} - f_{c,\mathbf{k}}) - i \langle \Omega_{\mathbf{k}}(t) \Delta p_{\mathbf{k}} \rangle_t = 0, \quad (4.36a)$$

$$\gamma_0 (n_{v,\mathbf{k}} - f_{v,\mathbf{k}}) + i \langle \Omega_{\mathbf{k}}(t) \Delta p_{\mathbf{k}} \rangle_t = 0, \quad (4.36b)$$

$$(\partial_t - i\omega_{\mathbf{k}} + \gamma_p) p_{cv,\mathbf{k}} = +i\Omega_{\mathbf{k}}(t) \Delta n_{\mathbf{k}}, \quad (4.36c)$$

$$(\partial_t + i\omega_{\mathbf{k}} + \gamma_p) p_{vc,\mathbf{k}} = -i\Omega_{\mathbf{k}}(t) \Delta n_{\mathbf{k}}, \quad (4.36d)$$

where we use  $\langle \rangle_t$  for time average. The solution to this set of equations is of the form:

$$p_{cv,\mathbf{k}}(t) = A_1(\omega_p) e^{i\omega_p t} + B_1(\omega_p) e^{-i\omega_p t}, \quad (4.37a)$$

$$p_{vc,\mathbf{k}}(t) = A_2(\omega_p) e^{i\omega_p t} + B_2(\omega_p) e^{-i\omega_p t}, \quad (4.37b)$$

where  $A_i, B_i$  can be obtained from Eqs. (4.36c) and (4.36d) as:

$$A_1(\omega_p) = -\frac{n_{c,\mathbf{k}} - n_{v,\mathbf{k}}}{\omega_p - \omega_{\mathbf{k}} - i\gamma_p} \frac{\bar{\Omega}_{\mathbf{k}}}{2}, \quad (4.38a)$$

$$B_1(\omega_p) = -\frac{n_{c,\mathbf{k}} - n_{v,\mathbf{k}}}{-\omega_p - \omega_{\mathbf{k}} - i\gamma_p} \frac{\bar{\Omega}_{\mathbf{k}}^*}{2}, \quad (4.38b)$$

$$A_2(\omega_p) = -\frac{n_{v,\mathbf{k}} - n_{c,\mathbf{k}}}{\omega_p + \omega_{\mathbf{k}} - i\gamma_p} \frac{\bar{\Omega}_{\mathbf{k}}}{2}, \quad (4.38c)$$

$$B_2(\omega_p) = -\frac{n_{v,\mathbf{k}} - n_{c,\mathbf{k}}}{-\omega_p + \omega_{\mathbf{k}} - i\gamma_p} \frac{\bar{\Omega}_{\mathbf{k}}^*}{2}, \quad (4.38d)$$

with:

$$\bar{\Omega}_{\mathbf{k}} = \frac{ea_0\epsilon_0 \cdot \nabla_{\mathbf{k}} \Theta_{\mathbf{k}}}{2\hbar}. \quad (4.39)$$

If we define:

$$\alpha_{\mathbf{k}} = \tau_0 \tau_p |\bar{\Omega}_{\mathbf{k}}|^2 \frac{1 + \tau_p^2 (\omega_{\mathbf{k}}^2 + \omega_p^2)}{\tau_p^4 (\omega_p^2 - \omega_{\mathbf{k}}^2)^2 + 2\tau_p^2 (\omega_p^2 + \omega_{\mathbf{k}}^2) + 1}, \quad (4.40)$$

with  $\tau_0 = 1/\gamma_0, \tau_p = 1/\gamma_p$ , we have from Eqs. (4.36a) and (4.36b) that:

$$n_{c,\mathbf{k}} - f_{c,\mathbf{k}} = \alpha_{\mathbf{k}} (n_{v,\mathbf{k}} - n_{c,\mathbf{k}}), \quad (4.41a)$$

$$n_{v,\mathbf{k}} - f_{v,\mathbf{k}} = \alpha_{\mathbf{k}} (n_{c,\mathbf{k}} - n_{v,\mathbf{k}}). \quad (4.41b)$$

Note that expression for  $\alpha_{\mathbf{k}}$  is well defined even taking the collisionless regime  $(\tau_0, \tau_p) \rightarrow \infty$ .

## 4.B. Semi-analytical formula for the charge-charge correlation function

In the long wavelength limit, the susceptibility for finite frequency is written in power of  $q^2$ . If we expand  $v_{\mathbf{k}+\mathbf{q}}$  and  $\omega_{\mathbf{k},\mathbf{q}}$  until order  $q^2$ , we have:

$$\chi_{\text{pump}}^{\text{intra}}(\mathbf{q}, \omega) = \frac{2e}{\hbar a_0^2} \sum_{\lambda} \int \frac{d^2\mathbf{k}}{(2\pi)^2} \frac{\lambda \nabla_{\mathbf{k}} v_{\mathbf{k}} \cdot \mathbf{q}}{\omega - \lambda \nabla_{\mathbf{k}} E_{\mathbf{k}} \cdot \mathbf{q} + i\gamma_0}, \quad (4.42)$$

where we used that  $N(\mathbf{k}, \mathbf{q}) = 1 + \mathcal{O}(q^2)$ . Expanding also the denominator we find:

$$\chi_{\text{pump}}^{\text{intra}}(\mathbf{q}, \omega) = \frac{4e}{\hbar a_0^2} \frac{1}{(\omega + i\gamma_0)^2} \int \frac{d^2\mathbf{k}}{(2\pi)^2} \nabla_{\mathbf{k}} v_{\mathbf{k}} \cdot \mathbf{q} \nabla_{\mathbf{k}} E_{\mathbf{k}} \cdot \mathbf{q}, \quad (4.43)$$

and thus we can define:

$$C_{ij} = \int \frac{d^2\mathbf{k}}{(2\pi)^2} \partial_i v_{\mathbf{k}} \partial_j E_{\mathbf{k}}. \quad (4.44)$$

In terms of  $C_{ij}$  we rewrite Eq. (4.43) as:

$$\chi_{\text{pump}}^{\text{intra}}(\mathbf{q}, \omega) = \frac{4e}{\hbar a_0^2} \frac{1}{(\omega + i\gamma_0)^2} \sum_{ij} C_{ij} q_i q_j. \quad (4.45)$$

Making  $q_x = q \cos \varphi$  and  $q_y = q \sin \varphi$  it follows that:

$$\begin{aligned} \frac{1}{q^2} \sum_{ij} C_{ij} q_i q_j &= C_{xx} \cos^2 \varphi + C_{yy} \sin^2 \varphi \\ &+ (C_{xy} + C_{yx}) \sin \varphi \cos \varphi. \end{aligned} \quad (4.46)$$

With an integration by parts we can show from Eq. (4.44) that  $C_{xy} = C_{yx}$ . Using trigonometric identities we can write Eq. (4.46) as:

$$\frac{1}{q^2} \sum_{ij} C_{ij} q_i q_j = \frac{C_{xx} + C_{yy}}{2} + \frac{C_{xx} - C_{yy}}{2} \cos 2\varphi + C_{xy} \sin 2\varphi. \quad (4.47)$$

Defining:

$$f_0 = \frac{1}{\pi} \frac{C_{xx} + C_{yy}}{2}, \quad (4.48a)$$

$$f_m = \frac{1}{\pi} \sqrt{\left(\frac{C_{xx} - C_{yy}}{2}\right)^2 + C_{xy}^2}, \quad (4.48b)$$

$$\phi = \arctan \frac{2C_{xy}}{C_{xx} - C_{yy}}, \quad (4.48c)$$

the susceptibility (4.45) is written as:

$$\chi_{\text{pump}}^{\text{intra}}(q, \varphi, \omega) = \frac{4e (f_0 + f_m \cos(2\varphi - \phi))}{\hbar^2 a_0^2 \pi} \frac{q^2}{(\omega + i\gamma_0)^2}. \quad (4.49)$$

It is then possible to defined an effective Fermi energy  $E_F^{\text{eff}}(\varphi) = E_F + f_0 + f_m \cos(2\varphi - \phi)$ , which allows to write the total susceptibility as:

$$\chi(q, \varphi, \omega) = \frac{4e E_F^{\text{eff}}(\varphi)}{\hbar^2 a_0^2 \pi} \frac{q^2}{(\omega + i\gamma_0)^2}. \quad (4.50)$$

The last result has the same functional form on frequency as that of the charge-charge susceptibility in the independent electron gas model.





The study of excitons in bulk transition-metal dichalcogenides (TMDCs) is a research topic in condensed matter physics that dates back to 1960's [97, 98]. With the advent of two-dimensional materials [99], this topic regained interest since it became possible to study single- and few-layers of TMDCs [100, 101]. Together with its two-dimensional nature, this new class of materials also has a hexagonal lattice structure as does graphene. On the other hand, while the low-energy electronic excitations are in graphene described by a massless Dirac equation, in monolayer TMDCs the same excitations can be described by a massive (with a gap) Dirac equation. The absence of a gap in graphene prohibits the existence of bound-states of excitons (but not of excitonic resonances [102]). On the contrary, we find in TMDCs absorption spectrum fingerprints of both excitonic bound states (including the presence of a Rydberg series) and of excitonic resonances, due to electron-hole scattering processes, with energies above the non-interacting gap.

As a consequence of optical experimental studies in few-layers TMDCs, the study of a new type of excitons in these novel 2D materials became possible. This has attracted a wealth of scientific research [103, 104, 105, 106, 53, 107, 108, 109, 110, 111, 112, 113, 114, 115, 116, 117]. The signature of excitons appeared first in the optical measurements of monolayer MoS<sub>2</sub> [101], where two peaks in the absorbance, with energies  $\sim 1.9$  eV and  $\sim 2.1$  eV, were identified. These two peaks correspond approximately to the same results found in several layers of MoS<sub>2</sub> [97].

The optical studies of other monolayers of TMDCs soon followed at the pace of their synthesis. The optical properties of MX<sub>2</sub>, M={Mo,W}, X={S,Se}, in the range 1.5 – 3 eV were experimentally studied by Li *et al.* [53], with reflectance and transmittance measurements followed by a Kramers-Kronig analyses, and by Morozov and Kuno [106], with differential transmission and reflectance measurements. It should be noted that all these four materials have similar optical properties. Their optical absorbance spectra show signatures of the spin-orbit splitting for excitons at the **K**(**K'**) points in the Brillouin zone, as well as signatures of excitonic resonances at the  $\Gamma$ -point.

The properties of the excitons at the  $\mathbf{K}$ -point were extensively studied in the framework of tight-binding and Bethe-Salpeter equation (BSE) [112, 113], DFT + GW + BSE [110, 111], and gapped 2D Dirac-equation [113]. One of the most prominent features in the optical spectra of these materials is its dependence on the Berry phase, which generates a modified Rydberg series [114, 115]. The form of the electron-electron interaction potential, which deviates from the Coulomb one, also contributes to a modified Rydberg series [118]. The C-excitonic resonance in monolayer MoS<sub>2</sub>, due to transitions at the  $\Gamma$ -point, was first calculated by Qiu *et al.* [111], and it was associated with a minimum in the optical band structure around the  $\Gamma$ -point by Klots *et al.* [116]. The effects of temperature and carrier density in MoS<sub>2</sub> were studied either solving the semiconductor Bloch equation (SBE) with a tight-binding Hamiltonian, whose parameters were obtained from a  $G_0W$  calculation [117], or by combining a LDA+BSE approach with the inclusion of electron-phonon coupling [103].

In the present chapter we use the polarization concept formalism [69, 102] for describing the excitonic properties of monolayer TMDCs. This formalism is easily applied to any system, both using low-energy effective models or tight-binding ones. The development of the formalism boils down to the solution of an eigenvalue problem for determining the excitonic bound states and to the solution of a linear system of equations for computing the optical conductivity of the system. We apply the resulting equations to a two-band gapped Dirac equation for describing the physics around the  $\mathbf{K}$ -point; this originates the physics of the A and B excitons in the TMDCs and of a modified Rydberg series. On the other hand, using as a starting point the three-band model for TMDCs [119] we describe the formation of an excitonic resonance near the  $\Gamma$ -point. This approach allows us to make much analytical progress and clearly identify the origin of different bound-states and resonances in the absorption spectrum. In this regard, our approach is distinct from previous ones that consider the full band structure as a starting point. The advantage of our approach lies in the possibility of clearly identify the origin of the different peaks in the optical conductivity, or absorbance for the same matters, of TMDCs.

We show that the optical properties have a strong dependence on external parameters, namely, temperature and dielectric function of the environment. This dependence on external parameters opens the possibility of engineering at will nanomaterials showing strong optical response in the spectral range from the IR to visible. The application of these systems to opto-electronics, including photo-detectors, will launch a new set of devices in this area. Another possibility that these 2D materials may provide is the engineering Bose-Einstein condensation of excitons when a TMDC is put inside an optical cavity [120].

The chapter is organized as follows: in section 5.1 we introduce the second quantized form of the Hamiltonian, which is composed of three pieces: the non-interacting part, the light-matter interaction term, and the Coulomb interaction. Using this Hamiltonian the excitonic properties at the Dirac point are worked out. In section 5.1 we derive the optical properties of four TMDCs around the  $\mathbf{K}$ -point in the Brillouin

zone. Using a three-band tight-binding model we describe the excitonic properties of four TMDCs in section 5.2. The excitonic effects around the  $\Gamma$ -point in the Brillouin zone are actually resonances, as they are above the continuum. In section 5.3 the optical properties of four TMDCs are discussed in detail and compared with the existent experimental data for the absorption. We find a good agreement with the experimental data, although, since we do not include electron-phonon interaction, the agreement is not quantitative. We also note that the experimental values for the absorption present discrepancies among different experiments. This led us to conclude that there is a clear sample-dependence in the absorption measurements. In two of the TMDCs we stress the absence of the B-excitonic series in the experimental data, which is a noticeable discrepancy with our theoretical calculations. This led us to believe that the experiments need to be repeated for encapsulated TMDCs in h-BN at low temperatures. This approach screens away the effect of extrinsic disorder, and reduces the impact of phonons in the absorption spectrum, due to low temperatures. Finally, in section 5.4 we provide a summary of the main conclusions of the chapter. A set of appendices give details of the calculations.

## 5.1. K-point excitons

In this section we introduce the effective model for electronic properties of TMDCs around the  $K$ -point in the Brillouin zone. Since we are dealing with a many-body problem, the second quantization formalism is used throughout the chapter. Using the full interacting Hamiltonian, the equations of motion for the density matrix are obtained and from it the total polarization is derived. The electron-electron interaction generates a hierarchy of correlation functions that are truncated at the random-phase approximation (RPA) level. This procedure is equivalent, in a diagrammatic approach, to the inclusion diagrams considering only the interaction in the electron-hole propagator. The diagrams relevant to our calculation are given in figure 5.1, where  $K$  represents the BSE kernel (see ahead). Although the diagrammatic approach is a possible route to solve the problem of excitonic effects in TMDCs, it is also possible to address it using an equation-of-motion approach. The latter formalism enables treating at the same level of approximation the exchange-energy correction and the excitonic effects, and that is the path we will follow in this chapter.

The band structure implied by Hamiltonian (5.1) around the  $K$ -point in the Brillouin zone is depicted in figure 5.2 (different colors correspond to opposite spin projections).

The low-energy single-particle electronic-excitations of TMDC materials can be described, in the  $\mathbf{k} \cdot \mathbf{p}$  approximation, by a 2D gapped Dirac equation. When we consider spin-orbit coupling (SOC), the effective mass and chemical potential become valley and spin dependent. With these aspects in mind, we can write the single-

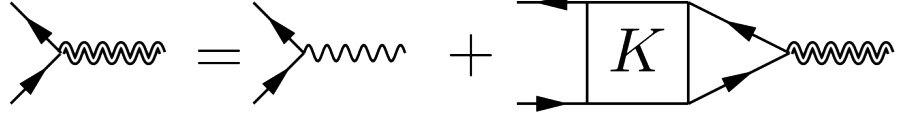


**Figure 5.1.:** Diagrammatic expression of the Bethe-Salpeter equation for the vertex function. Our truncation of the equation-of-motion for the density matrix (when we introduced the RPA approximation) is equivalent to consider the kernel of the BSE in the ladder approximation. However, a more precise approach would require more diagrams to be summed in the kernel.

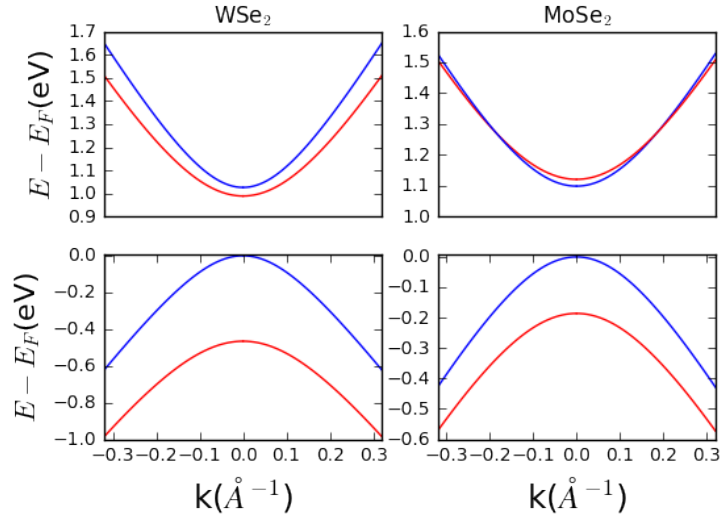


**Figure 5.2.:** Band structure of WSe<sub>2</sub> and MoSe<sub>2</sub> around the  $\mathbf{K}$ -point in the Brillouin zone, as described by Hamiltonian (5.1). Note that for WSe<sub>2</sub> the bands of different spin projections (different colors) do not cross, whereas for MoSe<sub>2</sub> there is a crossing in the conduction bands. Due to these differences, the optical response of the two materials as function of doping differs from each other. In particular, in WSe<sub>2</sub> the highest-energy exciton peak is suppressed upon doping when compared to the lowest one. (We have located the chemical potential at the top of the valence band.)

particle Hamiltonian for a single combination of valley( $\tau$ )/spin( $s$ ) index as:

$$H_0^{s\tau}(\mathbf{k}) = \hbar v_F (\tau \sigma_1 k_x + \sigma_2 k_y) + \sigma_3 m_{s\tau} v_F^2 - \mu_{s\tau} I, \quad (5.1)$$

with  $\sigma_i$  the usual Pauli matrices and  $I$  the identity matrix,  $\tau = \pm$  the valley index, and  $s = \pm$  the spin index. The effective mass,  $m_{s\tau}$ , and the on-site energy,  $\mu_{s\tau}$ , can

be written in terms of the SOC parameters,  $\Lambda_1$  and  $\Lambda_2$  [121], and of the mass  $\Delta$  as:

$$m_{s\tau} = \Delta - \frac{s\tau}{2} \frac{\Lambda_1}{v_F^2}, \quad (5.2)$$

$$\mu_{s\tau} = \frac{1}{2} s\tau \Lambda_2. \quad (5.3)$$

with  $\Lambda_1 = \Delta_{\text{VB}} - \Delta_{\text{CB}}$  and  $\Lambda_2 = \Delta_{\text{VB}} + \Delta_{\text{CB}}$ , with  $\Delta_{\text{VB}}$  ( $\Delta_{\text{CB}}$ ) the spin-splitting of the valence (conduction) band.

In three dimensions (3D), the electron-electron interaction in a dielectric medium is given by the Coulomb potential in vacuum but with the permittivity of free space  $\varepsilon_0$  replaced by the medium permittivity  $\varepsilon_m \varepsilon_0$ . Contrary to 3D, the same procedure does not hold in 2D materials. In contrast, the electron-electron interaction is described by the Keldysh potential [6, 122]. This takes into account the surface charge polarization from a dielectric thin film and reads in momentum space:

$$V(q) = -\frac{e}{2\varepsilon_0} \frac{1}{q(r_0 q + \varepsilon_m)}, \quad (5.4)$$

*See appendix D for a discussion between the relation of the Keldysh potential and the static RPA.*

where  $q$  is the 2D transferred momentum,  $\varepsilon_m$  and  $r_0$  are the capping dielectric function of the environment and a material-dependent constant, respectively, the latter measuring the deviation from the 2D Coulomb potential. Note that we recover the 2D Coulomb potential making  $r_0 \rightarrow 0$ . The potential (5.4) is written in a slightly different manner than in reference [122] for removing the dependence of the parameter  $r_0$  on the external dielectric constant.

To calculate the optical properties of TMDCs, we consider the interaction of the electron gas with a time-dependent electric field  $\mathcal{E}(t)$  polarized along the  $x$  axis. For describing the light-matter interaction in this problem we use the dipole-coupling Hamiltonian

$$\hat{H}_I(t) = e\mathcal{E}(t)\hat{x}, \quad (5.5)$$

with  $\hat{x}$  the position operator and  $e > 0$  the magnitude of the electron charge. For the external field, we only consider the interband terms of the Hamiltonian  $\hat{H}_I$  as we are discussing a neutral system. In this condition  $\hat{H}_I$  reads:

$$\hat{H}_I = -\mathcal{E}(t) \sum_{s\tau\lambda_1\mathbf{k}} d_{\lambda_1}^{s\tau}(\mathbf{k}) \hat{\rho}_{\lambda_1-\lambda_1}^{s\tau}(\mathbf{k}, t), \quad (5.6)$$

where  $\lambda = \pm$  stands for the conductance (+) and valence (-) bands. The interband dipole matrix element  $d_{\lambda_1}^{s\tau}(\mathbf{k})$  is given by:

$$d_{\lambda_1}^{s\tau}(\mathbf{k}) = -ie\hbar \frac{v_{\lambda_1}^{s\tau}(\mathbf{k})}{2\lambda_1 E_k^{s\tau}}. \quad (5.7)$$

with  $v_{\lambda_1}^{s\tau}(\mathbf{k})$  the matrix element of the velocity operator (E.10). See appendix E for the derivation and explicit formulas.

From now on, we consider the full many-body Hamiltonian as:

$$\hat{H} = \hat{H}_0 + \hat{H}_I(t) + \hat{H}_{ee}, \quad (5.8)$$

where  $\hat{H}_0$  is built from the single-particle Hamiltonian (5.1) and  $\hat{H}_{ee}$  is the electron-electron interaction:

$$\hat{H}_{ee} = -\frac{e}{2} \int d\mathbf{r}_1 d\mathbf{r}_2 \hat{\psi}^\dagger(\mathbf{r}_1) \hat{\psi}^\dagger(\mathbf{r}_2) V(\mathbf{r}_1 - \mathbf{r}_2) \hat{\psi}(\mathbf{r}_2) \hat{\psi}(\mathbf{r}_1), \quad (5.9)$$

where  $\hat{\psi}(\mathbf{r})$  is the field operator (5.10) defined below and  $V(\mathbf{q})$  is the Fourier transform of the Keldysh potential given by equation (5.4). For simplicity, from here on we choose units such that  $v_F = \hbar = e = 1$ ; the usual units are reintroduced at the end of the calculations. The field operator is given by:

$$\hat{\psi}(\mathbf{r}, t) = \frac{1}{\sqrt{S}} \sum_{\mathbf{k}, \lambda, s, \tau} \phi_{\lambda}^{s\tau}(\mathbf{k}) \hat{a}_{\lambda \mathbf{k} s \tau}(t) e^{i\mathbf{k} \cdot \mathbf{r}}, \quad (5.10)$$

with  $S$  the square-box area,  $\hat{a}_{\mathbf{k} \lambda s \tau}$  the usual annihilation operator that obeys anti-commutation relations and  $\phi_{\mathbf{k} \lambda s \tau}$  the eigenfunctions of  $H_0^{s\tau}$ ,  $H_0^{s\tau} \phi_{\tau}^{s\lambda}(\mathbf{k}) = (\lambda E_k^{s\tau} - \mu_{s\tau}) \phi_{\tau}^{s\lambda}(\mathbf{k})$ , with  $\lambda = - (+)$  for the valence (conduction) band. The eigenfunctions and positive eigenvalues are given by:

$$\phi_{\lambda}^{s\tau}(\mathbf{k}) = \sqrt{\frac{E_k^{s\tau} + \lambda m_{s\tau}}{2E_k^{s\tau}}} \begin{pmatrix} 1 \\ \frac{\tau k_x - i k_y}{\lambda E_k^{s\tau} + m_{s\tau}} \end{pmatrix}, \quad (5.11)$$

$$E_k^{s\tau} = \sqrt{k^2 + m_{s\tau}^2}. \quad (5.12)$$

The eigenfunctions (5.11) will be used extensively in this chapter for determining the four-body structure factor. The electron-electron interaction can be written as (see Sec. 3.A):

$$\begin{aligned} \hat{H}_{ee} = -\frac{1}{2S} \sum_{s\tau \lambda_1 \lambda_2 \lambda_3 \lambda_4} \sum_{\mathbf{k} \mathbf{k}' \mathbf{q}} V(|\mathbf{q}|) F_{\lambda_1 \lambda_2 \lambda_3 \lambda_4}^{s\tau}(\mathbf{k}, \mathbf{k}', \mathbf{q}) \hat{a}_{\lambda_1 \mathbf{k}' - \mathbf{q} s \tau}^\dagger(t) \hat{a}_{\lambda_3 \mathbf{k} + \mathbf{q} s \tau}^\dagger(t) \times \\ \times \hat{a}_{\lambda_4 \mathbf{k} s \tau}(t) \hat{a}_{\lambda_2 \mathbf{k}' s \tau}(t). \end{aligned} \quad (5.13)$$

where the four spinor product is (3.29):

$$F_{\lambda_1, \lambda_2, \lambda_3, \lambda_4}^{s\tau}(\mathbf{k}_1, \mathbf{k}_2) = \phi_{\lambda_1}^{s\tau \dagger}(\mathbf{k}_1) \phi_{\lambda_2}^{s\tau}(\mathbf{k}_2) \phi_{\lambda_3}^{s\tau \dagger}(\mathbf{k}_2) \phi_{\lambda_4}^{s\tau}(\mathbf{k}_1). \quad (5.14)$$

### 5.1.1. EQUATION OF MOTION AND OPTICAL PROPERTIES

Here we will consider that the dynamics of each pair spin/valley separated, i.e., we will neglect the interaction that can occur between pairs of different valleys and spins: from this we start now to add a  $s\tau$  label in each quantity that depends on the spin/valley. In chapter 5 we derived the SBE for a two-bandy system, obtaining (3.64):

$$-i\partial_t p_\lambda^{s\tau}(\mathbf{k}, t) = -\tilde{\omega}_{\lambda\mathbf{k}}^{s\tau} p_\lambda^{s\tau}(\mathbf{k}, t) + \tilde{\Omega}_{\mathbf{k}\lambda}^{s\tau}(t) \Delta f_\lambda^{s\tau}(\mathbf{k}), \quad (5.15)$$

where the renormalized Rabi frequency is given by:

$$\tilde{\Omega}_{\mathbf{k}\lambda}^{s\tau}(\mathbf{k}, t) = \varepsilon(t) d_{-\lambda}^{s\tau}(\mathbf{k}) + \mathcal{B}_{\mathbf{k}\lambda}^{s\tau}(t), \quad (5.16)$$

the difference in occupation is given by  $\Delta f_\lambda^{s\tau}(\mathbf{k}) = f_\lambda^{s\tau}(\mathbf{k}) - f_{-\lambda}^{s\tau}(\mathbf{k})$ , where  $f_\lambda^{s\tau}(\mathbf{k})$  is the Fermi-Dirac distribution:

$$f_\lambda^{s\tau}(\mathbf{k}) = \left\{ \exp \left[ \frac{\lambda E_k^{s\tau} - \mu_{s\tau} - E_F}{k_B T} \right] + 1 \right\}^{-1}, \quad (5.17)$$

with  $T$  the temperature,  $k_B$  the Boltzmann constant and  $E_F$  the Fermi energy.

We have that  $\mathcal{B}_{\mathbf{k}\lambda}^{s\tau}(t)$  is given by Eq. (3.58):

$$\mathcal{B}_{\mathbf{k}\lambda}^{s\tau}(t) = -\frac{1}{S} \sum_{\mathbf{q}} V(|\mathbf{k} - \mathbf{q}|) \left[ p_\lambda(\mathbf{q}, t) F_{-\lambda-\lambda\lambda\lambda}^{s\tau}(\mathbf{k}, \mathbf{q}) + p_{-\lambda}^{s\tau}(\mathbf{q}, t) F_{-\lambda\lambda-\lambda\lambda}^{s\tau}(\mathbf{k}, \mathbf{q}) \right], \quad (5.18)$$

and the renormalized transition energy is (3.59):

$$\hbar\tilde{\omega}_{\lambda\mathbf{k}}^{s\tau} = 2\lambda E_k^{s\tau} + \lambda \Sigma_{\mathbf{k}, \lambda}^{\text{xc}, s\tau}, \quad (5.19)$$

with the exchange self-energy given by (3.60):

$$\Sigma_{\mathbf{k}, \lambda}^{\text{xc}, s\tau}(t) = -\frac{\lambda}{S} \sum_{\mathbf{q}} V(q) \Delta f_\lambda^{s\tau}(\mathbf{k} - \mathbf{q}) \left[ F_{-\lambda\lambda\lambda-\lambda}^{s\tau}(\mathbf{k}, \mathbf{k} - \mathbf{q}) - F_{\lambda\lambda\lambda\lambda}^{s\tau}(\mathbf{k}, \mathbf{k} - \mathbf{q}) \right]. \quad (5.20)$$

The external electrical field is written as  $\varepsilon(t) = \varepsilon_0 e^{-i\omega t}$ , and the linear-response is obtained from the terms proportional to  $e^{-i\omega t}$ ,  $p_\lambda^{s\tau}(\mathbf{k}, t) = p_\lambda^{s\tau}(\mathbf{k}, \omega) e^{-i\omega t}$ . The equation-of-motion (5.15) in the linear regime becomes:

$$(\omega + \tilde{\omega}_{\lambda\mathbf{k}}^{s\tau}) p_\lambda^{s\tau}(\mathbf{k}, \omega) = -(\varepsilon_0 d_{-\lambda, x}^{s\tau}(\mathbf{k}) + \mathcal{B}_{\mathbf{k}\lambda}^{s\tau}(\omega)) \Delta f_\lambda^{s\tau}(\mathbf{k}), \quad (5.21)$$

with  $\mathcal{B}_{\mathbf{k}\lambda}^{s\tau}(\omega)$  obtained replacing  $p_\lambda^{s\tau}(\mathbf{k}, t)$  by  $p_\lambda^{s\tau}(\mathbf{k}, \omega)$  in equation (5.18):

$$\mathcal{B}_{\mathbf{k}\lambda}^{s\tau}(\omega) = \frac{1}{S} \sum_{\mathbf{q}} V(|\mathbf{k} - \mathbf{q}|) \left[ p_\lambda(\mathbf{q}, \omega) F_{-\lambda-\lambda\lambda\lambda}^{s\tau}(\mathbf{k}, \mathbf{q}) + p_{-\lambda}(\mathbf{q}, \omega) F_{-\lambda\lambda-\lambda\lambda}^{s\tau}(\mathbf{k}, \mathbf{q}) \right]. \quad (5.22)$$

Once equation (5.21) is solved for the transition probabilities  $p_\lambda^{s\tau}(\mathbf{k}, \omega)$ , the total polarization  $P(t) = P(\omega)e^{-i\omega t}$  can be obtained from the expectation value of equation (E.13):

See Appendix E.1 for the derivation.

$$P(\omega) = S \sum_{s\tau\lambda} \int \frac{d\mathbf{k}}{(2\pi)^2} d_\lambda^{s\tau}(\mathbf{k}) p_\lambda^{s\tau}(\mathbf{k}, \omega), \quad (5.23)$$

and the optical conductivity follows from the macroscopic relation between the polarization current density and the polarization density  $\mathbf{J}(t) = \partial_t \mathbf{P}(t)$ :

$$\sigma(\omega) = -i \frac{\omega}{S\epsilon_0} P(\omega). \quad (5.24)$$

The presence of the excitonic term, equation (5.30) in  $\Omega_{\mathbf{k}\lambda}^{1s\tau}(\omega)$ , makes the equation of motion (5.21) a system of two coupled Fredholm integral equations of the second kind for the transitions probabilities  $p_\lambda^{s\tau}(\mathbf{k}, \omega)$ ,  $\lambda = \pm$ , that has to be solved for each spin/valley pair  $s\tau$ . The correspondent homogeneous equation [that can be obtained making  $\epsilon_0 = 0$  in equation (5.21)], corresponds to a Fredholm integral equation of the first kind. The solution of the latter will be explored in the next section.

### 5.1.2. CALCULATION OF THE EXCHANGE ENERGY

The exchange self-energy (3.60) reshapes the electronic bands and, as will be shown later, it is essential to correctly describe the optical properties of TMDCs, specially the value of the independent-particle energy gap.

For graphene, described by a massless Dirac equation ( $m^{s\tau} = 0$ ), the exchange self-energy was calculated in [123] and [124] with the use of the Coulomb potential. Here we calculate the exchange self-energy using the Keldysh interaction for the gapped Dirac equation ( $m \neq 0$ ).

The self-energy for the optical band structure,  $\Sigma^{s\tau,xc}(\mathbf{k})$ , is calculated from equation (3.60) using the expressions in 3.3. Its calculation boils down to an integral over all possible momentum values:

$$\Sigma^{s\tau,xc}(\mathbf{k}) = \int \frac{d\mathbf{q}}{4\pi^2} V(q) \Delta f_{\mathbf{k}-\mathbf{q}}^{s\tau} \frac{\mathbf{k} \cdot \mathbf{q} + m_{s\tau}^2}{E_k^{s\tau} E_q^{s\tau}}, \quad (5.25)$$

where the difference between the electronic valence and conduction distribution functions is defined as  $\Delta f_{\mathbf{q}}^{s\tau} = f_+^{s\tau}(\mathbf{q}) - f_-^{s\tau}(\mathbf{q})$ .

The direct gap renormalization, for each pair spin/valley, is given by the difference of the spin/valley top valence band and bottom conduction band energies, that is:

$$\Delta_{s\tau} = 2m_{s\tau} + \Sigma^{s\tau,xc}(\mathbf{k} = 0), \quad (5.26)$$



TMDC	MoS <sub>2</sub>	MoSe <sub>2</sub>	WS <sub>2</sub>	WSe <sub>2</sub>
$\Delta$ (eV)	0.797	0.648	0.685	0.524
$\hbar v_F$ (eVÅ)	2.76	2.53	3.34	3.17
$\Lambda_1$ (eV)	0.076	0.104	0.164	0.215
$\Lambda_2$ (eV)	0.073	0.082	0.230	0.252
$r_0$ (Å)	31.4	51.7	37.9	45.1
$\Delta_K$ (eV)	2.82	2.37	2.78	2.31
Experimental gap	2.5 [125]	2.18 [125]	2.14 [126]	2.51 [127]
	2.14 [128]	2.02, 2.22 [129]	2.41 [130]	1.58 [131]
	1.86 [126]			2.0, 2.18 [129]

**Table 5.1.:** The first five columns give the material parameters used in all calculations in this chapter. The parameters in the first four columns come from Ref. [121] and in the fifth column from Ref. [107]. The sixth column is the direct gap at the **K**-point calculated with the exchange self-energy obtained from our model. The last columns are experimental data (numbers in square braces refer to references). See also [132] for a different set of parameters and, in particular, the prediction of SOC induced splitting in the conduction band at the **K**-point.

and for  $T = 0$ , the exchange energy can be calculated analytically from equation (5.25), resulting in

$$\Sigma^{s\tau,xc}(\mathbf{k} = 0) = \frac{\alpha m_{s\tau}}{\varepsilon_m \beta} \frac{Q(r_0 m_{s\tau}, k_F^{s\tau}/m_{s\tau})}{\sqrt{1 + (r_0 m_{s\tau})^2}}, \quad (5.27)$$

$$Q(\zeta, \xi) = \ln \left[ \frac{\zeta \left( \zeta - \xi + \sqrt{\xi^2 + 1} \sqrt{\zeta^2 + 1} \right)}{(\zeta \xi + 1)(\sqrt{1 + \zeta^2} - 1)} \right], \quad (5.28)$$

with  $\alpha \approx 1/137$  the fine structure constant,  $\beta = v_F/c$  the ratio between Fermi-velocity and the speed of light, and the valley-spin dependent Fermi momentum  $k_F^{s\tau}$  is given by:

$$k_F^{s\tau} = \sqrt{(E_F + \mu_{s\tau})^2 - m_{s\tau}^2}. \quad (5.29)$$

We depict the dependence of gap-renormalization on the environment dielectric constant in figure (5.3). The temperature dependence of the same quantity is given in figure (5.4), and the renormalized band in figure (5.5). We can see the strong dependence of the exchange energy on the external parameters (temperature and dielectric constant of the medium surrounding the TMDC), showing that the environment plays a key role on the optical properties of these materials.

A more accurate approach to the calculation of renormalization of the band gap due to electron-electron interactions requires a self-consistent approach, where the unperturbed Hamiltonian  $H_0^{s\tau}$  (5.1) is defined including the self-energy from electron-electron interactions. For graphene this procedure is used to study the possibility of dynamical generation of a gap in the spectrum [133, 134].

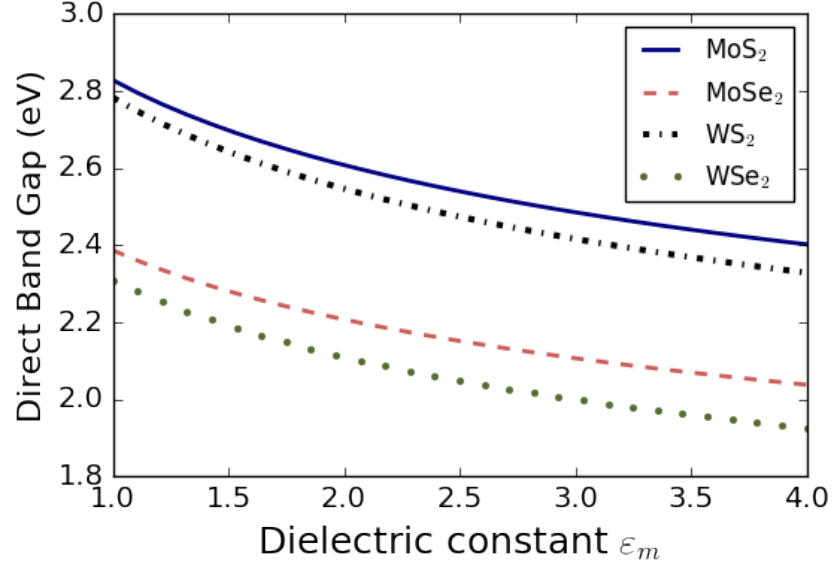


**Figure 5.3.:** Dependence of the bandgap renormalization in TMDCs (5.28), computed from the exchange self-energy, on the capping dielectric function at  $T = 0$  K. A higher dielectric constant suppresses the electron-electron interactions and thus the renormalization of the band gap by exchange energy becomes smaller. The parameters used are from table 5.1.

### 5.1.3. EXCITONIC EFFECTS IN THE RABI FREQUENCY

The electron-electron interaction induces the creation of electron-hole bound states below the non-interacting energy gap (corrected by the exchange self-energy), that corresponds to excitonic bound states. Also excitonic resonances appear above the energy gap. These two effects are routinely measured in optical experiments in semiconductors [69]. In the equation-of-motion description, the electron-electron interaction renormalizes the Rabi frequency, and, as will be shown later, this corresponds to solve the Bethe-Salpeter equation in the ladder approximation and in the center-of-mass reference frame. This procedure allows the calculation of the renormalized expectation value of the  $\hat{x}$  operator.

The renormalized Rabi frequency (5.18), term  $\mathcal{B}_{\mathbf{k}\lambda}^{s\tau}(t)$ , can be split into two parts (addition of two terms):

$$\begin{aligned} \mathcal{B}_{\mathbf{k}\lambda}^{s\tau}(t) = & -\frac{1}{S} \sum_{\mathbf{q}} V(|\mathbf{k} - \mathbf{q}|) p_{\lambda}^{s\tau}(\mathbf{q}, t) F_{-\lambda-\lambda\lambda\lambda}^{s\tau}(\mathbf{k}, \mathbf{q}) - \\ & -\frac{1}{S} \sum_{\mathbf{q}} V(|\mathbf{k} - \mathbf{q}|) p_{-\lambda}^{s\tau}(\mathbf{q}, t) F_{-\lambda\lambda-\lambda\lambda}^{s\tau}(\mathbf{k}, \mathbf{q}). \end{aligned} \quad (5.30)$$

The Eq. (5.21) corresponds to two coupled integral equations, with the unknown

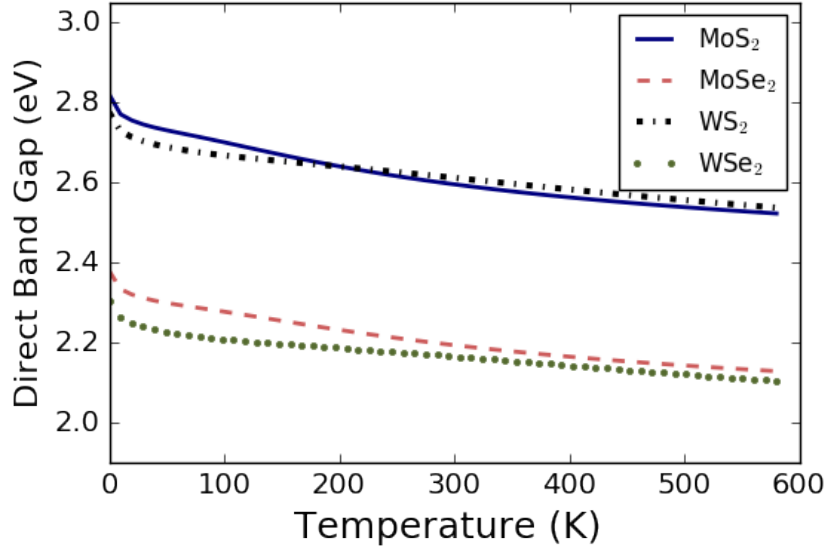


**Figure 5.4.:** Temperature dependence of the bandgap renormalization in TMDs computed from the exchange self-energy (5.25). Parameters used are from table 5.1. The chemical potential is set at the top of the valence band, but any other location would give qualitatively similar results. As the temperature increases, for a fixed chemical potential, the valence band depopulates, less carriers are available in the band and, as a consequence, the exchange self-energy decreases.

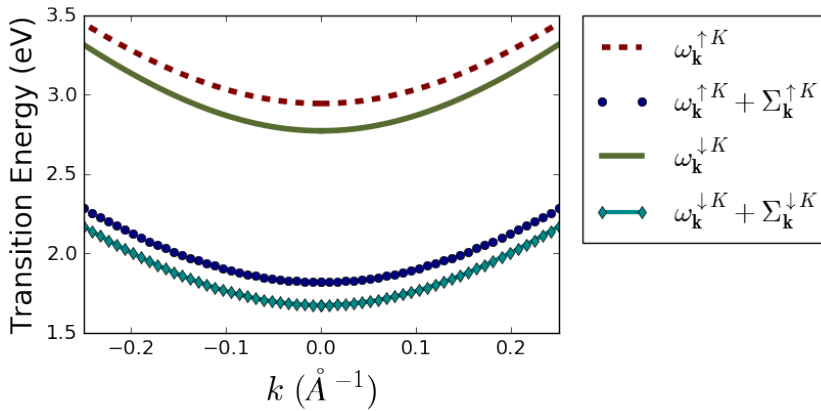


**Figure 5.5.:** Renormalization of the transition energy  $\omega_{\mathbf{k}} = 2E_{\mathbf{k}}$  in MoS<sub>2</sub> due to the exchange self-energy (5.25). We can see the band gap shift and an increase in the curvature of the band, relatively to the independent particle approach. Parameters used were  $m = 0.796$  eV and  $q_0 = 1/33 \text{ \AA}^{-1}$

functions  $p_{\pm}^{s\tau}(\mathbf{k}, t)$ . The first term of Eq. (5.30) depends on the same function  $p_{\lambda}^{s\tau}(\mathbf{k}, t)$  of the equation of motion, while the second term couples with the transition amplitude  $p_{-\lambda}^{s\tau}(\mathbf{k}, t)$ . Neglecting this latter term we have two independent equations of motion for  $p_{+}^{s\tau}(\mathbf{k}, t)$  and  $p_{-}^{s\tau}(\mathbf{k}, t)$ .

#### 5.1.4. STUDY OF HOMOGENEOUS BETHE-SALPETER EQUATION: EXCITONIC STATES

The set of equations (5.21), in the homogeneous case, corresponds to the Bethe-Salpeter equation for the exciton wave function  $\psi_{n\ell}^{s\tau}$  with energy  $E_{n\ell}^{s\tau, \text{exc}}$ . In this limit this equation is also known as the Wannier equation [69]. Once the excitonic wave functions are known we can calculate the absorbance coefficient  $\mathcal{A}(\omega)$  using Elliot's formula [69], in a form appropriate for TMDCs; this formula is derived in F.1 following a procedure described in [112]; this approach leads to

$$\mathcal{A}(\omega) \approx \frac{4\pi\alpha\omega\gamma}{\sqrt{\epsilon_m}} \sum_{s\tau, l=\{0,2\}, n} \frac{M_{n\ell}^{s\tau}}{(\omega - E_{n\ell}^{s\tau}/\hbar)^2 + \gamma^2}, \quad (5.31)$$

where  $M_{n\ell}^{s\tau}$  is the oscillator strength, given by:

$$M_{n\ell}^{s\tau} = \frac{v_F^2}{2\pi} \left| \int_0^\infty q dq d_{\ell,+x}^{s\tau}(q) [\psi_{n\ell}^{s\tau}(q)]^* \right|^2, \quad (5.32)$$

with  $\ell$  and  $n$  the angular and radial quantum numbers,  $d_{\ell,-}^{s\tau}(q)$  is the angular decomposition of the dipole matrix element, and we have explicitly reintroduced the Fermi velocity  $v_F$  for defining the oscillator strength as a dimensionless quantity.

In the system of equations (5.21) we neglect the non-resonant term  $p_{+}^{s\tau}(\mathbf{k}, \omega)$ , consider the system at zero temperature, and at the charge neutrality point,  $\Delta f_{\lambda}^{s\tau}(\mathbf{k}) = -\lambda$ . Thus, we have for the homogeneous problem an integral equation for  $p_{-}^{s\tau}(\mathbf{k}, \omega)$ :

$$(\omega + \tilde{\omega}_{-k}^{s\tau}) p_{-}^{s\tau}(\mathbf{k}, \omega) = \int \frac{d\mathbf{q}}{(2\pi)^2} V(|\mathbf{k} - \mathbf{q}|) F_{++--}^{s\tau}(\mathbf{k}, \mathbf{q}) p_{-}^{s\tau}(\mathbf{q}, \omega). \quad (5.33)$$

If we also neglect the exchange self-energy term in the previous result, equation (5.33) is formally equal to the Bethe-Salpeter equation for the two-body electron-hole wave function obtained in the center-of-mass reference frame in a gapped Dirac system. We can write equation (5.33) in the following matrix form:

$$(E_{\text{exc}} - K^{BS}) \Psi = 0, \quad (5.34)$$

with  $E_{\text{exc}} = \omega$  the Exciton energy and  $K^{BS}$  the integral operator of equation (5.33). We can use the cylindrical symmetry to write the eigenfunctions of equation (5.33) as:

$$p_{-}^{s\tau}(k, \theta, \omega) = \sum_{n\ell} \psi_{n\ell}^{s\tau}(k) e^{i\theta} e^{i\ell\theta}, \quad (5.35)$$

with  $\ell$  the angular quantum number (note that we have omitted the dependence of  $\psi_{n\ell}^{s\tau}(k)$  in  $\omega$ ). The extra phase in definition (5.35) allows to write equation (5.33) in the heavy mass limit  $m \rightarrow \infty$  as a hydrogen-atom equation in momentum space with a screened potential [108]. The introduction of a factor  $e^{i\theta}$  to classify the excitons can be seen as arbitrary. Since the spinors, given by equation (5.11), also have an arbitrary global phase that propagates to the four-spinor product (5.14), the best way to define the  $s$ -wave is by a limit condition, that is, taking the limit  $m \rightarrow \infty$  we should recover the spectrum of the hydrogen atom.

Substituting (5.35) into (5.33), and using the orthogonal relations for the wave function  $\psi_{n\ell}^{s\tau}(k)$ , equation (5.33) becomes the following Wannier formula:

$$(\omega + \tilde{\omega}_{-k}^{s\tau})\psi_{n\ell}^{s\tau}(k) = - \int_0^\infty dq \tilde{T}_\ell^{s\tau}(k, q)\psi_{n\ell}^{s\tau}(q), \quad (5.36)$$

with the kernel  $\tilde{T}_\ell^{s\tau}(k, q)$  given in appendix 5.B. Equation (5.36) was solved before in references [112, 113] without the exchange self-energy contribution in  $\tilde{\omega}_{+k}^{s\tau}$ . Here we include the effect of the exchange term.

The results for convergence of the binding energies,  $E_{n\ell}^{\text{binding}} = \Delta_{s\tau} - E_{n\ell}$ , with  $\Delta_{s\tau}$  given by equation (5.26), of the integral equation for the  $s$ -wave ( $\ell = 0$ ) and the  $p$ -waves ( $\ell = \pm 1$ ) are presented in columns labeled “3000” and “GL” of table 5.2 (in it we also discuss convergence issues of our numerical methods). In this table we compare our results with those of reference [113], and because of this we have neglected the exchange correction as those authors also did. The wave functions for the  $s$ -wave are presented in Fig. (5.6), where we can see the usual increase of nodes for higher modes. The breakdown of degeneracy in  $p$ -waves comes from the  $\ell$  dependence in the matrix element of the four body spinor product, that appears inside the integral (5.61), and is a consequence of the Berry curvature of the Dirac Hamiltonian [114, 115].

The Rydberg series for excitons including exchange corrections is presented in figure 5.7 for all four TMDCs considered in this chapter with the parameters of table 5.2. There are four combinations of spin/valley, but the time-reversal symmetry reduces this number to two independent combinations. Each of these will generate a distinct Rydberg series, that we call A for the lowest fundamental energy and B for the highest one. Note that the A and B series are split due to SOC. For WS<sub>2</sub> we compare the Rydberg series with the experimental work of ref. [130]; our results show a good agreement with the experimental data, with a deviation smaller than 5 meV.

### 5.1.5. INTEGRAL EQUATION FOR THE VERTEX FUNCTION

With the knowledge of the solution of the homogeneous equation, we come back to the integral equation (5.21), where we add a phenomenological interband relaxation rate  $\gamma_p$  to include disorder effects.

We write  $p_\lambda^{s\tau}(k, \theta, \omega) = \varepsilon_0 \Psi_\lambda^{s\tau}(k, \theta)$  and proceed as we did in equation (5.35) expanding  $\Psi_\lambda^{s\tau}(k, \theta)$  in the eigenstates of the homogeneous Bethe-Salpeter equation

	50	100	300	600	1200	3000	GL	LM Ref.[113]
1s	0.224	0.264	0.304	0.318	0.327	0.333	0.331	0.301
2s	0.033	0.055	0.081	0.092	0.099	0.104	0.103	0.099
2p <sup>+</sup>	0.051	0.077	0.107	0.119	0.126	0.132	0.132	0.125
2p <sup>-</sup>	0.062	0.090	0.122	0.134	0.142	0.148	0.147	0.150

**Table 5.2.:** Binding energy (in eV) for four different excitonic states of MoS<sub>2</sub> corresponding to the A-series. The first six data rows show the results for the numerical procedure based on a constant grid discretization; convergence is obtained only for very large grids of the order of 3000. GL accounts for Gauss-Legendre/Laguerre, where the integral in  $q$  is divided in three intervals  $[0, 0.3\Delta]$ ,  $[0.3\Delta, 0.6\Delta]$ ,  $[0.6\Delta, \infty]$ . For the first interval we use 100 points, and for the second and third 50 points are used. In the first two intervals we use Gauss-Legendre quadrature, and the last one Gauss-Laguerre with a rescale of  $m/150$ . The last row (LM) is the data from reference [113], with excitonic binding energy computed using a lattice (tight-binding) model. We want to stress that the discretization procedure in a linear mesh of 3000 points takes several hours to run in a conventional laptop, whereas the GL method takes only few minutes in the same computer. At a given stage the calculation requires performing an angular integral of the Keldysh potential  $V(\mathbf{k} - \mathbf{q})$ . Although the integral can be proven finite, numerically the integral is ill behaved when  $k = q$ . For avoiding this pathology a finite constant of the order of the grid spacing is added to  $p_{k,q}(\theta)$  in Eq. (5.61); this renders the integral finite, as it should.

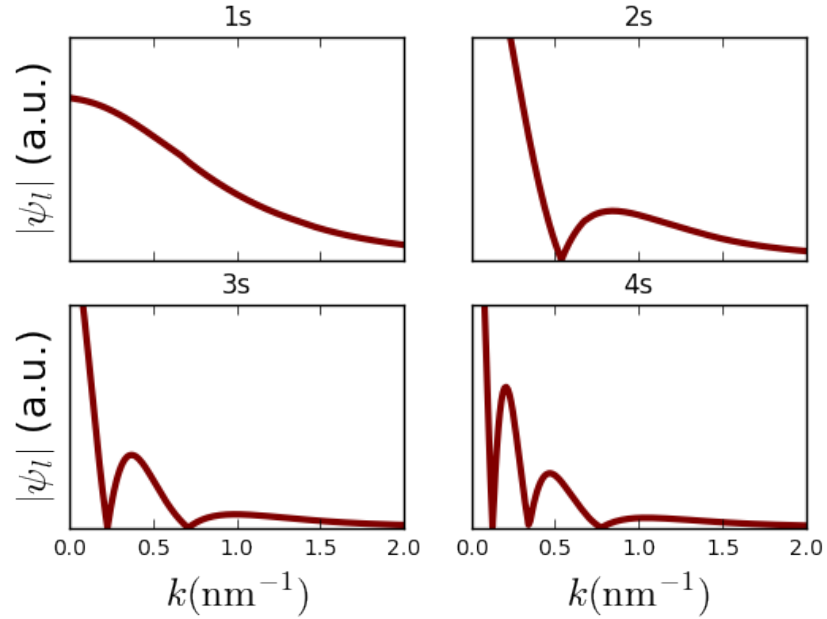


**Figure 5.6.:** (Color on-line) Unnormalized radial excitonic wave function for MoS<sub>2</sub> from the solution of equation (5.36) for  $\ell = 0$  at the  $\mathbf{K}$ -point. We can see the usual increase of nodes with the higher modes. The size of the exciton, estimated as  $2\pi/k$ , is of the order of  $\sim 10$  nm, or about few of unit cells.

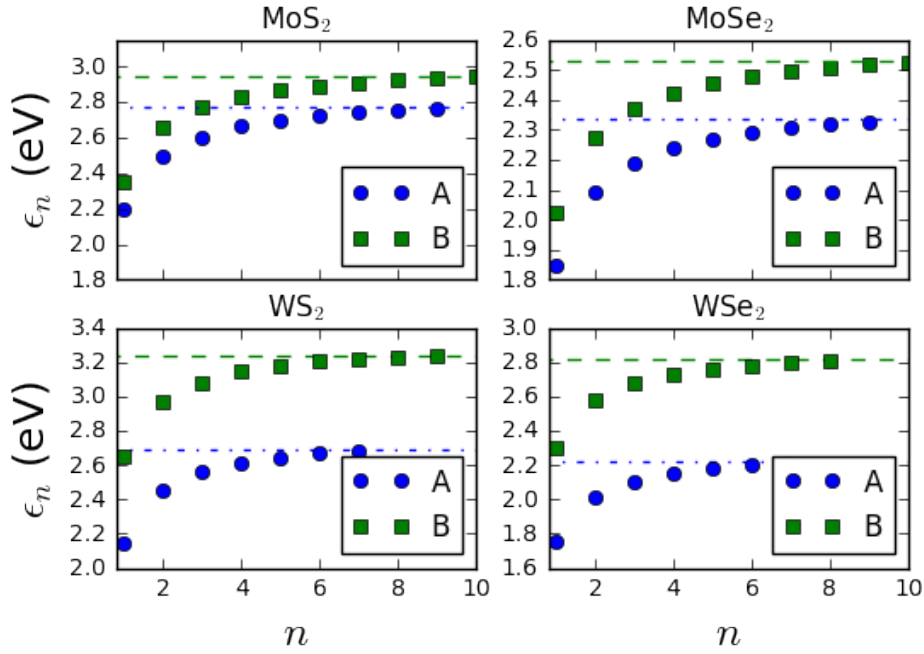


**Figure 5.7.:** Exciton eigenvalues of equation (5.34), with exchange effects included, as function of the radial quantum number  $n$  for  $\ell = 0$ . The dashed line corresponds to the spin/valley dependent gap, given by equation (5.28). The blue circles (green squares) corresponds to the  $\uparrow K, \downarrow K'$  ( $\downarrow K, \uparrow K'$ ) series. Note that for WS<sub>2</sub> and WSe<sub>2</sub> the B excitons are all but one ( $1s=B$ ) inside the continuum of the A excitonic series. This fact is expected to have important consequences in the absorbance spectrum of these two materials (see section 5.3).

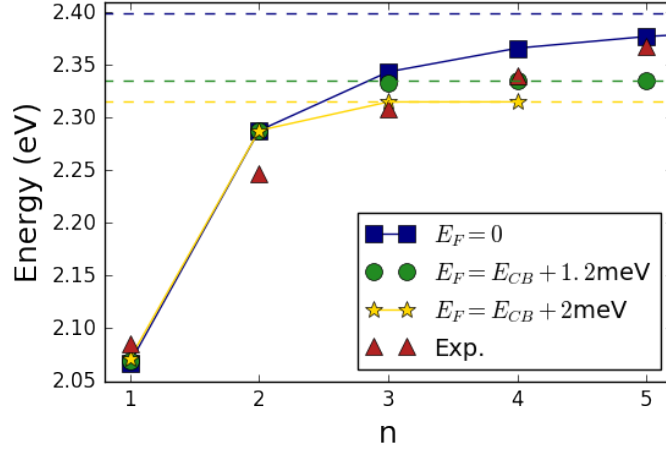


**Figure 5.8.:** Comparison between experimental data (red triangles) from Ref. [130] and our theoretical model, considering a small amount of doping (green circles and yellow stars), and the neutral case (blue squares). Exciton eigenvalues of equation (5.34) for  $\text{WS}_2$ , with exchange effects included, as function of the radial quantum number  $n$  for  $\ell = 0$ . The dashed line corresponds to the spin/valley dependent gap, given by equation (5.28). The parameters of the mass, Fermi velocity and SOC are from table 5.2. We set  $r_0 = 40.92 \text{ \AA}$ , slightly larger than that given in reference [107],  $37.89 \text{ \AA}$ . The effective dielectric constant, including the effect of the substrate ( $\text{SiO}_2$ ), is  $\epsilon = 2.45$ .

and angular momentum states:

$$\Psi_\lambda^{s\tau}(k, \theta) = \sum_{\ell=-\infty}^{\infty} \psi_{\lambda\ell}^{s\tau}(k) e^{i\theta} e^{i\ell\theta}, \quad (5.37)$$

and as a consequence:

$$(\omega + \tilde{\omega}_{\lambda k}^{s\tau} + i\gamma) \psi_{\lambda\ell}^{s\tau}(k) = -\Delta f_\lambda^{s\tau}(k) \left[ d_{-\lambda,0}^{s\tau}(k) \delta_{\ell,0} + d_{-\lambda,-2}^{s\tau}(k) \delta_{\ell,-2} + \int_0^\infty dq \left( T_{\lambda,\ell}^{1,s\tau}(k, q) \psi_{\lambda\ell}^{s\tau}(k) + T_{\lambda,\ell}^{2,s\tau}(k, q) \psi_{-\lambda\ell}^{s\tau}(k) \right) \right], \quad (5.38)$$

where  $\delta_{\ell,s}$  is the Kronecker-delta, and the kernels  $T_{\lambda,\ell}^{1,s\tau}(k, q)$  and  $T_{\lambda,\ell}^{2,s\tau}(k, q)$  are given in appendix 5.B, and the dipole decomposition  $d_{\ell,\lambda}^{s\tau}(k)$  in appendix F.1.

The diagrammatic representation of equation (5.38) is shown in figure 5.1, where the internal electron-hole legs are understood to be dressed by the exchange interaction.



### 5.1.6. BRIGHT AND DARK EXCITONS: OPTICAL SELECTION RULES

We are now in position to discuss the conditions that an exciton can absorb a photon. From the coupled set of equations (5.38), only  $\ell = 0$  ( $s$ -excitons) and  $\ell = -2$  ( $d$ -excitons) contribute to the optical conductivity, but from our numerical calculations, the  $\ell = -2$  mode contribution is negligible for real TMDCs parameters. After performing the  $\theta$ -integration in equation (5.23), we obtain for the polarization:

$$\frac{P(\omega)}{S\mathcal{E}_0} = \sum_{s\tau\lambda} \int \frac{kdk}{2\pi} d_{0,\lambda}^{s\tau}(k) \psi_{\lambda,-2}^{s\tau}(k) + d_{-2,\lambda}^{s\tau}(k) \psi_{\lambda,0}^{s\tau}(k). \quad (5.39)$$

Finally, the numerical procedure to calculate the optical conductivity is the following: we solve the integral equation (5.38) to determine the eigenfunctions  $\psi_{\lambda\ell}^{s\tau}(k)$ , calculate the polarization from the integral in equation (5.39), and lastly the optical conductivity is calculated from relation (5.24). The absorbance for a MoS<sub>2</sub> suspended sheet for a TEM wave with normal incidence can be obtained from the optical conductivity as [15]:

$$\mathcal{A}(\omega) = \alpha\pi \frac{4\Re[f(\omega)]}{4 + \pi^2\alpha^2|f(\omega)|^2}, \quad (5.40)$$

with  $f(\omega) = \sigma(\omega)/\sigma_0$  and  $\sigma_0 = e^2/4\hbar$ .

## 5.2. Excitons at the $\Gamma$ -point

To describe accurately the optical absorption in the frequency domain after the two first excitonic peaks (A and B), that is the region roughly located in the interval 2.3 – 3.5 eV, we need to describe the excitonic effects due to electronic transitions at the  $\Gamma$ -point. This implies going beyond the  $\mathbf{k} \cdot \mathbf{p}$  model at  $\mathbf{K}$ -point. To accomplish this, we use the three-band model of Liu *et al.* [119], which was shown to describe accurately the GGA band structure. We use the same equation of motion approach introduced in previous section. The dipole matrix element is calculated using a Peierls approximation [135, 117]:

$$\langle \lambda\mathbf{k} | \hat{x} | \lambda'\mathbf{k} \rangle = \frac{i}{E_{\mathbf{k}}^{\lambda'} - E_{\mathbf{k}}^{\lambda}} \langle \lambda\mathbf{k} | \partial_{\mathbf{k}} H_{\mathbf{k}} | \lambda'\mathbf{k} \rangle, \quad (5.41)$$

which takes in account vertical interband transitions only.

To proceed with the discussion about excitons (actually excitonic resonances) at the  $\Gamma$ -point, we have to look in detail into the TMDC band structure depicted in figure 5.9; this band-structure was calculated using a full relativistic method (see figure caption for details), that is necessary to correctly account for the spin-orbit coupling [139] in TMDCs. Very close to the  $\Gamma$ -point, the top of the valence band (that from now on we label band 0) and the last four conduction bands (that, from

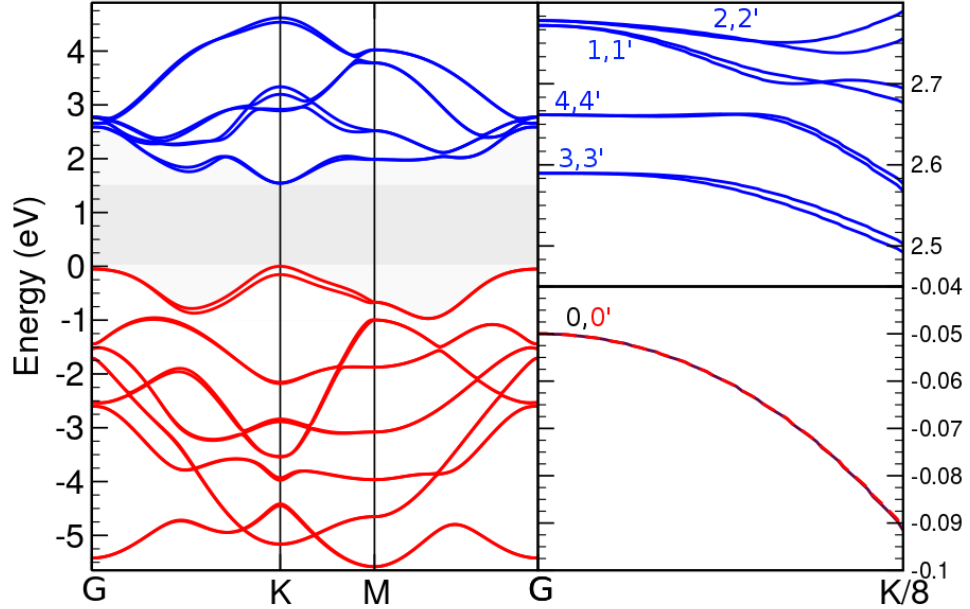


**Figure 5.9.:** Electronic bands diagram of single layer MoS<sub>2</sub>. In red are the valence bands and in blue the conduction bands. On the right panels a zoom-in of the conduction bands (top) and valence bands (bottom) near the  $\Gamma$  point is shown. The band diagrams were obtained using Density Functional Theory in the GGA (PBE)[136] approximation, as implemented in the QUANTUM ESPRESSO[137] package. An energy cutoff of 70 Ry and a Monkhorst-Pack[138] grid of  $16 \times 16 \times 1$  were used. Mo and S atoms are represented by norm conserving pseudopotentials generated with fully relativistic calculations including spin-orbit interaction. To avoid interaction between different images of the layer, a 45 bohr supercell in the  $c$  direction is included. (Courtesy of Ricardo Ribeiro).

here on, are labeled 1, 1', 2 and 2', in increasing energy order) are essentially due to contributions from electrons belonging to the transition-metal  $d$ -orbitals. We note in passing that the bands 0, 1, and 2 are also used in the effective Hamiltonian valid near the  $K$ -point. The four lowest conduction bands at the  $\Gamma$  point (labeled 3, 3', 4 and 4', in increasing energy order) are mostly composed of  $p$ -orbitals from the chalcogenides atoms. From here on, we do not consider SOC effects in the three band model as they are very small at the  $\Gamma$ -point (see right panels in Fig. 5.9). Therefore, we drop the prime notation of the bands, that is, the bands  $i$  and  $i'$  are treated as spin-degenerated (at the computation level this amounts to a multiplicative factor

of two affecting the absorbance curves).

The mirror symmetry, with respect to the plane formed by the metallic atoms, is important to discuss the optical properties of TMDCs. The bands 0, 1 and 2 all have even symmetry, while the bands 3 and 4 both have odd symmetry. Therefore, the dipole matrix elements between bands with different mirror symmetry vanish (note that the mirror symmetry refers here to the  $z$ -coordinate). As a consequence, the existence of excitons composed of holes from the 0 band and electrons from the bands 3 and 4, they are optically dark under a single-photon experiment. This implies that we restrict the calculation of excitonic effects near the  $\Gamma$ -point considering only the optical properties of excitons composed of holes from band 0 and electrons from bands 1 and 2. These optical transitions generate a modified Rydberg series, which is a consequence of the non-parabolic dispersion relation of the *optical band* [see equation (5.45)] and finite Berry curvature at the  $\Gamma$ -point and as well as from the form of the Keldysh potential.

To calculate the optical properties of the excitons at the  $\Gamma$ -point, we use the same equation of motion method developed in previous section. We define transition probabilities  $p_{0i}(\mathbf{k}, t) = \langle \hat{a}_{i\mathbf{k}}^\dagger(t) \hat{a}_{0\mathbf{k}}(t) \rangle$ , that represent the annihilation of an electron at the valence band 0 and a creation of an electron at the conduction band  $i = 1, 2$ . The equation of motion is given by (3.31), making  $\lambda_1 = 0$  and  $\lambda_2 = 1, 2$ , the latter two values represent the two possible bright excitons at the  $\Gamma$ -point. On the other hand, the  $H_0 = H_0^{3b}$  Hamiltonian is the three-band model given by Liu *et al.* [119], that describes, up to the next-nearest-neighbor order, the effective tight-binding model between the metal atoms  $M = \{\text{Mo}, \text{W}\}$ . We are interested only in the term equivalent to the Bethe-Salpeter equation (encoded in the Rabi frequency renormalization term):

$$\mathcal{B}_{\mathbf{k}i}^{3b}(\omega) = -\frac{1}{S} \sum_{\mathbf{q}} V(|\mathbf{k} - \mathbf{q}|) F_{0i}^{3b}(\mathbf{k}, \mathbf{q}) p_{0i}(\mathbf{q}, \omega), \quad (5.42)$$

which is obtained from equation (3.31) from the terms with  $\lambda_3 = 0$ ,  $\lambda_4 = 0$ ,  $i$  and  $\lambda_5 = i$ . For the model we are considering, the four-body spinor is given by:

$$F_{0i}^{3b}(\mathbf{k}, \mathbf{q}) = \phi_0^\dagger(\mathbf{k} + \mathbf{q}) \phi_0(\mathbf{k}) \phi_i^\dagger(\mathbf{k}) \phi_i(\mathbf{k} + \mathbf{q}), \quad (5.43)$$

and is obtained numerically from the diagonalization of the  $3 \times 3$  matrix defining the three-band model, with  $\phi_i$  the wave function of the  $i$ -band.

In our calculation, the exchange self-energy is included as an energy shift from the renormalization of the band gap [see equation (5.28)]. We also ignore spin-orbit effects in the calculations at the  $\Gamma$ -point, as these are very small. The equation that we need to solve for obtaining the transition probability  $p_{0i}(k, \theta, \omega)$  reads:

$$\begin{aligned} [\omega - \omega_i(k, \theta)] p_{0i}(k, \theta, \omega) &= -\Delta f_i d_i^\Gamma(k, \theta) \mathcal{E}_0 + \\ \Delta f_i \frac{1}{S_c} \sum_{q, \theta'} V(k, q, \theta - \theta') F_i(k, q, \theta, \theta') p_{0i}(q, \theta', \omega), \end{aligned} \quad (5.44)$$

with  $S_c$  the unit cell area,  $\omega_i(k, \theta) = E_{ik, \theta} - E_{0k, \theta}$ ,  $E_{ik, \theta}$ , and  $E_{0k, \theta}$  the eigenvalues of the three-band Hamiltonian  $H_0^{3b}$ ,  $\Delta f_i = f_{ik, \theta} - f_{0k, \theta}$  is the difference in occupation numbers between bands  $i$  and 0 (given in terms of the Fermi-Dirac function), and the dipole element  $d_i^\Gamma(k, \theta) = \langle \lambda \mathbf{k} | \hat{x} | \lambda' \mathbf{k} \rangle$ , with the expectation value calculated using equation (5.41).

Since we only need the band-structure near the  $\Gamma$ -point we approximate the optical band structure near this point by the Fourier series:

$$\omega_i(k, \theta) \approx h_0^i(k) + h_6^i(k) \cos(6\theta) + h_{12}^i(k) \cos(12\theta), \quad (5.45)$$

with  $h_\ell^i(k)$ ,  $\ell = 0, 6, 12$  are polynomials of degree six (this expression is valid up to momentum values of the order of  $2\pi/(3a_0)$ , where  $a_0$  is the lattice parameter). Expression (5.45) describes accurately the optical band structure near the  $\Gamma$ -point. For  $k \rightarrow \infty$  the optical band approximation (5.45) diverges. Although the contributions for  $k \rightarrow \infty$  becomes negligible to the excitons' wavefunction, the approximation (5.45) makes the numerical convergence faster. Using the angular decomposition (5.10),  $p_{i0}(k, \theta, \omega) = \varepsilon_0 \sum_\ell c_\ell^i(k) e^{i\ell\theta}$  (note that we have omitted the dependence of  $c_\ell^i(k)$  in  $\omega$ ), we can write the Bethe-Salpeter equation (5.44) as (where we have made  $\Delta f_i = -1$  since are interested in a neutral system):

$$\begin{aligned} \omega c_\ell^i(k) - \sum_{\ell'} \tilde{\omega}_{\ell'}^i(k) c_{\ell-\ell'}^i(k) &= d_{i,\ell}^\Gamma(k) - \sum_{\ell'} \int q \frac{dq}{2\pi} \int \frac{d\theta}{2\pi} \int \frac{d\theta'}{2\pi} e^{-i\ell\theta} e^{i\ell'\theta'} \times \\ &\times V(k, q, \theta - \theta') F_{0i}^{3b}(k, q, \theta, \theta') c_{\ell'}^i(k), \end{aligned} \quad (5.46)$$

$$\text{and } \tilde{\omega}_\ell^i(k) = \int_0^{2\pi} \frac{d\theta}{2\pi} e^{i\ell\theta} \omega_i(k, \theta).$$

The previous equation couples coefficients  $c_\ell^i$  with different angular momentum numbers  $\ell$  through two terms: the kinetic term  $\sum_{\ell'} \tilde{\omega}_{\ell'}^i(k) c_{\ell-\ell'}^i(k)$  and the electron-electron interaction term (Rabi frequency renormalization term). The kinetic term couples only coefficients having different angular momentum values, but this term gives a negligible contribution to the optical response when  $\ell \neq \ell'$ . This is a consequence of the fast vanishing of the potential  $V(k, q, \theta - \theta')$  whenever  $\theta - \theta' \neq 0$  and  $\theta - \theta'$  is varied. Therefore, we can replace the four-body spinor function  $F_{0i}^{3b}(k, q, \theta, \theta')$  by its average angular value as follows:

$$\tilde{F}_{0i}^{3b}(k, q, \theta') = \int_0^{2\pi} \frac{d\theta}{2\pi} F_{0i}^{3b} \left( k, q, \theta - \frac{\theta'}{2}, \theta + \frac{\theta'}{2} \right). \quad (5.47)$$

and the effective potential is given in this approximation by:

$$\tilde{V}_\ell^i(k, q) = \int_0^{2\pi} \frac{d\theta'}{2\pi} e^{i\ell\theta'} V(k, q, \theta') \tilde{F}_{0i}^{3b}(k, q, \theta'). \quad (5.48)$$

The approximation (5.48) and (5.47) keeps the hermiticity of equation (5.46). Finally, we replace the potential term in equation (5.46) by (5.48), where we arrive at

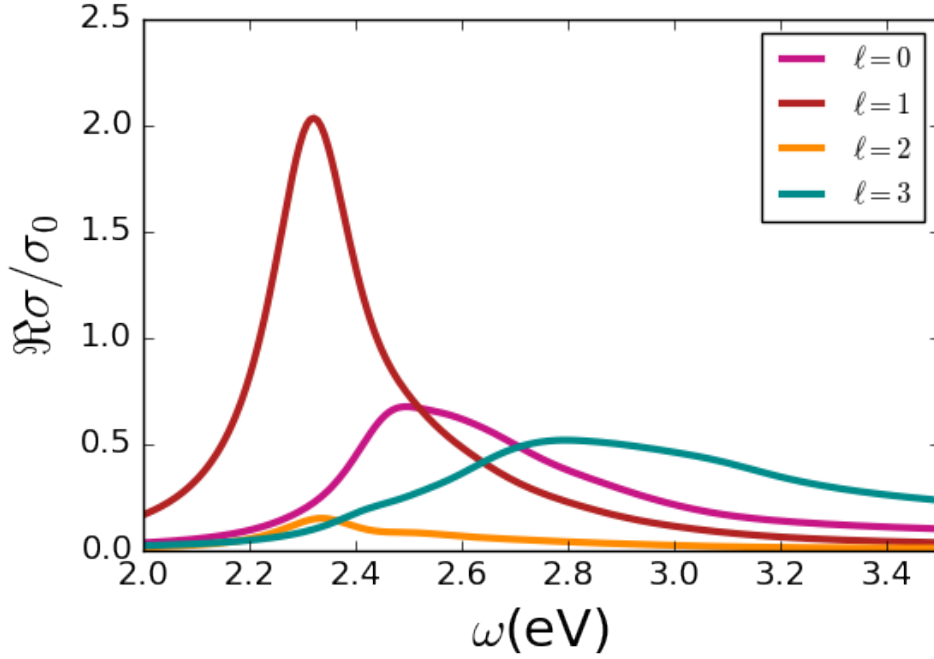


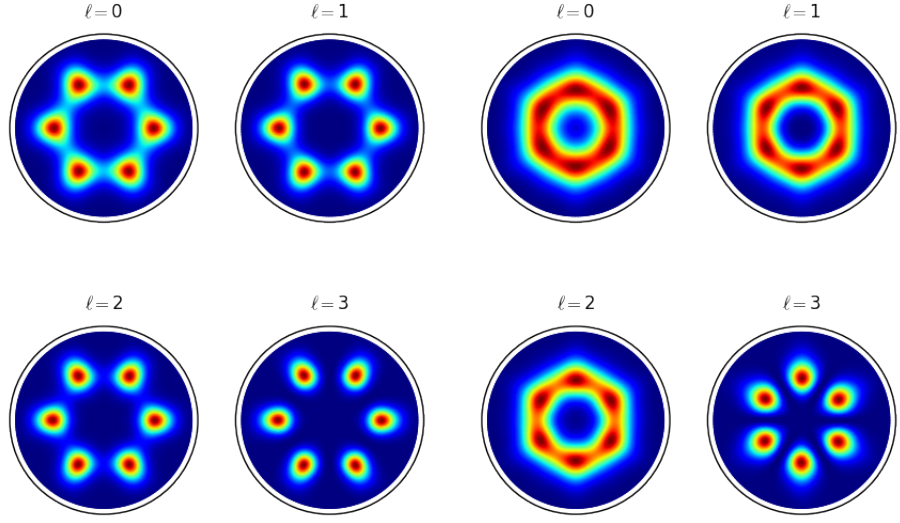
**Figure 5.10.:** Angular decomposition from each contribution to the optical conductivity for the exciton at the  $\Gamma$ -point for the 01 exciton (see section 5.2 for the definition). In the calculation we have used the example of  $\text{MoS}_2$ . This exciton is composed of Mo  $d$ -states. Each angular decomposition has also angular components  $\ell \pm 6$  and  $\ell \pm 12$ , a consequence of the optical band structure (5.45).

the coupled set of integral equations:

$$\omega c_\ell^i(k) - \sum_{\ell'=0,\pm 6,\pm 12} \tilde{\omega}_{\ell'}^i(k) c_{\ell-\ell'}^i(k) = d_{i,\ell}^\Gamma(k) - \int_0^\infty q dq \tilde{V}_\ell^i(k, q) c_\ell^i(q). \quad (5.49)$$

To solve (5.49), the summation in  $\ell'$  gives five additional terms [ $\ell' = 0, \pm 6, \pm 12$ ; see equation (5.45)] that are coupled together. This generates a hierarchy of equations for the coefficients  $c_\ell^i(k)$ . Therefore, the solution of equation (5.49) has to be truncated at some  $\ell$  value. In this procedure we have assumed that the contributions above  $c_{18}^i(k)$  are vanishing small. This is confirmed by figure 5.10, which shows that for  $\ell = 5$  the contribution is already small (note that for this curve we have all the coefficients  $c_\ell^i(k)$ , with  $\ell = -7, -1, 11, 17$  entering the calculation of the conductivity, see below). In terms of the coefficients  $c_\ell^i(k)$  the conductivity is computed as follows. The expectation value of the polarization operator can be calculated as we did in section 5.1, and results in:

$$P(\omega) = -2S \sum_{i=0,1} \int_0^\infty \int_0^{2\pi} k \frac{dk}{2\pi} \frac{d\theta}{2\pi} [d_i^\Gamma(k, \theta)]^* p_{i0}(k, \theta, \omega), \quad (5.50)$$



(a) Excitons composed of bands 0 and 1 (b) Excitons composed of bands 0 and 2. Note that all excitons have nodes along the  $\Gamma - \mathbf{M}$  direction (vertical). Note that the all exciton have nodes along the  $\Gamma - \mathbf{K}$  direction (horizontal).

Figure 5.11.: Exciton wave function in momentum space at the  $\Gamma$  point.

where we account for the spin degeneracy introducing a factor of two. The conductivity can be obtained from equation (5.24), and we can separate the contribution for each band  $i$ . Performing the angular integral in the equation for  $P(\omega)$  we obtain:

$$\frac{\sigma_i(\omega)}{\sigma_0} = -8i\omega \sum_{\ell=-\infty}^{\infty} \int_0^{\infty} k \frac{dk}{2\pi} [d_{i,\ell}^{\Gamma}(k)]^* c_{\ell}^i(k). \quad (5.51)$$

Once the coefficients  $c_{\ell}^i(k)$  are determined from the solution of (5.49) the conductivity follows from the previous equation.

The solution of (5.49) also give us the excitonic wave functions in momentum space. The results for the first excitonic energy, for each angular momentum mode, is shown in figure 5.11a for the exciton composed from an electron in band 1, and in figure 5.11b for an electron in band 2. From a careful inspection of figures 5.11a and 5.11b, we can see that the nodes of exciton with band index  $i = 1, \ell = 0$  lies along the  $\Gamma - \mathbf{K}$  direction, while the nodes of exciton with band index  $i = 2, \ell = 0$  lies along the  $\Gamma$ -M point.

### 5.3. Results

In this section we have performed a thorough analysis of the absorption spectrum of four TMDCs. For computing the absorbance, the optical conductivity is needed. Taking the example of MoS<sub>2</sub>, the decomposition of the real part of the optical conductivity, coming from different angular momentum contributions of the exciton at  $\Gamma$ -point, associated with the transition  $0 \rightarrow 1$ , is shown in figure 5.10; remember that each contribution is composed of  $\ell = 0$ ,  $\ell \pm 6$ , and  $\ell \pm 12$  angular momentum components.

It is important to introduce here a note on notation: the peak at lowest energy is denoted by  $A=1s$  and the next Rydberg energy level in the A-series is denoted by  $A'=2s$ ; this corresponds in a given valley and to a given spin projection. In the same valley, and for the other spin projection, the peaks belong to the B-series, with the lowest energy is denoted by  $B=1s$  and the next one by  $B'=2s$ . For MoX<sub>2</sub> TMDC's the energy order is A, B, A', and B', whereas for WX<sub>2</sub> TMDCs the energy order is A, A', B, and B'. This agrees with the notation introduced in figure 5.7.

The absorbance, and the real and the imaginary parts of the optical conductivity, for four TMDCs considered in this chapter, are shown in figure 5.12, with the parameters of table 5.1. That is, in this figure we do not try to fit the data but simply use the parameters characterizing the potential and the band-structure of the TMDCs given in other papers. In figure 5.13, on the contrary, we fit the A peak position changing  $r_0$  and we also add a chemical potential, since, as noted in Refs. [140, 141] all TMDCs samples have a certain and undetermined amount of negative doping. We note in passing that at the time of writing different experiments report distinct percentages for absorption of radiation for two, supposedly identical, TMDCs. Table 5.3 gives, from four different references, the measured values of the absorbance of MoS<sub>2</sub> samples; as it can be seen the values fluctuate among different experiments. Also, our model predicts, at low temperatures, larger absorption peaks than those measured at room temperature. This result makes sense, but when we increase the temperature we never obtain values as small as those reported in the experiments for MoS<sub>2</sub>. It is now known [142] that excitonic spectrum of TMDC's samples in SiO<sub>2</sub> are strongly influenced by the disorder of the substrate. In this reference it is shown that encapsulated samples in h-BN have much narrower excitonic peaks. Therefore our results should agree with absorbance measurements in these encapsulated samples (measurements yet to be made).

Next, we analyze each aspect of the optical spectrum of each TMDC and compare our results with the experimental measurements available to date in a large frequency window. The parameters used in our calculations are: (i) at the  $\mathbf{K}$ -point we used the values in table 5.1 and a broadening  $\gamma_K = 50$  meV; (ii) at the  $\Gamma$ -point we used the GGA parameters of the three-band model given by Liu *et al.* [119], the same Keldysh parameters of table 5.1, and a broadening  $\gamma_\Gamma = 100$  meV. Note that exception made to the broadening parameters, all the other values were taken of the literature and



Excitonic peak	Model	[101]	[53]	[106]	[140]
A	14	10.8	7.4	3.8	7.5
B	15	10.5	8.6	5.0	8.0

**Table 5.3.:** Absorbance (in percentage) of A and B peaks for MoS<sub>2</sub>. The table gives a comparison between our theoretical model and the experimental results for samples deposited on silica ([101],[53],[106]), and a FET device [140], where the MoS<sub>2</sub> is deposited on top of silicon and under a voltage gate of  $-10$  V. The “Model” refers to the theoretical approach developed in this chapter and we have considered MoS<sub>2</sub> on top of silica ( $\epsilon_{\text{silica}} = 1.46$ ). This value of  $\epsilon_{\text{silica}}$  translates into an  $\epsilon_m = (1 + 2.13)/2$ , which is the value we use in our equations. Remember that in our model both the peak intensity and the peak width are dependent on the choice of the relaxation rate  $\gamma_K$ . We can artificially reduce the height of the peak at the expenses of increasing its width. It is worth noting the variation of the experimental values for the absorbance among themselves.

no attempt was made to choose them in order to fit the data, with exception to the case reported in figure 5.13.

- **MoS<sub>2</sub>** The two first peaks in the absorbance, A and B, correspond to the A(1s) and B(1s) excitons. The different position of the two peaks is a consequence of SOC splitting of the bands. The last two peaks in the absorbance spectrum,  $C_{01}$  and  $C_{02}$  (having about the same intensity –see the conductivity curve), correspond to the sum of different angular momenta contributions from the  $\Gamma$ -excitons (actually excitonic resonances). The third ( $C_{01}$ ) peak is associated with the transition from the top of the valence band to both the 1 and 1' conduction bands at the  $\Gamma$ -point (conduction bands number 5 and 6 in figure 5.9); we have considered these two degenerated since SOC is small in this case. Finally, the fourth peak ( $C_{02}$ ) comes from transitions connecting the top of the valence band and the 2 and 2' conduction bands (also taken degenerated; conduction bands 7 and 8 in figure 5.9).

The real part of the conductivity follows closely the absorbance spectra, as expected. Usually, the imaginary part of the conductivity from a single excitonic contribution is negative for  $\hbar\omega < E_b$  and positive for  $\hbar\omega > E_b$ , where  $E_b$  is the binding energy, a result that can be obtained by inspection of Elliot's formula for the optical conductivity (F.11).

Let us now discuss the differences between experimental data and our model. We note that the rigid shift to the left performed by Wu *et al.* [113], and Steinhoff *et al.* [117] is not necessary in our case. The difference in intensity of A and B peaks is probably a consequence of the phonons that exist at finite temperature. This effect was not considered in this chapter but was shown to be important for the peaks's broadening [111, 103].

Lastly, we discuss the excitonic effects at the  $\Gamma$ -point. The optical measurements identify only one peak, which seems to correspond to the  $C_{02}$  exciton.



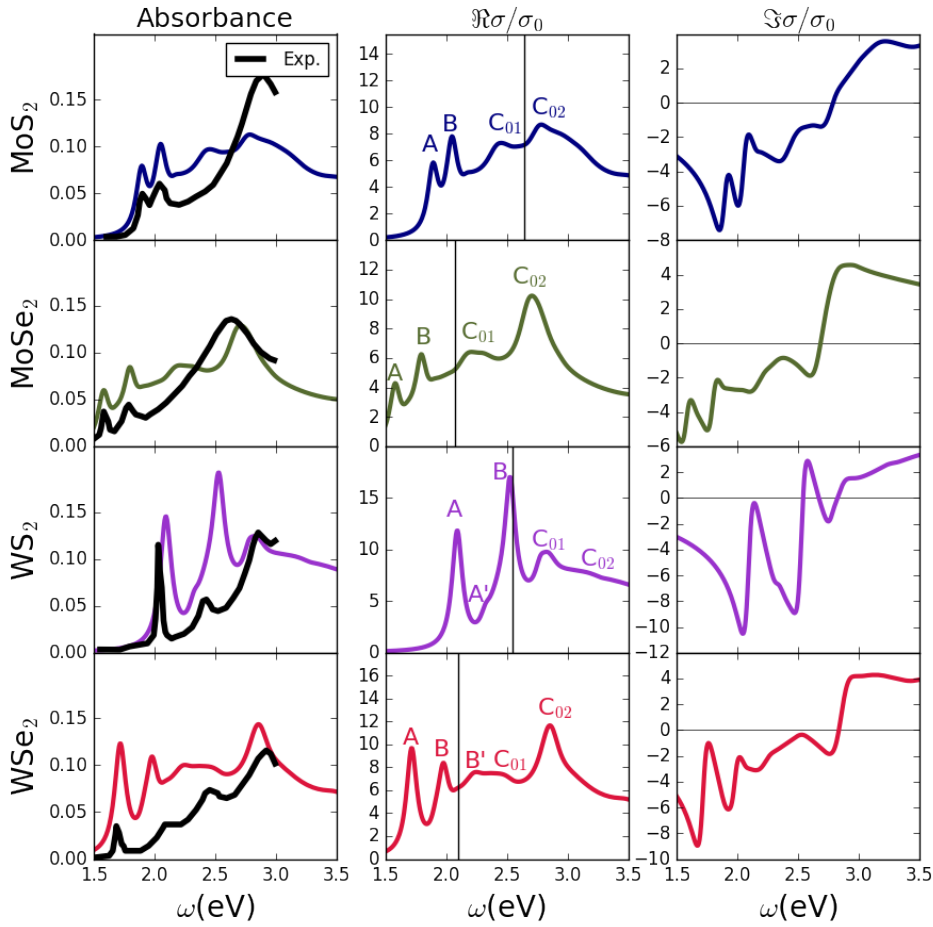


**Figure 5.12.:** Absorbance and optical conductivity of four TMDCs computed from formula (5.40), assuming the materials are neutral and in vacuum; there is no fitting of the data. The real part of the conductivity has the peaks labeled by the corresponding excitonic series, A ( $1s=A$  and  $2s=A'$ ), B ( $1s=B$  and  $2s=B'$ ), and C (all contributions from figure 5.10 for the transitions  $0 \rightarrow 1$  and  $0 \rightarrow 2$ ). The former two are due to transitions at the  $K$ -point and the latter to transition at the  $\Gamma$ -point. Experimental data for the absorbance (solid black curves) is taken from reference [53]. The model parameters are given in table 5.1 for the excitons at the  $K$ -point and in reference [119] for the  $\Gamma$ -point; for all but  $WS_2$  the parameter  $r_0$  has been replaced by  $r_0\epsilon$ , with  $\epsilon$  the effective dielectric constant for a fused silica substrate; a similar procedure was used in reference [130]. See section 5.3 for a discussion of the similarities and differences between the data and the computed spectra. The vertical black line in the central panels define the energy value above which we enter the continuum of the A-series. Note that for  $WX_2$  the first peak of the B series is inside the continuum of the A series (this accounts for the disappearance of the B peak in the experimental data; see figure 5.13). Excitons in the A and B series corresponding to  $\ell = -2$  have vanishing contribution to the optical properties at exciton energy, but are included in this calculation (note that  $\ell = 2$  is a dark exciton). The absorbance has been computed taking the substrate into account using the dielectric permittivity of fused silica at optical frequencies ( $\epsilon = 2.13$ ).

The work of Qiu *et al.* [111] obtain a rich structure of peaks in this region that was washed out when they include quasi-particle lifetimes from phonon terms.

- **MoSe<sub>2</sub>**

The absorbance spectrum of this TMDC share many similarities with MoS<sub>2</sub>: two peaks from the K-point split (A and B) by the SOC and two wider peaks from the  $\Gamma$ -point are also present. The exciton at the  $\Gamma$ -point contributes with two peaks at  $\sim 2.4$  eV and  $\sim 2.7$  eV. The experimental data shows a single peak at 2.6 eV. This discrepancy comes possibly from the phonons already discussed for the MoS<sub>2</sub>. Overall there is a good agreement between the data and the calculated curves, both in position of the peaks and in intensity.

The imaginary part of the conductivity is only positive for frequencies  $\hbar\omega > 2.6$  eV, meaning that exciton-polaritons can only be excited for energies in the visible.

- **WS<sub>2</sub>**

For this material we note the very good agreement of the position and magnitude of the calculated A peak in comparison with those in the experimental data. We also see that the second experimental peak coincides with a small computed peak from the 2s state (A') associated with the series of first exciton A-peak (see figure 5.7). There is at least three reports [143, 144, 145] of measurement of the A' peak in WS<sub>2</sub> in the temperature range of 4-300 K. Unfortunately, in the literature the A' peak has been dubbed B, using an analogy with the MoX<sub>2</sub> case. However, looking at the central panel of figure 5.12 we clearly see that the A'= 2s peak appears at lower energy than the B= 1s. Note that from our analysis we can separate each spin/valley contribution. Also note that the A' peak has a similar absorbance to the experimental one (identified in the experimental literature on WX<sub>2</sub> TMDCs as B, because it is the second to appear in the energy scale). Studying the dependence of light absorption of different peaks on an external magnetic field, for breaking spin degeneracy, together with the use of strong circular polarized light to populate the two valleys differently[86], is a possible way of clarifying the microscopic origin of the different peaks.

The third theoretical (B) peak (which is the SOC counterpart of the first peak) is absent in the experimental data. Note that from figure 5.7, all but one (1s=B) contributions from the B family of peaks are excitonic resonances (above the interacting band gap). The proximity of the B-peak to the continuum may provide a scattering channel to transfers spectral weight from this peak to the resonances in the continuum. An additional and possible mechanism is based on extrinsic doping of these materials as shown in figure 5.13. It has been shown that doping has a strong effect in attenuating the excitonic peaks [109], specially the B-peak in MoS<sub>2</sub>. There is no reason to believe that the same mech-

anism would not work in  $WX_2$  TMDCs. Indeed, from figure 5.2 we expect a strong attenuation of the high-energy excitonic peak whereas the low energy one should survive. This should happen since the doping with electrons tends to block first the higher energy transition whereas maintaining the low energy one. In figure 5.13 we see a comparison of the absorption spectrum of  $WS_2$  with the data taking into account the effect of doping; the agreement is excellent. The suppression of the B-peak is evident from our results, thus confirming doping by electrons as a possible mechanism for suppressing the B excitonic state. The first excitonic resonance ( $C_{01}$ ) at the  $\Gamma$ -point is in very good agreement with the experimental one, while the second excitonic ( $C_{02}$ ) resonance at the  $\Gamma$ -point is at an energy range above the measured one (although its intensity is rather small). Therefore nothing can be said about the possible agreement with the experimental data, since this does not cover that spectral region. Lastly the imaginary part of the optical conductivity becomes positive above the energy  $\sim 2.6$  eV and therefore the system can support exciton-polaritons in that spectral region.

- **WSe<sub>2</sub>**

We end our analysis with a comparison between the calculated absorbance curve and the one measured for  $WSe_2$ . For this material the disagreement between the calculated curves and the experimental data is the largest of the four TMDCs studied in this chapter. Indeed, the data seems stretched relatively to the calculated curves. The first peak in the  $WSe_2$  absorbance spectrum is in very good agreement with the experimental data, with a difference in position less than 0.1 eV.

As in the case of  $WS_2$ , we see that the B-family peak is present in the data as a small shoulder. The third and fourth experimental peaks, when compared with our theoretical model, come from resonances at the  $\Gamma$ -point. The theoretical calculations show a red shift of about 0.2 eV for these two peaks, indicating that higher order exchange corrections, which reshape the band structure around the  $\Gamma$ -point, might be important.

The imaginary part of the optical conductivity is positive above  $\sim 2.8$  eV, thus allowing for excitons-polaritons.

Next we present an analysis of the effects associated with changing the Fermi energy and the Keldysh potential parameter  $r_0$ . Given a Fermi energy the parameter  $r_0$  can be adjusted to fit the A peak. Results of this procedure are shown in figure (5.13) for  $WS_2$ . We can see an excellent agreement between our results and the experimental curve. This highlights the importance of a finite Fermi energy in describing the experimental data. As noted before a finite Fermi energy comes from the spontaneous negative doping observed in TMDCs samples. The better agreement

with the data shown in figure (5.13) relatively to the results of figure (5.12) shows the non-negligible effect of the doping in the optical properties. On the other hand, the parameter  $r_0$  should also be a function of the electronic density. At the moment of writing this dependence is unknown.

One aspect that our calculation does not take into account in an exact way is the self-consistent solution of the exchange energy. Since this calculation is outside the scope of this thesis, we can mimic it using a different value of  $\Lambda_2$  [see Eq. (5.3)]. This leads to a narrow A peak and a broaden B peak in  $WS_2$ , as seen in the experimental data. In this regime, the B peak is no longer an exciton but rather an excitonic resonance. The mechanism leading to the broaden of the B peak can be explained by the self-consistent solution of the exchange energy. For a given carrier density, the iterative calculation of the exchange energy reduces its value and therefore the importance of the doping increases for the lowest conduction band. In  $WS_2$  the effect is much stronger in the lowest band than in the next conduction band due to the large spin-orbit splitting. This mechanism due to exchange increases the splitting on the two conduction bands.

Another aspect of the doping is its influence on the decreasing of the band gap. We show in figure (5.14) the dependence of the band gap and the exciton energies on the Fermi energy. We can see that increasing Fermi energy makes the binding energy (difference between the thick blue curve and all the others) smaller. The energy of the first excited state (squares) increases with the doping while the energy the second (triangles) and third (circles) have the opposite behavior. We also see that it exists a critical doping that makes the exciton states collapsing into resonances when they merge with the band gap. For the energy of first and third excited states we see the same qualitative behavior as measured in Ref. [141].

This concludes the analysis of our theoretical results when compared with the experimental data. Globally, the agreement is good, but some points need further research. Measurements performed at low temperatures in encapsulated TMDCs using hexagonal boron-nitride should reveal the fine structure of the excitonic spectrum predicted by our model.

## 5.4. Discussion and conclusions

In summary, we have performed a study of excitons in TMDCs monolayers including in the same foot both excitons at the  $K$ - and  $\Gamma$ -points. The excitons at the  $K$ -point were calculated with a gapped Dirac equation including electron-electron interactions and SOC. The excitonic resonances at the  $\Gamma$ -point were calculated with the tight-binding three-band model expanded around that point in the Brillouin zone. We compared our theoretical results with the experimental data available from reference [53]. We clarified the microscopic origin of each observed excitonic peak and discussed the reasons for some disagreement between our theoretical model and

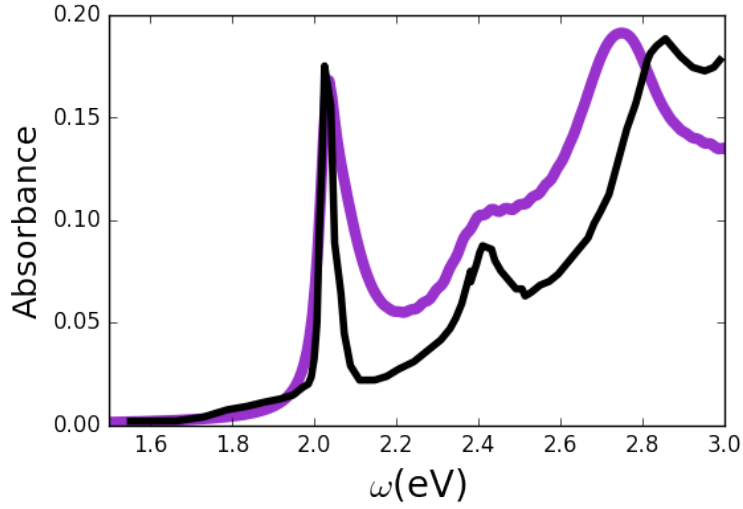


**Figure 5.13.:** Fitting of the experimental optical absorption for  $\text{WS}_2$ . The parameters are those of table 5.1 unless otherwise said. The new parameters are  $r_{0,A} = 55.7$ ,  $E_F = 5$  meV,  $\gamma_A = \gamma_B = 26$  meV, and  $\gamma_T = 0.1$  eV. Temperature is 300 K and we also changed the value of  $\Lambda_2 \rightarrow \Lambda_2 + 0.12$ . The figure is discussed in detail in the main text.

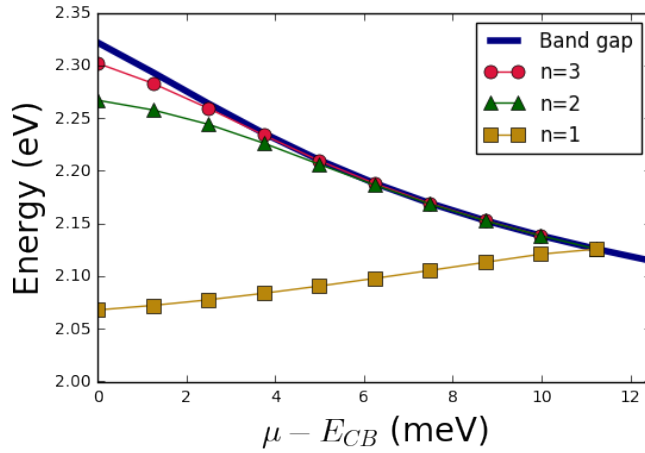


**Figure 5.14.:** Dependence of the band gap and of the three first exciton s-states for  $\text{WSe}_2$  on the Fermi energy.  $E_{CB}$  is the lowest conduction band energy. The parameters of the mass, Fermi velocity and SOC are from table 5.2. We set  $r_0 = 40.92$  Å, slightly larger than that given in reference [107], 37.89 Å. The effective dielectric constant, including the effect of the substrate ( $\text{SiO}_2$ ), is  $\epsilon = 2.45$ . We used a temperature of 77 K.

the experimental data. Note that the measurements were made at room temperature. Therefore, the effect of a self-energy, which will be energy dependent, due to electron-phonon interactions might play an important role in modeling the absorbance spectrum at room temperature. We note here that our equation of motion method also allows for treating electron-phonon interactions at the expense of a more lengthy calculation.

Also, as noted by Mak *et al.* [140]: “Spontaneous negative doping, presumably from defects within the MoS<sub>2</sub> layer and/or substrate interactions, has been commonly reported in mechanically exfoliated samples”. This seems to be the reason [109] why the B-series is not visible in WX<sub>2</sub> when the material is electron-doped (see figure 5.13). To conclude, given the uncertainties in the experimental data reported in table 5.3 we consider the agreement between our calculation and the data to be quite good.

We have also studied the variation of the 1s =A peak with the dielectric function of the capping medium (results not shown). We found that the A-peak position varies little with  $\epsilon_m$ . This happens because the exchange energy correction compensates the binding energy coming from the BSE.

Although we have considered in this chapter the response to linearly polarized electromagnetic radiation, it is simple to generalize the calculation to circularly polarized one. This would allow us to discuss the additional appearance of more selection rules associated with spin.

## 5.A. Overlap of the four-body wavefunctions

The four-body overlap functions are explicitly defined below for the massive Dirac Hamiltonian:

$$F_{\lambda_1, \lambda_2, \lambda_3, \lambda_4}^{s\tau}(\mathbf{k}_1, \mathbf{k}_2) = \phi_{\lambda_1}^{s\tau\dagger}(\mathbf{k}_1) \phi_{\lambda_2}^{s\tau}(\mathbf{k}_2) \phi_{\lambda_3}^{s\tau\dagger}(\mathbf{k}_2) \phi_{\lambda_4}^{s\tau}(\mathbf{k}_1). \quad (5.52)$$

For simplicity of writing, we omit in this appendix the superscript  $s\tau$  in the  $F$ 's-functions and in the energy  $E_k^{s\tau}$ . For the case  $\lambda_1 = \lambda_4$  and  $\lambda_2 = \lambda_3$  the overlap function reads:

$$F_{\lambda_1, \lambda_2, \lambda_2, \lambda_1}(\mathbf{k}_1, \mathbf{k}_2) = \frac{1}{2} \left( 1 + \lambda_1 \lambda_2 \frac{\mathbf{k}_1 \cdot \mathbf{k}_2 + m^2}{E_{\mathbf{k}_1} E_{\mathbf{k}_2}} \right), \quad (5.53)$$

whereas when  $\lambda_1 = \lambda_4$ ,  $\lambda_2 = -\lambda_3$  we find:

$$F_{\lambda_1, \lambda_2, -\lambda_2, \lambda_1}(\mathbf{k}_1, \mathbf{k}_2) = \frac{\lambda_1 m [\mathbf{k}_2 \cdot (\mathbf{k}_2 - \mathbf{k}_1)] + i \lambda_2 E_{\mathbf{k}_2} (\mathbf{k}_1 \times \mathbf{k}_2) \cdot \mathbf{u}_z}{2 k_2 E_{\mathbf{k}_1} E_{\mathbf{k}_2}}. \quad (5.54)$$

Finally, in the conditions  $\lambda_1 = -\lambda_4, \lambda_2 = -\lambda_3$  we have:

$$F_{\lambda_1, \lambda_2, -\lambda_2, -\lambda_1}(\mathbf{k}_1, \mathbf{k}_2) = \frac{1}{2} \frac{k_1 k_2}{E_{\mathbf{k}_1} E_{\mathbf{k}_2}} \left[ 1 + \frac{\mathbf{k}_1 \cdot \mathbf{k}_2 (\lambda_1 \lambda_2 E_{\mathbf{k}_1} E_{\mathbf{k}_2} + m^2)}{k_1^2 k_2^2} + \frac{im(\mathbf{k}_2 \times \mathbf{k}_1) \cdot \mathbf{u}_z (\lambda_1 E_{\mathbf{k}_1} + \lambda_2 E_{\mathbf{k}_2})}{k_1^2 k_2^2} \right]. \quad (5.55)$$

When  $\lambda_1 = -\lambda_4$  and  $\lambda_2 = \lambda_3$  we have the following symmetry:

$$\begin{aligned} F_{\lambda_1 \lambda_2 \lambda_3 \lambda_4}^*(\mathbf{k}_1, \mathbf{k}_2) &= \phi_{\lambda_2}^\dagger(\mathbf{k}_2) \phi_{\lambda_1}(\mathbf{k}_1) \phi_{\lambda_4}^\dagger(\mathbf{k}_1), \phi_{\lambda_3}(\mathbf{k}_2) \\ &= F_{\lambda_2 \lambda_1 \lambda_4 \lambda_3}(\mathbf{k}_2, \mathbf{k}_1), \end{aligned} \quad (5.56)$$

that is, in expression (5.55) we have an identity upon the exchange of indexes  $\lambda_1 \leftrightarrow \lambda_2, \mathbf{k}_1 \leftrightarrow \mathbf{k}_2$ .

## 5.B. The Bethe-Salpeter kernel

In this appendix we give the explicit forms of the BSE kernel. Firstly, from equation (5.18) we have:

$$\mathcal{B}_{\mathbf{k}\lambda}^{s\tau}(t) = -\frac{1}{S} \sum_{\mathbf{q}} V(|\mathbf{k} - \mathbf{q}|) \left[ p_{\lambda}^{s\tau}(\mathbf{q}, t) F_{-\lambda-\lambda\lambda\lambda}^{s\tau}(\mathbf{k}, \mathbf{q}) + p_{-\lambda}^{s\tau}(\mathbf{q}, t) F_{-\lambda\lambda-\lambda\lambda}^{s\tau}(\mathbf{k}, \mathbf{q}) \right]. \quad (5.57)$$

For the homogeneous case we only consider the first term in the previous equation and choose with  $\lambda = -$ , which corresponds to the resonant term. Thus we have the BSE kernel reading:

$$K_{\lambda}^{s\tau}(k, q, \theta) = V(|\mathbf{k} - \mathbf{q}|) F_{-\lambda-\lambda\lambda\lambda}^{s\tau}(\mathbf{k}, \mathbf{q}). \quad (5.58)$$

Using the expression (5.55) for the  $F_{+-+--}^{s\tau}(\mathbf{k}, \mathbf{q})$ , and the Keldysh potential (5.4), and after the angular decomposition

$$\tilde{T}_{\ell}^{s\tau}(k, q) = \int_0^{2\pi} \frac{d\theta}{2\pi} e^{i(\ell+1)\theta} K_{-}^{s\tau}(k, q, \theta), \quad (5.59)$$

we have the corresponding kernel  $\tilde{T}_{\ell}^{s\tau}(k, q)$ :

$$\tilde{T}_{\ell}^{s\tau}(k, q) = -\frac{\alpha}{4\pi\epsilon_m} \frac{c}{v_F} \frac{kq^2}{2E_k E_q} \left[ I_{\ell}(k, q) + c_{-}^{s\tau}(k, q) I_{\ell+1}(k, q) + c_{+}^{s\tau}(k, q) I_{\ell-1}(k, q) \right], \quad (5.60)$$

where we have defined:

$$I_{\ell}(k, q) = \int_0^{2\pi} d\theta e^{i(\ell+1)\theta} \frac{q_0}{p_{k,q}(\theta)(p_{k,q}(\theta) + q_0)}, \quad (5.61)$$

$$c_{\pm}^{s\tau}(k, q) = \frac{1}{2kq} [E_k^{s\tau} E_q^{s\tau} + m_{s\tau}^2 \pm m_{s\tau}(E_k^{s\tau} + E_q^{s\tau})], \quad (5.62)$$

and

$$p_{k,q}(\theta) = \sqrt{q^2 + k^2 - 2kq \cos \theta}, \quad (5.63)$$

where  $\alpha \approx 1/137$  is the fine structure constant and  $c$  is the speed of light.

For the kernel in the non-homogeneous BSE, we write the renormalization of Rabi frequency as:

$$\begin{aligned} \mathcal{B}_{\mathbf{k}\lambda}^{s\tau}(t) = & - \int \frac{d\mathbf{q}}{(2\pi)^2} V(|\mathbf{k} - \mathbf{q}|) F_{-\lambda-\lambda\lambda\lambda}^{s\tau}(\mathbf{k}, \mathbf{q}) p_{\lambda}^{s\tau}(\mathbf{q}, \omega) + \\ & - \int \frac{d\mathbf{q}}{(2\pi)^2} V(|\mathbf{k} - \mathbf{q}|) F_{-\lambda\lambda-\lambda\lambda}^{s\tau}(\mathbf{k}, \mathbf{q}) p_{-\lambda}^{s\tau}(\mathbf{q}, \omega). \end{aligned} \quad (5.64)$$

Thus, we have two kernels to consider:

$$K_{\lambda}^{1,s\tau} = V(|\mathbf{k} - \mathbf{q}|) F_{-\lambda-\lambda\lambda\lambda}^{s\tau}(\mathbf{k}, \mathbf{q}), \quad (5.65a)$$

$$K_{\lambda}^{2,s\tau} = V(|\mathbf{k} - \mathbf{q}|) F_{-\lambda\lambda-\lambda\lambda}^{s\tau}(\mathbf{k}, \mathbf{q}). \quad (5.65b)$$

Note that, in this case and contrary to the homogeneous BSE, we have to keep both terms in the renormalization of the Rabi frequency, as otherwise the real part of the optical conductivity would not have the correct positive sign. That is because both the resonant and off-resonance terms contribute to the optical conductivity, as is well known in the non-interacting case. Proceeding as before, the angular decomposition (5.59) of the kernels leads to:

$$T_{\lambda,\ell}^{1/2,s\tau}(k, q) = C_{k,q}^{s\tau} [I_{\ell}(k, q) + c_{\lambda-}^{1/2,s\tau}(k, q) I_{\ell+1}(k, q) + c_{\lambda+}^{1/2,s\tau}(k, q) I_{\ell-1}(k, q)], \quad (5.66)$$

with

$$C_{k,q}^{s\tau} = -\frac{\alpha}{4\pi\epsilon_m} \frac{c}{v_F} \frac{kq^2}{2E_k^{s\tau} E_q^{s\tau}}, \quad (5.67)$$

and

$$c_{\lambda\pm}^{1,s\tau}(k, q) = \frac{1}{2kq} [E_k^{s\tau} E_q^{s\tau} + m_{s\tau}^2 \pm \lambda m_{s\tau}(E_k^{s\tau} + E_q^{s\tau})], \quad (5.68)$$

$$c_{\lambda\pm}^{2,s\tau}(k, q) = \frac{1}{2kq} [-E_k^{s\tau} E_q^{s\tau} + m_{s\tau}^2 \pm \lambda m_{s\tau}(E_k^{s\tau} - E_q^{s\tau})], \quad (5.69)$$

where  $\lambda = \pm$  and  $\lambda' = -\lambda$ , and  $I_{\ell}(k, q)$  is defined in equation (5.61).



### 5.C. Exchange correction around the $\Gamma$ point

From equation (3.31), the exchange self-energy correction to the transition energy between bands  $i$  and  $j$  is:

$$\Sigma_{ij}^{xc}(\mathbf{k}) = S \sum_{\mathbf{q}} V(\mathbf{q}) \sum_{\lambda} n_{\lambda}(\mathbf{k} - \mathbf{q}) [F_{i\lambda\lambda i}(\mathbf{k}, \mathbf{k} - \mathbf{q}) - F_{j\lambda\lambda j}(\mathbf{k}, \mathbf{k} - \mathbf{q})]. \quad (5.70)$$

Neglecting temperature and doping effects, for the three band-model of reference [119], the only term that contributes to the exchange self-energy is the one with  $\lambda = 0$  (the valence band):

$$\Sigma_{ij}^{xc}(\mathbf{q}) = S \sum_{\mathbf{q}} V(\mathbf{q}) [F_{i00i}(\mathbf{k}, \mathbf{k} - \mathbf{q}) - F_{j00j}(\mathbf{k}, \mathbf{k} - \mathbf{q})]. \quad (5.71)$$

and we make  $i = 1, 2$  and  $j = 0$ .

To remove the integrable divergence at  $q = 0$ , that comes from the Keldysh potential, we use polar coordinates leading to the need of computing the following integral

$$\Sigma_{i0}^{xc}(\mathbf{k}) = - \sum_{j=1}^6 \int_{j\pi/3}^{(j+1)\pi/3} \frac{d\theta}{2\pi} \int_0^{q_0 \sec(\theta - \pi/6 - j\pi/3)} \frac{qdq}{2\pi} V(q) Q_i(\mathbf{k}, q, \theta) \quad (5.72)$$

where  $Q_i(\mathbf{k}, q, \theta) = F_{i00i}(\mathbf{k}, \mathbf{k} - \mathbf{q}) - F_{0000}(\mathbf{k}, \mathbf{k} - \mathbf{q})$  and  $q_0$  reads

$$q_0 = \frac{2\pi}{a_0\sqrt{3}}. \quad (5.73)$$



## 6.1. Introduction

Graphene is a promising candidate to overcome one of the major existing hurdles to bring optics and electronics together, namely the efficient conversion between optical and electronic signals. Indeed, this can be facilitated by the fact that graphene enables strong, electric field-tunable optical transitions, and resonantly enhances light-matter interactions in sub-wavelength volumes. In practice this can be achieved, for instance, by integrating a graphene layer into a photonic crystal nanocavity [146]. The presence of graphene also allows for an efficient electro-optical modulation of photonic crystal nanocavities by electrostatic gating [147, 148]. However, the integration of graphene into photonic crystals is naturally prone to unavoidable disorder associated to the fabrication process. This constitutes *per se* a motivation to investigate the effects of disorder in photonic crystals containing graphene layers which. In addition to this technological and practical motivation, there is a very fundamental one as well, namely to understand the impact of graphene on Anderson localization of light.

The concept of Anderson localization (AL) was originally conceived in the realm of condensed matter physics as a disorder driven metal-insulator transition [149]. Being an interference wave phenomenon, this concept has been extended to light [150], acoustic waves [151], and even Bose-Einstein condensed matter waves [152]. As a result, Anderson localization is today a truly interdisciplinary topic, and important contributions have emerged from different areas, ranging from condensed matter, photonics, acoustics, atomic physics, and seismology [153]. Dimensionality is crucial to AL, and in 1D the vast majority of states is exponentially localised on a length scale given by the localization length  $\xi$ , regardless of the disorder strength. In optical systems exceptions do exist, and delocalised modes may occur in low-dimensional systems as a result of the presence of correlations [154], necklace modes [155], or metamaterials with negative refraction [156, 157, 158]. The question of whether these anomalies occur when graphene is integrated into disordered optical superlattices

remains an open question.

Bearing in mind both these technological and fundamental motivations, in the present chapter we undertake an analytical and numerical investigation of Anderson localization of light in one-dimensional disordered superlattices composed of dielectric stacks with graphene layers in between, as depicted in Fig. 6.1. We consider two possible, realistic ways to model disorder: compositional and structural disorder. In the former case disorder is introduced in graphene's material parameters, such as the Fermi energy, whereas in the latter the dielectric components of the superlattice have random widths. In both cases, we derive an analytic expression for the localization length  $\xi$ , and compare it to numerical simulations using a transfer matrix technique; an overall very good agreement is found. In the case where the medium impedances match, we find that  $\xi$  exhibits an oscillatory behaviour as a function of frequency  $\omega$ , in contrast to the usual asymptotic decay  $\xi \propto \omega^{-2}$ . We demonstrate that graphene may strongly suppress the anomalously delocalised Brewster modes, as it induces additional reflexions at the superlattice interfaces. We also investigate the effects of inter and intraband transitions of the graphene conductivity on  $\xi$ , identifying the regimes where Anderson localization and absorption dominates light transmission.

This chapter is organised as follows. In Sec. II we present the analytical results, where we derive an expression for the localization length of disordered superlattices containing graphene sheets. In Sec. III we present and discuss the numerical simulations, based on transfer matrix technique, which are also compared to the analytical calculations. Finally, Sec. IV is devoted to the concluding remarks. We also present a number of appendices giving the details of the calculations and aiming at making the text as self-contained as possible. To our best knowledge, there are only two published papers[159, 160] dealing with similar problems to the one we consider in this chapter, but in the context a metals, in which case only Drude's conductivity plays a role.

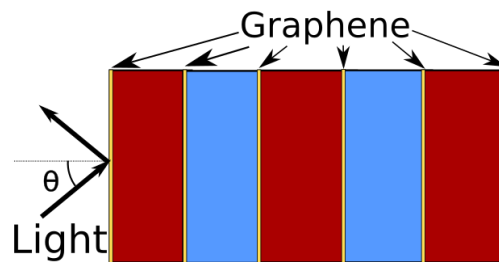


**Figure 6.1.:** Schematic representation of the system, a photonic crystal whose unit cell is: graphene/dielectric 1/graphene/dielectric 2.

## 6.2. Analytical calculation of the localization length

Light propagation in a 1D superlattice containing graphene layers (Fig. 6.1) is modelled by the transfer matrix formalism [161]. The  $M^n = \{m_{ij}^n\}$  transfer matrix connects the fields at the right of the  $n$ -th unit cell to those at left according to:

$$\psi^{n+1} = M^n \psi^n, \quad (6.1)$$

where  $\psi^n = [\psi_R^n \quad \psi_L^n]^T$ , and  $\psi_R^n$  ( $\psi_L^n$ ) refers to the right (left) propagating field in the  $n$ -th cell. For transverse electric (TE) and transverse magnetic (TM) modes,  $\psi$  refers to the electric and magnetic field, respectively. We consider the particular case where  $\det M^n = 1$ , which occurs for systems with preserved time reversal symmetry [161]. In this case, one can show that  $M^n$  may be written as

$$M^n = \begin{pmatrix} \cosh \phi_1^n e^{i\phi_2^n} & \sinh \phi_1^n e^{i\phi_3^n} \\ \sinh \phi_1^n e^{-i\phi_3^n} & \cosh \phi_1^n e^{-i\phi_2^n} \end{pmatrix}, \quad (6.2)$$

where  $\phi_i^n$  are parameters that depend on the composition of the  $n$ -th cell. (from here on we omit the  $n$  dependence in  $\phi_i$ , except when strictly necessary to avoid any confusion.) For periodic systems with preserved time-reversed symmetry,  $\phi_i$  are real numbers and all the  $M^n$ 's are equal. We thus write  $M^n = M^0$ . One can write the photonic dispersion relation [161] as  $\cos g = (m_{11}^0 + m_{22}^0)/2$ , where

$$\cos g = \cosh \phi_1^0 \cos \phi_2^0. \quad (6.3)$$

Disorder is introduced in the parameters  $\phi_i$ :

$$\phi_i = \phi_i^0 + \delta\phi_i \quad (6.4)$$

where  $\delta\phi_i$  describes random fluctuations around the average value, and which may have different origins, as it will be detailed later in the chapter. For a periodic system, a transformation  $M_{\text{transf}} = M_{\text{circle}} M_{\text{real}}$  (see appendix 6.A) exists that maps the variables  $\psi_{R,L}^n$  into a new set of variables, denoted by  $Q_n$  and  $P_n$ , such that  $X^T = [Q^n \ P^n]^T = M_{\text{transf}} [\psi_R^n \ \psi_L^n]^T$ . These new variables describe a circle in phase space [162], with radius  $\sqrt{Q_n^2 + P_n^2}$  proportional to the electric field amplitude. Applying this transformation to Eq. (6.1), the transformed matrix  $M' = M_{\text{transf}} M^n M_{\text{transf}}^{-1}$  reads

$$M' = \begin{pmatrix} E_n & F_n \\ G_n & H_n \end{pmatrix}, \quad (6.5)$$

where:

$$E_n = \cosh \phi_1 \cos \phi_2 - \sinh \phi_1 \sin \delta\phi_3, \quad (6.6)$$

$$F_n = -v^2 (\cosh \phi_1 \sin \phi_2 + \sinh \phi_1 \cos \delta\phi_3), \quad (6.7)$$

$$G_n = v^{-2} (\cosh \phi_1 \sin \phi_2 - \sinh \phi_1 \cos \delta\phi_3), \quad (6.8)$$

$$H_n = \cosh \phi_1 \cos \phi_2 + \sinh \phi_1 \sin \delta\phi_3. \quad (6.9)$$

with  $v$  and  $\tau$  defined in appendix 6.A. When  $\phi_i = \phi_i^0$ , we have  $\delta\phi_3 = 0$  and Eqs. (6.6)-(6.9) lead to  $E_n = H_n = \cos g$  and  $F_n = -G_n = \sin g$ . When weak disorder is introduced, the trajectory of the points  $(Q_n, P_n)$  results in a perturbation of the circle. The recurrence equations defined by  $X^{n+1} = M'X^n$  are similar to a Hamiltonian map of the classical harmonic oscillator subjected to a parametric impulsive force [163], where  $Q_n$  and  $P_n$  are the coordinate and conjugated moments, respectively, and  $g$  is the phase between successive kicks.

The presence of disorder introduces a key length scale, the localization length  $\xi$ . In 1D electronic systems all eigenmodes are exponentially localised, although some exceptions do exist in the realm of optical systems [156, 157, 158, 155] (see Introduction). The length  $\xi$  characterises the exponential decay of the eigenfunctions and is defined in terms of the reciprocal of the Lyapunov exponent  $\lambda$ . In 1D  $\lambda$  can be written as [161, 162]:

$$\lambda = \frac{1}{2} \left\langle \ln \left| \frac{\psi_R^{n+1}}{\psi_R^n} \right|^2 \right\rangle. \quad (6.10)$$

In Eq. (6.10) the brackets denote averaging over both ensembles and the system unit cells, while the usual definition of the localization length considers only averages over ensembles [161]. The two definitions are equivalent. The relation between  $\lambda$  and  $\xi$  is:

$$\text{Re}\lambda = \frac{d}{\xi}, \quad (6.11)$$

where  $d$  is the mean length of the unit cell. The advantage of the approach based on the parameters  $P_n$  and  $Q_n$  is that we can use polar (or action-angles) coordinates:

$$\begin{aligned} P_n &= R_n \sin \Theta_n, \\ Q_n &= R_n \cos \Theta_n. \end{aligned} \quad (6.12)$$

Without disorder,  $R_n$  is a constant and  $\Theta_n$  increases by minus the Bloch phase,  $-g$ , as we move from unit cell to unit cell. With disorder, the radius  $R_n$  changes in every step, with  $R_{n+1}$  a function of  $R_n$ ,  $\Theta_n$ , and of the matrix elements of  $M^n$ . The angle  $\Theta_{n+1}$  only depends on  $\Theta_n$  and  $M^n$ . For weak disorder a recurrence equation (6.48) exists that, in the continuum limit, becomes a stochastic Itô equation which has a corresponding Fokker-Planck equation [164]. In this case, the first approximation for the density probability function of  $\Theta_n$  is uniform in the interval  $[0, 2\pi]$  for  $g \neq 0, \pi/2, \pi$ .

Writing Eq. (6.10) in terms of  $R$  and  $\Theta$ , and averaging over  $\Theta$  with uniform density probability, we obtain, up to second order in  $\delta\phi_i$ :

$$\lambda = \frac{1}{2} \left\langle Y_1 + Y_2 \cos 2\Theta_n + Y_3 \sin 2\Theta_n - \frac{1}{4}Y_2^2 - \frac{1}{4}Y_3^2 \right\rangle, \quad (6.13)$$

where  $Y_i$ , with  $i = 1, 2, 3$  are defined in Appendix 6.B and depend on the matrix elements  $M^n$ .

In the following sections we will study the propagation of light through a disordered structure of alternating graphene sheets and dielectric layers. In this case each propagation matrix  $M^n$  is determined by the widths  $z_i$ , the incidence angle  $\theta_i$ , the dielectric material parameters  $\mu_i$  and  $\varepsilon_i$ , and the graphene conductivity  $\sigma$ . In the present work we focus on the cases where disorder is present in the widths of the stacks (structural disorder) and on graphene conductivities (compositional disorder). Both are realistic situations that may occur in the fabrication of these structures.

For the type of structural disorder studied here the width of each layer  $i$  of the  $n^{\text{th}}$  cell is a random variable

$$z_i(n) = z_i^0 + \zeta_i(n), \quad (6.14)$$

where  $\zeta_i$  are uncorrelated random variables with zero mean and mean standard deviation  $\delta_i$ :

$$\langle [\zeta_i(n)]^2 \rangle = \delta_i^2, \quad (6.15)$$

$z_i^0$  is the mean width of the  $i$  slab.

In the case of compositional disorder, the Fermi energy  $E_F$  is a random variable in each layer  $n$

$$E_F(n)/\hbar = \omega_F(n) = \omega_F^0 + \zeta_F(n), \quad (6.16)$$

with  $\zeta_F$  a random variable with zero mean and  $\langle \zeta_F^2 \rangle = \delta_F^2$ . This determines how the graphene conductivity, given in Appendix B, is affected by disorder.

In the next section we derive analytical expressions for  $\lambda$  (Eq. 6.13) in different regimes. To this end, we need to map  $\phi_i$  in the system variables, calculate the differentials  $\delta_i$ , and use the results given in Appendix 6.B.

### 6.2.1. UNIT CELL MADE OF TWO DIFFERENT DIELECTRIC MATERIALS AND A GRAPHENE SHEET AT THE INTERFACE

We consider a disordered superlattice composed of dielectric bilayers with a graphene sheet in between. The transfer matrix for the  $n$  unit cell is given by  $M^n = \{m_{jl}^n\}$  and is explicitly derived in Appendix G.1.

To proceed with the calculation of the Lyapunov exponent it is necessary to map the system parameters of the transfer matrix (G.1) into the parametric matrix (6.2). There is not a unique way of doing this, but in what follows we make the simplest choice.

#### DISORDERED PHOTONIC SUPER LATTICE WITHOUT GRAPHENE

To model a disordered photonic super-lattice without the graphene layer we put  $f = 0$  in Eq. (G.1) and map  $\phi_i$  into the system parameters  $\alpha_1, \alpha_2, \chi, \Delta$  (defined in

Appendix G):

$$\begin{aligned}\sinh \phi_1 &= \Delta^x \sin \alpha_2, \\ \phi_2 &= \alpha_1 + \arctan(\chi^x \tan \alpha_2), \\ \phi_3 &= \alpha_1 + \pi/2,\end{aligned}\tag{6.17}$$

where  $x = \text{TE, TM}$ . According to this mapping we can replace  $\phi_i$  in the expressions for  $Y_i$  in Appendix 6.B and calculate the differentials  $\delta\phi_i$  using Eq. (6.14) with  $\zeta_i \ll z_i^0$ . This will enable us to compute the Lyapunov exponent, given by Eq. (6.13); the final result is

$$\lambda = \frac{\Delta^2}{2 \sin^2 g} (\sin^2 \alpha_2 k_1^2 \beta_1^2 + \sin^2 \alpha_1 k_2^2 \beta_2^2),\tag{6.18}$$

which agrees with the result of Ref. [162] for uncorrelated disorder. The described procedure is repeated to calculate the Lyapunov exponents in the next sections.

#### DISORDERED SUPERLATTICE CONTAINING GRAPHENE LAYERS

The presence of graphene at the interface between the dielectrics results in a discontinuity in the tangential component of the magnetic field. The role of graphene on the optical properties of the superlattice increases as the value of the dimensionless parameter  $\beta_i^x f$  increases, with  $f = \sigma c \mu_0 / 2$  and  $\beta_i^x$  given in Appendix G. We are interested in the lossless regime in which the Bloch phase  $g$ , given by Eq. (G.3), is real. This regime sets up when (i)  $\sigma$  (and therefore  $f$ ) is a pure complex number and  $\theta_i$ , with  $i = 1, 2$ , is a pure real number; or (ii)  $\sigma$  is a pure real number so that evanescent propagation occurs in one of the layers.

In the first case, we define  $B^x = i\tilde{B}^x$  (see Appendix G), where  $\tilde{B}$  is real, and we map the parameters  $\phi_i$  in:

$$\begin{aligned}\sinh \phi_1 &= -\tilde{B}^x \cos \alpha_2 + (\Delta - D^x) \sin \alpha_2, \\ \phi_2 &= \alpha_1 + \arg [A_+^x \cos \alpha_2 + i(\chi + C_+^x) \sin \alpha_2], \\ \phi_3 &= \alpha_1 + \pi/2.\end{aligned}\tag{6.19}$$

Following the procedure of Sec. 6.2.1, the Lyapunov exponent is given by:

$$\lambda = \frac{1}{2 \sin^2 g} (K_2^2 k_1^2 \beta_1^2 + K_1^2 k_2^2 \beta_2^2),\tag{6.20}$$

where:

$$K_1 = -2\tilde{f}\lambda^x \beta_2^x \cos \alpha_1 + [-\Delta + 2\tilde{f}^2 \lambda^x \beta_1^x \beta_2^x] \sin \alpha_1,\tag{6.21}$$

and  $f = i\tilde{f}$ ,  $K_2$  is obtained by interchanging  $1 \leftrightarrow 2$  and  $\Delta \rightarrow -\Delta$ . Notice that if one plugs Eq. (6.21) with  $f = 0$  into Eq. (6.20), Eq. (6.18) is obtained, as it should be.



### 6.2.2. UNIT CELL MADE OF ONE DIELECTRIC MATERIAL AND A GRAPHENE SHEET AT THE INTERFACE

For systems composed of bilayers of the same dielectric material with a graphene sheet in between, it is much easier to calculate the transfer matrix, which is given in Eq. (G.6). In this case, the  $\phi_i$  parameters read

$$\begin{aligned}\sinh \phi_1 &= -\lambda^x \beta^x \tilde{f}, \\ \phi_2 &= \alpha, \\ \phi_3 &= \alpha + \pi/2,\end{aligned}\tag{6.22}$$

Using Eq. (6.13) and the results of the Appendix 6.B we calculate the Lyapunov exponent for structures containing both random graphene conductivities (compositional disorder) and random widths (structural disorder), as detailed in the following.

#### COMPOSITIONAL DISORDER

Using the same procedure of subsection 6.2.1, we obtain the Lyapunov exponent:

$$\lambda = \frac{1}{2} \left( \frac{\sin 2\alpha}{\sin 2g} \beta^x \frac{\pi \alpha_c}{2} \delta_g \right)^2,\tag{6.23}$$

where  $\alpha_c$  is the fine structure constant and  $\sigma_g$  is the mean standard deviation of the normalized graphene conductivity

$$\delta_g^2 = \frac{\langle \sigma^2 \rangle - \langle \sigma \rangle^2}{\sigma_0^2}.\tag{6.24}$$

#### STRUCTURAL DISORDER

For structural disorder where the stacks' widths are given by Eq. (6.14), the Lyapunov exponent reads

$$\lambda = \frac{\tilde{f}^2 \beta^{x^2} k^2 \delta^2}{2 \sin^2 g}.\tag{6.25}$$

This concludes the analytical part of our work, which shall be compared to numerical simulations in the following section.

## 6.3. Numerical Simulations: Results and Discussions

### 6.3.1. SIMULATION PROCEDURE

The numerical calculations are based on the transfer matrix method; the total transfer matrix for light propagating in a  $N$ -layered system is

$$M = \prod_{n=1}^N M^n.\tag{6.26}$$

where the elements of  $M^n$  are given by Eq. (G.1). Transmission is calculated by applying the boundary condition related to the fact that there is no incoming wave from the left:

$$T = \frac{1}{|m_{22}|^2}, \quad (6.27)$$

and the localization length  $\xi$  is calculated by:

$$\frac{L}{\xi} = -\frac{1}{2} \langle \ln T \rangle, \quad (6.28)$$

where  $L = Nd$  and  $N$  is the total number of unit cells with mean width  $d$ . The length  $L$  is chosen to be large enough to ensure the numerical calculation of the localization length converges. In the numerical procedure we first generate random variables  $\zeta_i$  (or  $\zeta_F$ ) [see Eqs. (6.14) and (6.16)] from a uniform distribution, and then calculate the transfer matrix using Eq. (6.26). With the help of the results introduced in Appendix G, we obtain the localization length using Eq. (6.28). The procedure is repeated over  $n_{\text{samples}}$  and the mean value of the localization length is calculated. We have verified that, for a sufficiently large  $N$ , the value of  $\xi$  calculated for a single disorder realisation coincides with its average over many disorder realisations for smaller systems; in other words, we have verified that  $\xi$  is a self-averaging quantity. Further details of the transfer matrix method are given in Appendix G.

### 6.3.2. RESULTS

Light transmission depends on the graphene conductivity  $\sigma$  and on the medium impedances, defined as ( see Appendix G):

$$Z_i^{\text{TE}} = \frac{\sqrt{\mu_i \varepsilon_i}}{\mu_i} \cos \theta_i, Z_i^{\text{TM}} = \frac{\sqrt{\mu_i \varepsilon_i}}{\varepsilon_i} \cos \theta_i. \quad (6.29)$$

We shall focus in the lossless regime with  $\Im m \cos g = 0$  and  $\Re e \cos g \leq 1$ . From Eq. (G.3), this regime occurs whenever  $f$  (and consequently  $\sigma$ ) is a pure complex number or for  $\Im \sigma = 0$ , in which case one of the slabs supports a evanescent mode. When the Drude term dominates, the imaginary part of the conductivity is positive (see Appendix B). For frequencies slightly below  $2\omega_F$ , the inter-band term dominates and the imaginary part of the conductivity is negative (see Appendix B). When the frequency becomes larger than  $2\omega_F$ , the imaginary part goes to zero and the real part tends to  $\sigma_0 = e^2/4\hbar$ .

In the following numerical calculations, random variables have a uniform distribution with  $\zeta_x \in [-\Upsilon_x/2, \Upsilon_x/2]$ , with  $x = 1, 2$  for structural disorder and  $x = F$  for compositional disorder.

### 6.3.3. DRUDE REGIME WHEN: $\Re\sigma \approx 0$ , $\Im\sigma > 0$

When  $\omega_F\gamma \ll \omega^2 \ll \omega_F^2$  (where  $\gamma$  is the broadening entering in the conductivity), graphene conductivity can be approximated by (see Appendix B.105):

$$\sigma = i\sigma_0 \frac{4\omega_F}{\pi\omega}. \quad (6.30)$$

For  $E_F \approx 0.3$  eV (a typical value for the graphene Fermi energy), the range of frequencies corresponds to the infrared spectral regime. In the following we focus in three regimes: impedance matching in the double layered system [ $Z_1 = Z_2$ , in Eq. (6.29)] with structural disorder, compositional disorder in one layered system, and the attenuated field regime (ATR) with structural disorder.

#### IMPEDANCE MATCHING IN TWO-LAYERED SYSTEM WITH STRUCTURAL DISORDER

Using the Snell-Descartes law, Eq. (G.2), and the impedances in Appendix G, one can verify that for materials without magnetic response ( $\mu_1 = \mu_2 = 1$ ), there is no TE mode that allows the impedance matching. In the TM mode the impedance matching occurs when the angle of incidence in layer 1 obeys the relation  $\sin^2 \theta_1 = \varepsilon_2/(\varepsilon_1 + \varepsilon_2)$ , for  $\varepsilon_1 \neq \varepsilon_2$ .

When  $Z_i = Z$ ,  $\beta_i = \beta$ , it follows from Eqs. (6.20) and Eq. (6.21) that:

$$\lambda = 2 \left( \frac{4\tilde{f}\beta^x\omega_F}{\pi c \sin g} \right)^2 \sum_{i=1}^2 \varepsilon_i \mu_i \cos^2 \alpha_i \cos^2 \theta_i \delta_i^2, \quad (6.31)$$

where we neglected the term  $\tilde{f}^2$  in comparison to  $\tilde{f}$  (which in the Drude regime is always valid for a sufficient large  $\omega$ ). In this case, in Fig. 6.2b the localization length  $\xi$  is calculated, both analytically and numerically, as a function of frequency. The dispersion relation is also shown in Fig. 6.2a. It is important to point out that the agreement between the analytical and numerical calculations is very good, except when  $g$  approach 0 or  $\pi$ . This is due to the fact that, in the analytical derivation of the Lyapunov exponent, the recurrence equation (6.48) is ill defined at these points, so that the distribution of random variables is not uniform. Remarkably, Fig. 6.2b reveals that in the impedance matching regime,  $\xi$  does not follow the well-known asymptotic power law  $\omega^{-2}$  behaviour for low frequencies. Rather,  $\xi$  exhibits a periodic dependence on  $\omega$  for low frequencies, a result that is intrinsically related to the graphene conductivity properties. Indeed, it can be explained by the fact that the linear increase of the wavenumber with frequency is cancelled by the simultaneous decrease of graphene's conductivity (Drude term, see Eq. 6.30), which scales with  $1/\omega$ . The periodicity in  $\xi$  follows from the periodicity in the dispersion relation, shown in Fig. 6.2a. For the lossy and Drude regimes,  $\xi$  approaches the same value as the frequency increases, and the real part of the Drude conductivity goes to zero.

Figure 6.3 shows  $\xi$  as a function of frequency for two different values of the incidence angle  $\theta$ . It reveals that the presence of graphene layers has also an important effect in the so-called Brewster modes in disordered systems. In 1D disordered optical systems, the so-called Brewster modes occur at some specific frequencies and incident angles for which  $\xi$  reaches anomalously high values, larger than the system size [165, 156]. For non-magnetic ( $\mu_1 = \mu_2 = 1$ ) superlattices made of positive refractive-index media, these anomalously delocalised modes arise from the suppression of reflexion at the interfaces of a 1D disordered system illuminated by a TM incident wave [165, 156]. As a result, the system becomes fully transparent. The presence of graphene induces additional reflections at each interface of the superlattice, resulting in an attenuation of this Brewster mode, as it can be seen from fig. 6.4.

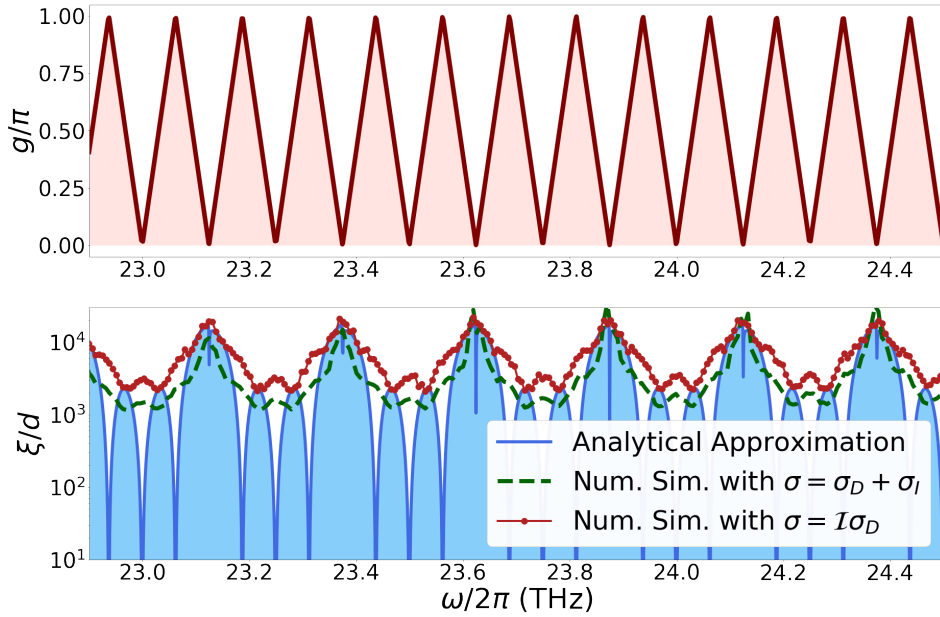


**Figure 6.2.:** (a) Dispersion relation in the impedance matching regime and TM mode. (b) Localization length as a function of frequency with  $\Upsilon_i = 5\mu\text{m}$ ,  $z_i^0 = 1.2\text{mm}$ ,  $E_F = 0.2\text{ eV}$ ,  $\hbar\gamma = 260\mu\text{eV}$ ,  $N = 5000$ ,  $n_{\text{samples}} = 100$ ,  $\varepsilon_1 = \mu_1 = \mu_2 = 1$ ,  $\varepsilon_2 = 3$ ,  $\theta = \pi/3$ . The blue solid line in (b) is the analytical result, whereas the dots and dashed line correspond to two different numerical simulations for different regimes of the optical conductivity of graphene: (i)  $\sigma = \Im m\sigma_D$  (red points) and (ii)  $\sigma = \sigma_D + \sigma_I$  (green dashed line).

#### ATR REGIME IN ONE-LAYERED SYSTEM

The plasmon-polariton mode in graphene can be excited for example, by a prism in the Otto configuration [166]. This is the regime we will explore in this section. We consider a periodic array of graphene/air unit cells (medium 2) in between a dielectric (medium 1). In this case the total transfer matrix  $M$  is obtained considering the

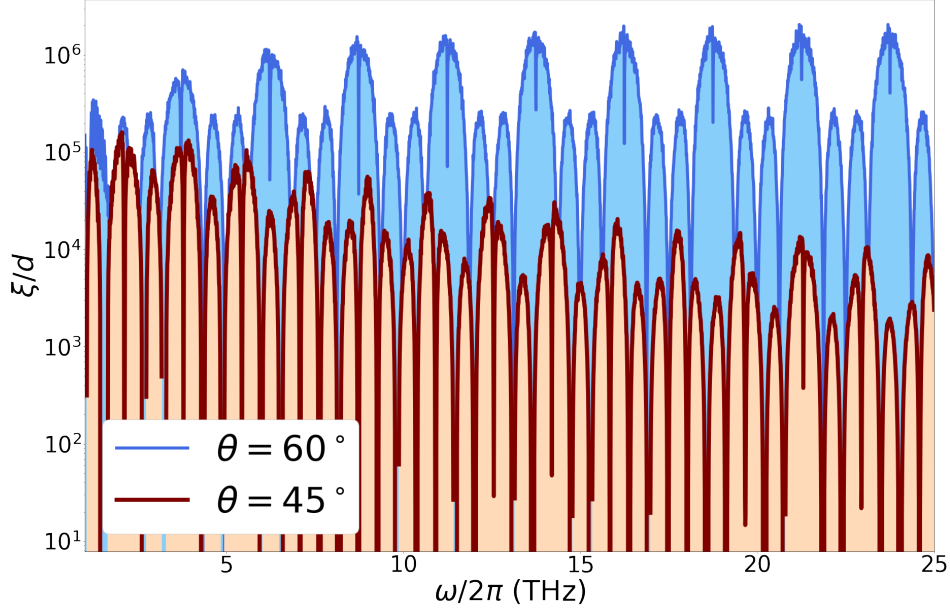


**Figure 6.3.:** Localization length as a function of frequency in the impedance matched regime for two values of incidence angle:  $\theta = 60^\circ$  (blue line),  $\theta = 45^\circ$  (red line).  $\Upsilon_i = 0.5\mu\text{m}$ ,  $z_i^0 = 120\mu\text{m}$ ,  $E_F = 0.2\text{ eV}$ ,  $\hbar\gamma = 0\mu\text{eV}$ ,  $N = 5000$ ,  $n_{\text{samples}} = 100$ .

boundaries between the prism and the superlattice:

$$M = M_{1 \rightarrow 2} \prod_j (M_j) M_{2 \rightarrow 1}, \quad (6.32)$$

where  $M_{1 \rightarrow 2}$  refers to the transfer matrix describing light propagation from the medium 1 (dielectric) to medium 2 (air);  $M_{2 \rightarrow 1}$  refers to the reverse propagation.  $M_j$  is the transfer matrix of the unit cell air/graphene with random widths (medium 2).

From Eq. (G.7) one can see that for the evanescent mode  $\alpha$  is a pure complex number and the first term in the right hand side becomes a hyperbolic cosine, which is greater than 1 for any  $\alpha$ . As a result, the Bloch phase is real only if the second term in the right hand side of G.7 is negative. This situation occurs for pure positive complex  $f$ ; in this case  $\beta$  is also a pure positive complex number, which is only possible in the TM mode [see Eqs. (6.33) and (G.4)].

For an incidence angle  $\theta_1$  above the critical angle for total reflection at the interface 1/2, a plasmon-polariton can be excited, allowing for frustrated total internal reflection. In this case light propagation occurs due to the presence of periodic graphene sheets. The effective impedance in the medium 2 depends on the properties of the layer 1 as:

$$Z_2^{\text{TE}} = i \frac{\kappa}{\mu_2}, \quad Z_2^{\text{TM}} = i \frac{\kappa}{\varepsilon_2}, \quad (6.33)$$

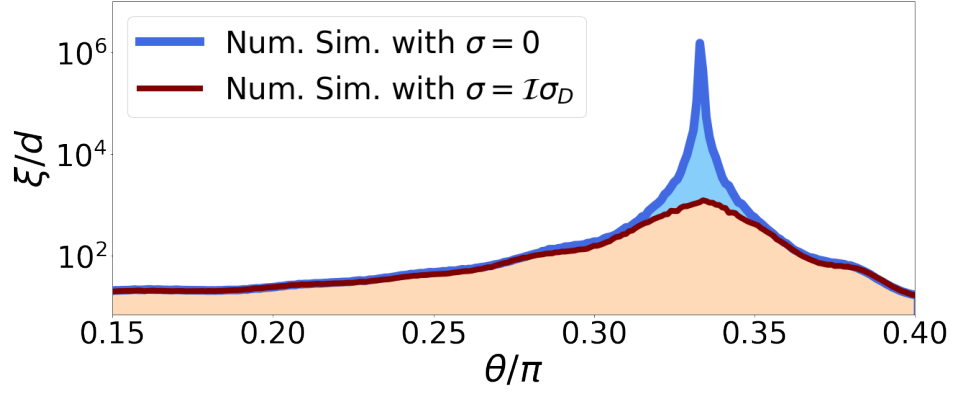


**Figure 6.4.:** Localization length as a function of incidence angle in the impedance matched regime at the vicinities of a Brewster mode.  $\Upsilon_i = 50\mu\text{m}$ ,  $z_i^0 = 120\mu\text{m}$ ,  $N = 5000$ ,  $n_{\text{samples}} = 100$ . The blue line corresponds to the grapheneless case; blue line correspond to the case where graphene is present in the superlattice ( $E_F = 0.2$  eV and  $\hbar\gamma = 0$  eV.)

where

$$\kappa = \sqrt{\varepsilon_1\mu_1 \sin^2 \theta_1 - \varepsilon_2\mu_2}. \quad (6.34)$$

In Fig. 6.5 the localization length is calculated in the ATR regime using both numerical and analytical methods; the agreement is excellent. In the Drude regime  $\xi$  is inversely proportional to the Fermi energy. Also shown is the localization length when the dielectric necessary to excite the ATR field is removed; we call this situation the normal field. The ATR field is characterized by exponentials with argument  $\pm\omega\kappa z/c$ . When the frequency increases and the length  $c/\kappa\omega$  becomes smaller than the width  $z$  of the dielectric slab (air in this case) light propagation comes to a halt, as the plasmon-polariton localized in a graphene layer cannot excite the adjacent layer. We can see that the ATR for the parameters of Fig. 6.5 fills the band gap of the normal field. Also the increase of disorder implies in the decrease of  $\xi$ , as expected.

Notice that ignoring the interband term and making  $E_F = 0$  is equivalent to remove the graphene sheets, therefore making disorder in random widths of air meaningless. Hence the localization length diverges, as can be seen in Eq. (6.25), where  $\sigma \rightarrow 0$  implies in a vanishing Lyapunov exponent.

#### ONE LAYER SYSTEM WITH COMPOSITIONAL DISORDER

In the compositional disorder regime and for the one layered system,  $\xi$  decreases as  $\beta$  increases. For the TE mode,  $\beta$  can only be greater than 1 for materials with magnetic response,  $\mu > 1$ . For the TM mode,  $\beta$  is proportional to the dielectric constant and to  $\cos \theta$ , thus for grazing incidence, the system becomes fully opaque.

In the Drude regime the asymptotic behaviour of the localization length goes as

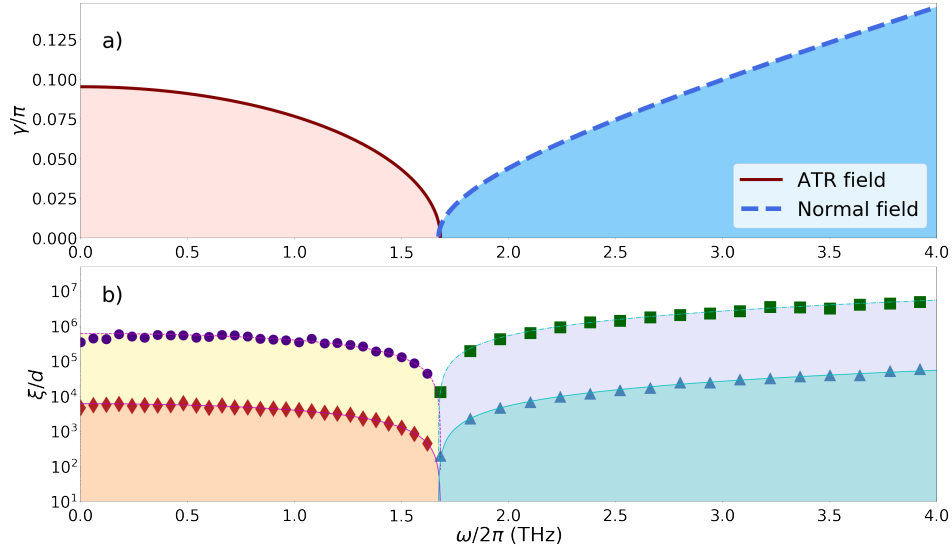


**Figure 6.5.:** (a) Dispersion relation for the ATR regime (red) and for normal field (blue). (b) Localization length as a function of frequency for  $z^0 = 12\mu\text{m}$ ,  $E_F = 0.1$  eV,  $\theta_1 = \pi/3$ ,  $\epsilon_1 = 2, \mu_1 = \mu_2 = \epsilon_1 = 1$ ,  $N = 50000$ ,  $n_{\text{samples}} = 1$ . The purple circles (green squares) and red diamonds (blue triangles) refer to the ATR (normal) field with  $\Upsilon = 0.5\mu\text{m}$  and  $\Upsilon = 5\mu\text{m}$ , respectively. The cyan and red lines refer to the analytical approximation.

$\omega^2$ . This can be understood as follows: as the frequency increases the graphene conductivity decreases as  $\omega^{-1}$  and thus the influence of the graphene layer disappears.

The effect of compositional disorder is shown in Fig. 6.6, where the Fermi energy is randomly distributed around the mean value  $E_F^0 = 0.6$  eV.  $\xi$  is inversely proportional to the mean standard deviation of the Fermi energy. We study the effect of increasing absorption in graphene layers, which depends on the real part of the conductivity and is proportional to the relaxation rate  $\gamma$ . The length  $\xi$  decays rapidly when the frequency reaches  $2\omega_F$ , and interband transitions start to occur, an effect that may be related either to absorption or to Anderson localization. The numerical calculation is performed with the full graphene conductivity (Drude plus interband) and then compared to the case where only the Drude term is present. The analytical approximation is calculated with the Drude term only, and agrees very well with the numerical simulation except at the band edges  $g = 0, \pi/2, \pi$ . As already discussed, this disagreement is related to the fact that the probability distribution of  $\Theta_n$  is not uniform for these values of  $g$ . The analytical approximation has a peak at  $g = \pi/2$  (see denominator of Eq. 6.23). The numerical calculations show that near the band gap ( $g = 0, \pi$  see Eq. 6.23)  $\xi$  goes to zero, and the peak at  $g = \pi/2$  does not occur.

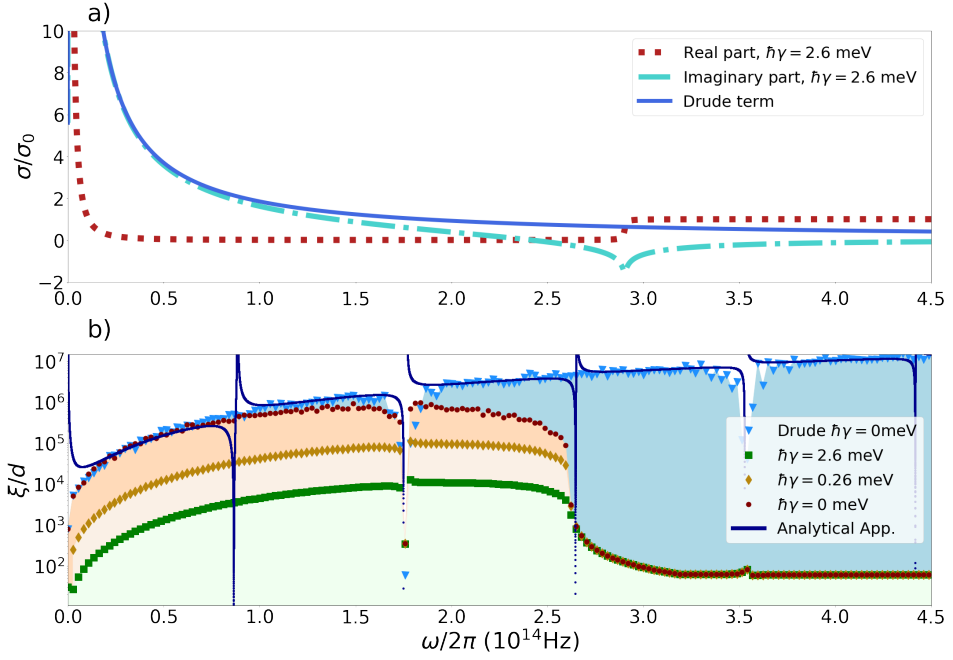


**Figure 6.6.:** (a) Real and imaginary parts of the graphene optical conductivity in the compositional disordered case,  $\sigma = \sigma_D + \sigma_I$ , and the Drude conductivity  $\sigma_D$  when  $\gamma = 0$ . (b) Localization length as a function of frequency with  $z^0 = 1.2\mu\text{m}$ ,  $\theta = \pi/4$ ,  $\varepsilon = \mu = 1$ ,  $E_F^0 = 0.6$  eV,  $\Upsilon_F = 0.12$  eV,  $N = 5000$  and increasing relaxation rate  $\gamma$ .  $\omega_F \approx 3 \times 10^{14}$  Hz. The blue triangles (and solid blue line) refer to a calculation where only the Drude conductivity with  $\gamma = 0$  is used. The other data sets refer to the use of the full optical conductivity of graphene with different  $\gamma$  values.

#### 6.3.4. COMPLEX INTERBAND REGIME WHEN: $\Re\sigma \approx 0$ , $\Im\sigma < 0$

When  $\omega \lesssim 2\omega_F$ , the imaginary part of the optical conductivity of graphene becomes negative and can be approximated by

$$\sigma = \sigma_I'' + i\sigma_0 \frac{4\omega_F}{\pi\omega}, \quad (6.35)$$

where  $\sigma_I''$  is given by Eq. (B.107). In this case the imaginary part of  $\sigma$  becomes negative, and the ratio between the imaginary and real parts of  $\sigma$  becomes lower than in the Drude regime for typical values of  $\gamma$  and  $E_F$ . Therefore, in this case the exponential decay of transmission is essentially due to absorption rather than to Anderson localization. Therefore, in this case, our approach for studying Anderson localization using the localization length is inadequate. It is worth commenting that experimentally it is possible to distinguish between absorption and Anderson localization by investigating the variance of the normalized total transmission, as proposed in Ref. [167]. For a one-layered system in the ATR regime with transfer matrix given by Eq.



(G.6), the change in the sign of  $f$  has qualitatively the same effect in the dispersion relation (G.7) of interchanging TE and TM modes, which changes the sign of  $\beta$ .

When the frequency becomes larger than  $2\omega_F$ , the real part of the conductivity approaches  $\sigma_0$  while the imaginary part vanishes. In this regime, the role of the graphene sheets consists, essentially, in absorbing light leading to a vanishing transmission after few stacks.

## 6.4. Conclusions

In conclusion, we have investigated light propagation in 1D disordered superlattices composed of dielectric stacks and graphene sheets in between. We introduced disorder either in the graphene material parameters (compositional disorder), such as the Fermi energy, or in the widths of the dielectric stacks (structural disorder). For both cases we derived an analytical expression for the localization length  $\xi$  and compared the results with numerical calculations based on the transfer matrix method. A very good agreement between numerics and the analytical expression was found. We demonstrated that, for structural disorder and when the impedances of the layers are equal, the localization length does not follow the well-known asymptotic behaviour  $\xi \propto \omega^{-2}$ . Rather, it exhibits an oscillatory dependence on frequency, as a result of the presence of the Drude term in the graphene conductivity. Also in the impedance matching regime, we show that graphene has an important impact on the Brewster modes, anomalously delocalised modes at given frequencies and incident angles at which  $\xi$  diverges. Indeed, the presence of graphene induces additional reflections inside the disordered medium, leading to a strong attenuation of the Brewster modes. We investigated how intra and interband transitions in the graphene conductivity impact on  $\xi$ , identifying the regimes where Anderson localization and absorption dominates light transmission. Altogether, our findings unveil the role of graphene on Anderson localization of light, paving the way for the design of graphene-based, disordered photonic devices in the THz spectral range.

### 6.A. Matrix transformation

The relation  $\psi^{n+1} = M^n \psi^n$  can be interpreted as a discrete set of points in the phase space  $\psi_R, \psi_L$ . With the transformation  $M_{\text{real}}$ :

$$M_{\text{real}} = \frac{1}{2} \begin{pmatrix} 1 - i & 1 + i \\ -1 + i & 1 + i \end{pmatrix}, \quad (6.36)$$

the matrix  $M_{\text{real}} M^n M_{\text{real}}^{-1}$  is now real, and defining  $\psi'^n = M_{\text{real}} \psi^n$ , we have in the phase space  $\psi'_R, \psi'_L$  that in the system without disorder the trajectory is given by a

ellipse. From this we can find a transformation  $M_{\text{circle}}$  to a circle:

$$M_{\text{circle}} = \begin{pmatrix} v^{-1} \cos \tau & v \sin \tau \\ -v^{-1} \sin \tau & v \cos \tau \end{pmatrix}, \quad (6.37)$$

where:

$$v^2 = -\frac{\sin g}{\cosh \phi_1^0 \sin \phi_2^0 + \sinh \phi_1^0}, \quad (6.38)$$

$$\tau = \frac{\pi}{4} - \frac{\phi_3^0}{2},$$

and making  $[Q \ P]^T = M_{\text{circle}} \psi'$ ,

$$\begin{pmatrix} Q_n \\ P_n \end{pmatrix} = \begin{pmatrix} v^{-1} \cos \tau & v \sin \tau \\ -v^{-1} \sin \tau & v \cos \tau \end{pmatrix} \begin{pmatrix} x_n \\ y_n \end{pmatrix}, \quad (6.39)$$

## 6.B. Lyapunov Exponent

The Lyapunov exponent is given by:

$$\lambda = \frac{1}{2} \left\langle Y_1 + Y_2 \cos 2\Theta_n + Y_3 \sin 2\Theta_n - \frac{1}{4} Y_2^2 - \frac{1}{4} Y_3^2 \right\rangle, \quad (6.40)$$

where

$$Y_1 = \frac{1}{\sin^2 g} [U_1 \delta \phi_1^2 + U_2 \delta \phi_2^2 + U_3 \delta \phi_3^2 + U_4 \delta \phi_1 \delta \phi_2], \quad (6.41)$$

with:

$$U_1 = 2 \sin^2 \phi_2^0, \quad (6.42)$$

$$U_2 = 2 \sinh^2 \phi_1^0 \cos^2 g, \quad (6.43)$$

$$U_3 = 2 \sinh^2 \phi_1^0 \sin^2 g, \quad (6.44)$$

$$U_4 = -\sinh 2\phi_1^0 \sin 2\phi_2^0, \quad (6.45)$$

$$Y_2 = [-2 \sin \phi_2^0 \delta \phi_1 + \cos \phi_2^0 \sinh 2\phi_1^0 (\delta \phi_2 - \delta \phi_3)], \quad (6.46)$$

$$Y_3 = 2 \frac{\sinh \phi_1^0 (\cos^2 g \delta \phi_2 + \sin^2 g \delta \phi_3) - \cos g \sin \phi_2^0 \delta \phi_1}{-\sin g}. \quad (6.47)$$

the angle  $\Theta$  obeys the recurrence equation:

$$\Theta_{n+1} = \Theta_n - g + \epsilon_n \csc g, \quad (6.48)$$

with:

$$\epsilon_n = [\cos g \sinh \phi_1^0 \delta \phi_2 - \sin \phi_2^0 \delta \phi_1] \cos (2\Theta_n - g) + \sinh \phi_1^0 \cos g \sin (2\Theta_n - g) \delta \phi_3. \quad (6.49)$$

## CONCLUDING REMARKS

---

# 7

*“To go past the Bojador, one must go beyond pain”*, as Fernando Pessoa said. During the Middle Ages seafarers believed that beyond the african cape Bojador, the world ended in boiling seas inhabited by monstrous mythic creatures. Only after a series of voyages by brave Portuguese navigators those ungrounded beliefs were dissipated, the Discovery Age began, and slowly all the world would be connected. It is possible to make a parallel with the 2D material field: the Mermin-Wagner theorem stated that phonon fluctuations would destroy any long-range order in a crystalline membrane. However, in 2004, Geim and Novoselov discovered a single atomic layer of carbon from exfoliation of graphite. As the expedition to go beyond the cape Bojador opened the gates for new maritime routes around all the world, the synthesis of graphene started the search for other two-dimensional materials. As a consequence, dozens of new 2D materials were discovered and a lot more were predicted. This recently discovered two-dimensional world can be seen as a playground both to discover new physical effects and to create novel technological devices.

This thesis explored a small bit of this new world, focusing on the relation between light and 2D materials. We went from a microscopic view, studying non-equilibrium distribution in graphene and excitons in transition metal dichalcogenides, to macroscopic properties, the passage of light through a disordered array of dielectrics and graphene sheets. The interplay of quantum and classical description in this field of research is a beautiful way to see that “physics is only one”. The tools developed throughout this thesis are as important as the choice of problems to study. They are not meant to be an end in itself: the author intention is to go far beyond where this thesis finishes in search of uncharted seas. To quote Pessoa again: *“God gave the sea the danger and the abyss, but it was in it that He mirrored the sky”*.

*The Mermin-Wagner theorem is not violated, but bypassed, see ref. [1] for details.*



# A

## TIGHT-BINDING MODEL OF GRAPHENE

---

The graphene tight-binding Hamiltonian, considering nearest neighbors only, in second quantization reads [168]:

$$\hat{H}_0 = \sum_{i,n} t_{\text{TB}} \hat{a}_{\mathbf{R}_n}^\dagger \hat{b}_{\mathbf{R}_n + \delta_i} + \text{h.c.}, \quad (\text{A.1})$$

where  $\hat{a}_{\mathbf{R}_n}^\dagger$  and  $\hat{b}_{\mathbf{R}_n + \delta_i}$  obey anti-commutation relations and  $\delta_i$  are the nearest neighbors vectors connecting an atom in sub-lattice *A* to another one in sub-lattice *B*. We can define the Fourier transform as:

$$\hat{a}_{\mathbf{k}} = \frac{1}{\sqrt{N_c}} \sum_n e^{-i\mathbf{k} \cdot \mathbf{R}_n} \hat{a}_{\mathbf{R}_n}, \quad (\text{A.2a})$$

$$\hat{b}_{\mathbf{k}} = \frac{1}{\sqrt{N_c}} \sum_n e^{-i\mathbf{k} \cdot (\mathbf{R}_n + \delta_i)} \hat{b}_{\mathbf{R}_n + \delta_i}, \quad (\text{A.2b})$$

with the inverse transform:

$$\hat{a}_{\mathbf{R}_n} = \frac{1}{\sqrt{N_c}} \sum_{\mathbf{k} \in 1B.Z.} e^{i\mathbf{k} \cdot \mathbf{R}_n} \hat{a}_{\mathbf{k}}, \quad (\text{A.3a})$$

$$\hat{b}_{\mathbf{R}_n + \delta_i} = \frac{1}{\sqrt{N_c}} \sum_{\mathbf{k} \in 1B.Z.} e^{i\mathbf{k} \cdot (\mathbf{R}_n + \delta_i)} \hat{b}_{\mathbf{k}}, \quad (\text{A.3b})$$

where the sum over *n* is performed over the entire lattice and the sum in *k* is performed over the first Brillouin zone.

After a Bogoliubov transformation the basis that diagonalize  $H_0$  is:

$$\hat{c}_{\mathbf{k}} = \frac{e^{i\varphi_{\mathbf{k}}}}{\sqrt{2}} \left( \hat{a}_{\mathbf{k}} + e^{i\Theta_{\mathbf{k}}} \hat{b}_{\mathbf{k}} \right), \quad (\text{A.4a})$$

$$\hat{d}_{\mathbf{k}} = \frac{e^{i\varphi_{\mathbf{k}}}}{\sqrt{2}} \left( \hat{a}_{\mathbf{k}} - e^{i\Theta_{\mathbf{k}}} \hat{b}_{\mathbf{k}} \right), \quad (\text{A.4b})$$

and the inverse transformation reads:

$$\hat{a}_{\mathbf{k}} = \frac{e^{-i\varphi_{\mathbf{k}}}}{\sqrt{2}} \left( \hat{c}_{\mathbf{k}} + \hat{d}_{\mathbf{k}} \right), \quad (\text{A.5a})$$

$$\hat{b}_{\mathbf{k}} = \frac{e^{-i\varphi_{\mathbf{k}}} e^{-i\Theta_{\mathbf{k}}}}{\sqrt{2}} \left( \hat{c}_{\mathbf{k}} - \hat{d}_{\mathbf{k}} \right), \quad (\text{A.5b})$$

where  $\varphi_{\mathbf{k}}$  is a global arbitrary phase. The phase  $\Theta_{\mathbf{k}}$  is the argument of

$$\phi_{\mathbf{k}} = \sum_{i=1}^3 e^{i\mathbf{k} \cdot \boldsymbol{\delta}_i}, \quad (\text{A.6})$$

that is,  $\Theta_{\mathbf{k}} = \arg \phi_{\mathbf{k}}$ . In the basis (A.4) the Hamiltonian  $H_0$  is written as:

$$\hat{H}_0 = \sum_{\mathbf{k}} E_{\mathbf{k}} \left( \hat{c}_{\mathbf{k}}^\dagger \hat{c}_{\mathbf{k}} - \hat{d}_{\mathbf{k}}^\dagger \hat{d}_{\mathbf{k}} \right). \quad (\text{A.7})$$

where the eigenvalue is:

$$E_{\mathbf{k}} = t_{\text{TB}} |\phi(\mathbf{k})|. \quad (\text{A.8})$$

For writing the interaction term with the electric field,  $\hat{H}_I = e\mathbf{E} \cdot \hat{\mathbf{R}}$ , we need the position operator written as:

$$\hat{\mathbf{R}}_A = \sum_n \mathbf{R}_n \hat{a}_{\mathbf{R}_n}^\dagger \hat{a}_{\mathbf{R}_n}, \quad (\text{A.9a})$$

$$\hat{\mathbf{R}}_B = \sum_n (\mathbf{R}_n + \boldsymbol{\delta}_1) \hat{b}_{\mathbf{R}_n + \boldsymbol{\delta}_1}^\dagger \hat{b}_{\mathbf{R}_n + \boldsymbol{\delta}_1}, \quad (\text{A.9b})$$

which in the basis given by Eq. (A.4) it reads:

$$\begin{aligned} \mathbf{R} = & -\frac{(2\pi)^2 i}{2N_c a_0^2} \sum_{\mathbf{k}, \mathbf{q}} [\nabla_{\mathbf{q}} \delta(\mathbf{q})] e^{i(\varphi_{\mathbf{k}+\mathbf{q}} - \varphi_{\mathbf{k}})} \left[ \left( 1 + e^{i(\Theta_{\mathbf{k}+\mathbf{q}} - \Theta_{\mathbf{k}})} \right) \left( \hat{c}_{\mathbf{k}+\mathbf{q}}^\dagger \hat{c}_{\mathbf{k}} + \hat{d}_{\mathbf{k}+\mathbf{q}}^\dagger \hat{d}_{\mathbf{k}} \right) + \right. \\ & \left. + \left( 1 - e^{i(\Theta_{\mathbf{k}+\mathbf{q}} - \Theta_{\mathbf{k}})} \right) \left( \hat{c}_{\mathbf{k}+\mathbf{q}}^\dagger \hat{d}_{\mathbf{k}} + \hat{d}_{\mathbf{k}+\mathbf{q}}^\dagger \hat{c}_{\mathbf{k}} \right) \right], \end{aligned} \quad (\text{A.10})$$

where  $\delta(\mathbf{q})$  is the Dirac delta-function of zero momentum. The dipole-coupling Hamiltonian  $\hat{H}_I = e\boldsymbol{\mathcal{E}} \cdot \hat{\mathbf{R}}$  is written as:

$$\hat{H}_I = e\boldsymbol{\mathcal{E}} \cdot \sum_{\mathbf{k}} \left[ i\nabla_{\mathbf{k}} (\hat{n}_{c,\mathbf{k}} + \hat{n}_{v,\mathbf{k}}) + \frac{\nabla_{\mathbf{k}} \Theta_{\mathbf{k}}}{2} (\hat{p}_{cv,\mathbf{k}} + \hat{p}_{vc,\mathbf{k}}) \right], \quad (\text{A.11})$$

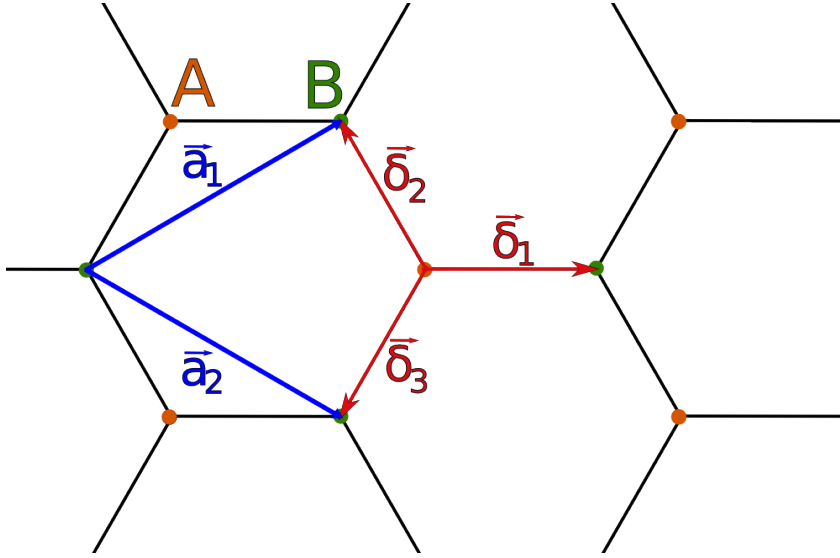


**Figure A.1.:** Graphene crystal lattice. A and B are carbons in different sublattices. The blue vectors  $\vec{a}_1$ ,  $\vec{a}_2$  are primitive vectors and the red vectors  $\vec{\delta}_i$ ,  $i = 1, 2, 3$  are the three possible choices of basis vector.

where we have defined:

$$\hat{n}_{c,\mathbf{k}} = c_{\mathbf{k}}^\dagger c_{\mathbf{k}}, \quad (\text{A.12a})$$

$$\hat{n}_{v,\mathbf{k}} = d_{\mathbf{k}}^\dagger d_{\mathbf{k}}, \quad (\text{A.12b})$$

$$\hat{p}_{cv,\mathbf{k}} = c_{\mathbf{k}}^\dagger d_{\mathbf{k}}, \quad (\text{A.12c})$$

$$\hat{p}_{vc,\mathbf{k}} = d_{\mathbf{k}}^\dagger c_{\mathbf{k}}, \quad (\text{A.12d})$$

$$\varphi_{\mathbf{k}+\mathbf{q}} = -\frac{\Theta_{\mathbf{k}+\mathbf{q}}}{2}. \quad (\text{A.12e})$$

### EXPRESSIONS FOR THE GRADIENT OF THE PHASE $\Theta_{\mathbf{k}}$

In this subsection we present some useful functions that appear in the Chapter 4. First we recall the function defined in Eq. (A.6):

$$\phi_{\mathbf{k}} = \sum_{j=1}^3 e^{i\mathbf{k} \cdot \vec{\delta}_j}, \quad (\text{A.13})$$

where we have used the following choice of vectors for the orientation of the nearest neighbor hopping (see Fig. A.1):

$$\delta_1 = a_0(1, 0), \quad (\text{A.14a})$$

$$\delta_2 = a_0/2 \left( -1, -\sqrt{3} \right), \quad (\text{A.14b})$$

$$\delta_3 = a_0/2 \left( -1, \sqrt{3} \right). \quad (\text{A.14c})$$

With this choice of vectors, the eigenvalues of  $H_0$  are the solution of:

$$\left( \frac{E_{\mathbf{k}}}{t_{TB}} \right)^2 = 1 + 4 \cos \left( \frac{3}{2} k_x \right) \cos \left( \frac{\sqrt{3}}{2} k_y \right) + 4 \cos^2 \left( \frac{\sqrt{3}}{2} k_y \right), \quad (\text{A.14d})$$

and the  $\Theta_{\mathbf{k}}$  function (the argument of  $\phi_{\mathbf{k}}$ ) is written as:

$$\tan \Theta_{\mathbf{k}} = \frac{\sin k_x - 2 \sin \frac{k_x}{2} \cos \frac{\sqrt{3} k_y}{2}}{\cos k_x + 2 \cos \frac{k_x}{2} \cos \frac{\sqrt{3} k_y}{2}}. \quad (\text{A.15})$$

We can calculate  $\nabla_{\mathbf{k}} \Theta_{\mathbf{k}}$  through:

$$\nabla_{\mathbf{k}} \Theta_{\mathbf{k}} = \frac{u \nabla_{\mathbf{k}} v - v \nabla_{\mathbf{k}} u}{E_{\mathbf{k}}^2}, \quad (\text{A.16})$$

where we have split the function  $\phi_{\mathbf{k}}$  in Eq. (A.13) into real and imaginary parts  $\phi_{\mathbf{k}} = u + iv$ . It then follows that we can obtain the components of the gradient of the  $\Theta_{\mathbf{k}}$  function as:

$$\partial_{k_x} \Theta_{\mathbf{k}} = \frac{1 - 2 \cos^2 \left( \frac{\sqrt{3}}{2} k_y \right) + \cos \left( \frac{3}{2} k_x \right) \cos \left( \frac{\sqrt{3}}{2} k_y \right)}{1 + 4 \cos \left( \frac{3}{2} k_x \right) \cos \left( \frac{\sqrt{3}}{2} k_y \right) + 4 \cos^2 \left( \frac{\sqrt{3}}{2} k_y \right)}, \quad (\text{A.17a})$$

$$\partial_{k_y} \Theta_{\mathbf{k}} = \frac{\sqrt{3} \sin \left( \frac{3}{2} k_x \right) \sin \left( \frac{\sqrt{3}}{2} k_y \right)}{1 + 4 \cos \left( \frac{3}{2} k_x \right) \cos \left( \frac{\sqrt{3}}{2} k_y \right) + 4 \cos^2 \left( \frac{\sqrt{3}}{2} k_y \right)}. \quad (\text{A.17b})$$



# B

## GRAPHENE SUSCEPTIBILITY AND OPTICAL CONDUCTIVITY

---

In this appendix we calculate explicitly the bare graphene susceptibility and from this the optical conductivity.

The susceptibility in graphene, considering that electronic excitations are described by the massless 2D Dirac equation, is given by [15]:

$$\chi(\mathbf{q}, \omega) = \sum_{\alpha, \alpha' = \pm} \chi^{\alpha\alpha'}(\mathbf{q}, \omega), \quad (\text{B.1})$$

where:

$$\chi^{\alpha\alpha'}(\mathbf{q}, \omega) = 4 \int \frac{d^2\mathbf{k}}{4\pi^2} \frac{n_F(\alpha E_{\mathbf{k}}) - n_F(\alpha' E_{\mathbf{k}+\mathbf{q}})}{\hbar\omega + \alpha E_{\mathbf{k}} - \alpha' E_{\mathbf{k}+\mathbf{q}} + i\eta} F_{\alpha\alpha'}(\mathbf{q}, \mathbf{k}) \quad (\text{B.2})$$

with  $\alpha, \alpha' = +, -$  labeling the conductance and valence bands,  $n_F$  is the Fermi-Dirac distribution and the limit  $\eta \rightarrow 0$  is implicit. We define the overlap of graphene wavefunctions as:

$$F_{\alpha\alpha'}(\mathbf{q}, \mathbf{k}) = \frac{1}{2} \left( 1 + \alpha\alpha' \frac{k^2 + \mathbf{k} \cdot \mathbf{q}}{k|\mathbf{k} + \mathbf{q}|} \right), \quad (\text{B.3})$$

$$n_F(E) = [\exp(\beta(E - \mu)) + 1]^{-1}, \quad (\text{B.4})$$

now we consider  $\mu > 0$  and  $T = 0$ , that implies  $n_F(E) \rightarrow \theta(E - \mu)$ , with  $\theta$  the Heaviside step function.

We define:

$$\chi_U^{\alpha\alpha'}(\mathbf{q}, \omega) = 4 \int \frac{d^2\mathbf{k}}{4\pi^2} \frac{1}{\alpha'\omega - E_{\mathbf{k}} - E_{\mathbf{k}+\mathbf{q}} + i\eta} F_{+-}(\mathbf{q}, \mathbf{k}), \quad (\text{B.5})$$

with  $\alpha \neq \alpha'$ . and is given by:

$$\chi_U(\mathbf{q}, \omega) = \chi_U^{+-}(\mathbf{q}, \omega) + \chi_U^{-+}(\mathbf{q}, \omega), \quad (\text{B.6})$$

where  $\chi_U$  is the susceptibility when  $\mu = 0$ . We define  $\chi_D$  as

$$\chi_D(\mathbf{q}, \omega) = \chi_D(\mathbf{q}, \omega) - \chi_U(\mathbf{q}, \omega). \quad (\text{B.7})$$

The susceptibility can be split in doped and undoped parts:

$$\chi(\mathbf{q}, \omega) = \chi_D(\mathbf{q}, \omega) + \chi_U(\mathbf{q}, \omega), \quad (\text{B.8})$$

now before we proceed to calculate each piece of the susceptibility we recall the Sokhotski-Plemelj formula:

$$\frac{1}{x \pm i\eta} = \mathcal{P} \frac{1}{x} \mp i\pi\delta(x), \quad (\text{B.9})$$

this can be used to separate the real and imaginary part of the integration of a real function as:

$$\mathcal{G} = \int dx \frac{f(x)}{x \pm i\eta} = \mathcal{P} \int dx \frac{f(x)}{x} \mp i\pi f(x), \quad (\text{B.10})$$

and so the real part is:

$$\Re \mathcal{G} = \mathcal{P} \int dx \frac{f(x)}{x} \quad (\text{B.11})$$

and the imaginary part is:

$$\Im \mathcal{G} = \mp i\pi f(x). \quad (\text{B.12})$$

From now we will hide the  $(\mathbf{q}, \omega)$  dependence of the susceptibility.

## B.1. Undoped susceptibility

### IMAGINARY PART

The imaginary part of  $\chi_U^{+-}$  is null and the imaginary part of  $\chi_U^{-+}$  is given by:

$$\Im \chi_U = -\pi \int \frac{kdkd\theta}{\pi^2} \delta(\omega - k - |\mathbf{k} + \mathbf{q}|) F_{-+}(\mathbf{q}, \mathbf{k}), \quad (\text{B.13})$$

where we used the Sokhotski-Plemelj theorem. First we perform the integral in  $\theta$  and we arrive:

$$\Im I \chi_U = \int_{\frac{q+\omega}{2}}^{\omega} \frac{kdk}{\pi} \frac{2|\omega - k|\theta(q - \omega)}{\sqrt{4k^2q^2 - (\omega^2 - 2k\omega - q^2)^2}} \left( \frac{2k^2 + \omega^2 - 2k\omega - q^2}{2k(\omega - k)} - 1 \right), \quad (\text{B.14})$$

$$\Im I \chi_U = \int_{\frac{\omega-q}{2}}^{\frac{q+\omega}{2}} \frac{kdk}{\pi} \frac{2|\omega - k|\theta(\omega - q)}{\sqrt{4k^2q^2 - (\omega^2 - 2k\omega - q^2)^2}} \left( \frac{2k^2 + \omega^2 - 2k\omega - q^2}{2k(\omega - k)} - 1 \right), \quad (\text{B.15})$$

where we used also  $\omega - k = |\mathbf{k} + \mathbf{q}|$ . A factor of 2 appear because of there's two solutions of the Dirac delta zero in the trigonometric plane. The first integral (B.14) is null because necessary  $\omega < (q + \omega)/2$ .

The above integrals can be simplified to

$$\Im\chi_U = 0, q > \omega, \quad (\text{B.16a})$$

$$\Im\chi_U = -\frac{1}{\pi} \int_{\frac{\omega-q}{2}}^{\frac{q+\omega}{2}} dk \frac{q^2 - \omega^2 + 4k\omega - 4k^2}{\sqrt{(\omega^2 - q^2)(q^2 - \omega^2 + 4k\omega - 4k^2)}}, q < \omega, \quad (\text{B.16b})$$

and Eq. (B.16b) can be simplified:

$$\Im\chi_U = -\frac{1}{\pi\sqrt{\omega^2 - q^2}} \int_{\frac{\omega-q}{2}}^{\frac{q+\omega}{2}} dk \sqrt{q^2 - \omega^2 + 4k\omega - 4k^2}, q < \omega, \quad (\text{B.17})$$

and after performing the integral, we have finally:

$$\begin{aligned} \Im\chi_U &= 0, q > \omega, \\ \Im\chi_U &= -\frac{q^2}{4\sqrt{\omega^2 - q^2}}, q < \omega. \end{aligned} \quad (\text{B.18a})$$

### REAL PART

To obtain the real part of the susceptibility we use the Kramers-Kronig relation:

$$\Re\chi_x = \frac{2}{\pi} \mathcal{P} \int_0^\infty d\omega' \frac{\omega' \Im\chi_x(\mathbf{q}, \omega')}{\omega'^2 - \omega^2}, \quad (\text{B.19})$$

that is valid for both components  $x = U, D$ . Using equation (B.18a) we have:

$$\Re\chi_U = -\frac{q^2}{2\pi} \mathcal{P} \int_q^\infty d\omega' \frac{\omega'}{\omega'^2 - \omega^2} \frac{1}{\sqrt{\omega'^2 - q^2}}, \quad (\text{B.20})$$

making the change of variables  $x = \omega'^2 - \omega^2$  with  $dx = 2\omega' d\omega'$  we have:

$$\Re\chi_U = -\frac{q^2}{4\pi} \mathcal{P} \int_{q^2 - \omega^2}^\infty dx \frac{1}{x} \frac{1}{\sqrt{x + \omega^2 - q^2}}, \quad (\text{B.21})$$

if  $q > \omega$  then we can make  $x = (q^2 - \omega^2)y$  and

$$\Re\chi_U = -\frac{q^2}{4\pi\sqrt{q^2 - \omega^2}} \mathcal{P} \int_1^\infty dy \frac{1}{y} \frac{1}{\sqrt{y-1}}, \quad (\text{B.22})$$

and

$$\Re\chi_U = -\frac{q^2}{4\sqrt{q^2 - \omega^2}}, \text{ if } q > \omega, \quad (\text{B.23})$$

else

$$\Re\chi_U = 0, \text{ if } q < \omega. \quad (\text{B.24})$$

We can combine the real and imaginary part in a single expression:

$$\chi_U = -\frac{q^2 \text{Sign}[q - \omega]}{4\sqrt{q^2 - \omega^2}}. \quad (\text{B.25})$$

where we use the convention  $\sqrt{-x} = i\sqrt{x}$  for  $x > 0$ .

## B.2. Contribution from the Fermi sea

First we start with the intraband term:

$$\chi_D^{++} = 4 \int \frac{d^2\mathbf{k}}{4\pi^2} \frac{n_F(E_{\mathbf{k}}) - n_F(E_{\mathbf{k}+\mathbf{q}})}{\omega + E_{\mathbf{k}} - E_{\mathbf{k}+\mathbf{q}} + i\eta} F_{++}(\mathbf{q}, \mathbf{k}), \quad (\text{B.26})$$

splitting the above integral in two:

$$\begin{aligned} \chi_D^{++} = \chi_D^{\text{intra1}} + \chi_D^{\text{intra2}} &= 4 \int \frac{d^2\mathbf{k}}{4\pi^2} \frac{n_F(E_{\mathbf{k}})}{\omega + E_{\mathbf{k}} - E_{\mathbf{k}+\mathbf{q}} + i\eta} F_{++}(\mathbf{q}, \mathbf{k}) + \\ &4 \int \frac{d^2\mathbf{k}}{4\pi^2} \frac{-n_F(E_{\mathbf{k}+\mathbf{q}})}{\omega + E_{\mathbf{k}} - E_{\mathbf{k}+\mathbf{q}} + i\eta} F_{++}(\mathbf{q}, \mathbf{k}), \end{aligned} \quad (\text{B.27})$$

and making in the second integral  $\mathbf{k} \rightarrow \mathbf{k} - \mathbf{q}$  we have:

$$\chi_D^{\text{intra2}} = 4 \int \frac{d^2\mathbf{k}}{4\pi^2} \frac{-n_F(E_{\mathbf{k}})}{\omega + E_{\mathbf{k}-\mathbf{q}} - E_{\mathbf{k}} + i\eta} F_{++}(\mathbf{q}, \mathbf{k} - \mathbf{q}), \quad (\text{B.28})$$

but

$$\begin{aligned} F_{\alpha\alpha'}(\mathbf{q}, \mathbf{k} - \mathbf{q}) &= \frac{1}{2} \left( 1 + \alpha\alpha' \frac{|\mathbf{k} - \mathbf{q}|^2 + (\mathbf{k} - \mathbf{q}) \cdot \mathbf{q}}{|\mathbf{k} - \mathbf{q}|k} \right) \\ &= \frac{1}{2} \left( 1 + \alpha\alpha' \frac{k^2 - \mathbf{k} \cdot \mathbf{q}}{k|\mathbf{k} - \mathbf{q}|} \right) = F_{\alpha\alpha'}(\mathbf{q}, -\mathbf{k}), \end{aligned} \quad (\text{B.29})$$

making  $k \rightarrow -k$  in (B.28) and using  $E_{\mathbf{k}} = E_{-\mathbf{k}}$  we arrive at:

$$\chi_D^{\text{intra2}} = 4 \int \frac{d^2\mathbf{k}}{4\pi^2} \frac{-n_F(E_{\mathbf{k}})}{\omega + E_{\mathbf{k}+\mathbf{q}} - E_{\mathbf{k}} + i\eta} F_{++}(\mathbf{q}, \mathbf{k}), \quad (\text{B.30})$$

$$\chi_D^{\text{intra1}} = 4 \int \frac{d^2\mathbf{k}}{4\pi^2} \frac{n_F(E_{\mathbf{k}})}{\omega + E_{\mathbf{k}} - E_{\mathbf{k}+\mathbf{q}} + i\eta} F_{++}(\mathbf{q}, \mathbf{k}). \quad (\text{B.31})$$

The interband part is:

$$\chi_D^{+-} = 4 \int \frac{d^2\mathbf{k}}{4\pi^2} \frac{n_F(E_{\mathbf{k}})}{\omega + E_{\mathbf{k}} + E_{\mathbf{k}+\mathbf{q}} + i\eta} F_{+-}(\mathbf{q}, \mathbf{k}), \quad (\text{B.32})$$

and

$$\chi_D^{-+} = 4 \int \frac{d^2\mathbf{k}}{4\pi^2} \frac{-n_F(E_{\mathbf{k}+\mathbf{q}})}{\omega - E_{\mathbf{k}} - E_{\mathbf{k}+\mathbf{q}} + i\eta} F_{-+}(\mathbf{q}, \mathbf{k}), \quad (\text{B.33})$$

using the same trick of the intraband part, the integral in (B.33) becomes:

$$\chi_D^{-+} = -4 \int \frac{d^2\mathbf{k}}{4\pi^2} \frac{n_F(E_{\mathbf{k}})}{\omega - E_{\mathbf{k}+\mathbf{q}} - E_{\mathbf{k}} + i\eta} F_{+-}(\mathbf{q}, \mathbf{k}), \quad (\text{B.34})$$

we sum B.32 and B.31 to obtain  $\chi_D^1$ , B.34 and B.30 to obtain  $\chi_D^2$ :

$$\chi_D^1 = \frac{1}{\pi^2} \int_0^{2\pi} d\theta \int_0^{k_F} dk \frac{2k^2 + k\omega + kq \cos \theta}{\omega^2 + 2\omega k - q^2 - 2kq \cos \theta + i\eta}, \quad (\text{B.35})$$

$$\chi_D^2 = -\frac{1}{\pi^2} \int_0^{2\pi} d\theta \int_0^{k_F} dk \frac{k\omega - 2k^2 - kq \cos \theta}{\omega^2 - 2\omega k - q^2 - 2kq \cos \theta + i\eta \text{Sign}(\omega - k)}, \quad (\text{B.36})$$

using the Sokhotski-Plemelj theorem we can calculate the complex part as:

$$\Im I \chi_D^1(\mathbf{q}, \omega) = - \int_0^{2\pi} \frac{d\theta}{\pi} \int_0^{k_F} dk [2k^2 + k\omega + kq \cos \theta] \delta(\omega^2 + 2\omega k - q^2 - 2kq \cos \theta), \quad (\text{B.37})$$

$$\Im I \chi_D^2(\mathbf{q}, \omega) = \int_0^{2\pi} \frac{d\theta}{\pi} \int_0^{k_F} dk [k\omega - 2k^2 - kq \cos \theta] \delta(\omega^2 - 2\omega k - q^2 - 2kq \cos \theta) \times \\ \times \text{Sign}(\omega - k), \quad (\text{B.38})$$

the  $\delta$  integral can be performed in the angle variable  $\theta$ , resulting in:

$$\Im I \chi_D^1 = -\frac{2}{2\pi} \int_0^{k_F} dk \frac{4k^2 + 2k\omega + A_+}{\sqrt{B^2 - A_+^2}} G_1(k), \quad (\text{B.39})$$

$$\Im I \chi_D^2 = \frac{2}{2\pi} \int_0^{k_F} dk \frac{2k\omega - 2k^2 - A_-}{\sqrt{B^2 - A_-^2}} G_2(k) \text{Sign}(\omega - k) \quad (\text{B.40})$$

where we used:

$$\cos \theta = \frac{A_{\pm}}{B} \quad (\text{B.41})$$

and:

$$A_{\pm} = \omega^2 \pm 2k\omega - q^2, \quad B = 2kq, \quad (\text{B.42})$$

$$G_i(k) = \begin{cases} 1, & \text{if } k \text{ solve the } \delta \text{ function} \\ 0, & \text{otherwise} \end{cases} \quad (\text{B.43})$$

after some algebra we can write:

$$\Im\chi_D^1 = \frac{2}{2\pi} \int_0^{k_F} dk \frac{q^2 - (2k + \omega)^2}{\sqrt{(\omega^2 - q^2)(q^2 - (2k + \omega)^2)}} G_1(k), \quad (\text{B.44})$$

$$\Im\chi_D^2 = \frac{1}{\pi} \int_0^{k_F} dk \frac{q^2 - (\omega - 2k)^2}{\sqrt{(\omega^2 - q^2)(q^2 - (2k - \omega)^2)}} G_2(k) \text{Sign}(\omega - k) \quad (\text{B.45})$$

### CALCULATION OF $\Im\chi_D^1$

For  $q > \omega > q - 2k_F$ :

$$\Im\chi_D^1 = -\frac{1}{\pi\sqrt{q^2 - \omega^2}} \int_{\frac{q-\omega}{2}}^{k_F} dk \sqrt{(2k + \omega)^2 - q^2}, \quad (\text{B.46})$$

that results in:

$$\Im\chi_D^1 = -\frac{q^2}{4\pi\sqrt{q^2 - \omega^2}} \left[ -\text{acosh}\left(\frac{2k_F + \omega}{q}\right) + \frac{2k_F + \omega}{q} \sqrt{\left(\frac{\omega + 2k_F}{q}\right)^2 - 1} \right], \quad (\text{B.47})$$

otherwise is null.

### CALCULATION OF $\Im\chi_D^2$

First for  $\omega > q$ :

$$\Im\chi_D^2 = \frac{1}{\pi\sqrt{\omega^2 - q^2}} \int_{\frac{\omega-q}{2}}^{k_F} dk \sqrt{q^2 - (\omega - 2k)^2} \theta(\omega + q - 2k) \text{Sign}(\omega - k), \quad (\text{B.48})$$

if  $2k_F > \omega + q$  then  $\text{Sign}(\omega - k) = +1$  and:

$$\Im\chi_D^2 = \frac{q^2}{4\sqrt{\omega^2 - q^2}}, \quad (\text{B.49})$$

else if  $\omega - q < 2k_F$  and  $\omega + q > 2k_F$ :

$$\Im\chi_D^2 = \frac{q^2}{4\pi\sqrt{\omega^2 - q^2}} \left( \frac{\pi}{2} + \arcsin\left(\frac{2k_F - \omega}{q}\right) + \frac{2k_F - \omega}{q} \sqrt{1 - \left(\frac{\omega - 2k_F}{q}\right)^2} \right), \quad (\text{B.50})$$

after some trigonometric steps we can write:

$$\Im\chi_D^2 = \frac{q^2}{4\pi\sqrt{\omega^2 - q^2}} \left( \pi - \arccos\left(\frac{2k_F - \omega}{q}\right) + \frac{2k_F - \omega}{q} \sqrt{1 - \left(\frac{\omega - 2k_F}{q}\right)^2} \right). \quad (\text{B.51})$$

For  $q > \omega$  and  $2k_F > \omega + q$ :

$$\Im\chi_D^2 = \frac{1}{\pi\sqrt{q^2 - \omega^2}} \int_{\frac{\omega+q}{2}}^{k_F} dk \sqrt{(\omega - 2k)^2 - q^2}, \quad (\text{B.52})$$

that results:

$$\Im\chi_D^2 = \frac{q^2}{4\pi\sqrt{q^2 - \omega^2}} \left( \frac{2k_F - \omega}{q} \sqrt{\left(\frac{2k_F - \omega}{q}\right)^2 - 1} - \operatorname{arcosh}\left(\frac{2k_F - \omega}{q}\right) \right), \quad (\text{B.53})$$

otherwise is null.

### REAL PART

The real part is given by the Cauchy principal value of the expressions (B.35) and (B.36):

$$\Re\chi_D^1 = \frac{1}{\pi^2} \mathcal{P} \int_0^{2\pi} d\theta \int_0^{k_F} dk \frac{2k^2 + k\omega + kq \cos \theta}{\omega^2 + 2\omega k - q^2 - 2kq \cos \theta}, \quad (\text{B.54})$$

$$\Re\chi_D^2 = -\frac{1}{\pi^2} \mathcal{P} \int_0^{2\pi} d\theta \int_0^{k_F} dk \frac{k\omega - 2k^2 - kq \cos \theta}{\omega^2 - 2\omega k - q^2 - 2kq \cos \theta}, \quad (\text{B.55})$$

the above numerators can be written as a

$$2k^2 + k\omega + kq \cos \theta = \frac{q^2 - \omega^2}{2} - \omega k + kq \cos \theta + \frac{\omega^2 - q^2 + 4k^2 + 4k\omega}{2}, \quad (\text{B.56})$$

$$k\omega - 2k^2 - kq \cos \theta = \frac{\omega^2 - q^2}{2} - \omega k - kq \cos \theta + \frac{q^2 - \omega^2 + 4\omega k - 4k^2}{2}, \quad (\text{B.57})$$

and B.54 and B.55 become:

$$\Re\chi_D^1 = \frac{1}{2\pi^2} \mathcal{P} \int_0^{2\pi} d\theta \int_0^{k_F} dk \left[ \frac{\omega^2 - q^2 + 4k^2 + 4k\omega}{\omega^2 + 2\omega k - q^2 - 2kq \cos \theta} - 1 \right], \quad (\text{B.58})$$

$$\Re\chi_D^2 = -\frac{1}{2\pi^2} \mathcal{P} \int_0^{2\pi} d\theta \int_0^{k_F} dk \left[ \frac{q^2 - \omega^2 + 4\omega k - 4k^2}{\omega^2 - 2\omega k - q^2 - 2kq \cos \theta} + 1 \right] \quad (\text{B.59})$$

and

$$\Re\chi_D^1 = \frac{1}{2\pi^2} \left[ -2\pi k_F + \mathcal{P} \int_0^{2\pi} d\theta \int_0^{k_F} dk \frac{(2k + \omega)^2 - q^2}{\omega^2 + 2\omega k - q^2 - 2kq \cos \theta} \right], \quad (\text{B.60})$$

$$\Re\chi_D^2 = -\frac{1}{2\pi^2} \left[ 2\pi k_F + \mathcal{P} \int_0^{2\pi} d\theta \int_0^{k_F} dk \frac{q^2 - (\omega - 2k)^2}{\omega^2 - 2\omega k - q^2 - 2kq \cos \theta} \right], \quad (\text{B.61})$$

integrating in  $\theta$  we have:

$$\begin{aligned} \Re\chi_D^1 = \frac{1}{2\pi^2} & \left[ -2\pi k_F + 2\pi\theta(\omega - q) \int_0^{k_F} dk \frac{(2k + \omega)^2 - q^2}{\sqrt{(\omega^2 + 2\omega k - q^2)^2 - 4k^2 q^2}} + \right. \\ & \left. + 2\pi\theta(q - \omega) \int_0^{k_2} dk \frac{(2k + \omega)^2 - q^2}{\sqrt{(\omega^2 + 2\omega k - q^2)^2 - 4k^2 q^2}} \text{sign}(2k + \omega - q) \right], \quad (\text{B.62}) \end{aligned}$$

$$\begin{aligned} \Re\chi_D^2 = \frac{1}{2\pi^2} & \left[ -2\pi k_F - 2\pi\theta(\omega - q) \int_0^{k_1} + \int_{k_2}^{k_F} dk \frac{q^2 - (\omega - 2k)^2}{\sqrt{(\omega^2 - 2\omega k - q^2)^2 - 4k^2 q^2}} + \right. \\ & \left. - 2\pi\theta(q - \omega) \int_0^{k_2} dk \frac{q^2 - (\omega - 2k)^2}{\sqrt{(\omega^2 - 2\omega k - q^2)^2 - 4k^2 q^2}} \text{sign}(2k - \omega - q) \right] \quad (\text{B.63}) \end{aligned}$$

where  $k_1 = \min(|\omega - q|/2, k_F)$ ,  $k_2 = \min((\omega + q)/2, k_F)$ . We can rework the above integrals to:

$$\begin{aligned} \Re\chi_D^1 = \frac{1}{2\pi^2} & \left[ -2\pi k_F + \frac{2\pi\theta(\omega - q)}{\sqrt{\omega^2 - q^2}} \int_0^{k_F} dk \sqrt{(2k + \omega)^2 - q^2} + \right. \\ & \left. - \frac{2\pi\theta(q - \omega)}{\sqrt{q^2 - \omega^2}} \int_0^{k_1} dk \sqrt{q^2 - (2k + \omega)^2} \text{sign}(2k + \omega - q) \right], \quad (\text{B.64}) \end{aligned}$$

$$\begin{aligned} \Re\chi_D^2 = \frac{1}{2\pi^2} & \left[ -2\pi k_F + \frac{2\pi\theta(\omega - q)}{\sqrt{\omega^2 - q^2}} \int_0^{k_1} + \int_{k_2}^{k_F} dk \sqrt{(2k - \omega)^2 - q^2} \right. \\ & \left. - \frac{2\pi\theta(q - \omega)}{\sqrt{q^2 - \omega^2}} \int_0^{k_2} dk \sqrt{q^2 - (2k - \omega)^2} \text{sign}(2k - \omega - q) \right]. \quad (\text{B.65}) \end{aligned}$$

Integrating we arrive at the final expressions for the real part of the susceptibility:

$$\begin{aligned} \Re\chi_D^1 = -\frac{k_F}{\pi} + \frac{q^2}{4\pi\sqrt{\omega^2 - q^2}} & \left[ F\left(\frac{2k_F + \omega}{q}\right) - F\left(\frac{\omega}{q}\right) \right] \theta(\omega - q) + \\ & + \frac{q^2}{4\pi\sqrt{q^2 - \omega^2}} \left[ F_2\left(\frac{2k_1 + \omega}{q}\right) - F_2\left(\frac{\omega}{q}\right) \right] \theta(q - \omega), \quad (\text{B.66}) \end{aligned}$$

If  $2k_F < \omega - q$ :

$$\Re\chi_D^2 = -\frac{k_F}{\pi} + \frac{q^2}{4\pi\sqrt{\omega^2 - q^2}} \left[ F\left(\frac{\omega}{q}\right) - F\left(\frac{\omega - 2k_F}{q}\right) \right]. \quad (\text{B.67})$$



If  $\omega - q < 2k_F < \omega + q$ :

$$\Re\chi_D^2 = -\frac{k_F}{\pi} + \frac{q^2}{4\pi\sqrt{\omega^2 - q^2}} F\left(\frac{\omega}{q}\right). \quad (\text{B.68})$$

If  $2k_F > \omega + q$ :

$$\Re\chi_D^2 = -\frac{k_F}{\pi} + \frac{q^2}{4\pi\sqrt{\omega^2 - q^2}} \left[ F\left(\frac{\omega}{q}\right) - F\left(\frac{2k_F - \omega}{q}\right) \right], \quad (\text{B.69})$$

and if  $q > \omega$

$$\Re\chi_D^2 = -\frac{k_F}{\pi} + \frac{q^2}{4\pi\sqrt{q^2 - \omega^2}} \left[ F_2\left(\frac{2k_F - \omega}{q}\right) - F_2\left(-\frac{\omega}{q}\right) \right], \quad (\text{B.70})$$

where

$$F(x) = x\sqrt{x^2 - 1} - \text{arcosh}(x), \quad (\text{B.71})$$

$$F_2(x) = x\sqrt{1 - x^2} + \arcsin(x), \quad (\text{B.72})$$

we can rewrite  $F_2$  as:

$$F_2(x) = x\sqrt{1 - x^2} + \frac{\pi}{2} - \arccos(x) = \frac{\pi}{2} + C(x), \quad (\text{B.73})$$

where

$$C(x) = x\sqrt{1 - x^2} - \arccos(x), \quad (\text{B.74})$$

where the image of arccos is defined to be  $[0, \pi]$ .

Summing all the contributions we have for each region in the plane  $(q, \omega)$ , that we separate in six pieces (see Fig. B.1):

1B:  $\omega > q$  and  $\omega + q < 2k_F$

$$\Re\chi_D = -\frac{2k_F}{\pi} + \frac{q^2}{4\pi\sqrt{\omega^2 - q^2}} \left[ F\left(\frac{2k_F + \omega}{q}\right) - F\left(\frac{2k_F - \omega}{q}\right) \right], \quad (\text{B.75})$$

2B:  $\omega > q, \omega + q > 2k_F$  and  $\omega - q < 2k_F$

$$\Re\chi_D = -\frac{2k_F}{\pi} + \frac{q^2}{4\pi\sqrt{\omega^2 - q^2}} \left[ F\left(\frac{2k_F + \omega}{q}\right) \right], \quad (\text{B.76})$$

3B:  $\omega - q > 2k_F$

$$\Re\chi_D = -\frac{2k_F}{\pi} + \frac{q^2}{4\pi\sqrt{\omega^2 - q^2}} \left[ F\left(\frac{2k_F + \omega}{q}\right) - F\left(\frac{\omega - 2k_F}{q}\right) \right], \quad (\text{B.77})$$

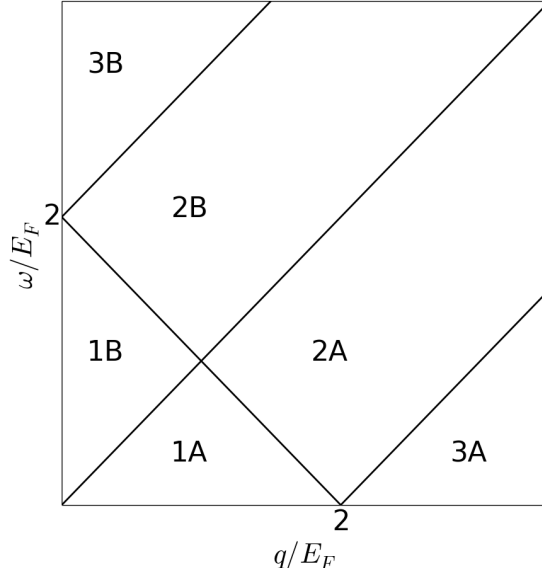


**Figure B.1.:** The analytical integration defines six regions in the  $q \times \omega$  space.

1A:  $q > \omega$  and  $\omega + q < 2k_F$ :

$$\Re\chi_D = -\frac{2k_F}{\pi} + \frac{q^2}{4\sqrt{q^2 - \omega^2}}, \quad (\text{B.78})$$

2A:  $q - 2k_F < \omega < q$  and  $\omega + q > 2k_F$ ,

$$\Re\chi_D = -\frac{2k_F}{\pi} + \frac{q^2}{4\pi\sqrt{q^2 - \omega^2}} \left[ \pi + C\left(\frac{2k_F - \omega}{q}\right) \right], \quad (\text{B.79})$$

3A:  $q - 2k_F > \omega$

$$\Re\chi_D = -\frac{2k_F}{\pi} + \frac{q^2}{4\pi\sqrt{q^2 - \omega^2}} \left[ \pi + C\left(\frac{2k_F + \omega}{q}\right) + C\left(\frac{2k_F - \omega}{q}\right) \right], \quad (\text{B.80})$$

### B.3. Summary

Now summing the undoped and doped contributions, we have for the susceptibility, recovering the units:

**REAL PART****1B:**  $\omega > v_F q$  and  $\omega + v_F q < 2v_F k_F$ 

$$\Re\chi = -\frac{2k_F}{\hbar v_F \pi} + \frac{q^2}{4\pi\hbar\sqrt{\omega^2 - v_F^2 q^2}} \left[ F\left(\frac{2v_F k_F + \omega}{v_F q}\right) - F\left(\frac{2v_F k_F - \omega}{v_F q}\right) \right], \quad (\text{B.81})$$

**2B:**  $\omega > v_F q$ ,  $\omega + v_F q > 2v_F k_F$  and  $\omega - v_F q < 2v_F k_F$ 

$$\Re\chi = -\frac{2k_F}{\hbar v_F \pi} + \frac{q^2}{4\pi\hbar\sqrt{\omega^2 - v_F^2 q^2}} \left[ F\left(\frac{2v_F k_F + \omega}{v_F q}\right) \right], \quad (\text{B.82})$$

**3B:**  $\omega - v_F q > 2v_F k_F$ 

$$\Re\chi = -\frac{2k_F}{\hbar v_F \pi} + \frac{q^2}{4\pi\hbar\sqrt{\omega^2 - v_F^2 q^2}} \left[ F\left(\frac{2v_F k_F + \omega}{v_F q}\right) - F\left(\frac{\omega - 2v_F k_F}{v_F q}\right) \right], \quad (\text{B.83})$$

**1A:**  $v_F q > \omega$  and  $\omega + v_F q < 2v_F k_F$ :

$$\Re\chi = -\frac{2k_F}{\hbar v_F \pi}, \quad (\text{B.84})$$

**2A:**  $q - 2v_F k_F < \omega$ ,  $v_F q > \omega$  and  $\omega + v_F q > 2v_F k_F$ ,

$$\Re\chi = -\frac{2k_F}{\hbar v_F \pi} + \frac{q^2}{4\pi\hbar\sqrt{v_F^2 q^2 - \omega^2}} \left[ C\left(\frac{2v_F k_F - \omega}{v_F q}\right) \right], \quad (\text{B.85})$$

**3A:**  $v_F q - 2v_F k_F > \omega$ 

$$\Re\chi = -\frac{2k_F}{\hbar v_F \pi} + \frac{q^2}{4\pi\hbar\sqrt{v_F^2 q^2 - \omega^2}} \left[ C\left(\frac{2v_F k_F + \omega}{v_F q}\right) + C\left(\frac{2v_F k_F - \omega}{v_F q}\right) \right]. \quad (\text{B.86})$$

**IMAGINARY PART****1B:**

$$\Im\chi = 0, \quad (\text{B.87})$$

**2B:**

$$\Im\chi = \frac{q^2}{4\pi\hbar\sqrt{\omega^2 - v_F^2 q^2}} C\left(\frac{2v_F k_F - \omega}{v_F q}\right), \quad (\text{B.88})$$

**3B:**

$$\Im\chi = -\frac{q^2}{4\hbar\sqrt{\omega^2 - v_F^2 q^2}}, \quad (\text{B.89})$$

1A:

$$\Im\chi = \frac{q^2}{4\pi\hbar\sqrt{v_F^2q^2 - \omega^2}} \left[ F\left(\frac{2v_Fk_F - \omega}{v_Fq}\right) - F\left(\frac{2v_Fk_F + \omega}{v_Fq}\right) \right], \quad (\text{B.90})$$

2A:

$$\Im\chi = -\frac{q^2}{4\pi\hbar\sqrt{v_F^2q^2 - \omega^2}} F\left(\frac{2v_Fk_F + \omega}{v_Fq}\right), \quad (\text{B.91})$$

3A:

$$\Im\chi = 0. \quad (\text{B.92})$$

Equations (B.81–B.92) are ready to use, however, we can put all those equations together into a single expression with the correct analytical continuation:

$$\chi(\mathbf{q}, \omega) = -\frac{2k_F}{\hbar v_F \pi} + \frac{q^2}{\hbar} S(\omega^2 - v_F^2 q^2) \left[ \tilde{F}\left(\frac{2v_Fk_F + \omega}{v_Fq}\right) \text{Sign}\left[\frac{2v_Fk_F + \omega}{v_Fq} - 1\right] - \tilde{F}\left(\frac{2v_Fk_F - \omega}{v_Fq}\right) \right], \quad (\text{B.93})$$

where we recovered the units ( $\hbar$  and  $v_F$ ) and  $S(x)$  and  $F(x)$  are functions with image in the complex domain:

$$S(x) = \begin{cases} x^{-\frac{1}{2}} & \text{if } x > 0, \\ -i(-x)^{-\frac{1}{2}} & \text{if } x < 0, \end{cases} \quad (\text{B.94})$$

and

$$\tilde{F}(x) = \begin{cases} F(x), & \text{if } x > 1, \\ -iC(x), & \text{if } 1 > x > -1, \\ i\pi + F(-x), & \text{if } x < -1, \end{cases} \quad (\text{B.95})$$

and  $F(x)$  is defined in Eq. (B.71) and  $C(x)$  in Eq. (B.74).

## B.4. Mermin's Formula and Optical Conductivity

Using the Mermin's equation for the susceptibility [92, 169] we have:

$$\chi_M(\mathbf{q}, \omega) = \frac{(1 - i\omega\tau)\chi(\mathbf{q}, \omega + i\gamma)\chi(\mathbf{q}, 0)}{-i\omega\tau\chi(\mathbf{q}, 0) + \chi(\mathbf{q}, \omega + i\gamma)}, \quad (\text{B.96})$$

where  $\chi$  was calculated in the previous section and  $\tau$  is the relaxation time and  $\gamma$  the relaxation rate:  $\tau = 1/\gamma$ .

The longitudinal component of the optical conductivity is given by

$$\sigma_L(\mathbf{q}, \omega) = \frac{ie^2\omega}{q^2} \chi_M(\mathbf{q}, \omega), \quad (\text{B.97})$$

and taking the limit  $\mathbf{q} \rightarrow 0$

$$\sigma(\omega) = \lim_{\mathbf{q} \rightarrow 0} \sigma_L(\mathbf{q}, \omega), \quad (\text{B.98})$$

From the equations (B.25) we have the following long wavelength limits:

$$\chi(\mathbf{q}, 0) = -\frac{q}{4} - \frac{2k_F}{\pi} + \frac{q}{4} + O(q^2), \quad (\text{B.99a})$$

$$\chi(\mathbf{q}, \omega) = \frac{k_F q^2}{\pi \omega^2} - i \frac{q^2}{4\omega} + \begin{cases} \frac{q^2}{4\pi\omega} \ln \left( \frac{2k_F + \omega}{2k_F - \omega} \right) + i \frac{q^2}{4\omega} + O(q^4), & \omega < 2k_F \\ \frac{q^2}{4\pi\omega} \ln \left( \frac{2k_F + \omega}{\omega - 2k_F} \right) + O(q^4), & \omega > 2k_F. \end{cases} \quad (\text{B.99b})$$

The limit (B.98) can be written as:

$$\sigma(\omega) = (1 - i\omega\tau) \sigma_M(\omega + i\gamma) \lim_{\mathbf{q} \rightarrow 0} \frac{\chi(\mathbf{q}, 0)}{-i\omega\tau\chi(\mathbf{q}, 0) + \chi(\mathbf{q}, \omega + i\gamma)}, \quad (\text{B.100})$$

*We can separate those two limits because both are finite.*

where, using (B.99):

$$\begin{aligned} \sigma_M(\omega + i\gamma) &= \lim_{\mathbf{q} \rightarrow 0} \frac{ie^2\omega}{q^2} \chi(\mathbf{q}, \omega + i\gamma) = \\ &ie^2\omega \frac{k_F}{\pi\omega^2} + e^2\omega \frac{1}{4\omega} + ie^2\omega \times \begin{cases} \frac{1}{4\pi\omega} \ln \left( \frac{2k_F + \omega}{2k_F - \omega} \right) + i \frac{1}{4\omega}, & \omega < 2k_F \\ \frac{1}{4\pi\omega} \ln \left( \frac{2k_F + \omega}{\omega - 2k_F} \right), & \omega > 2k_F, \end{cases} \end{aligned} \quad (\text{B.101})$$

taking the  $q \rightarrow 0$  limit with the help of (B.99) we have

$$\lim_{\mathbf{q} \rightarrow 0} \frac{\chi(\mathbf{q}, 0)}{-i\omega\tau\chi(\mathbf{q}, 0) + \chi(\mathbf{q}, \omega + i\gamma)} = \frac{1}{-i\omega\tau}, \quad (\text{B.102})$$

and so:

$$\sigma(\omega) = \frac{1}{4} + i \frac{k_F}{\pi\omega'} + \begin{cases} \frac{i}{4\pi} \ln \left[ \frac{2k_F - \omega'}{2k_F + \omega'} \right] - \frac{1}{4}, & \omega < 2k_F \\ \frac{i}{4\pi} \ln \left[ \frac{\omega' - 2k_F}{2k_F + \omega'} \right], & \omega > 2k_F \end{cases} \quad (\text{B.103})$$

where  $\omega' = \omega + i\gamma$ .

Using  $\ln r e^{i\theta} = \ln r + i\theta$  for  $r > 0$  and  $-\frac{\pi}{2} < \theta < \frac{\pi}{2}$  we have:

$$\frac{\sigma(\omega)}{\sigma_0} = -\frac{4k_F}{\pi(i\omega - \gamma)} + \frac{i}{2\pi} \ln \left[ \frac{(2k_F - \omega)^2 + \gamma^2}{(2k_F + \omega)^2 + \gamma^2} \right] + \frac{1}{\pi} \arctan \left( \frac{\omega - 2k_F}{\gamma} \right) - \frac{1}{\pi} \arctan \left( \frac{\omega + 2k_F}{\gamma} \right), \quad (\text{B.104})$$

## B. GRAPHENE SUSCEPTIBILITY AND OPTICAL CONDUCTIVITY

where  $\sigma_0 = e^2/4\hbar$ , and we separate the conductivity into a Drude and an interband terms:

$$\sigma(\omega) = \sigma_{\text{Drude}}(\omega) + \sigma_I(\omega), \quad (\text{B.105})$$

now we define  $\omega_F = E_F/\hbar$  so we can recover the units:

$$\frac{\sigma_{\text{Drude}}(\omega)}{\sigma_0} = -\frac{4\omega_F}{\pi} \frac{1}{i\omega - \gamma}, \quad (\text{B.106})$$

and the interband conductivity

$$\begin{aligned} \frac{\sigma_I(\omega)}{\sigma_0} = 1 + \frac{1}{\pi} \arctan\left(\frac{\omega - 2\omega_F}{\gamma}\right) - \frac{1}{\pi} \arctan\left(\frac{\omega + 2\omega_F}{\gamma}\right) + \\ + \frac{i}{2\pi} \ln\left[\frac{(2\omega_F - \omega)^2 + \gamma^2}{(2\omega_F + \omega)^2 + \gamma^2}\right]. \end{aligned} \quad (\text{B.107})$$

In figure B.2 we show the graphene conductivity given by Eq. B.105.

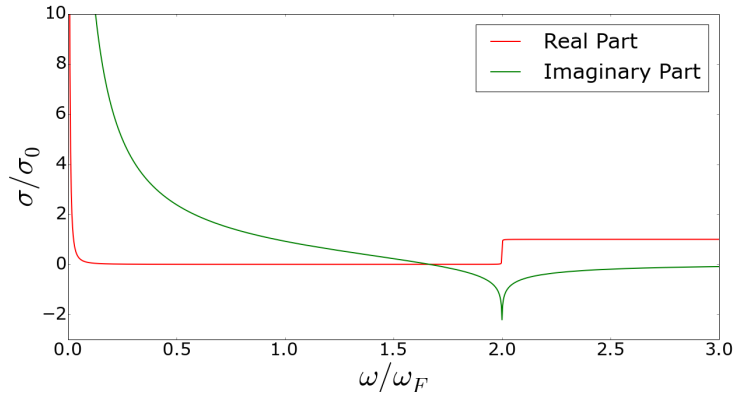


**Figure B.2.:** Graphene optical conductivity.  $E_F = 0.5$  eV,  $\hbar\gamma = 260$   $\mu$ eV.

# SIMPLIFIED FORM OF SBE IN TIME DOMAIN

# C

The Bloch equations for graphene was calculated in section and reads:

$$-\partial_t n_{c,\mathbf{k}} = \gamma_0 (n_{c,\mathbf{k}} - f_{c,\mathbf{k}}) - i\Omega_{\mathbf{k}}(t)\Delta p_{\mathbf{k}}, \quad (\text{C.1a})$$

$$-\partial_t n_{v,\mathbf{k}} = \gamma_0 (n_{v,\mathbf{k}} - f_{v,\mathbf{k}}) + i\Omega_{\mathbf{k}}(t)\Delta p_{\mathbf{k}}, \quad (\text{C.1b})$$

$$(\partial_t - i\omega_{\mathbf{k}} + \gamma_p) p_{cv,\mathbf{k}} = i\Omega_{\mathbf{k}}(t)\Delta n_{\mathbf{k}}, \quad (\text{C.1c})$$

$$(\partial_t + i\omega_{\mathbf{k}} + \gamma_p) p_{vc,\mathbf{k}} = -i\Omega_{\mathbf{k}}(t)\Delta n_{\mathbf{k}}, \quad (\text{C.1d})$$

where  $\hbar\omega_{\mathbf{k}} = 2E_{\mathbf{k}}$ ,  $\Delta n_{\mathbf{k}} = n_{c,\mathbf{k}} - n_{v,\mathbf{k}}$ ,  $\Delta p_{\mathbf{k}} = p_{cv,\mathbf{k}} - p_{vc,\mathbf{k}}$ ,  $f_{c/v,\mathbf{k}}$  is the Fermi-Distribution for the conduction/valence band, and  $\gamma_0(\gamma_p)$  is a relaxation term. The time dependence on  $n_{c/v,\mathbf{k}}$ ,  $p_{vc/cv,\mathbf{k}}$ , and  $\mathcal{E}$  is omitted, and we have defined:

$$\Omega_{\mathbf{k}}(t) = \frac{ea_0\mathcal{E}(t) \cdot \nabla_{\mathbf{k}}\Theta_{\mathbf{k}}}{2\hbar}, \quad (\text{C.2})$$

where  $a_0$  is the graphene lattice parameter.

Summing Eqs. (C.1a) and (C.1b) we obtain:

$$\partial_t(n_{c,\mathbf{k}} + n_{v,\mathbf{k}}) = -\gamma_0 (n_{c,\mathbf{k}} + n_{v,\mathbf{k}} - (f_{c,\mathbf{k}} + f_{v,\mathbf{k}})), \quad (\text{C.3})$$

which has the exact solution:

$$n_{c,\mathbf{k}}(t) + n_{v,\mathbf{k}}(t) = c(\mathbf{k})e^{-\gamma_0 t} + f_{c,\mathbf{k}} + f_{v,\mathbf{k}}, \quad (\text{C.4})$$

where  $c(\mathbf{k})$  depends on the initial conditions.

For a system that is initially in thermal equilibrium,  $c(\mathbf{k}) = 0$  and:

$$n_{c,\mathbf{k}}(t) + n_{v,\mathbf{k}}(t) = f_{c,\mathbf{k}} + f_{v,\mathbf{k}}, \quad (\text{C.5})$$

thus we introduce the deviation  $v_{\mathbf{k}}(t)$  through:

$$n_{c,\mathbf{k}}(t) = f_{c,\mathbf{k}} + v_{\mathbf{k}}(t), \quad (\text{C.6a})$$

$$n_{v,\mathbf{k}}(t) = f_{v,\mathbf{k}} - v_{\mathbf{k}}(t). \quad (\text{C.6b})$$

We also note that the complex conjugate of (C.1d) reads:

$$(\partial_t - i\omega_{\mathbf{k}} + \gamma_p) p_{vc,\mathbf{k}}^* = i\Omega_{\mathbf{k}}(t)\Delta n_{\mathbf{k}}, \quad (\text{C.7})$$

and using Eq. (C.1c)

$$(\partial_t - i\omega_{\mathbf{k}} + \gamma_p) (p_{cv,\mathbf{k}}(t) - p_{vc,\mathbf{k}}^*(t)) = 0, \quad (\text{C.8})$$

we find the solution:

$$p_{cv,\mathbf{k}}(t) = p_{vc,\mathbf{k}}^*(t) + c_1(\mathbf{k})e^{(-i\omega_{\mathbf{k}} - \gamma_p)t}, \quad (\text{C.9})$$

where again  $c_1(\mathbf{k})$  depends on the initial conditions. If we assume that the system is initially in thermal equilibrium it follows that  $c_1(\mathbf{k}) = 0$  and:

$$p_{vc,\mathbf{k}}(t) = p_{cv,\mathbf{k}}^*(t) \equiv x_{\mathbf{k}}(t) + iy_{\mathbf{k}}(t). \quad (\text{C.10})$$

The set of four complex equations (C.1) can be reduced to a set of three real equations for the functions  $x_{\mathbf{k}}$ ,  $y_{\mathbf{k}}$ , and  $v_{\mathbf{k}}$ . From Eqs. C.1 we have:

$$\partial_t v_{\mathbf{k}} = -\gamma_0 v_{\mathbf{k}} - 2\Omega_{\mathbf{k}}(t)y_{\mathbf{k}}, \quad (\text{C.11a})$$

$$(\partial_t + i\omega_{\mathbf{k}} + \gamma_p) [x_{\mathbf{k}} + iy_{\mathbf{k}}] = -i\Omega_{\mathbf{k}}(t) (\Delta n_{\mathbf{k}}^0 + 2v_{\mathbf{k}}), \quad (\text{C.11b})$$

where  $\Delta f_{\mathbf{k}} = f_{c,\mathbf{k}} - f_{v,\mathbf{k}}$ . From Eq. (C.11b) finally follows that:

$$\dot{x}_{\mathbf{k}} = -\gamma_p x_{\mathbf{k}} + \omega_{\mathbf{k}} y_{\mathbf{k}}, \quad (\text{C.12a})$$

$$\dot{y}_{\mathbf{k}} = -\omega_{\mathbf{k}} x_{\mathbf{k}} - y_{\mathbf{k}} \gamma_p + \Omega_{\mathbf{k}}(t) (2v_{\mathbf{k}} + \Delta f_{\mathbf{k}}), \quad (\text{C.12b})$$

$$\dot{v}_{\mathbf{k}} = -\gamma_0 v_{\mathbf{k}} - 2\Omega_{\mathbf{k}}(t)y_{\mathbf{k}}. \quad (\text{C.12c})$$

These latter set of equations is the one we have solved in chapter 4.



## KELDYSH POTENTIAL: A RPA ANALYSIS

---

The effective potential in the random phase approximation for a bare scalar potential  $V_0(\mathbf{q})$  is given by [4]:

$$V_{\text{RPA}}(\mathbf{q}) = \frac{V_0(\mathbf{q})}{1 - V_0(\mathbf{q})\chi(\mathbf{q})}, \quad (\text{D.1})$$

where the static susceptibility is written as:

$$\chi(\mathbf{q}) = \frac{1}{S} \sum_{\mathbf{k}, \mathbf{q}, \lambda_1, \lambda_2} \frac{f_{\mathbf{k}+\mathbf{q}, \lambda_1} - f_{\mathbf{k}, \lambda_2}}{E_{\mathbf{k}+\mathbf{q}, \lambda_1} - E_{\mathbf{k}, \lambda_2}} \langle \mathbf{k} + \mathbf{q}, \lambda_1 | \mathbf{k}, \lambda_2 \rangle. \quad (\text{D.2})$$

For a 2D material, de Coulomb potential reads:

$$V_0(\mathbf{q}) = \frac{e^2}{2\varepsilon_m q}, \quad (\text{D.3})$$

and thus the RPA potential reads:

$$V_{\text{RPA}}(\mathbf{q}) = \frac{e^2}{2\varepsilon_m \varepsilon_0 q - e^2 \chi(\mathbf{q})}. \quad (\text{D.4})$$

Supposing that in the long wavelength limit  $\mathbf{q} \rightarrow 0$   $\chi(\mathbf{q})$  is an analytic function and so it has a power series expansion, we can write:

$$e^2 \chi(\mathbf{q}) = -2\varepsilon_0 k_{\text{TF}} - 2\varepsilon_0 \varepsilon_i q - 2r_0 q^2 + O(q^3), \quad (\text{D.5})$$

where  $k_{\text{TF}}$ ,  $\varepsilon_i$  and  $r_0$  are the coefficients of the expansion. Substituting in (D.4):

$$V_{\text{RPA}}(\mathbf{q}) = \frac{e^2}{2\varepsilon_0 k_{\text{TF}} + (\varepsilon_m + \varepsilon_i)q + r_0 q^2}. \quad (\text{D.6})$$

For  $r_0 = 0$ , we have the Thomas-Fermi screened potential in a 2D material. For  $k_{\text{TF}} = 0$ , this potential reduces to the Keldysh potential[170, 6, 122]:

$$V_{\text{RPA}}(\mathbf{q}) = \frac{e^2}{2\varepsilon_0} \frac{1}{q(\varepsilon_m + \varepsilon_i + r_0 q)}. \quad (\text{D.7})$$

This expression can be obtained as the electrostatic field of a charge inside a thin slab with width  $w$  in the limit  $w \rightarrow 0$  [170]. Also can be obtained as the electrostatic potential of a charge bounded to a 2D material [122].

## D.1. Gapless 2D Dirac system

For the 2D Dirac equation with  $m = 0$ , we calculated the static susceptibility in appendix B. We can consider three cases:  $k_F = 0$ ,  $q < k_F$  and  $q \gg k_F$ .

**$k_F = 0$  CASE:**

In the first one, we have that the static susceptibility is (B.25):

$$\chi(q) = -\frac{N_f q}{16\hbar v_F} = -\frac{\varepsilon_0 c \pi \alpha N_f q}{4e^2 v_F}, \quad (\text{D.8})$$

where  $N_f$  is the degeneracy number,  $c$  is the speed of light, and  $\alpha$  the fine structure constant. In this case the exact RPA potential is:

*For graphene,  $N_f = 4$   
because of spin and valley  
degeneracy.*

$$V_{\text{RPA}}(\mathbf{q}) = \frac{e^2}{2\varepsilon_0 \left( \varepsilon_m + \alpha \pi \frac{N_f c}{8v_F} \right) q}, \quad (\text{D.9})$$

where the intrinsic dielectric constant is  $\varepsilon_i = \alpha \pi \frac{N_f c}{8v_F}$ , in agreement with [171]. In the case of graphene,  $v_F \approx c/300$ , and we have  $\varepsilon_i^{\text{graphene}} \approx 3.44$ . Note that (D.9) is an exact result in the static RPA for graphene: it was not necessary a power series expansion.

**$q < k_F$  CASE:**

For this case, the static susceptibility reads (B.84):

$$\chi(q) = -\frac{N_f k_F}{2\hbar v_F \pi} = \frac{2\varepsilon_0 c \alpha N_f k_F}{e^2 v_F}, \quad (\text{D.10})$$

thus the potential reads:

$$V_{\text{RPA}}(\mathbf{q}) = \frac{e^2}{2\varepsilon_0 (\varepsilon_m q + k_{\text{TF}}^0)}, \quad (\text{D.11})$$

where the Thomas-Fermi wavenumber for the gapless Dirac system is:

$$k_{\text{TF}}^0 = \frac{\alpha c N_f k_F}{v_F}. \quad (\text{D.12})$$

and for graphene  $k_{\text{TF}}^0 \approx 8.76 k_F$ .

$q \gg k_F$  CASE:

For  $k > k_F$ , the static susceptibility of a gapless Dirac system is (B.86):

$$\chi(q) = -\frac{N_f k_F}{2\hbar v_F \pi} + \frac{N_f q}{8\pi\hbar v_F} C\left(\frac{2k_F}{q}\right), \quad (\text{D.13})$$

with  $C(x) = x\sqrt{1-x^2} - \arccos(x)$ . The first term is the same of the previous section, and when  $q \gg k_F$  we can show that:

$$\chi(q) \rightarrow -\frac{N_f k_F}{\hbar\pi v_F} - \frac{N_f q}{16\hbar v_F} + O\left(\frac{k_F^2}{q^2}\right), \quad (\text{D.14})$$

in this case the potential is:

$$V_{\text{RPA}}(\mathbf{q}) = \frac{e^2}{2\varepsilon_0} \frac{1}{\left(\varepsilon_m + \alpha\pi\frac{N_f c}{8v_F}\right)q + k_{\text{TF}}^1} \quad (\text{D.15})$$

where in this case the Thomas-Fermi wavenumber is half of what we found in the previous case (D.12):

$$k_{\text{TF}}^1 = \frac{\alpha c N_f k_F}{2v_F}. \quad (\text{D.16})$$

## D.2. Gapped 2D Dirac system

The static susceptibility of a gapped Dirac system reads [172, 173]:

$$\chi(q) = -\frac{N_f E_F}{2\pi\hbar^2 v_F^2} \left[ 1 - \theta(q - 2k_F) \left( \frac{\sqrt{q^2 - 4k_F^2}}{2q} - \frac{\hbar^2 v_F^2 q^2 - 4\Delta^2}{4\hbar v_F q E_F} \times \right. \right. \\ \left. \left. \times \arctan \frac{\hbar v_F \sqrt{q^2 - 4k_F^2}}{2E_F} \right) \right], \quad (\text{D.17})$$

where  $\Delta$  is half the band gap and  $E_F = \sqrt{(\hbar v_F k_F)^2 + \Delta^2}$ , now we consider the same three cases of the previous section.

TMDC	MoS <sub>2</sub>	MoSe <sub>2</sub>	WS <sub>2</sub>	WSe <sub>2</sub>
$\Delta$ (eV)	0.797	0.648	0.685	0.524
$r_0^{\text{DFT}}$ (Å)	41.4	51.7	37.9	45.1
$r_0$ (Å)	12.1	14.8	14.0	18.3

**Table D.1.:** Comparison of the  $r_0$  parameter, gapped Dirac model for TMDCs and DFT [107].

**$k_F = 0$  CASE:**

In this case Eq. (D.17) becomes:

$$\chi(q) = -\frac{N_f \Delta}{2\pi \hbar^2 v_F^2} \left[ \frac{1}{2} + \frac{\hbar^2 v_F^2 q^2 - 4\Delta^2}{4\hbar v_F q \Delta} \arctan \frac{\hbar v_F q}{2\Delta} \right], \quad (\text{D.18})$$

and after a power series expansion up to second order in  $q$  we obtain:

$$\chi(q) = -\frac{N_f \Delta}{2\pi \hbar^2 v_F^2} \left[ \frac{1}{2} + \frac{\hbar^2 v_F^2 q^2 - 4\Delta^2}{4\hbar v_F q \Delta} \left( \frac{\hbar v_F q}{2\Delta} - \frac{1}{3} \left( \frac{\hbar v_F q}{2\Delta} \right)^3 \right) \right] + O(q^4), \quad (\text{D.19})$$

and after simplifying:

$$\chi(q) \approx -\frac{N_f q^2}{12\pi \Delta}, \quad (\text{D.20})$$

and the correspondent potential reads:

$$V(q) = \frac{e^2}{2\varepsilon_0 q} \frac{1}{\varepsilon_m + r_0 q}, \quad (\text{D.21})$$

where

$$r_0 = \frac{N_f \alpha \hbar c}{24\pi \Delta}, \quad (\text{D.22})$$

we can compare the RPA  $r_0$  with the ones from a DFT calculation for the TMDCs, and we show the results in the table D.1.

**$q < k_F$  CASE:**

From Eq. (D.17) we obtain:

$$\chi(q) = -\frac{N_f E_F}{2\pi \hbar^2 v_F^2}, \quad (\text{D.23})$$

thus the correspondent potential has the form of a Thomas-Fermi one:

$$V(q) = \frac{e^2}{2\varepsilon_0} \frac{1}{\varepsilon_m q + k_{\text{TF}}^1}, \quad (\text{D.24})$$

where:

$$k_{\text{TF}}^1 = \frac{\alpha c N_f E_F}{\hbar v_F^2}. \quad (\text{D.25})$$

$q \gg k_F$  CASE:

In this case is possible to show that:

$$\chi(q) \rightarrow -\frac{N_f q}{16\hbar v_F}, \quad (\text{D.26})$$

thus the potential is the same as we found before in Eq. (D.9):

$$V_{\text{RPA}}(q) = \frac{e^2}{2\varepsilon_0 \left( \varepsilon_m + \alpha\pi \frac{N_f c}{8v_F} \right) q}. \quad (\text{D.27})$$

### D.3. Final comments

The RPA approach is valid when  $N_f \gg 1$ , in the case of graphene and TMDCs, we have  $N_f = 4$ . Thus all the results presented in this appendix can be somewhat questioned. The electron-electron interaction of graphene was intensively studied and is still an active area of research with open questions [174]. The first aspect to note is that the effective intrinsic dielectric constant obtained for graphene in Eq. (D.9), that corresponds to an one-loop calculation, is not accurate. A two-loop analysis [175] shows a contribution of the same order of the one loop. This happens because the effective “fine structure” constant of graphene is  $\alpha c/v_F/\varepsilon_m \approx 2.2/\varepsilon_m$  and cannot be treated perturbatively in the same way as it is done in QED with  $\alpha \approx 137^{-1}$ . A renormalization group analysis of electron-electron correlations in graphene in the strong coupling regime [176, 174] shows that the electron-electron interaction is not screened and is marginally irrelevant in the charge neutrality point. The gapped Dirac equation has a different behavior [174] but has not yet had a careful analysis as the Dirac equation in the context of graphene.

Here we have shown that the Keldysh potential does not applies in graphene described by the Dirac equation, however, it can be applied as an effective potential in the gapped Dirac equation depending on the values of the Fermi moment. The evidences found in table D.1 shows that the static RPA of the Dirac model is not enough to describe the Keldysh potential. However, a more careful analysis is beyond the scope of this appendix.



# OPTICAL CONDUCTIVITY FOR A GAPPED DIRAC SYSTEM

---

In this appendix we will calculate the optical conductivity of a gapped Dirac system neglecting the electron-electron interactions. Those equations can be combined with the Elliot formula (see appendix F) to describe approximately the optical properties of TMDCs and hBN, two materials whose low energy excitations are described by a 2D gapped Dirac equation.

We consider the Dirac Hamiltonian:

$$H_0 = v_F \tau \sigma_1 p_x + v_F \sigma_2 p_y + \sigma_3 m v_F^2 - I \mu, \quad (\text{E.1})$$

where  $\sigma_i$  are the Pauli matrices,  $I$  is the identity matrix,  $v_F$  is a material dependent velocity,  $m$  the excitation mass,  $\mu$  the diagonal element of the Hamiltonian, and  $\tau = \pm$  is the valley index. From now we choose units with  $v_F = \hbar = e = 1$ . The eigenvectors and eigenvalues are:

$$\phi_\lambda(\mathbf{k}) = \sqrt{\frac{E_k + \lambda m}{2E_k}} \begin{pmatrix} 1 \\ \frac{\tau k_x - i k_y}{\lambda E_k + m} \end{pmatrix}, \quad (\text{E.2})$$

$$E_k = \sqrt{k^2 + m^2}. \quad (\text{E.3})$$

The dipole coupling Hamiltonian reads:

$$\hat{H}_I = \mathcal{E}_x(t) \hat{x} + \mathcal{E}_y(t) \hat{y}, \quad (\text{E.4})$$

The optical conductivity can be obtained from the polarization  $\mathbf{P}$  from  $\mathbf{J} = \partial_t \mathbf{P}$  [76], for a electric field with time dependence as  $\mathcal{E}(t) = \mathcal{E}_0 e^{-i\omega t}$ . For a electric field in the  $i$  direction, the current in the  $j$  direction will be:  $J_j = \sigma_{ij}(\omega) \mathcal{E}_i$ :

$$\sigma_{ij}(\omega) = -i\omega \frac{P_j(\omega)}{S \mathcal{E}_i}. \quad (\text{E.5})$$

## E.1. Polarization operator and dipole-coupling Hamiltonian

For obtaining the optical conductivity and the absorbance, we have to compute the expectation value of the polarization operator. Using the field operators:

$$\hat{\psi}(\mathbf{r}, t) = \frac{1}{\sqrt{S}} \sum_{\mathbf{k}, \lambda} \phi_{\lambda}(\mathbf{k}) \hat{a}_{\lambda \mathbf{k}}(t) e^{i\mathbf{k} \cdot \mathbf{r}}, \quad (\text{E.6})$$

the polarization operator reads:

$$\hat{\mathbf{P}}(t) = \int d\mathbf{r} \hat{\psi}^{\dagger}(\mathbf{r}, t) (-e\mathbf{r}) \hat{\psi}(\mathbf{r}, t). \quad (\text{E.7})$$

The integral can be explicitly computed with the help of the eigenfunctions of  $H_0$  in position space:  $\phi_{\mathbf{k}\lambda}(\mathbf{r}) = \phi_{\lambda}(\mathbf{k}) e^{i\mathbf{k} \cdot \mathbf{r}}$ . Using these eigenfunctions it follows that

$$\int d\mathbf{r} \phi_{\mathbf{k}'\lambda'}^{\dagger}(\mathbf{r}) \mathbf{r} \phi_{\mathbf{k}\lambda}(\mathbf{r}) = \langle \mathbf{k}', \lambda' | \mathbf{r} | \mathbf{k}, \lambda \rangle = \frac{\langle \mathbf{k}', \lambda' | [\mathbf{r}, H_0(\mathbf{r})] | \mathbf{k}, \lambda \rangle}{\lambda E_{\mathbf{k}} - \lambda' E_{\mathbf{k}'}}. \quad (\text{E.8})$$

Noting that  $[\mathbf{r}, H_0(\mathbf{r})] = -i(\tau \mathbf{u}_x \sigma_1 + \mathbf{u}_y \sigma_2)$  we obtain for the dipole matrix element the result:

$$\langle \mathbf{k}', \lambda' | -\mathbf{r} | \mathbf{k}, \lambda \rangle = -\delta_{\mathbf{k}\mathbf{k}'} \frac{iv_{\lambda'}(\mathbf{k})}{2\lambda' E_{\mathbf{k}}}, \quad (\text{E.9})$$

for  $\lambda \neq \lambda'$  (inter-band transitions). We defined the matrix element of the velocity operator  $(\tau \mathbf{u}_x \sigma_1 + \mathbf{u}_y \sigma_2)$  as

$$\mathbf{v}_{\lambda}(\mathbf{k}) = \langle \mathbf{k}, \lambda | (\tau \mathbf{u}_x \sigma_1 + \mathbf{u}_y \sigma_2) | \mathbf{k}, -\lambda \rangle, \quad (\text{E.10})$$

the dipole matrix elements in each direction read as:

$$d_{\lambda,x}(\mathbf{k}) \equiv \langle \mathbf{k}, \lambda | -x | \mathbf{k}, \lambda' \rangle = i \frac{iE_{\mathbf{k}} \lambda \sin \theta + \tau m \cos \theta}{2\lambda E_{\mathbf{k}}^2}, \quad (\text{E.11})$$

$$d_{\lambda,y}(\mathbf{k}) \equiv \langle \mathbf{k}, \lambda | -y | \mathbf{k}, \lambda' \rangle = i \frac{m \sin \theta - i\lambda E_{\mathbf{k}} \tau \cos \theta}{2\lambda E_{\mathbf{k}}^2}, \quad (\text{E.12})$$

with  $\theta = \arctan k_y/k_x$ .

Finally, we can express the polarization operator as:

$$\hat{\mathbf{P}}(\omega) = \sum_{\mathbf{k}\lambda} \mathbf{d}_{\lambda}(\mathbf{k}) \hat{\rho}_{\mathbf{k}\lambda, -\lambda}(\omega), \quad (\text{E.13})$$

to obtain the expectation value of the polarization operator we need to calculate the expectation value of the density matrix  $\hat{\rho}_{\mathbf{k}\lambda, -\lambda}(\omega)$ . This can be done with the SBE (3.64), where we neglect the electron-electron interaction terms:

$$-\omega p_{\lambda}(\mathbf{k}, \omega) = \omega_{\lambda \mathbf{k}} p_{\lambda}(\mathbf{k}, \omega) + \boldsymbol{\varepsilon}_0 \cdot \mathbf{d}_{-\lambda}(\mathbf{k}) \Delta f_{\lambda}(\mathbf{k}), \quad (\text{E.14})$$



where we recognized  $\mathbf{d}_{-\lambda,\lambda}^{\mathbf{k},\mathbf{k}} = \mathbf{d}_{-\lambda}(\mathbf{k})$ , and so:

$$p_\lambda(\mathbf{k}, \omega) = -\frac{\boldsymbol{\varepsilon}_0 \cdot \mathbf{d}_{-\lambda}(\mathbf{k}) \Delta f_\lambda(\mathbf{k})}{\omega + \omega_{\lambda\mathbf{k}} + i\gamma}, \quad (\text{E.15})$$

where we added a relaxation rate  $\gamma$ , as done before. The expectation value of the polarization reads:

$$\langle \hat{\mathbf{P}}(\omega) \rangle = -S \int \frac{d\mathbf{k}}{(2\pi)^2} \mathbf{d}_\lambda(\mathbf{k}) \frac{\boldsymbol{\varepsilon}_0 \cdot \mathbf{d}_{-\lambda}(\mathbf{k}) \Delta f_\lambda(\mathbf{k})}{\omega + \omega_{\lambda\mathbf{k}} + i\gamma}, \quad (\text{E.16})$$

and so the conductivity reads

$$\sigma_{ij}(\omega) = i\omega \sum_\lambda \int \frac{d\mathbf{k}}{(2\pi)^2} \frac{\mathbf{d}_{\lambda,i}(\mathbf{k}) \mathbf{d}_{-\lambda,j}(\mathbf{k}) \Delta f_\lambda(\mathbf{k})}{\omega + \omega_{\lambda\mathbf{k}} + i\gamma}, \quad (\text{E.17})$$

following appendix (E.1), where we show that in the Mermin Formula for the optical conductivity we need to make to multiply by a factor  $1 + i\frac{\gamma}{\omega}$ , doing this we have:

$$\sigma_{ij}(\omega) = i(\omega + i\gamma) \sum_\lambda \int \frac{d\mathbf{k}}{(2\pi)^2} \frac{\mathbf{d}_{\lambda,i}(\mathbf{k}) \mathbf{d}_{-\lambda,j}(\mathbf{k}) \Delta f_\lambda(\mathbf{k})}{\omega + \omega_{\lambda\mathbf{k}} + i\gamma}, \quad (\text{E.18})$$

now we consider the system at  $T = 0$  and with an effective chemical potential  $\mu_{\text{eff}} > 0$ , that means the system has the conductance band partially populated, so the electronic distribution is given by:

$$\Delta f_\lambda(\mathbf{k}) = -\lambda \theta(E_{\mathbf{k}} - \mu_{\text{eff}}), \quad (\text{E.19})$$

the neutral system corresponds to  $\mu_{\text{eff}} < m$ .

## E.2. Longitudinal conductivity

From Eq. (E.18) we have for the longitudinal conductivity  $i = j = x$ :

$$\sigma_{xx}(\omega) = -i(\omega + i\gamma) \sum_\lambda \lambda \int \frac{d\mathbf{k}}{(2\pi)^2} \frac{E_{\mathbf{k}}^2 \sin^2 \theta + m^2 \cos^2 \theta}{\omega + 2\lambda \sqrt{k^2 + m^2} + i\gamma} \frac{\theta(E_{\mathbf{k}} - \mu_{\text{eff}})}{4E_{\mathbf{k}}^4}, \quad (\text{E.20})$$

performing the angular integral we obtain:

$$\sigma_{xx}(\omega) = -i(\omega + i\gamma) \sum_\lambda \lambda \int \frac{k dk}{4\pi} \frac{E_{\mathbf{k}}^2 + m^2}{\omega + 2\lambda \sqrt{k^2 + m^2} + i\gamma} \frac{\theta(E_{\mathbf{k}} - \mu_{\text{eff}})}{4E_{\mathbf{k}}^4}, \quad (\text{E.21})$$

now performing the change of variables  $u^2 = E_{\mathbf{k}}^2 = k^2 + m^2$ , we have:

$$\sigma_{xx}(\omega) = -i(\omega + i\gamma) \sum_\lambda \lambda \int_{\mu_{\text{eff}}}^{\infty} \frac{du}{4\pi} \frac{u^2 + m^2}{\omega + 2\lambda u + i\gamma} \frac{1}{4u^3}, \quad (\text{E.22})$$

now doing the variable change  $z = 2\lambda u$  and calling  $\omega' = \omega + i\gamma$ , we have:

$$\sigma_{xx}(\omega) = -\frac{i(\omega + i\gamma)}{16\pi} \sum_{\lambda} \lambda \int_{2\lambda\mu_{\text{eff}}}^{\infty} du \frac{z^2 + 4m^2}{\omega' + z} \frac{1}{z^3}. \quad (\text{E.23})$$

Now we use the following primitives:

$$\int dz \frac{1}{z+a} \frac{1}{z^3} = -\frac{1}{2a^3} \left[ \frac{a(a-2z)}{z^2} + 2 \ln \left( \frac{a+z}{z} \right) \right], \quad (\text{E.24a})$$

$$\int dz \frac{1}{z+a} \frac{1}{z} = -\frac{1}{a} \ln \left( \frac{a+z}{z} \right), \quad (\text{E.24b})$$

therefore:

$$\begin{aligned} \sigma_{xx}(\omega) = -\frac{i\omega'}{16\pi} \sum_{\lambda} \lambda \left\{ \frac{1}{2\omega'^3} \left[ \frac{\omega'(\omega' - 4\lambda\mu_{\text{eff}})}{4\mu_{\text{eff}}^2} + 2 \ln \left( \frac{\omega' + 2\lambda\mu_{\text{eff}}}{2\lambda\mu_{\text{eff}}} \right) \right] 4m^2 + \right. \\ \left. + \frac{1}{\omega'} \ln \left( \frac{\omega' + 2\lambda\mu_{\text{eff}}}{2\lambda\mu_{\text{eff}}} \right) \right\}, \quad (\text{E.25}) \end{aligned}$$

and reordering:

$$\sigma_{xx}(\omega) = -\frac{i}{32\pi\omega'^2} \sum_{\lambda} \lambda \left\{ \frac{\omega'(\omega' - 4\lambda\mu_{\text{eff}})}{\mu_{\text{eff}}^2} m^2 + (8m^2 + 2\omega'^2) \ln \left( \frac{\omega' + 2\lambda\mu_{\text{eff}}}{2\lambda\mu_{\text{eff}}} \right) \right\}, \quad (\text{E.26})$$

and performing the sum in  $\lambda$ :

$$\sigma_{xx}(\omega) = -\frac{i\omega}{16\pi\omega'^3} \left\{ -\frac{4m^2\omega'}{\mu_{\text{eff}}} + (4m^2 + \omega'^2) \left[ \ln \left( \frac{\omega' + 2\mu_{\text{eff}}}{\omega' - 2\mu_{\text{eff}}} \right) + i\pi \right] \right\}, \quad (\text{E.27})$$

where we used that  $\ln(-1) = i\pi$  (this is the correct analytic continuation for this term), and the other logarithm term can be written as:

$$\begin{aligned} \ln \left( \frac{\omega' + 2\mu_{\text{eff}}}{\omega' - 2\mu_{\text{eff}}} \right) = -\frac{1}{2} \ln \left( \frac{(\omega - 2\mu_{\text{eff}})^2 + \gamma^2}{(\omega + 2\mu_{\text{eff}})^2 + \gamma^2} \right) + i \arctan \left( \frac{\omega - 2\mu_{\text{eff}}}{\gamma} \right) \\ - i \arctan \left( \frac{\omega + 2\mu_{\text{eff}}}{\gamma} \right), \quad (\text{E.28}) \end{aligned}$$

so the total conductivity reads:

$$\begin{aligned} \sigma_{xx}(\omega) = \frac{1}{16\pi} \left\{ i \frac{4m^2}{\mu_{\text{eff}}(\omega + i\gamma)} + \left( \frac{4m^2}{(\omega + i\gamma)^2} + 1 \right) \left[ \pi + \arctan \left( \frac{\omega - 2\mu_{\text{eff}}}{\gamma} \right) + \right. \right. \\ \left. \left. - \arctan \left( \frac{\omega + 2\mu_{\text{eff}}}{\gamma} \right) + \frac{i}{2} \ln \left( \frac{(\omega - 2\mu_{\text{eff}})^2 + \gamma^2}{(\omega + 2\mu_{\text{eff}})^2 + \gamma^2} \right) \right] \right\}, \quad (\text{E.29}) \end{aligned}$$

here  $\mu_{\text{eff}}$  should be replaced by  $m$  if  $\mu_{\text{eff}} < m$ . Also we have that  $\sigma_{yy}(\omega) = \sigma_{xx}(\omega)$ .

*At the end of the calculation, it is a bit tricky to take the correct value of the multivaluated logarithm: this is done checking some limits.*

### E.3. Transverse conductivity

The transverse conductivity,  $i = x, j = y$  in Eq. Eq. (E.18), reads:

$$\sigma_{xy}(\omega) = (\gamma - i\omega) \sum_{\lambda} \int \frac{d\mathbf{k}}{(2\pi)^2} \frac{\Delta f_{\lambda}(\mathbf{k})}{4E_{\mathbf{k}}^4} \frac{[i\tau\lambda E_{\mathbf{k}} \sin\theta + m \cos\theta] [m \sin\theta + i\tau\lambda E_{\mathbf{k}} \cos\theta]}{\omega + 2\lambda E_{\mathbf{k}} + i\gamma}, \quad (\text{E.30})$$

the terms with  $\sin\theta \cos\theta$  will disappear after the angular integration, so:

$$\sigma_{xy}(\omega) = (\gamma - i\omega)\tau \sum_{\lambda} \lambda \int \frac{d\mathbf{k}}{(2\pi)^2} \frac{1}{4E_{\mathbf{k}}^3} \frac{i\lambda m \sin^2\theta + i\lambda m \cos^2\theta}{\omega + 2\lambda E_{\mathbf{k}} + i\gamma} \theta(E_{\mathbf{k}} - \mu_{\text{eff}}), \quad (\text{E.31})$$

after the angular integration:

$$\sigma_{xy}(\omega) = 2(\omega + i\gamma)\tau m \sum_{\lambda} \int \frac{kdk}{4\pi} \frac{1}{4E_{\mathbf{k}}^3} \frac{1}{\omega + 2\lambda E_{\mathbf{k}} + i\gamma} \theta(E_{\mathbf{k}} - \mu_{\text{eff}}), \quad (\text{E.32})$$

now making the variable change  $z = 2\lambda E_{\mathbf{k}}$ , we have:

$$\sigma_{xy}(\omega) = 2(\omega + i\gamma)\tau m \sum_{\lambda} \int_{2\lambda\mu_{\text{eff}}}^{\infty} \frac{dz}{8\pi} \frac{1}{z^2} \frac{1}{\omega' + z}, \quad (\text{E.33})$$

where again we did  $\omega' = \omega + i\gamma$ . We have the following primitive:

$$\int dz \frac{1}{z^2} \frac{1}{z + a} = -\frac{1}{a^2} \left[ \frac{a}{z} + \ln\left(\frac{z}{a + z}\right) \right], \quad (\text{E.34})$$

and so

$$\sigma_{xy}(\omega) = \frac{\omega'\tau m}{4\pi} \sum_{\lambda} \frac{1}{\omega'^2} \left[ \frac{\omega'}{2\lambda\mu_{\text{eff}}} + \ln\left(\frac{2\lambda\mu_{\text{eff}}}{\omega' + 2\lambda\mu_{\text{eff}}}\right) \right], \quad (\text{E.35})$$

and performing the sum in  $\lambda$ :

$$\sigma_{xy}(\omega) = \frac{\tau m}{4\pi} \frac{1}{\omega'} \ln\left(\frac{-4\mu_{\text{eff}}^2}{\omega'^2 - 4\mu_{\text{eff}}^2}\right), \quad (\text{E.36})$$

we can write the logarithm as:

$$\ln\left(\frac{-4\mu_{\text{eff}}^2}{\omega'^2 - 4\mu_{\text{eff}}^2}\right) = \frac{1}{2} \ln\left(\frac{16\mu_{\text{eff}}^4}{\gamma^4 + (\omega^2 - 4\mu_{\text{eff}}^2)^2 + 2\gamma^2(\omega^2 + 4\mu_{\text{eff}}^2)}\right) + i \arctan\left(\frac{\omega + 2\mu_{\text{eff}}}{\gamma}\right) + i \arctan\left(\frac{\omega - 2\mu_{\text{eff}}}{\gamma}\right), \quad (\text{E.37})$$

the transverse conductivity reads:

$$\sigma_{xy}(\omega) = \frac{\tau m}{4\pi} \frac{1}{\omega + i\gamma} \left[ \frac{1}{2} \ln\left(\frac{16\mu_{\text{eff}}^4}{\gamma^4 + (\omega^2 - 4\mu_{\text{eff}}^2)^2 + 2\gamma^2(\omega^2 + 4\mu_{\text{eff}}^2)}\right) + i \arctan\left(\frac{\omega + 2\mu_{\text{eff}}}{\gamma}\right) + i \arctan\left(\frac{\omega - 2\mu_{\text{eff}}}{\gamma}\right) \right]. \quad (\text{E.38})$$

*We have that  $\sigma_{yx}(\omega) = -\sigma_{xy}(\omega)$ . Note that when we sum the contributions for the two valleys ( $\tau = \pm$ ) the transverse conductivity is zero.*

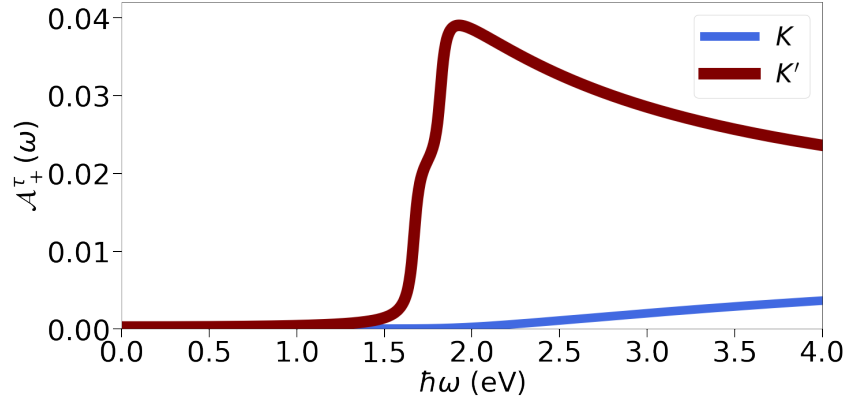


**Figure E.1.:** MoS<sub>2</sub> optical absorption for a circular polarized left handed wave. Parameters used are  $\hbar v_F = 2.76$  eV,  $mv_F^2 = 0.872$  eV,  $\Lambda_1 = 0.027$  eV, the effective mass is given by  $m_{s\tau}v_F^2 = mv_F^2 - s\tau\Lambda_1$ ,  $E_F = 0$ , and  $\hbar\gamma = 26$  meV.

#### E.4. Absorption by a circular polarized light

From  $\mathbf{J}_\pm = \begin{pmatrix} \sigma_L(\omega) & \sigma_T(\omega) \\ -\sigma_T(\omega) & \sigma_L(\omega) \end{pmatrix} \boldsymbol{\epsilon}_\pm$  we can obtain that  $\mathbf{J}_\pm = (\sigma_L(\omega) \pm i\sigma_T(\omega)) \boldsymbol{\epsilon}_\pm$ : this results comes from the particular case of a circular polarized electric field is an eigenvector of this conductivity tensor. From this we can define the circular polarized conductivity  $\sigma_\pm(\omega)$ , as the corresponding eigenvector.

For a polarized circular field, with  $\boldsymbol{\epsilon}_\pm = (\mathbf{u}_x \pm i\mathbf{u}_y) \boldsymbol{\epsilon}_0 e^{-i\omega t}$ , the conductivity reads:

$$\sigma_\pm(\omega) = \sigma_L(\omega) \pm i\sigma_T(\omega), \quad (\text{E.39})$$

where the  $\pm$  refers to the right- and left-hand circular polarization,  $\sigma_L(\omega) = \sigma_{xx}(\omega)$  and  $\sigma_T(\omega) = \sigma_{xy}(\omega) = -\sigma_{yx}(\omega)$ . The absorbance coefficient for small conductivities ( $\pi\alpha\sigma(\omega)/\sigma_0 \ll 1$ ) can be written as [15]:

$$\mathcal{A}_\pm(\omega) = \pi\alpha \Re \frac{\sigma_\pm(\omega)}{\sigma_0}, \quad (\text{E.40})$$

where  $\alpha$  is the fine structure constant. For a TMDC, the conductivity has a valley  $\tau$  and a spin  $s$  index. To use Eqs. (E.29) and (E.38) we need to make the substitution  $m \rightarrow m_{s\tau}$  and  $\mu_{\text{eff}} \rightarrow \mu_{\text{eff}}^{s\tau}$ . In the small absorption regime, we can decompose the absorbance for each valley as:

$$\mathcal{A}_\pm^\tau(\omega) = \sum_s \pi\alpha \Re \frac{\sigma_\pm^{s\tau}(\omega)}{\sigma_0}, \quad (\text{E.41})$$

and we plot each component of the absorbance for MoS<sub>2</sub> in Fig. E.1 for a left handed circular polarized field. For the right handed one, the result is exactly the same if we switch the K and K' valley labels.

# THE ELLIOT FORMULA FOR EXCITONS IN 2D MATERIALS

## F.1. Derivation of Elliot's formula

The solution of the homogeneous problem presented in equation (5.36) can be used to calculate the optical conductivity of the system. We now detail the derivation of Elliot's formula for TMDCs. First we decompose the excitonic wave function into a complete set of eigenfunctions of (5.36):

$$\Psi_\ell^{s\tau}(k) = \sum_n c_{\ell n}^{s\tau} \psi_{\ell, n}^{s\tau}(k) + \int_0^\infty dq g_\ell^{s\tau}(q) \psi_\ell^{s\tau}(q, k), \quad (\text{F.1})$$

where we have separated the discrete and continuum states of the exciton spectrum, with  $n$  and  $q$  the radial quantum numbers, respectively. We further recall the orthogonality relations:

$$\int_0^\infty dk k [\psi_{\ell, n'}^{s\tau}(k)]^\dagger \psi_{\ell, n}^{s\tau}(k) = \delta_{n', n} \quad (\text{F.2})$$

$$\int_0^\infty dk k [\psi_{\ell, n}^{s\tau}(k)]^\dagger \psi_\ell^{s\tau}(q, k) \psi = 0, \quad (\text{F.3})$$

$$\int_0^\infty dk k [\psi_\ell^{s\tau}(q', k)]^\dagger \psi_\ell^{s\tau}(q, k) = \delta(q - q'), \quad (\text{F.4})$$

The non-homogeneous equation (5.21) for  $p_-^{s\tau}(\mathbf{k}, \omega)$  (the resonant part), neglecting the term proportional to  $p_+^{s\tau}(\mathbf{k}, \omega)$ , after we substitute the expansion for  $\Psi_\ell^{s\tau}(k)$  into the eigenfunctions of the Kernel  $K^{BS}$  (5.34) that appears in Eq. (5.33), and integrating in  $\theta$ , becomes:

$$(\omega - K_\ell^{BS}) \left( \sum_n c_{\ell n}^{s\tau} \psi_{\ell, n}^{s\tau}(k) + \int_0^\infty dq g_\ell^{s\tau}(q) \psi_\ell^{s\tau}(q, k) \right) = -d_{\ell, +, x}^{s\tau}(k). \quad (\text{F.5})$$

where the angular decomposition of the dipole matrix element (5.7) is  $d_{\ell,\lambda,x}^{s\tau}(k) = \int_0^{2\pi} \frac{d\theta}{2\pi} d_{\lambda,x}^{s\tau}(\mathbf{k}) e^{-i(\ell+1)\theta}$ , is composed of two terms:  $d_{\ell,\lambda,x}^{s\tau} = d_{0,\ell,x}^{s\tau} \delta_{0,\lambda} + d_{-2,\lambda,x}^{s\tau} \delta_{-2,\ell}$ , remembering that the angular decomposition has an extra  $\theta$  phase:

$$d_{0,\lambda,x}^{s\tau}(k) = i \frac{E_{\mathbf{k}} \lambda + \tau m}{4\lambda E_{\mathbf{k}}^2}, \quad (\text{F.6a})$$

$$d_{-2,\lambda,x}^{s\tau}(k) = i \frac{-E_{\mathbf{k}} \lambda + \tau m}{4\lambda E_{\mathbf{k}}^2}. \quad (\text{F.6b})$$

Using the eigenfunction orthogonality and neglecting the continuum part  $\psi_{\ell}^{s\tau}(q, k)$ , we arrive at:

$$\sum_n (\omega - E_{\ell n}^{s\tau}) c_{\ell n}^{s\tau} \psi_{\ell,n}^{s\tau}(k) = -d_{\ell,+x}^{s\tau}(k), \quad (\text{F.7})$$

from where it follows the coefficients  $c_{\ell n}^{s\tau}$  after using (F.4):

$$c_{\ell n}^{s\tau} = -\frac{1}{\omega - E_{\ell n}^{s\tau}} \int_0^{\infty} k dk [\psi_{\ell,n}^{s\tau}(k)]^{\dagger} d_{\ell,+x}^{s\tau}(k), \quad (\text{F.8})$$

Using the last result, the exciton contribution to the polarization is, using equation (5.23), given by:

$$\frac{P(\omega)}{S} = -\frac{1}{2\pi} \sum_{s\tau, \ell=\{0,2\}, n} \left| \int_0^{\infty} q dq d_{\ell,+x}^{s\tau}(q) [\psi_{\ell n}^{s\tau}(q)]^* \right|^2 \frac{1}{\omega - E_{\ell n}^{s\tau} + i\gamma} \varepsilon_0, \quad (\text{F.9})$$

remembering here that we are using units such that  $v_F = \hbar = e = 1$ . We also introduced a phenomenological relaxation rate  $\gamma$ . Note that the  $\theta$  integral has been performed, and we are summing over all the spin/valley indexes. Now we define the weight function  $M_{n\ell}^{s\tau}$  as  $M_{n\ell}^{s\tau} = \frac{v_F^2}{2\pi} \left| \int_0^{\infty} q dq d_{\ell,+x}^{s\tau}(q) [\psi_{\ell n}^{s\tau}(q)]^* \right|^2$ , where we explicitly wrote the  $v_F^2$  term so the weight function is an adimensional quantity. The polarization follows as

$$\frac{P(\omega)}{S} = - \sum_{s\tau, \ell=\{0,2\}, n} \frac{M_{\ell n}^{s\tau}}{\omega - E_{\ell n}^{s\tau} + i\gamma} \varepsilon_0, \quad (\text{F.10})$$

where we have introduced a phenomenological relaxation rate  $\gamma$ . From  $\sigma(\omega) = -i\omega P(\omega)/S$ , the conductivity reads after reintroducing the units:

$$\frac{\sigma(\omega)}{\sigma_0} = 4i\hbar\omega \sum_{s\tau, \ell=\{0,2\}, n} \frac{M_{\ell n}^{s\tau}}{\hbar\omega - E_{\ell n}^{s\tau} + i\hbar\gamma}. \quad (\text{F.11})$$

Finally, the absorbance coefficient  $\mathcal{A}(\omega) = 1 - \mathcal{T}(\omega) - \mathcal{R}(\omega)$ , where  $\mathcal{T}(\omega)$  [ $\mathcal{R}(\omega)$ ] is the electromagnetic transmission [reflection] for a TEM wave, is given by:

$$\mathcal{A}(\omega) \approx \frac{\omega}{c\sqrt{\varepsilon_m}} \Im \{ \chi_{2D}(\omega) \} = \frac{4\pi\alpha\omega\gamma}{\sqrt{\varepsilon_m}} \sum_{s\tau, \ell=\{0,2\}, n} \frac{M_{\ell n}^{s\tau}}{(\omega - E_{\ell n}^{s\tau}/\hbar)^2 + \gamma^2}, \quad (\text{F.12})$$

where  $\alpha \approx 1/137$  is the fine-structure constant.

# TRANSFER MATRIX ELEMENTS FOR A PHOTONIC CRYSTAL

# G

## G.1. Unit cell made of two different dielectrics and a graphene sheet at the interfaces

The transfer matrix whose elements are [28]<sup>1</sup>

$$\begin{aligned}
 m_{11}^j &= [A_-^x \cos \alpha_2 + i(\chi + C_+^x) \sin \alpha_2] e^{-i\alpha_1}, \\
 m_{12}^j &= [B^x \cos \alpha_2 + i(\Delta + D^x) \sin \alpha_2] e^{i\alpha_1}, \\
 m_{21}^j &= [-B^x \cos \alpha_2 - i(\Delta + D^x) \sin \alpha_2] e^{-i\alpha_1}, \\
 m_{22}^j &= [A_+^x \cos \alpha_2 - i(\chi + C_-^x) \sin \alpha_2] e^{i\alpha_1},
 \end{aligned} \tag{G.1}$$

where  $x = \text{TE}, \text{TM}$  and the diverse parameters are given in appendix G.

The Snell-Decartes law hold:

$$\sqrt{\varepsilon_1 \mu_1} \sin \theta_1 = \sqrt{\varepsilon_2 \mu_2} \sin \theta_2, \tag{G.2}$$

and the dispersion relation is given by:

$$\begin{aligned}
 \cos g &= \cos \alpha_1 \cos \alpha_2 - (\chi + 2f^2 \beta_1^x \beta_2^x) \sin \alpha_1 \sin \alpha_2 \\
 &+ 2if (\beta_1^x \cos \alpha_1 \sin \alpha_2 + \beta_2^x \cos \alpha_2 \sin \alpha_1).
 \end{aligned} \tag{G.3}$$

with:

$$\beta_i^{TM} = Z_i^{TM}, \quad \beta_i^{TE} = \frac{1}{Z_i^{TE}}, \tag{G.4}$$

---

<sup>1</sup>there are some typos in the transfer matrix elements given in reference [28]

where:

$$\begin{aligned}
 k_i &= \sqrt{\varepsilon_i \mu_i} \omega / c \cos \theta_i, \\
 \alpha_i &= k_i z_i, \\
 A_{\pm}^x &= (1 \pm 2f \beta_1^x), \\
 B^x &= 2f \lambda^x \beta_1^x, \\
 C_{\pm}^x &= \pm 2f \beta_2^x + 2f^2 \beta_1^x \beta_2^x, \\
 D^x &= 2f^2 \lambda^x \beta_1^x \beta_2^x, \\
 \eta^x &= \frac{Z_1^x}{Z_2^x}, \\
 \Delta^x &= \frac{1}{2} (\eta^x - \eta^{x-1}), \\
 \chi^x &= \frac{1}{2} (\eta^x + \eta^{x-1}), \\
 f &= \frac{\sigma c \mu_0}{2}, \\
 Z_i^{\text{TE}} &= \frac{\sqrt{\mu_i \varepsilon_i}}{\mu_i} \cos \theta_i, \\
 Z_i^{\text{TM}} &= \frac{\sqrt{\mu_i \varepsilon_i}}{\varepsilon_i} \cos \theta_i,
 \end{aligned} \tag{G.5}$$

with  $\lambda^{\text{TM}} = +1$ ,  $\lambda^{\text{TE}} = -1$ .

## G.2. Unit cell made of one dielectric and a graphene sheet at the interface

When there is only one dielectric, with width  $z$  and  $\varepsilon, \mu$  permmissivity and permeability, intercalated by graphene sheets, the transfer matrix is given by:

$$M = \begin{pmatrix} (1 - \beta^x f) e^{i\alpha} & -\lambda^x \beta^x f e^{i\alpha} \\ \lambda^x \beta^x f e^{-i\alpha} & (1 + \beta^x f) e^{-i\alpha} \end{pmatrix}, \tag{G.6}$$

where  $\alpha = \sqrt{\mu \varepsilon} z \cos \theta$  with the dispersion relation:

$$\cos g = \cos \alpha - i \beta^x f \sin \alpha. \tag{G.7}$$



# BIBLIOGRAPHY

---

- [1] K. S. Novoselov, A. Mishchenko, A. Carvalho, and A. H. C. Neto, “2d materials and van der waals heterostructures,” *Science*, vol. 353, no. 6298, p. aac9439, 2016.
- [2] P. Miró, M. Audiffred, and T. Heine, “An atlas of two-dimensional materials,” *Chemical Society Reviews*, vol. 43, no. 18, pp. 6537–6554, 2014.
- [3] F. Xia, H. Wang, D. Xiao, M. Dubey, and A. Ramasubramaniam, “Two-dimensional material nanophotonics,” *Nat. Phot.*, vol. 8, no. 12, p. 899, 2014.
- [4] A. L. Fetter and J. D. Walecka, *Quantum Theory of Many-Particle Systems*. Dover Publications, 2003.
- [5] R. Knox, “Introduction to exciton physics,” in *Collective Excitations in Solids*, pp. 183–245, Springer, 1983.
- [6] P. Cudazzo, I. V. Tokatly, and A. Rubio, “Dielectric screening in two-dimensional insulators: Implications for excitonic and impurity states in graphene,” *Phys. Rev. B*, vol. 84, p. 085406, Aug 2011.
- [7] J. Frenkel, “On the transformation of light into heat in solids. i,” *Phys. Rev.*, vol. 37, no. 1, p. 17, 1931.
- [8] G. H. Wannier, “The structure of electronic excitation levels in insulating crystals,” *Phys. Rev.*, vol. 52, no. 3, p. 191, 1937.
- [9] L. Sham and T. Rice, “Many-particle derivation of the effective-mass equation for the wannier exciton,” *Phys. Rev.*, vol. 144, no. 2, p. 708, 1966.
- [10] G. D. Mahan, *Many-particle physics*. Springer Science & Business Media, 2013.
- [11] B. A. C. Amorim, *Phonons and electrons in 2D materials and layered structures*. Madrid: PhD Thesis, 2016.
- [12] Y. V. Bludov, A. Ferreira, N. M. R. Peres, and M. I. Vasilevskiy, “A primer on surface plasmon-polaritons in graphene,” *Int. J. of Mod. Phys. B*, vol. 27, no. 10, p. 1341001, 2013.

## BIBLIOGRAPHY

- [13] D. Basov, M. Fogler, and F. G. de Abajo, "Polaritons in van der waals materials," *Science*, vol. 354, no. 6309, p. aag1992, 2016.
- [14] T. Low, A. Chaves, J. D. Caldwell, A. Kumar, N. X. Fang, P. Avouris, T. F. Heinz, F. Guinea, L. Martin-Moreno, and F. Koppens, "Polaritons in layered two-dimensional materials," *Nat. Mater.*, vol. 16, no. 2, p. 182, 2017.
- [15] P. A. D. Gonçalves and N. M. R. Peres, *An Introduction to Graphene Plasmonics*. World Scientific, 2016.
- [16] M. J. Allen, V. C. Tung, and R. B. Kaner, "Honeycomb carbon: a review of graphene," *Chem. Rev.*, vol. 110, no. 1, pp. 132–145, 2009.
- [17] A. H. Castro Neto, F. Guinea, N. M. R. Peres, K. S. Novoselov, and A. K. Geim, "The electronic properties of graphene," *Rev. of Mod. Phys.*, vol. 81, no. 1, pp. 109–162, 2009.
- [18] N. M. R. Peres, "Colloquium: The transport properties of graphene: An introduction," *Rev. of Mod. Phys.*, vol. 82, no. 3, pp. 2673–2700, 2010.
- [19] F. Bonaccorso, Z. Sun, T. Hasan, and A. C. Ferrari, "Graphene photonics and optoelectronics," *Nat. Phot.*, vol. 4, no. 9, pp. 611–622, 2010.
- [20] Y. Zhang, L. Zhang, and C. Zhou, "Review of chemical vapor deposition of graphene and related applications," *Acc. of Chem. Res.*, vol. 46, no. 10, pp. 2329–2339, 2013.
- [21] R. R. Nair, P. Blake, A. N. Grigorenko, K. S. Novoselov, T. J. Booth, T. Stauber, N. M. Peres, and A. K. Geim, "Fine structure constant defines visual transparency of graphene," *Science*, vol. 320, no. 5881, pp. 1308–1308, 2008.
- [22] A. Ferreira, N. M. R. Peres, and A. C. Neto, "Confined magneto-optical waves in graphene," *Phys. Rev. B*, vol. 85, no. 20, p. 205426, 2012.
- [23] F. Hipolito, A. J. Chaves, R. M. Ribeiro, M. I. Vasilevskiy, V. M. Pereira, and N. M. R. Peres, "Enhanced optical dichroism of graphene nanoribbons," *Phys. Rev. B*, vol. 86, p. 115430, Sep 2012.
- [24] V. M. Pereira, R. Ribeiro, N. Peres, and A. C. Neto, "Optical properties of strained graphene," *EPL*, vol. 92, no. 6, p. 67001, 2010.
- [25] A. J. Chaves, T. Frederico, O. Oliveira, W. de Paula, and M. C. Santos, "Optical conductivity of curved graphene," *J. Phys. Condens. Matter*, vol. 26, no. 18, p. 185301, 2014.
- [26] P. Avouris and M. Freitag, "Graphene photonics, plasmonics, and optoelectronics," *IEEE J. Sel. Top. Quantum Electron*, vol. 20, pp. 72–83, Jan 2014.

- [27] Y. V. Bludov, N. M. R. Peres, and M. I. Vasilevskiy, "Unusual reflection of electromagnetic radiation from a stack of graphene layers at oblique incidence," *J. of Opt.*, vol. 15, no. 11, p. 114004, 2013.
- [28] T. Zhan, X. Shi, Y. Dai, X. Liu, and J. Zi, "Transfer matrix method for optics in graphene layers," *J. of Phys. Cond. Matt.*, vol. 25, no. 21, p. 215301, 2013.
- [29] F. Xia, T. Mueller, Y. Lin, A. Valdes-Garcia, and P. Avouris, "Ultrafast graphene photodetector," *Nat. Nanotechnol.*, vol. 4, p. 839, 2009.
- [30] M. Liu, X. Yin, E. Avila, B. Geng, T. Zentgraf, L. Ju, F. Wang, and X. Zhang, "A graphene-based broadband optical modulator," *Nature*, vol. 474, p. 64, 2011.
- [31] F. Garcia de Abajo, "Graphene plasmonics: Challenges and opportunities," *ACS Photonics*, vol. 1, p. 135, 2014.
- [32] L. Ju, B. Geng, J. Horng, C. Girit, M. Martin, Z. Hao, H. Bechtel, X. Liang, A. Zettl, Y. Shen, and F. Wang, "Graphene plasmonics for tunable terahertz metamaterials," *Nat. Nanotechnol.*, vol. 6, p. 630, 2011.
- [33] T. Echtermeyer, L. Britnell, P. Jasnos, A. Lombardo, R. Gorbachev, A. Grigorenko, A. Geim, A. Ferrari, and K. Novoselov, "Strong plasmonic enhancement of photovoltage in graphene," *Nat. Commun.*, vol. 2, p. 458, 2011.
- [34] Z. Sun, T. Hasan, F. Torrisi, D. Popa, G. Privitera, F. Wang, F. Bonaccorso, D. Basko, and A. Ferrari, "Graphene mode-locked ultrafast laser," *ACS Nano*, vol. 4, p. 803, 2010.
- [35] A. Grigorenko, M. Polini, and K. Novoselov, "Graphene plasmonics," *Nat. Phot.*, vol. 6, no. 11, p. 749, 2012.
- [36] A. J. Chaves, N. M. R. Peres, G. Smirnov, and N. A. Mortensen, "Hydrodynamic model approach to the formation of plasmonic wakes in graphene," *Phys. Rev. B*, vol. 96, no. 19, p. 195438, 2017.
- [37] A. Nagashima, N. Tejima, Y. Gamou, T. Kawai, and C. Oshima, "Electronic dispersion relations of monolayer hexagonal boron nitride formed on the Ni(111) surface," *Phys. Rev. B*, vol. 51, no. 7, pp. 4606–4613, 1995.
- [38] Y. Cai, L. Zhang, Q. Zeng, L. Cheng, and Y. Xu, "Infrared reflectance spectrum of bn calculated from first principles," *Solid State Commun.*, vol. 141, no. 5, pp. 262–266, 2007.
- [39] A. Kumar, T. Low, K. H. Fung, P. Avouris, and N. X. Fang, "Tunable light–matter interaction and the role of hyperbolicity in graphene–hbn system," *Nano letters*, vol. 15, no. 5, pp. 3172–3180, 2015.

## BIBLIOGRAPHY

- [40] J. D. Caldwell, A. V. Kretinin, Y. Chen, V. Giannini, M. M. Fogler, Y. Francescato, C. T. Ellis, J. G. Tischler, C. R. Woods, A. J. Giles, *et al.*, “Sub-diffractive volume-confined polaritons in the natural hyperbolic material hexagonal boron nitride,” *Nat. Commun.*, vol. 5, p. 5221, 2014.
- [41] S. Dai, Q. Ma, T. Andersen, A. Mcleod, Z. Fei, M. Liu, M. Wagner, K. Watanabe, T. Taniguchi, M. Thiemens, *et al.*, “Subdiffractive focusing and guiding of polaritonic rays in a natural hyperbolic material,” *Nat. Commun.*, vol. 6, p. 6963, 2015.
- [42] P. Li, M. Lewin, A. V. Kretinin, J. D. Caldwell, K. S. Novoselov, T. Taniguchi, K. Watanabe, F. Gaussmann, and T. Taubner, “Hyperbolic phonon-polaritons in boron nitride for near-field optical imaging and focusing,” *Nat. Commun.*, vol. 6, p. 7507, 2015.
- [43] B. E. A. Saleh and M. C. Teich, “Fundamentals of photonics. 2007,” *John Wiley & Sons, Inc*, pp. 260–269.
- [44] J. Lekner, “Reflection and refraction by uniaxial crystals,” *J. of Phys. Cond. Matt.*, vol. 3, no. 32, p. 6121, 1991.
- [45] T. Galvani, F. Paleari, H. P. C. Miranda, A. Molina-Sánchez, L. Wirtz, S. Latil, H. Amara, and F. m. c. Ducastelle, “Excitons in boron nitride single layer,” *Phys. Rev. B*, vol. 94, p. 125303, Sep 2016.
- [46] L. Wirtz, A. Marini, and A. Rubio, “Excitons in boron nitride nanotubes: Dimensionality effects,” *Phys. Rev. Lett.*, vol. 96, p. 126104, Mar 2006.
- [47] P. Cudazzo, L. Sponza, C. Giorgetti, L. Reining, F. Sottile, and M. Gatti, “Exciton band structure in two-dimensional materials,” *Phys. Rev. Lett.*, vol. 116, p. 066803, Feb 2016.
- [48] B. Radisavljevic, A. Radenovic, J. Brivio, i. V. Giacometti, and A. Kis, “Single-layer mos<sub>2</sub> transistors,” *Nat. Nanotechnol.*, vol. 6, no. 3, pp. 147–150, 2011.
- [49] F. Cadiz, E. Courtade, C. Robert, G. Wang, Y. Shen, H. Cai, T. Taniguchi, K. Watanabe, H. Carrere, D. Lagarde, *et al.*, “Excitonic linewidth approaching the homogeneous limit in mos<sub>2</sub>-based van der waals heterostructures,” *Phys. Rev. X*, vol. 7, no. 2, p. 021026, 2017.
- [50] O. A. Ajayi, J. V. Ardelean, G. D. Shepard, J. Wang, A. Antony, T. Taniguchi, K. Watanabe, T. F. Heinz, S. Strauf, X. Zhu, *et al.*, “Approaching the intrinsic photoluminescence linewidth in transition metal dichalcogenide monolayers,” *2D Materials*, vol. 4, no. 3, p. 031011, 2017.

- [51] K. F. Mak, C. Lee, J. Hone, J. Shan, and T. F. Heinz, "Atomically thin  $\text{mos}_2$ : a new direct-gap semiconductor," *Phys. Rev. Lett.*, vol. 105, no. 13, p. 136805, 2010.
- [52] S. Manzeli, D. Ovchinnikov, D. Pasquier, O. V. Yazyev, and A. Kis, "2d transition metal dichalcogenides," *Nat. Rev. Mater.*, vol. 2, no. 8, p. 17033, 2017.
- [53] Y. Li, A. Chernikov, X. Zhang, A. Rigosi, H. M. Hill, A. M. van der Zande, D. A. Chenet, E.-M. Shih, J. Hone, and T. F. Heinz, "Measurement of the optical dielectric function of monolayer transition-metal dichalcogenides:  $\text{Mos}_2$ ,  $\text{mose}_2$ ,  $\text{ws}_2$ , and  $\text{wse}_2$ ," *Phys. Rev. B*, vol. 90, no. 20, p. 205422, 2014.
- [54] H. Zeng, J. Dai, W. Yao, D. Xiao, and X. Cui, "Valley polarization in  $\text{mos}_2$  monolayers by optical pumping," *Nat. Nanotechnol.*, vol. 7, no. 8, p. 490, 2012.
- [55] A. Carvalho, M. Wang, X. Zhu, A. S. Rodin, H. Su, and A. H. C. Neto, "Phosphorene: from theory to applications," *Nat. Rev. Mater.*, vol. 1, no. 11, p. 16061, 2016.
- [56] T. Stauber, "Plasmonics in dirac systems: from graphene to topological insulators," *J. Phys. Condens. Matter*, vol. 26, no. 12, p. 123201, 2014.
- [57] A. Politano, V. Silkin, I. Nechaev, M. Vitiello, L. Viti, Z. Aliev, M. Babanly, G. Chiarello, P. Echenique, and E. Chulkov, "Interplay of surface and dirac plasmons in topological insulators: the case of  $\text{bi}_2\text{se}_3$ ," *Phys. Rev. Lett.*, vol. 115, no. 21, p. 216802, 2015.
- [58] E. V. Castro, K. S. Novoselov, S. Morozov, N. M. R. Peres, J. M. B. L. Dos Santos, J. Nilsson, F. Guinea, A. Geim, and A. H. C. Neto, "Biased bilayer graphene: semiconductor with a gap tunable by the electric field effect," *Phys. Rev. Lett.*, vol. 99, no. 21, p. 216802, 2007.
- [59] G. Li, A. Luican, J. L. Dos Santos, A. C. Neto, A. Reina, J. Kong, and E. Andrei, "Observation of van hove singularities in twisted graphene layers," *Nature Physics*, vol. 6, no. 2, p. 109, 2010.
- [60] J. L. dos Santos, N. M. R. Peres, and A. C. Neto, "Continuum model of the twisted graphene bilayer," *Phys. Rev. B*, vol. 86, no. 15, p. 155449, 2012.
- [61] Y. Chen, J. Xi, D. O. Dumcenco, Z. Liu, K. Suenaga, D. Wang, Z. Shuai, Y.-S. Huang, and L. Xie, "Tunable band gap photoluminescence from atomically thin transition-metal dichalcogenide alloys," *ACS Nano*, vol. 7, no. 5, pp. 4610–4616, 2013.
- [62] I. Guilhon, M. Marques, L. K. Teles, and F. Bechstedt, "Optical absorbance and band-gap engineering of  $(\text{bn})_{1-x}(\text{c}_2)_{x}$  two-dimensional alloys: Phase separation and composition fluctuation effects," *Phys. Rev. B*, vol. 95, no. 3, p. 035407, 2017.

## BIBLIOGRAPHY

- [63] P. A. Dirac, “Quantum mechanics of many-electron systems,” in *Proc. R. Soc. Lond. A*, vol. 123, pp. 714–733, The Royal Society, 1929.
- [64] F. Bloch, “Nuclear induction,” *Phys. Rev.*, vol. 70, no. 7-8, p. 460, 1946.
- [65] H. Haken, “Laser theory,” in *Light and Matter Ic/Licht und Materie Ic*, pp. 1–304, Springer, 1970.
- [66] A. Stahl, “Electrodynamics of the band-edge in a direct gap semiconductor,” *Solid State Commun.*, vol. 49, no. 1, pp. 91–93, 1984.
- [67] H. Haug, S. Koch, and M. Lindberg, “Optical nonlinearities and instabilities in semiconductors,” *Physica Scripta*, vol. 1986, no. T13, p. 178, 1986.
- [68] M. Lindberg and S. W. Koch, “Effective bloch equations for semiconductors,” *Phys. Rev. B*, vol. 38, no. 5, p. 3342, 1988.
- [69] H. Haug and S. W. Koch, *Quantum theory of the optical and electronic properties of semiconductors*, vol. 5. World Scientific, 2004.
- [70] M. Kira and S. W. Koch, *Semiconductor quantum optics*. Cambridge University Press, 2011.
- [71] W. Schäfer and M. Wegener, *Semiconductor optics and transport phenomena*. Springer Science & Business Media, 2013.
- [72] A. Girndt, F. Jahnke, A. Knorr, S. Koch, and W. Chow, “Multi-band bloch equations and gain spectra of highly excited ii-vi semiconductor quantum wells,” tech. rep., Sandia National Labs., Albuquerque, NM (United States), 1997.
- [73] W. W. Chow and S. W. Koch, “Theory of semiconductor quantum-dot laser dynamics,” *IEEE J. Quantum Electron*, vol. 41, no. 4, pp. 495–505, 2005.
- [74] S. Winnerl, M. Orlita, P. Plochocka, P. Kossacki, M. Potemski, T. Winzer, E. Malic, A. Knorr, M. Sprinkle, C. Berger, *et al.*, “Carrier relaxation in epitaxial graphene photoexcited near the dirac point,” *Phys. Rev. Lett.*, vol. 107, no. 23, p. 237401, 2011.
- [75] E. Malic, T. Winzer, E. Bobkin, and A. Knorr, “Microscopic theory of absorption and ultrafast many-particle kinetics in graphene,” *Phys. Rev. B*, vol. 84, p. 205406, Nov 2011.
- [76] J. D. Jackson, *Electrodynamics*. Wiley-VCH Verlag GmbH & Co. KGaA, 2007.
- [77] P. A. George, J. Strait, J. Dawlaty, S. Shivaraman, M. Chandrashekhara, F. Rana, and M. G. Spencer, “Ultrafast optical-pump terahertz-probe spectroscopy of the carrier relaxation and recombination dynamics in epitaxial graphene,” *Nano Letters*, vol. 8, no. 12, pp. 4248–4251, 2008.

- [78] M. Mittendorff, T. Winzer, E. Malic, A. Knorr, C. Berger, W. A. de Heer, H. Schneider, M. Helm, and S. Winnerl, “Anisotropy of excitation and relaxation of photogenerated charge carriers in graphene,” *Nano Letters*, vol. 14, no. 3, pp. 1504–1507, 2014. PMID: 24559191.
- [79] I. Gierz, J. C. Petersen, M. Mitrano, C. Cacho, I. E. Turcu, E. Springate, A. Stöhr, A. Köhler, U. Starke, and A. Cavalleri, “Snapshots of non-equilibrium dirac carrier distributions in graphene,” *Nat. Mater.*, vol. 12, no. 12, pp. 1119–1124, 2013.
- [80] B. Y. Sun, Y. Zhou, and M. W. Wu, “Dynamics of photoexcited carriers in graphene,” *Phys. Rev. B*, vol. 85, p. 125413, Mar 2012.
- [81] T. Li, L. Luo, M. Hupalo, J. Zhang, M. C. Tringides, J. Schmalian, and J. Wang, “Femtosecond population inversion and stimulated emission of dense dirac fermions in graphene,” *Phys. Rev. Lett.*, vol. 108, p. 167401, 2012.
- [82] A. F. Page, F. Ballout, O. Hess, and J. M. Hamm, “Nonequilibrium plasmons with gain in graphene,” *Phys. Rev. B*, vol. 91, p. 075404, Feb 2015.
- [83] G. Ni, L. Wang, M. Goldflam, M. Wagner, Z. Fei, A. McLeod, M. Liu, F. Keilmann, B. Özyilmaz, A. C. Neto, F. Fogler, and D. Basov, “Ultrafast optical switching of infrared plasmon polaritons in high-mobility graphene,” *Nat. Phot.*, vol. 10, p. 244, 2016.
- [84] J. M. Hamm, A. F. Page, J. Bravo-Abad, F. J. Garcia-Vidal, and O. Hess, “Nonequilibrium plasmon emission drives ultrafast carrier relaxation dynamics in photoexcited graphene,” *Phys. Rev. B*, vol. 93, p. 041408, Jan 2016.
- [85] A. Singh, K. I. Bolotin, S. Ghosh, and A. Agarwal, “Nonlinear optical conductivity of a generic two-band system with application to doped and gapped graphene,” *Phys. Rev. B*, vol. 95, no. 15, p. 155421, 2017.
- [86] A. Kumar, A. Nemilentsau, K. H. Fung, G. Hanson, N. X. Fang, and T. Low, “Chiral plasmon in gapped dirac systems,” *Phys. Rev. B*, vol. 93, p. 041413, Jan 2016.
- [87] Z. Fei, A. Rodin, G. Andreev, W. Bao, A. McLeod, M. Wagner, L. Zhang, Z. Zhao, M. Thiemens, G. Dominguez, *et al.*, “Gate-tuning of graphene plasmons revealed by infrared nano-imaging,” *Nature*, vol. 487, no. 7405, pp. 82–85, 2012.
- [88] J. Chen, M. Badioli, P. Alonso-González, S. Thongrattanasiri, F. Huth, J. Osmond, M. Spasenović, A. Centeno, A. Pesquera, P. Godignon, *et al.*, “Optical nano-imaging of gate-tunable graphene plasmons,” *Nature*, vol. 487, no. 7405, pp. 77–81, 2012.

## BIBLIOGRAPHY

- [89] V. G. Kravets, A. N. Grigorenko, R. R. Nair, P. Blake, S. Anissimova, K. S. Novoselov, and A. K. Geim, “Spectroscopic ellipsometry of graphene and an exciton-shifted van hove peak in absorption,” *Phys. Rev. B*, vol. 81, p. 155413, 2010.
- [90] T. Winzer, E. Malić, and A. Knorr, *Graphene Bloch Equations*, pp. 35–61. Dordrecht: Springer Netherlands, 2013.
- [91] L. Ju, B. Geng, J. Horng, C. Girit, M. Martin, Z. Hao, H. A. Bechtel, X. Liang, A. Zettl, Y. R. Shen, and F. Wang, “Graphene plasmonics for tunable terahertz metamaterials,” *Nat. Materials*, vol. 6, p. 630, 2011.
- [92] N. D. Mermin, “Lindhard dielectric function in the relaxation-time approximation,” *Phys. Rev. B*, vol. 1, pp. 2362–2363, Mar 1970.
- [93] M. Jablan, H. Buljan, and M. Soljačić, “Plasmonics in graphene at infrared frequencies,” *Phys. Rev. B*, vol. 80, p. 245435, Dec 2009.
- [94] A. J. Chaves, N. M. R. Peres, and T. Low, “Pumping electrons in graphene to the m point in the brillouin zone: Emergence of anisotropic plasmons,” *Phys. Rev. B*, vol. 94, no. 19, p. 195438, 2016.
- [95] D. J. Passos, G. B. Ventura, J. M. Lopes, J. M. B. Santos, and N. M. R. Peres, “Non-linear optical responses of crystalline systems: Results from a velocity gauge analysis,” *arXiv preprint arXiv:1712.04924*, 2017.
- [96] S. Xiao, X. Zhu, B.-H. Li, and N. A. Mortensen, “Graphene-plasmon polaritons: From fundamental properties to potential applications,” *Frontiers of Physics*, vol. 11, no. 2, pp. 1–13, 2016.
- [97] R. F. Frindt, “Optical absorption of a few unit-cell layers of  $\text{mos}_2$ ,” *Phys. Rev.*, vol. 140, pp. A536–A539, Oct 1965.
- [98] J. Wilson and A. Yoffe, “The transition metal dichalcogenides discussion and interpretation of the observed optical, electrical and structural properties,” *Advances in Physics*, vol. 18, no. 73, pp. 193–335, 1969.
- [99] K. S. Novoselov, A. K. Geim, S. V. Morozov, D. Jiang, Y. Zhang, S. V. Dubonos, I. V. Grigorieva, and A. A. Firsov, “Electric field effect in atomically thin carbon films,” *Science*, vol. 306, no. 5696, pp. 666–669, 2004.
- [100] M. Koperski, M. R. Molas, A. Arora, K. Nogajewski, A. O. Slobodeniuk, C. Faugeras, and M. Potemski, “Optical properties of atomically thin transition metal dichalcogenides: observations and puzzles,” *Nanophotonics*, vol. 6, no. 6, pp. 1289–1308, 2017.



- [101] K. F. Mak, C. Lee, J. Hone, J. Shan, and T. F. Heinz, "Atomically thin mos 2: a new direct-gap semiconductor," *Phys. Rev. Lett.*, vol. 105, no. 13, p. 136805, 2010.
- [102] N. M. R. Peres, R. M. Ribeiro, and A. H. Castro Neto, "Excitonic effects in the optical conductivity of gated graphene," *Phys. Rev. Lett.*, vol. 105, p. 055501, Jul 2010.
- [103] A. Molina-Sánchez, M. Palummo, A. Marini, and L. Wirtz, "Temperature-dependent excitonic effects in the optical properties of single-layer mos 2," *Phys. Rev. B*, vol. 93, no. 15, p. 155435, 2016.
- [104] A. Thilagam, "Exciton complexes in low dimensional transition metal dichalcogenides," *J. App. Phys.*, vol. 116, no. 5, p. 053523, 2014.
- [105] N. Lundt, S. Klembt, E. Cherotchenko, S. Betzold, O. Iff, A. V. Nalitov, M. Klaas, C. P. Dietrich, A. V. Kavokin, S. Höfling, *et al.*, "Room-temperature tamm-plasmon exciton-polaritons with a wse 2 monolayer," *Nat. Commun.*, vol. 7, p. 13328, 2016.
- [106] Y. V. Morozov and M. Kuno, "Optical constants and dynamic conductivities of single layer mos2, mose2, and wse2," *App. Phys. Lett.*, vol. 107, no. 8, p. 083103, 2015.
- [107] T. C. Berkelbach, M. S. Hybertsen, and D. R. Reichman, "Theory of neutral and charged excitons in monolayer transition metal dichalcogenides," *Phys. Rev. B*, vol. 88, no. 4, p. 045318, 2013.
- [108] T. C. Berkelbach, M. S. Hybertsen, and D. R. Reichman, "Bright and dark singlet excitons via linear and two-photon spectroscopy in monolayer transition-metal dichalcogenides," *Phys. Rev. B*, vol. 92, no. 8, p. 085413, 2015.
- [109] S. Gao, Y. Liang, C. D. Spataru, and L. Yang, "Dynamical excitonic effects in doped two-dimensional semiconductors," *Nano Letters*, vol. 16, no. 9, pp. 5568–5573, 2016.
- [110] A. Molina-Sánchez, D. Sangalli, K. Hummer, A. Marini, and L. Wirtz, "Effect of spin-orbit interaction on the optical spectra of single-layer, double-layer, and bulk mos<sub>2</sub>," *Phys. Rev. B*, vol. 88, no. 4, p. 045412, 2013.
- [111] D. Y. Qiu, H. Felipe, and S. G. Louie, "Optical spectrum of mos 2: many-body effects and diversity of exciton states," *Phys. Rev. Lett.*, vol. 111, no. 21, p. 216805, 2013.
- [112] G. Berghäuser and E. Malic, "Analytical approach to excitonic properties of mos<sub>2</sub>," *Phys. Rev. B*, vol. 89, no. 12, p. 125309, 2014.

BIBLIOGRAPHY

- [113] F. Wu, F. Qu, and A. H. MacDonald, “Exciton band structure of monolayer  $\text{mos}_2$ ,” *Phys. Rev. B*, vol. 91, p. 075310, Feb 2015.
- [114] J. Zhou, W.-Y. Shan, W. Yao, and D. Xiao, “Berry phase modification to the energy spectrum of excitons,” *Phys. Rev. Lett.*, vol. 115, no. 16, p. 166803, 2015.
- [115] A. Srivastava and A. Imamoğlu, “Signatures of bloch-band geometry on excitons: nonhydrogenic spectra in transition-metal dichalcogenides,” *Phys. Rev. Lett.*, vol. 115, no. 16, p. 166802, 2015.
- [116] A. Klots, A. Newaz, B. Wang, D. Prasai, H. Krzyzanowska, J. Lin, D. Caudel, N. Ghimire, J. Yan, B. Ivanov, *et al.*, “Probing excitonic states in suspended two-dimensional semiconductors by photocurrent spectroscopy,” *Sci. Rep.*, vol. 4, 2014.
- [117] A. Steinhoff, M. Rosner, F. Jahnke, T. Wehling, and C. Gies, “Influence of excited carriers on the optical and electronic properties of  $\text{mos}_2$ ,” *Nano Letters*, vol. 14, no. 7, pp. 3743–3748, 2014.
- [118] A. Chernikov, T. C. Berkelbach, H. M. Hill, A. Rigosi, Y. Li, O. B. Aslan, D. R. Reichman, M. S. Hybertsen, and T. F. Heinz, “Exciton binding energy and nonhydrogenic rydberg series in monolayer  $\text{ws}_2$ ,” *Phys. Rev. Lett.*, vol. 113, no. 7, p. 076802, 2014.
- [119] G.-B. Liu, W.-Y. Shan, Y. Yao, W. Yao, and D. Xiao, “Three-band tight-binding model for monolayers of group-vib transition metal dichalcogenides,” *Phys. Rev. B*, vol. 88, p. 085433, Aug 2013.
- [120] M. I. Vasilevskiy, D. G. Santiago-Pérez, C. Trallero-Giner, N. M. Peres, and A. Kavokin, “Exciton polaritons in two-dimensional dichalcogenide layers placed in a planar microcavity: Tunable interaction between two bose-einstein condensates,” *Phys. Rev. B*, vol. 92, no. 24, p. 245435, 2015.
- [121] A. Kormányos, G. Burkard, M. Gmitra, J. Fabian, V. Zólyomi, N. D. Drummond, and V. Fal’ko, “ $k \cdot p$  theory for two-dimensional transition metal dichalcogenide semiconductors,” *2D Materials*, vol. 2, no. 2, p. 022001, 2015.
- [122] A. Rodin, A. Carvalho, and A. C. Neto, “Excitons in anisotropic two-dimensional semiconducting crystals,” *Phys. Rev. B*, vol. 90, no. 7, p. 075429, 2014.
- [123] N. M. R. Peres, F. Guinea, and A. H. Castro Neto, “Coulomb interactions and ferromagnetism in pure and doped graphene,” *Phys. Rev. B*, vol. 72, p. 174406, Nov 2005.

- [124] E. H. Hwang, B. Y.-K. Hu, and S. Das Sarma, “Density dependent exchange contribution to  $\partial\mu/\partial n$  and compressibility in graphene,” *Phys. Rev. Lett.*, vol. 99, p. 226801, Nov 2007.
- [125] M. M. Ugeda, A. J. Bradley, S.-F. Shi, H. Felipe, Y. Zhang, D. Y. Qiu, W. Ruan, S.-K. Mo, Z. Hussain, Z.-X. Shen, *et al.*, “Giant bandgap renormalization and excitonic effects in a monolayer transition metal dichalcogenide semiconductor,” *Nat. Mater.*, vol. 13, no. 12, pp. 1091–1095, 2014.
- [126] S. Jo, N. Ubrig, H. Berger, A. B. Kuzmenko, and A. F. Morpurgo, “Mono- and bilayer ws<sub>2</sub> light-emitting transistors,” *Nano Letters*, vol. 14, no. 4, pp. 2019–2025, 2014.
- [127] M.-H. Chiu, C. Zhang, H.-W. Shiu, C.-P. Chuu, C.-H. Chen, C.-Y. S. Chang, C.-H. Chen, M.-Y. Chou, C.-K. Shih, and L.-J. Li, “Determination of band alignment in the single-layer mos<sub>2</sub>/wse<sub>2</sub> heterojunction,” *Nat. Commun.*, vol. 6, 2015.
- [128] C. Zhang, A. Johnson, C.-L. Hsu, L.-J. Li, and C.-K. Shih, “Direct imaging of band profile in single layer mos<sub>2</sub> on graphite: Quasiparticle energy gap, metallic edge states, and edge band bending,” *Nano Letters*, vol. 14, no. 5, pp. 2443–2447, 2014.
- [129] C. Zhang, Y. Chen, A. Johnson, M.-Y. Li, L.-J. Li, P. C. Mende, R. M. Feenstra, and C.-K. Shih, “Probing critical point energies of transition metal dichalcogenides: Surprising indirect gap of single layer wse<sub>2</sub>,” *Nano Letters*, vol. 15, no. 10, pp. 6494–6500, 2015.
- [130] A. Chernikov, T. C. Berkelbach, H. M. Hill, A. Rigosi, Y. Li, O. B. Aslan, D. R. Reichman, and T. F. Hybertsen, Mark S. and, “Exciton binding energy and non-hydrogenic rydberg series in monolayer ws<sub>2</sub>,” *Phys. Rev. Lett.*, vol. 113, p. 076802, Aug 2014.
- [131] Y. Zhang, T.-R. Chang, B. Zhou, Y.-T. Cui, H. Yan, Z. Liu, F. Schmitt, J. Lee, R. Moore, Y. Chen, *et al.*, “Direct observation of the transition from indirect to direct bandgap in atomically thin epitaxial mose<sub>2</sub>,” *Nat. Nanotechnol.*, vol. 9, no. 2, pp. 111–115, 2014.
- [132] K. Kośmider, J. W. González, and J. Fernández-Rossier, “Large spin splitting in the conduction band of transition metal dichalcogenide monolayers,” *Phys. Rev. B*, vol. 88, p. 245436, 2013.
- [133] V. N. Kotov, B. Uchoa, V. M. Pereira, F. Guinea, and A. C. Neto, “Electron-electron interactions in graphene: Current status and perspectives,” *Reviews of Modern Physics*, vol. 84, no. 3, p. 1067, 2012.

## BIBLIOGRAPHY

- [134] A. J. Chaves, G. D. Lima, W. de Paula, C. E. Cordeiro, A. Delfino, T. Frederico, and O. Oliveira, “Dynamical gap generation in graphene nanoribbons: An effective relativistic field theoretical model,” *Phys. Rev. B*, vol. 83, p. 153405, Apr 2011.
- [135] J. M. Tomczak and S. Biermann, “Optical properties of correlated materials: Generalized peierls approach and its application to  $\text{VO}_2$ ,” *Phys. Rev. B*, vol. 80, p. 085117, 2009.
- [136] J. P. Perdew, K. Burke, and M. Ernzerhof, “Generalized gradient approximation made simple,” *Phys. Rev. Lett.*, vol. 77, no. 18, p. 3865, 1996.
- [137] P. Giannozzi, S. Baroni, N. Bonini, M. Calandra, R. Car, C. Cavazzoni, D. Ceresoli, G. L. Chiarotti, M. Cococcioni, I. Dabo, *et al.*, “Quantum espresso: a modular and open-source software project for quantum simulations of materials,” *J. Phys.: Cond. Matt.*, vol. 21, no. 39, p. 395502, 2009.
- [138] H. J. Monkhorst and J. D. Pack, “Special points for brillouin-zone integrations,” *Phys. Rev. B*, vol. 13, no. 12, p. 5188, 1976.
- [139] A. Carvalho, R. Ribeiro, and A. C. Neto, “Band nesting and the optical response of two-dimensional semiconducting transition metal dichalcogenides,” *Phys. Rev. B*, vol. 88, no. 11, p. 115205, 2013.
- [140] K. F. Mak, K. He, C. Lee, G. H. Lee, J. Hone, T. F. Heinz, and J. Shan, “Tightly bound trions in monolayer  $\text{MoS}_2$ ,” *Nat. Mater.*, vol. 12, no. 3, pp. 207–211, 2013.
- [141] A. Chernikov, A. M. van der Zande, H. M. Hill, A. F. Rigosi, A. Velauthapillai, J. Hone, and T. F. Heinz, “Electrical tuning of exciton binding energies in monolayer  $\text{WS}_2$ ,” *Phys. Rev. Lett.*, vol. 115, no. 12, p. 126802, 2015.
- [142] Z. Wang, L. Zhao, K. F. Mak, and J. Shan, “Probing the spin-polarized electronic band structure in monolayer transition metal dichalcogenides by optical spectroscopy,” *Nano letters*, vol. 17, no. 2, pp. 740–746, 2017.
- [143] A. Hanbicki, M. Currie, G. Kioseoglou, A. Friedman, and B. Jonker, “Measurement of high exciton binding energy in the monolayer transition-metal dichalcogenides  $\text{WS}_2$  and  $\text{WSe}_2$ ,” *Solid State Commun.*, vol. 203, pp. 16–20, 2015.
- [144] B. Zhu, X. Chen, and X. Cui, “Exciton binding energy of monolayer  $\text{WS}_2$ ,” *Sci. Rep.*, vol. 5, p. 9218, 2015.
- [145] H. M. Hill, A. F. Rigosi, C. Roquelet, A. Chernikov, T. C. Berkelbach, D. R. Reichman, M. S. Hybertsen, L. E. Brus, and T. F. Heinz, “Observation of excitonic rydberg states in monolayer  $\text{MoS}_2$  and  $\text{WS}_2$  by photoluminescence excitation spectroscopy,” *Nano Letters*, vol. 15, no. 5, pp. 2992–2997, 2015.

- [146] M. Engel, M. Steiner, A. Lombardo, A. Ferrari, H. Lohneysen, P. Avouris, and R. Krupke, “Light–matter interaction in a microcavity-controlled graphene transistor,” *Nat Commun.*, vol. 3, p. 906, 2012.
- [147] A. Majumdar, J. Kim, J. Vuckovic, and F. Wang, “Electrical control of silicon photonic crystal cavity by graphene,” *Nano Lett.*, vol. 92, p. 68001, 2013.
- [148] X. Gan, R. Shiue, Y. Gao, K. Mak, X. Yao, L. Li, A. Szep, D. Walker, J. Hone, T. Heinz, and D. Englund, “High-contrast electrooptic modulation of a photonic crystal nanocavity by electrical gating of graphene,” *Nano Lett.*, vol. 13, p. 69, 2013.
- [149] P. W. Anderson, “Absence of diffusion in certain random lattices,” *Phys. Rev.*, vol. 109, p. 1492, 1958.
- [150] M. Segev, Y. Silberberg, and D. N. Christodoulides, “Anderson localization of light,” *Nat. Photon.*, vol. 7, p. 197, 2013.
- [151] H. Hu, A. Strybulevych, J. H. Page, S. E. Skipetrov, and B. A. van Tiggelen, “Localization of ultrasound in a three-dimensional elastic network,” *Nature Phys.*, vol. 4, no. 12, p. 945, 2008.
- [152] J. Billy, V. Josse, Z. Zuo, A. Bernard, B. Hambrecht, P. Lugan, D. Clement, L. Sanchez-Palencia, P. Bouyer, and A. Aspect, “Direct observation of anderson localization of matter waves in a controlled disorder,” *Nature*, vol. 453, no. 7197, p. 891, 2008.
- [153] A. Lagendijk, B. A. van Tiggelen, and D. S. Wiersma, “Fifty years of anderson localization,” *Phys. Today*, vol. 62, no. 8, p. 24, 2009.
- [154] F. Izrailev, A. Krokhin, and N. Makarov, “Anomalous localization in low-dimensional systems with correlated disorder,” *Phys. Rep.*, vol. 512, pp. 125–254, 2012.
- [155] J. Bertolotti, S. Gottardo, D. Wiersma, M. Ghulinyan, and L. Pavesi, “Optical necklace states in anderson localized 1d systems,” *Phys. Rev. Lett.*, vol. 94, no. 11, p. 113903, 2005.
- [156] D. Mogilevtsev, F. A. Pinheiro, R. R. dos Santos, S. B. Cavalcanti, and L. E. Oliveira, “Suppression of anderson localization of light and brewster anomalies in disordered superlattices containing a dispersive metamaterial,” *Phys. Rev. B*, vol. 82, p. 081105, Aug 2010.
- [157] D. Mogilevtsev, F. A. Pinheiro, R. R. dos Santos, S. B. Cavalcanti, and L. E. Oliveira, “Light propagation and anderson localization in disordered superlattices containing dispersive metamaterials: effects of correlated disorder,” *Phys. Rev. B*, vol. 84, no. 9, p. 094204, 2011.

## BIBLIOGRAPHY

- [158] A. A. Asatryan, L. C. Botten, M. A. Byrne, V. D. Freilikher, S. A. Gredeskul, I. V. Shadrivov, R. C. McPhedran, and Y. S. Kivshar, "Suppression of anderson localization in disordered metamaterials," *Phys. Rev. Lett.*, vol. 99, p. 193902, Nov 2007.
- [159] V. Kuzmiak and A. Maradudin, "Photonic band structures of one-and two-dimensional periodic systems with metallic components in the presence of dissipation," *Phys. Rev. B*, vol. 55, no. 12, p. 7427, 1997.
- [160] D. Soto-Puebla, F. Ramos-Mendieta, and M. Xiao, "Disorder-tunable photonic properties of periodic dielectric/metal superlattices," *International Journal of Modern Physics B*, vol. 18, no. 01, pp. 125–135, 2004.
- [161] P. Markos and C. M. Soukoulis, *Wave Propagation: From electrons to photonic crystals and left-handed materials*. Princeton University Press, 2008.
- [162] F. M. Izrailev and N. M. Makarov, "Localization in correlated bilayer structures: From photonic crystals to metamaterials and semiconductor superlattices," *Phys. Rev. Lett.*, vol. 102, p. 203901, May 2009.
- [163] F. M. Izrailev, T. Kottos, and G. P. Tsironis, "Hamiltonian map approach to resonant states in paired correlated binary alloys," *Phys. Rev. B*, vol. 52, pp. 3274–3279, Aug 1995.
- [164] F. M. Izrailev, S. Ruffo, and L. Tessieri, "Classical Representation of the 1D Anderson Model," *J. Phys. A*, vol. 31, no. cond-mat/9801226, p. 5263, 1998.
- [165] J. E. Sipe, P. Sheng, B. S. White, and M. H. Cohen, "Brewster anomalies: a polarization-induced delocalization effect," *Phys. Rev. Lett.*, vol. 60, no. 2, p. 108, 1988.
- [166] Y. V. Bludov, M. Vasilevskiy, and N. Peres, "Mechanism for graphene-based optoelectronic switches by tuning surface plasmon-polaritons in monolayer graphene," *EPL*, vol. 92, no. 6, p. 68001, 2010.
- [167] A. A. Chabanov, M. Stoytchev, and A. Z. Genack, "Statistical signatures of photon localization," *Nature*, vol. 404, no. 6780, p. 850, 2000.
- [168] C. Bena and G. Montambaux, "Remarks on the tight-binding model of graphene," *New Journal of Physics*, vol. 11, no. 9, p. 095003, 2009.
- [169] A. K. Das, "The relaxation-time approximation in the RPA dielectric formulation," *J. Phys. F*, vol. 5, no. 11, p. 2035, 1975.
- [170] L. V. Keldysh, "Excitons and polaritons in semiconductor/insulator quantum wells and superlattices," *Superlattices and Microstructures*, vol. 4, no. 4-5, pp. 637–642, 1988.

- [171] T. Ando, "Screening effect and impurity scattering in monolayer graphene," *Journal of the Physical Society of Japan*, vol. 75, no. 7, p. 074716, 2006.
- [172] E. V. Gorbar, V. P. Gusynin, V. A. Miransky, and I. A. Shovkovy, "Magnetic field driven metal-insulator phase transition in planar systems," *Phys. Rev. B*, vol. 66, no. 4, p. 045108, 2002.
- [173] P. K. Pyatkovskiy, "Dynamical polarization, screening, and plasmons in gapped graphene," *J. Phys. Condens. Matter*, vol. 21, no. 2, p. 025506, 2008.
- [174] V. N. Kotov, B. Uchoa, V. M. Pereira, F. Guinea, and A. H. Castro Neto, "Electron-electron interactions in graphene: Current status and perspectives," *Rev. Mod. Phys.*, vol. 84, pp. 1067–1125, Jul 2012.
- [175] V. N. Kotov, B. Uchoa, and A. C. Neto, "Electron-electron interactions in the vacuum polarization of graphene," *Physical Review B*, vol. 78, no. 3, p. 035119, 2008.
- [176] D. Son, "Quantum critical point in graphene approached in the limit of infinitely strong coulomb interaction," *Physical Review B*, vol. 75, no. 23, p. 235423, 2007.